GEOLOGY AND MINERALIZATION IN THE VICINITY OF THE MORNING STAR PRECIOUS-METAL DEPOSIT OF THE IVANPAH MOUNTAINS, SAN BERNARDINO COUNTY, CALIFORNIA.

by

Ronald Wynn Sheets

Dissertation submitted to the Faculty of
Virginia Tech
in partial fulfillment of the requirements for the degree of

DOCTOR OF PHILOSOPHY

in

Geology

APPROVED:

Robert J. Bodnar

James R. Craig

J. Donald Rimstidt

Richard D. Law

Robert J. Tracy

September, 1996

Blacksburg, Virginia

Keywords: epithermal, Mojave Desert, gold, silver

GEOLOGY AND MINERALIZATION IN THE VICINITY OF THE MORNING STAR PRECIOUS-METAL DEPOSIT OF THE IVANPAH MOUNTAINS, SAN BERNARDINO COUNTY, CALIFORNIA.

by

Ronald Wynn Sheets

Committee Chairmen: Robert J. Bodnar and James R. Craig
Geology

(ABSTRACT)

Disseminated precious-metal mineralization occurs at the Morning Star deposit, in the upper-plate of the Morning Star thrust which represents intermediate age (105 and 90 Ma) faulting along the Mesozoic foreland fold and thrust belt (MFFTB). Deformation along the Morning Star thrust consists of both ductile and brittle events, and is different than deformation on other structures in the MFFTB in the northeastern Mojave Desert. The different style and episodic nature of deformation, together with the spatial relationship to the Teutonia batholith, accounts for mineralization on the Morning Star thrust and the absence of mineralization on other thrusts in the belt.

Two stages of mineralization have been identified in the Morning Star deposit. Six distinct types of electrum have been identified. Electrum occurs as free grains, fracture fillings, or as inclusions in minerals during primary mineralization, and as rims around early electrum or as intergrowths with covellite and acanthite during secondary mineralization. Textures and compositions of the electrum and Ag+Au-sulfides indicate Au and Ag remobilization was isochemical in the lower portions of the deposit, while remobilization at upper levels of the deposit resulted in gold enrichment.

Hydrothermal fluids (H_2O-CO_2-6 wt.% NaCl), that were driven by Late Cretaceous igneous activity, scavenged metals from the host rocks to form the Morning Star mineralization. Early mineralization is syn-tectonic, but the bulk of the mineralization is post-tectonics. The bulk of the main stage mineralization was precipitated into open spaces at temperatures between 280° and 330°C by a combination of reduction and increased acidity of the fluid due to wall rock reactions. Ore grades have subsequently been increased by Au and Ag remobilization.

DEDICATION

To William Ralph Massey and Reed William Massey who both succeeded because they achieved their goals, however unorthodox those ends were. They taught me all about success, but nothing about struggle. To Reverend Dolores Santos Sheets and Elton Craig Sheets who taught me to struggle and gave me the freedom to do so. May we always remember to struggle instead of accepting the cheap successes.

And especially to Carmen Barcenas and Dolores Santos Sheets who many years ago, unbeknownst to us all, started the process that lead to this dissertation. My only regret is that they never saw its completion. *Que Dios se aserca al lado de ella al mismo tiempo que ella nos cuida.*

ACKNOWLEDGMENTS

Financial support for this study and educational expenses were provided by Vanderbilt Gold Corporation, the Virginia Mining and Mineral Resources Research Institution, Dr. Richard Lefebvre and the American Federation of Mineralogical Societies Fellowship and Dr. Robert Bodnar. I would like to thank Drs. Robert J. Bodnar, Richard D. Law, Robert J. Tracy, James R. Craig and J. Donald Rimstidt for helpful discussions pertaining to my scientific development and several aspects of this research. Jack Jordan, Jr., Howard Urband, Kent E. Ausburn, Dan Ruminski, Scott McKeag, Joe Squires, John Rathburn and Abe Dayani of Vanderbilt Gold Corporation and Heavy Metals Development provided logistical support, background information, access to the Morning Star Mine and encouragement during my visits to the California desert. Special thanks to Todd Solberg for help running the SEM and EMPA at VPI&SU. All mistakes and misrepresentations in this study are the 'fault' of the author.

TABLE OF CONTENTS

Abstract	ii
Dedication	iii
Acknowledgments	iii
Table of Contents	iv
List of Figures	viii
List of Plates	ix
List of Tables	ix

Chapter 1: Geologic Evolution and Metallogeny of the Northeastern Mojave Desert area.

Introduction	1
Geological Setting	3
Previous Studies	8
Summary of Regional Geology	12
Stratigraphy	13
Precambrian Metamorphic Complex	13
Sedimentary Stratigraphy	14
Autochthonous Platform Sedimentary Sequence	14
Allochthonous Miogeoclinal Sedimentary Sequence	15
Teutonia Batholith	16
Cenozoic Volcanic Rocks	17
Structure of the Mesozoic Foreland Fold and Thrust Belt	17
Structural Geology of the Ivanpah Mountains	21
Mineralization of the Ivanpah Mountains	24
Summary of Geochronology	26
Geologic History of the Ivanpah Mountains	29
Implications for Mineralization	38
Summary and Conclusions	40

Chapter 2: Structural Petrology and Alteration of the Morning Star Fault System.

Introduction 42
Geologic Setting 43
Previous Work 47
Morning Star Fault System 51
Ductile Fault Rocks 57
    Macroscale Structures 57
    Microscale Structures 63
    Quartz Crystal Fabric Analyses 64
Brittle Fault Rocks 71
Chemistry Across the Fault Zone 83
Grain-Size Distribution 86
Mineralogy 92
Discussion 100
    Relationship to Mesozoic Foreland Fold and Thrust Belt 106
Appendix 2.1. Analytical Techniques 108
Appendix 2.2. Major Element Chemistry 112

Chapter 3: Geology and Mineralization at the Morning Star Precious-Metal Deposit.

Introduction 117
Geology of the Morning Star Deposit 120
Structural Geology 121
Structure of the Ore Horizon 128
Geochemistry 132
Hydrothermal Alteration 137
Mineralization 140
    Primary mineralization 143
    Secondary mineralization 153
Fluid Inclusions 155
Lead Isotopes 161
Physicochemical Conditions of Mineralization 164

Discussion 170
Summary and Conclusions 175

Chapter 4: Gold and Silver Mineralization at the Morning Star Deposit, San Bernardino County, California: Secondary Enrichment and Remobilization of Gold and Silver.
Abstract 177
Introduction 178
Location and History 179
Geology of the Morning Star Deposit 182
Occurrence and Composition of Precious-metal Mineralization 185
Electrum in Unoxidized Ore 186
Pyrite-hosted Electrum 191
Quartz-hosted Electrum 194
Electrum in Oxidized Ore 194
Goethite-hosted Electrum 195
Core and Rim Electrum 200
Wire Electrum 201
Composition of Electrum 202
Silver and Silver-gold Sulfides 203
Discussion 208
Conclusions 215
Appendix 4.1: Sample Descriptions 216
Appendix 4.2: Analytical Techniques 219
Appendix 4.3: Mineral Chemistry Data 221

Literature Cited 225

Appendix A: Petrology of the Teutonia Batholith in the Ivanpah Mountains. 240
Regional Geology 240
Teutonia Batholith 241
Plutonic Phases within the Ivanpah Mountains 245

Oro Wash Granodiorite 245
Striped Hills Granodiorite 246
Ivanpah Granite 247
Kessler Springs Adamellite 250
Morning Star Dike 251
Delfonte Formation Volcanics 253
Dikes 253
Plutonic Phases outside the Ivanpah Mountains 254
Rock Springs Monzodiorite 254
Mid Hills Adamellite 255
Black Canyon Hornblende Gabbro 255
Teutonia Adamellite 256
Live Oak Canyon Granodiorite 256
Dikes 257
Composition and Mineral Chemistry of the Batholith 262
Whole Rock Chemistry 262
Mineral Chemistry 265
Pyroxenes 265
Fe-Ti Oxides 266
Amphiboles 266
Biotites 271
Feldspars 272
Conditions of Pluton Emplacement 273
Depth of Melting 273
Crystallization Models 274
Estimates of T, P, fH_2O and fO_2 276
Summary and Conclusions 282
Appendix A.1: Modal Compositions 284
Appendix A.2: Whole Rock Chemistry 288

Vita 293

List of Figures

Figure 1.1.	Mesozoic and Cenozoic tectonic and magmatic map	4
Figure 1.2.	Geologic Map of the Teutonia Batholith	6
Figure 1.3.	Geologic Map of the Ivanpah Mountains	9
Figure 1.4.	Compilation of Age Dates for the Teutonia Batholith	27
Figure 1.5.	Tectonomagmatic Evolution of the Ivanpah Mountains	32
Figure 2.1.	Geologic Map of the Teutonia Batholith	44
Figure 2.2.	Geologic Map of the Morning Star Fault System	48
Figure 2.4.	Regional Orientations of Foliations and Lineations	58
Figure 2.6.	Quartz Crystallographic Fabric Patterns	65
Figure 2.7.	Quartz Crystallographic Fabric Patterns for Domains	69
Figure 2.8.	Quartz Crystallographic Fabric Patterns for Regional Samples	72
Figure 2.12.	Chemistry Across the Fault Zone	84
Figure 2.13.	Grain-size Distribution of Gouge Samples	87
Figure 2.14.	Grain-size Distribution of Gouge Samples on Bench 4550	89
Figure 2.15.	XRD Pattern for Clay Gouge	94
Figure 3.1.	Generalized Geologic Map of the Morning Star Deposit	118
Figure 3.2.	Block Diagram of the Morning Star Ore Horizon	122
Figure 3.5.	Trace Element Geochemistry verses Depth Plots	135
Figure 3.6.	Correlation between Gold and Silver Analyses	138
Figure 3.7.	Generalized Paragenesis Diagram	141
Figure 3.10.	Histograms of Fluid Inclusion Microthermometry	158
Figure 3.11.	Lead $^{207}/_{204}$ verses $^{206}/_{204}$ and $^{208}/_{204}$ verses $^{206}/_{204}$ Plots	162
Figure 3.12.	Activity-Activity Diagrams	167
Figure 4.1.	Generalized Geology and Mineralization of the Morning Star Mine	180
Figure 4.2.	Composition of the Six Electrum Types	189
Figure 4.3.	Line Drawing of Pyrite-hosted Electrum	192
Figure 4.7.	100°C Isothermal Section of the Au-Ag-S Ternary Diagram	213
Figure A.1.	Modal Composition of Plutonic Rocks	243
Figure A.2.	Compositional Trends of Plutons	258
Figure A.3.	Whole Rock Chemistry	260
Figure A.4.	Classification of Amphiboles	267

Figure A.5. Classification of Biotites 269
Figure A.6. Al-in-Hornblende Barometry 280

List of Plates

Plate 2.3. Folded Mylonite 53
Plate 2.5. Photographs of Mylonites 60
Plate 2.9. Photographs of Morning Star Gouge 74
Plate 2.10. Photographs of Folded Gouge 79
Plate 2.11. Photographs of E-W Structures 81
Plate 3.3. Photographs of Foliated Fault Rocks 126
Plate 3.4. Photographs of Veins and Breccias 130
Plate 3.8. Photomicrograph of Early Deformed Vein 144
Plate 3.9. Photomicrograph of Typical Ore Assemblages 147
Plate 4.4. Photomicrograph of Geothite and Wire Electrum Types 196
Plate 4.5. Occurrence and Composition of Thick Electrum Rims 198
Plate 4.6. Elemental X-ray Maps of Wire and Thick Rim Electrum 204

List of Tables

Table 2.1. External and Internal Symmetry Elements for Petrofabric Diagrams 67
Table 2.2. Major Element Chemistry of Fault Rocks 77
Table 2.3. Mineralogy of Clay-size Fraction of Gouge Samples 93
Table 3.1. Trace Element Geochemistry 133
Table 3.2. Sphalerite Chemistry 151
Table 3.3. Fluid Inclusion Microthermometry 157
Table 3.4. Sphalerite-Pyrite-Argentite-Electrum Geothermometry 166
Table 4.1. Composition of Types of Electrum 187
Table 4.2. Representative Electron-microprobe Data 188
Table A.1. Modal Analyses 242
Table A.2. Average Chemical Analyses of Mafic Minerals 264

Chapter 1

Geologic Evolution and Metallogeny of the Northeastern Mojave Desert area.

Introduction

The interaction between Mesozoic, and possibly younger, igneous and tectonic activity produced numerous economic and sub-economic mineral occurrences in the Ivanpah Mountains and surrounding areas of the northeastern Mojave Desert (Tucker & Sampson, 1943a; Tucker & Sampson, 1943b; Bedford & Johnson, 1946; Wright et al., 1953; Hewett, 1956; Evans, 1971; Evans, 1974; Thompson, 1978; Wilkins, 1984; Barton et al., 1988, and references within). In order to understand mineralization in the northeastern Mojave Desert, the tectonic and magmatic evolution of the Ivanpah Mountains and surrounding areas was studied. This chapter reviews the geology of the Ivanpah Mountains and relates plutonism to structures within the Mesozoic foreland fold and thrust belt. The data presented in this chapter provides the background geology necessary for relating for unravelling the geologic history of the Morning Star deposit.

Precious-metal mineralization in the northeastern Mojave Desert, which occurs in a variety of host rocks ranging in age from Precambrian to Miocene (Wilkins, 1984), has become the target of resent exploration. Some of the more improtant gold deposits in the northeastern Mojave Desert include the Cretaceous (100 Ma) breccia-pipe-hosted Colloseum deposit in the Clark Mountains (Sharp, 1984), the Miocene (12 to 18 Ma) volcanic-hosted Hart district in the Castle Mountains (Ausburn, 1991; Capps & Moore, 1991) and the Morning Star deposit in the Ivanpah Mountains — the topic of this

dissertation. The Morning Star deposit is the only Ivanpah Mountain mineral occurence that produced significant quantities of metals in the past few decades. Because the Morning Star deposit is situated along the Morning Star fault system, an understanding of the tectonic and magmatic evolution of the Ivanpah Mountains and its relationship to regional tectonomagmatic evolution of the northeastern Mojave Desert is required to understand the genesis and timing of the Morning Star mineralization.

Mineralization at the Morning Star deposit is hosted by the Ivanpah granite in structurally prepared rocks deformed by movement along the Morning Star fault. Structural petrology of both the mylonite and fault gouge along the Morning Star fault was conducted to relate deformation to regional Mesozoic faulting within the Ivanpah Mountains and to unravel the structurally controlled nature of the Morning Star deposit (Chapter 2). The ultimate goal of the study is to understand the evolution of the Morning Star mineralization, so the remainder of the dissertation concentrates on constraining conditions of hypogene mineralization (Chapter 3) and remobilization of gold and silver at the deposit (Chapter 4).

To better constrain regional tectonic and magmatic activity and relate the regional tectonomagmatic activity to mineralization, a re-evaluation of the geology of the Ivanpah Mountains area was undertaken. Portions of the Mescal Range, Mineral Hills, Cima Dome, and Joshua 7 $^{1}/_{2}$ minute topographic sheets were mapped for geology and structure during the summer of 1988 and revisited briefly during February 1989 and April 1990. Detailed mapping concentrated on the eastern portions of the Ivanpah Mountains and especially the area around the Morning Star deposit. During fieldwork, samples were collected for petrographic investigation, major element chemistry, structural analyses and mineral deposit studies. Petrology and whole rock chemistry were performed on the plutonic phases of the Ivanpah Mountains (see Appendix A) to better characterize the

igneous intrusions in the vicinity of the deposit and to understand the geological evolution of the Ivanpah Mountains. The mapping results obtained during this study are compared to previous studies in the Ivanpah Mountains area and are presented here to establish the geologic evolution of the area.

Geological Setting

Crustal scale magmatic arcs and tectonic belts intersect in the northeastern Mojave Desert. The region is defined by the intersection of the eastern limit of both early and late Mesozoic foreland fold and thrust belts (Burchfiel & Davis, 1972; Burchfiel & Davis, 1975; Burchfiel & Davis, 1988) and Mesozoic magmatic arcs (Kistler, 1974; Barton et al., 1988), and lies between Tertiary extensional terranes (Howard & John, 1987; Dokka, 1989). The tectonic and magmatic blocks of interest to this study are shown in Figure 1.1 and the geology of the eastern Mojave Desert (indicated by the black rectangle in Figure 1.1) is shown on Figure 1.2. Multiple episodes of tectonic and magmatic activity, related to Andean-type subduction and back-arc basin formation, were activated as early as Permian time throughout the area (Burchfiel & Davis, 1972; Burchfiel & Davis, 1975; Walker, 1987). Hypozonal to epizonal plutonism related to the convergent plate motion has also been documented across the Mojave Desert (Anderson et al., 1989 and references within). The Ivanpah Mountains represent Jurassic and Cretaceous plutonism situated at the intersection of the eastern limits of the Mesozoic foreland fold and thrust belt, both of which are directly related to this subduction.

Decollement style brittle thrusting in the northern portions of the Mesozoic foreland fold and thrust belt switches to Precambrian crystalline basement involved ductile thrusting in the vicinity of the Ivanpah Mountains. The Mesozoic foreland fold and thrust

Figure 1.1. Mesozoic and Cenozoic tectonic and magmatic map of the southwestern United States showing the location of the study area (the black rectangle). The geology of the eastern Mojave Desert (study area) is shown in Figure 1.2. The map delineates structures after Burchfiel and Davis (1972; 1975), magmatism after Barton et al. (1988), the Mojave Extension Terrane (**M**) after Dokka, (1989) and the Colorado River Extension Terrane (**C**) after Howard and John (1987).

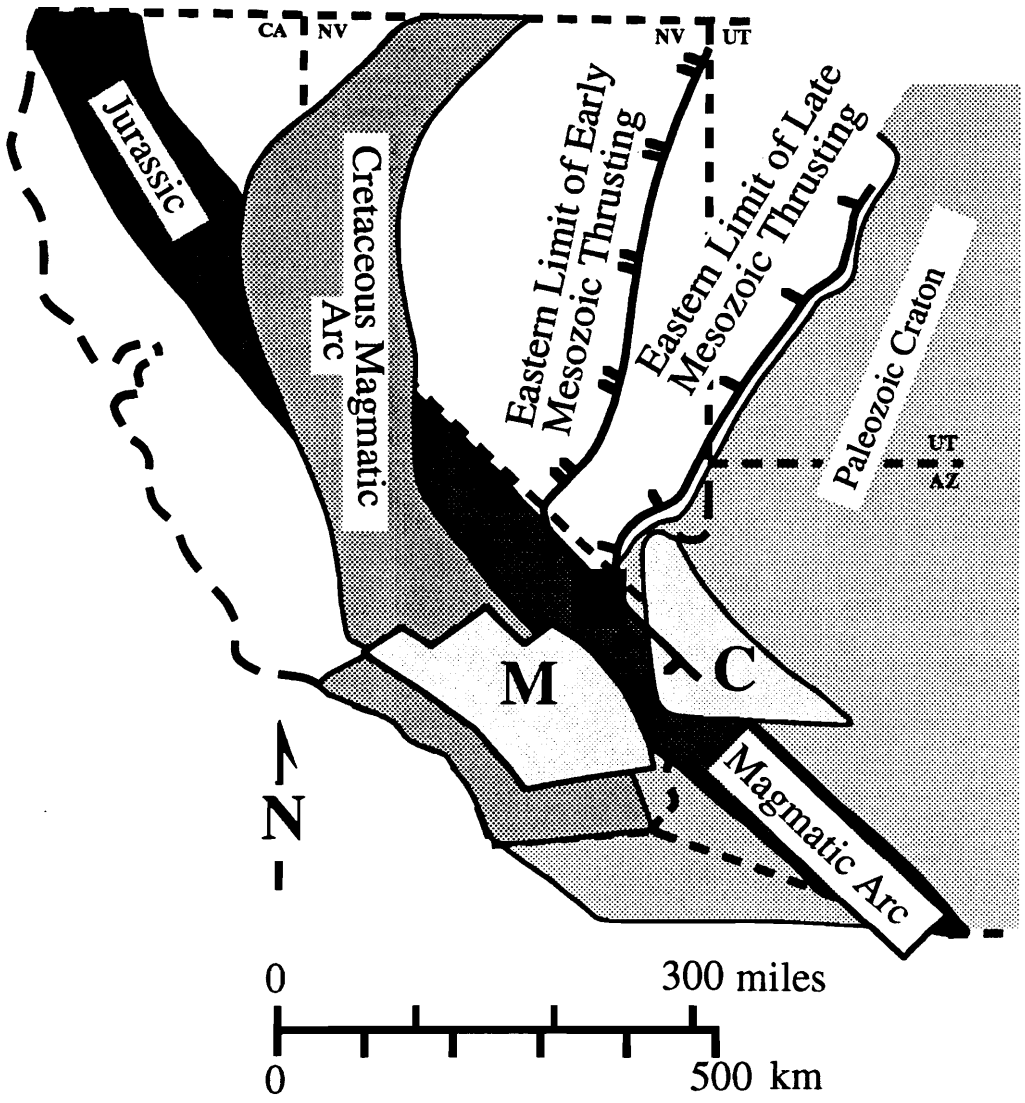
CA
NV
NV
UT
Jurassic
Cretaceous Magmatic Arc
Eastern Limit of Early Mesozoic Thrusting
Eastern Limit of Late Mesozoic Thrusting
Paleozoic Craton
UT
AZ
M
C
Magmatic Arc
N
0
300 miles
0
500 km

Figure 1.2. Generalized geologic map of the Teutonia batholith and surrounding areas [modified after Beckerman et al. (1982) with additional geology from Evans (1971; 1974), Burchfiel and Davis (1971; 1988), DeWitt et al. (1984) and this study]. A detailed map of the Ivanpah Mountains area (outlined) is shown in Figure 1.3. Faults shown on the map, listed from west to east, include Pachulka thrust (PT), Mesquite Pass thrust (MP), Mollusk Mine thrust (MMT), South fault (SF), Sterling thrust (ST), Mescal thrust (MT), Kokoweef fault (KF), Morning Star thrust (MS), Slaughterhouse fault (SHF), and New York Mountain thrust (NYM).

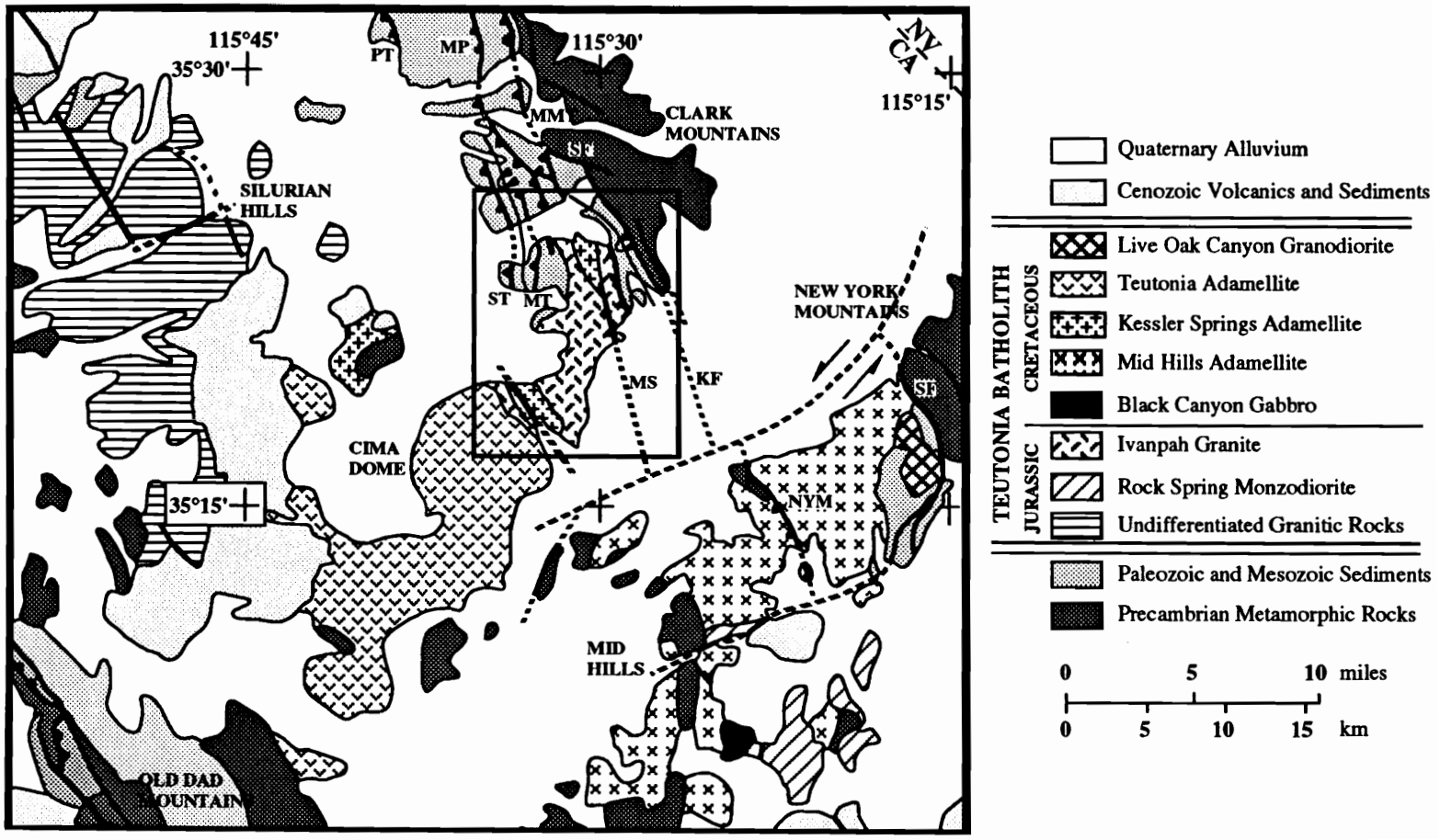
115°45'
35°30'
PT
MP
115°30'
MM
CLARK MOUNTAINS
SF
NV
CA
115°15'
SILURIAN HILLS
ST
MT
NEW YORK MOUNTAINS
MS
KF
SF
CIMA DOME
35°15'
NYM
MID HILLS
OLD DAD MOUNTAIN
Quaternary Alluvium
Cenozoic Volcanics and Sediments
TEUTONIA BATHOLITH
CRETACEOUS
Live Oak Canyon Granodiorite
Teutonia Adamellite
Kessler Springs Adamellite
Mid Hills Adamellite
Black Canyon Gabbro
JURASSIC
Ivanpah Granite
Rock Spring Monzodiorite
Undifferentiated Granitic Rocks
Paleozoic and Mesozoic Sediments
Precambrian Metamorphic Rocks
0 5 10 miles
0 5 10 15 km

belt steps southeastward from Paleozoic miogeoclinal sedimentary sequences into cratonic rocks and follows the eastern edge of the Jurassic magmatic arc in the northeastern Mojave Desert (Burchfiel & Davis, 1981). Thrusting in the Ivanpah Mountains and further south was complicated by intrusion of the Teutonia batholith (Figure 1.2) which constitutes the largest Mesozoic batholith in the eastern Mojave Desert (Beckerman et al., 1982). Regional metamorphic rocks are rare outside the Precambrian crystalline complex in the northeastern Mojave Desert compared with other areas of the southern California, but isotopic systematics exhibit regional Mesozoic and Early Cenozoic resetting (DeWitt et al., 1984; Labotka et al., 1985; Hoisch et al., 1988).

Previous Studies

The Ivanpah Quadrangle (1° X 2° map sheet) was originally mapped by Hewett (1956), during a regional geology and mineral resource reconnaissance study. Hewett (1956) originally assigned the name Teutonia Quartz monzonite (adamellite) to all granitoids in the Ivanpah Quadrangle. A portion of the Ivanpah Quadrangle containing the Ivanpah Mountains is shown in Figure 1.2. The geology of the Ivanpah Mountains proper is shown in Figure 1.3. Following Hewett's work, Evans (1971; 1974) remapped the structures and sedimentary rocks around the Striped Hills and Evening Star Spur of the western Ivanpah Mountains, but no attempt was made to distinguish plutonic phases of the Teutonia quartz monzonite. Thompson (1978) described the geology and mineral deposits in the Evening Star spur area. Regional structures and the tectonic evolution of the eastern Mojave Desert have recently been described by Burchfiel and Davis (1971; 1972; 1975; 1977; 1981; 1988) and their coworkers (Sutter, 1968; Weisenberg, 1973; Nelson & Burchfiel, 1979). Sutter (1968) established timing

Figure 1.3. Generalized geologic map of the Ivanpah Mountains area. See text for discussion of features shown on the geologic map.

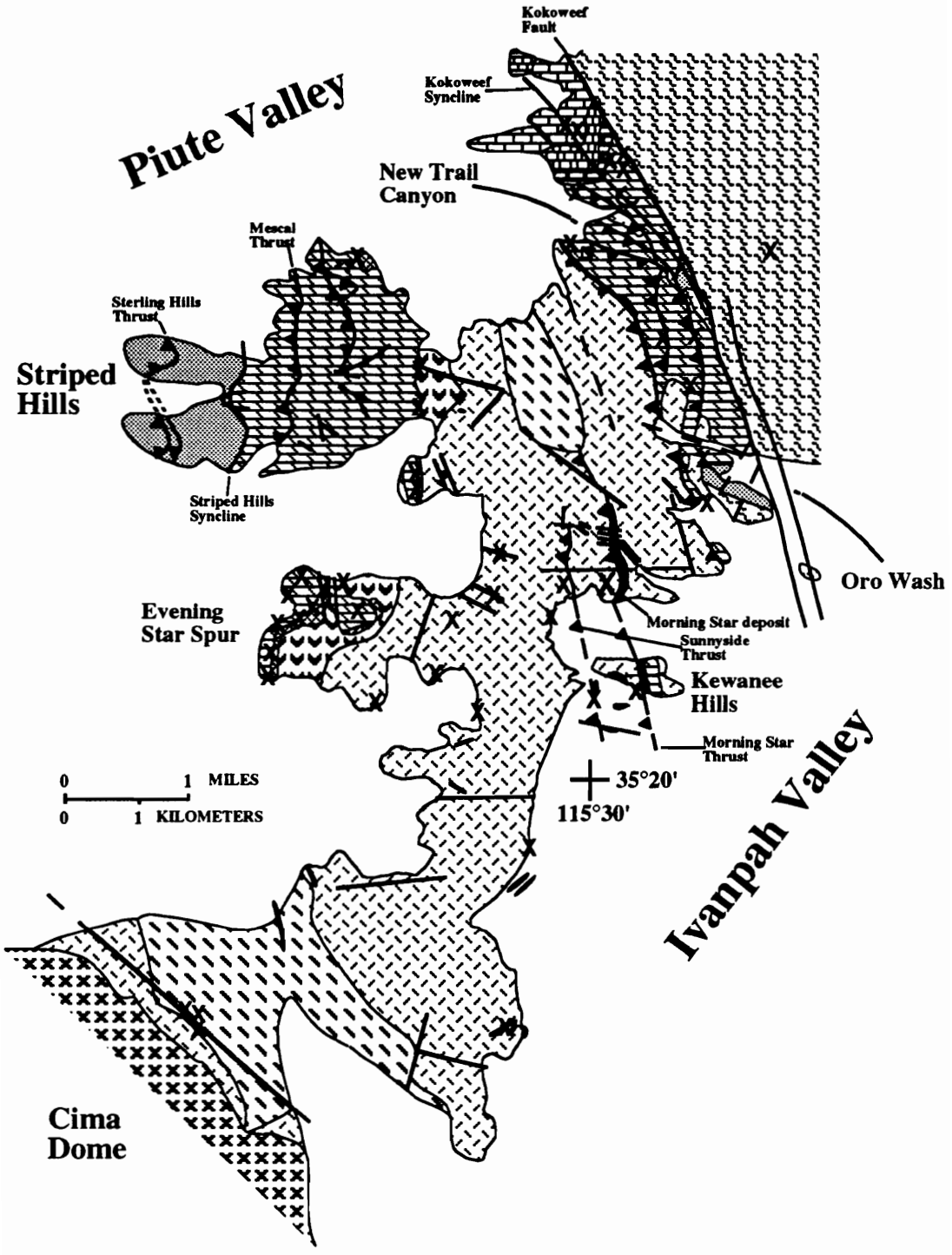
Kokoweef Fault
Kokoweef Syncline
Piute Valley
New Trail Canyon
Mescal Thrust
Sterling Hills Thrust
Striped Hills
Striped Hills Syncline
Oro Wash
Evening Star Spur
Morning Star deposit
Sunnyside Thrust
Kewanee Hills
Morning Star Thrust
0 1 MILES
0 1 KILOMETERS
35°20'
115°30'
Ivanpah Valley
Cima Dome

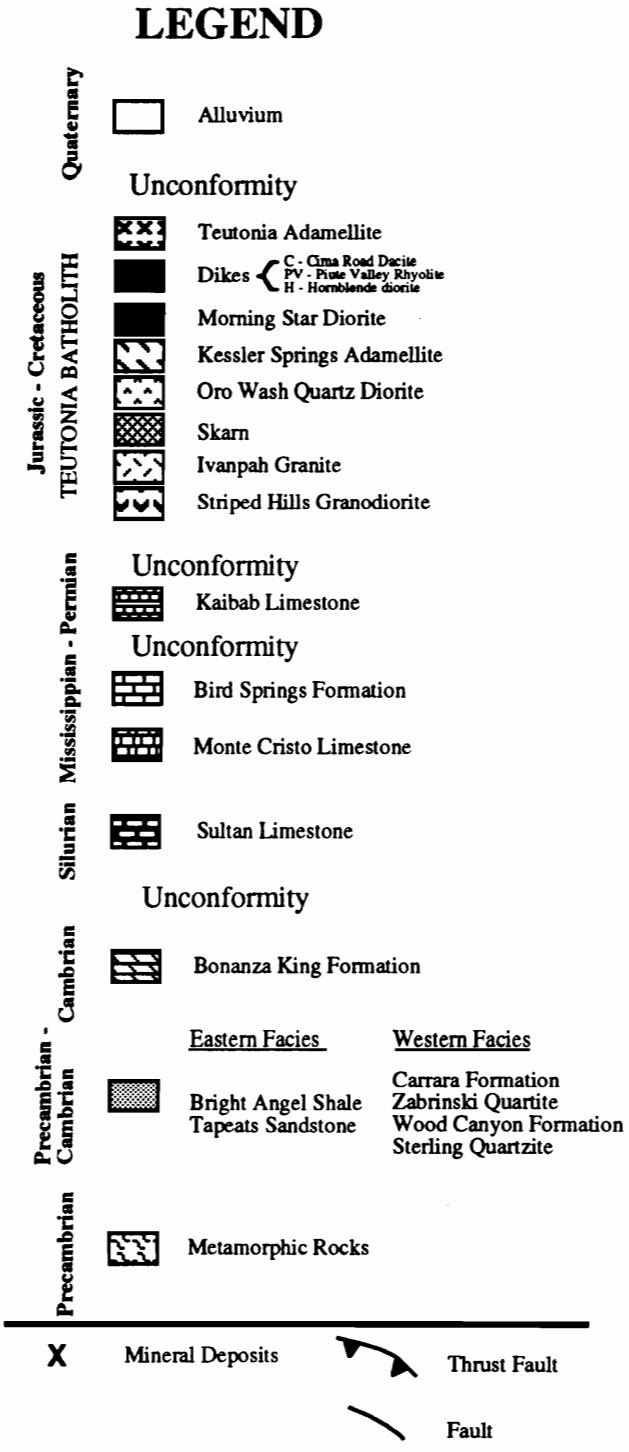
LEGEND
Quaternary
Alluvium
Unconformity
Jurassic - Cretaceous
TEUTONIA BATHOLITH
Teutonia Adamellite
Dikes
C - Cima Road Dacite
PV - Piute Valley Rhyolite
H - Hornblende diorite
Morning Star Diorite
Kessler Springs Adamellite
Oro Wash Quartz Diorite
Skarn
Ivanpah Granite
Striped Hills Granodiorite
Unconformity
Mississippian - Permian
Kaibab Limestone
Unconformity
Bird Springs Formation
Monte Cristo Limestone
Silurian
Sultan Limestone
Unconformity
Cambrian
Bonanza King Formation
Precambrian - Cambrian
Eastern Facies
Western Facies
Bright Angel Shale
Tapeats Sandstone
Carrara Formation
Zabrinski Quartite
Wood Canyon Formation
Sterling Quartzite
Precambrian
Metamorphic Rocks
X
Mineral Deposits
Thrust Fault
Fault

relationships by dating igneous intrusions that bracketed thrusting in the area, and Weisenberg (1973) described the igneous petrology of the New Trail Canyon and western Ivanpah Mountains. Robinson (1979) and Beckerman (1982) extended mapping to the Cima Dome area to the south, and into the New York Mountains and Mid Hills areas to the southeast, respectively, and their combined work (Beckerman et al., 1982) defined seven distinct plutonic phases. These workers named the intrusive complex the Teutonia Batholith. DeWitt et al. (1984) provided additional mapping and geochronologic constraints to batholith ages in the Silurian Hills, to the west of the Ivanpah Mountains. More recently Anderson et al. (1989) argued for restriction of the term Teutonia Batholith to Cretaceous age intrusions in the northeastern Mojave Desert and used data for these Cretaceous plutons to reconstruct the crustal evolution of the Mojave Desert. Mineral deposits studies around the Ivanpah Mountains have generally consisted of regional mineral surveys and short reports on mineral production (Tucker & Sampson, 1943a; Tucker & Sampson, 1943b; Bedford & Johnson, 1946; Wright et al., 1953; Hewett, 1956; Evans, 1974; Wilkins, 1984; Ausburn, 1991; Barton et al., 1988).

Summary of Regional Geology

This chapter summarizes the geology and structural relationships of the northeastern Mojave Desert and the Ivanpah Mountains in the vicinity of the Morning Star deposit. This summary is mostly from the literature but is supplemented by information obtained as a result of new mapping for this dissertation. Also presented in this dissertation are additional petrologic data for plutonic intrusions in the Ivanpah Mountains (Appendix A) which will be used to constrain the geological evolution of the northeastern Mojave Desert.

Stratigraphy

Precambrian Metamorphic Complex

The northeastern Mojave Desert is underlain by Precambrian crystalline basement which crops out as scattered remnants (Figure 1.2). The basement complex consists of 1.7 Ga amphibolite grade meta-igneous and metasedimentary rocks composed of predominantly granitic gneiss with subordinate amounts of amphibolite gneiss, augen gneiss, marble, metapelite and meta-arkose (Burchfiel & Davis, 1971; Robinson, 1979; Burchfiel & Davis, 1981; Beckerman, 1982). The metamorphic basement was intruded by 1.3 to 1.4 Ga syenites, shonkenites and granites (Olsen, 1954; Evans, 1974; Burchfiel & Davis, 1981).

The largest exposures of Precambrian metamorphic complex occurs in the eastern Clark Mountains, northeastern Ivanpah Mountains and northeastern New York Mountains (Figure 1.2). In the eastern New Trail Canyon area of the Ivanpah Mountains, Precambrian metamorphic rocks are in fault contact with Paleozoic strata along the Kokoweef Fault (Figure 1.3). Cambrian sediments rest unconformably over Precambrian metamorphic rocks only at the southern end of the Oro Wash and in the core of the Kokoweef syncline (Figure 1.3).

A thin exposure of Precambrian gneiss exists in the upper-plate of the Pachulka thrust in the northwestern Clark Mountains (Figure 1.2). At this exposure crystalline basement has been thrust over Cambrian sandstones during early Mesozoic thrusting (see below).

Sedimentary Stratigraphy

A thick section of platform and miogeoclinal sedimentary rocks (Burchfiel & Davis, 1971) are exposed in the northeastern and western Ivanpah Mountains, respectively (Figure 1.2 and 1.3). Similar sedimentary sequences are recognized throughout the Clark Mountains to the north and the northeastern New York Mountains to the south, as well as other areas of the northeastern Mojave Desert (Figure 1.2). Sedimentary stratigraphy has been divided into an eastern autochthonous and parautochthonous platform facies, seen in the New Trail Canyon area, and a western allochthonous miogeoclinal facies, seen in the Striped Hills area (Hewett, 1956; Burchfiel & Davis, 1971; Evans, 1971; Evans, 1974; Burchfiel & Davis, 1981; Burchfiel & Davis, 1988). These sedimentary sequences exhibit a weak regional metamorphism in the New York Mountains, which is absent in other areas of the northeast Mojave Desert, but a regional resetting of K-Ar and Ar-Ar isotopic signatures of Precambrian crystalline basement and early Mesozoic plutons provides evidence of this metamorphic event. Localized contact metamorphism occurs adjacent to igneous intrusions in the Ivanpah Mountains.

Autochthonous Platform Sedimentary Sequence

A 3200 m thick section of Paleozoic to Mesozoic platform sedimentary rocks rests unconformably on Precambrian granite and gneiss at the southern end of Oro Wash (Figure 1.3). The basal Cambrian Tapeats sandstone rests unconformably on granitic gneiss and is conformably overlain by Middle Cambrian Bright Angel shale. The Cambrian clastic units are overlain by greater than 2200 m of predominantly shallow-water marine carbonate rocks. The Cambrian Bonanza King Formation dolomites rest conformably on the Bright Angel shale and are unconformably overlain by the Middle Devonian Sultan Formation limestone, Mississippian Monte Cristo limestone and the

limestones of the Mississippian-Permian Bird Springs Formation. The Permian Kaibab Formation limestone overlie the Bird Springs Formation, but the contact is hidden under alluvium and the amount of missing section is not known, although Burchfiel and Davis (1971) define this contact as conformable in other areas of the western United States. The complete carbonate sequence forms the overturned to the east, northwest plunging Kokoweef syncline, which is in fault contact with Precambrian gneiss to the east (Kokoweef fault) and in fault contact with the Ivanpah granite to the west (Figure 1.3). Mesozoic sedimentary rocks, including the Moenkopi Formation terrigenous clastics and Aztec crossbedded sandstone, are partially exposed only in the Clark Mountains to the north of Piute Valley (Burchfiel & Davis, 1971). The Delfonte Formation volcanic series rests unconformably on the Aztec sandstone in the Clark Mountains and is folded and truncated by late Mesozoic thrusting along the Clark Mountain thrust complex (Sutter, 1968; Burchfiel & Davis, 1971).

Allochthonous Miogeoclinal Sedimentary Sequence

Miogeoclinal sedimentary rocks include up to 3000 m of Precambrian to Lower Cambrian clastic sedimentary rocks unconformably overlying Precambrian granite and granitic gneiss (Burchfiel & Davis, 1971). These units are overlain by up to 5000 m of Middle Cambrian to Permian shallow-water marine carbonate rocks which contain minor clastic sedimentary rocks (Burchfiel & Davis, 1971). In the Clark and Ivanpah Mountains thrusting and syntectonic folding have obscured many of the stratigraphic relationships within the miogeoclinal sequence. Further north in the Clark Mountains the basal clastic unit is the Precambrian Johnnie Formation which is conformably overlain by the Precambrian Sterling quartzite (Burchfiel & Davis, 1988). In the Ivanpah Mountains at the western end of Striped Hill the basal clastic unit is the Sterling quartzite (Figure

1.3). Within the overturned limb of the Striped Hills syncline is a complete conformable sequence composed of Precambrian to Middle Cambrian Sterling quartzite, Wood Canyon Formation shaley sandstone, Zabriskie quartzite, Carrara Formation limestone and Bonanza King Formation dolomite. The Devonian Sultan Formation limestone and Mississippian Monte Cristo Formation limestones are in fault contact with the Bonanza King Formation sedimentary rocks below the Mesquite fault. Stratigraphically higher sedimentary units are not found within the allochthonous portions of the Clark Mountain thrust complex or within the Ivanpah and New York Mountains.

Teutonia Batholith

The Teutonia batholith (Figure 1.2) is a large composite batholith that consists of at least seven non-comagmatic plutons which intruded the platform and miogeoclinal sedimentary sequences of the Clark, Ivanpah and New York Mountains between 190 and 70 Ma (Beckerman et al., 1982). The Ivanpah Mountains are underlain by the Jurassic Ivanpah granite throughout most of the mountain range (Figure 1.3). Other intrusions of the Teutonia batholith that outcrop in the Ivanpah Mountains include the Striped Hills granodiorite at the western margins of the Ivanpah Mountains and the Kessler Springs adamellite and Teutonia adamellite which crop out at the southern edge of the Ivapah Mountains near Cima Dome (Figure 1.3). A small stock cuts the Morning Star fault system in the northern Ivanpah Mountains (Figure 1.3) and is correlated to the Kessler Springs adamellite based on petrology, outcrop appearance and modal mineral abundances (Appendix A). A detailed discussion of the plutonic phases of the Teutonia batholith in the Ivanpah Mountains is given in Appendix A.

Cenozoic Volcanic Rocks

Thick sections of Miocene volcanic rocks occur on the western flanks of Cima Dome and southern Mid Hills areas (Katz & Boettcher, 1980; McCurry, 1980; Buesch, 1991). Cima Dome volcanics consist of alkali, olivine-bearing trachybasalts with scoria and amygdaloidal textures and form cindercones and associated flows (Robinson, 1979; Katz & Boettcher, 1980). Volcanic units south of Mid Hills area consist of relatively flat lying andesitic to rhyolitic ash flows, domes, tephra deposits and volcaniclastic beds. These Mid Hills volcanic units rest unconformably on plutonic phases of the Teutonia batholith. Other volcanic and volcaniclastic units in the area include a sequence of extension related Miocene (26 to 6 Ma) extrusives which are typical of Miocene volcanics found throughout the Mojave Desert of California, Nevada and Arizona (Glazner, 1990; Hazlett, 1990; Buesch, 1991; Smith et al., 1991). None of these Tertiary volcanic units crop out in the Ivanpah Mountains.

Structure of the Mesozoic Foreland Fold and Thrust Belt

Burchfiel and Davis (1971; 1977; 1988) outlined a sequence of structural events that define the Mesozoic foreland fold and thrust belt which occurs throughout the Clark, Ivanpah and New York Mountains. Decollement style thrusting is confined to Paleozoic platform sedimentary rocks (Burchfiel & Davis, 1988) and defines the Mesozoic foreland fold and thrust belt in the Spring Mountain (Nevada) thrust complex. In the Clark Mountain thrust complex thrusting of the Mesozoic foreland fold and thrust belt juxtaposes allochthonous miogeoclinal sedimentary rocks over autochthonous and parautochthonous platform sedimentary rocks (Burchfiel & Davis, 1988). The Clark Mountain thrust complex consists of three major eastward directed thrust plates which

account for a minimum of 65 to 80 kilometers of movement that occurred in two distinct episodes (Burchfiel & Davis, 1988).

The structurally lowest Keaney-Mollusk Mine (KMM) thrust plate, which cuts 86.2±1.0 Ma Delfonte Formation volcanics (Adams et al., 1967; Sutter, 1968), places relatively undeformed miogeoclinal sedimentary rocks above asymmetrically overturned to the northeast folded platform sedimentary rocks, and the latter that are in fault contact with the Precambrian metamorphic basement complex (Burchfiel & Davis, 1971; 1988). The basal Keaney and Mollusk Mine faults exhibit only brittle deformation and are characteristic of sole portions of decollement style thrusts which lie within 100 meters of the same stratigraphic horizon that controls Mesozoic brittle thrusting in the Spring Mountain thrust complex (Burchfiel & Davis, 1988). The KMM thrust plate was transported over a syntectonic gravel horizon which implies near surface transport (Burchfiel & Davis, 1971; 1988).

The basal bounding fault of the structurally higher Mesquite Pass (MP) thrust plate is comprised of an imbricated series of moderately west dipping thrust slices that repeat sets of overturned to the northeast, plunging folds. These folds have been interpreted as drag folds related to thrusting (Burchfiel & Davis, 1988). Although the MP thrust is structurally higher than, and to the west of, the KMM thrust plate, the basal imbricated sequence is intruded by the 190-200 Ma Breccia Pluton (Sutter, 1968; Burchfiel & Davis, 1971; 1988). Therefore, the Mesozoic foreland fold and thrust belt is a foreland propagating thrust complex. Compared to the KMM thrust plate, the MP thrust plate has significantly more internal deformation and is composed of three distinct thrust slices which exhibit increased amounts of internal deformation from the structurally lowest (easternmost) to structurally highest (westernmost) thrust slice. The increase in ductile style deformation for structurally higher thrust slices indicates each successive thrust slice

formed at a structurally deeper level from east to west across the MP thrust plate. A series of discrete mylonite selvages in Precambrian to Cambrian quartzites (e.g. Sterling thrust on Figure 1.2 and 1.3) occurs at the highest structural level within the Mescal thrust slice, which is the structurally highest of the three thrust slices. Ductile deformation fabrics in the Sterling thrust become more penetrative to the west (structurally higher) and grade into an ultramylonite that forms the basal thrust of the overlying Winter Pass (WP) thrust plate (Burchfiel & Davis, 1971; 1988).

The WP thrust plate is the only thrust plate in the Clark Mountain thrust complex marked by ductile deformation along the basal bounding fault and which contains Precambrian crystalline basement in the upper-plate (Burchfiel & Davis, 1971; 1988). The Winter Pass thrust plate only crops out in the northernmost Clark Mountains, so it is not shown on Figure 1.2, but correlates to the Winter Pass, Pachulka and Sterling thrust faults (Burchfiel & Davis, 1988). In the northern Clark Mountains the upper-plate of WP contains a complete miogeoclinal section from Precambrian crystalline basement through Cambrian Bonanza King Formation (Burchfiel & Davis, 1988). The basal Pachulka thrust (Figure 1.2), which is correlative to the Winter Pass thrust (Burchfiel & Davis, 1988), has a knife-edge sharp contact which places 100 meters of mylonitized Precambrian gneiss over 5 meters of mylonitized Precambrian to Cambrian quartzite (Burchfiel & Davis, 1971; 1988). Hinge zones of overturned folds within the MP thrust plate are at a high angle to mylonitic stretching lineations on the Pachulka thrust, which suggests folds developed due to thrust movement. Foliation development, small similar folds, boudinaged limestones, and syntectonic recrystallization occur throughout the zone of overturned folds in the lower MP plate (Burchfiel & Davis, 1988). Burchfiel and Davis (1971; 1988) hypothesize that eastward directed thrusting along the WP thrust caused the extensive plastic deformation observed in the MP thrust plate; thus movement

on the WP thrust is older than the 190 Ma minimum age of the MP thrust plate. Sutter (1968), however, obtained K-Ar whole rock ages of 75 to 90 Ma for the basal Pachulka ultramylonite and syntectonic recrystallization in the upper-plate of the thrust. These age determinations correspond to regional resetting of isotopic systematics due to Late Cretaceous magmatism, thus the WP thrust plate is probably part of the early Jurassic thrusting episode.

High angle normal faults define the contact between autochthonous platform sedimentary rocks and Precambrian metamorphic rocks in the eastern Clark, Ivanpah and New York Mountains. These high angle structures include the South, Kokoweef and Slaughterhouse faults (Figures 1.2 and 1.3) which Burchfiel and Davis (1977) correlate for over 45 km along strike. Left-lateral normal fault movement along this composite fault system predates emplacement of the KMM thrust plate and cuts the greater than 80 Ma Live Oak Canyon granodiorite in the New York Mountains (Burchfiel & Davis, 1977; Beckerman et al., 1982).

Cenozoic gravity sliding and detachment faulting, which cuts 12.0 to 12.5 Ma volcanic rocks and displaces parts of the thrust complex in the Clark and New York Mountains to the west, have been mapped by Burchfiel and Davis (1971; 1977; 1988). Hewett (1956) mapped two major normal faults in the Clark Mountains and Sharp (1984) mapped a low angle normal fault near the Colosseum mine in the northern Clark Mountains. Evans (1971) mapped several normal faults of uncertain origin in the Mescal Range. Regional uplift at the end of the Cretaceous or earliest Tertiary is reported to have caused east to west gravity sliding on the KMM thrust in the northern Clark Mountains (Sharp, 1984; Jessey & Fallis, 1989). Burchfiel and Davis (1988) argue against normal fault rejuvenation of the KMM thrust in the southern Clark Mountains, but did map detachment style faulting north of the Clark Mountains. No evidence of extensional

tectonic activity has been identified in the Ivanpah Mountains, but extensional tectonism is responsible for the Basin and Range topography throughout the northeastern Mojave Desert (Figure 1.2).

In the New York Mountain thrust complex four structurally distinct domains of unknown age occur within autochthonous platform sedimentary rocks (Burchfiel & Davis, 1977). Burchfiel and Davis (1977) correlate the high angle Slaughterhouse fault and an overturned syncline in the Sagamore Canyon-Slaughterhouse Springs area of the New York Mountains to structures in the New Trail Canyon area of the Ivanpah Mountains (Figure 1.2). Thrust blocks of the New York Mountains are structurally lower and east of the Clark Mountain thrust complex and only involve Precambrian metamorphic rocks and Paleozoic-Mesozoic platform sedimentary rocks (Burchfiel & Davis, 1977). Thus, the New York thrust complex represents the southern extension of the autochthonous sequence seen in the Clark Mountain and Spring Mountain thrust complexes.

Structural Geology of the Ivanpah Mountains

Three structural blocks are present in the Ivanpah Mountains. Each structural block is defined by its spatial distribution with respect to regional structures and lithologies within the structural block. The structural blocks were originally outlined by Burchfiel and Davis (1971) and further refined by fieldwork conducted during this project. These structural blocks of the Ivanpah Mountains include (1) autochthonous to parautochthonous platform sedimentary rocks of the New Trail Canyon area, (2) allochthonous Striped Hills miogeoclinal sedimentary rocks and (3) structures within the Jurassic Ivanpah granite.

The New Trail Canyon structural block is bounded on the east by the high angle Kokoweef fault, which juxtaposes Precambrian crystalline basement with folded Paleozoic platform sedimentary rocks, and on the west by the Ivanpah granite (Figure 1.3). The Kokoweef syncline, which constitutes the major structural feature of the New Trail Canyon, is a broad, overturned to the east, northwest plunging syncline containing a complete stratigraphic section from Precambrian basement to Mesozoic sedimentary rocks. The Mesozoic sedimentary section is exposed only in the Clark Mountains to the north. The eastern limb dips 40-80° southwest and the western limb is overturned 55-70° southwest. Burchfiel and Davis (1971) extend mapping to the west by inferring an overturned anticline which is now eroded to expose the Ivanpah granite that intruded the core of the hypothetical anticline. Sub-horizontal shortening of autochthonous platform sedimentary rocks formed the Kokoweef syncline while small folds, kink bands, and penetrative shear zones account for the majority of shortening strain in the crystalline basement (Nelson & Burchfiel, 1979).

West of the Kokoweef syncline, the New Trail Canyon structural block contains a series of north to northwest trending, 35 to 55° southwest dipping thrust zones that dissect platform sedimentary units. These thrusts dip subparallel to crystalline basement penetrative shear zones, the granite-sedimentary rock contact (to the west) and the Morning Star thrust fault system within the Ivanpah granite. Parautochthonous thrusts juxtapose Bonanza King Formation dolomite in both the upper- and lower-plates with local slivers of Sultan limestone and Ivanpah granite in the upper-plate. This juxtaposition of Bonanza King Formation implies the maximum vertical displacement on any parautochthonous thrust could not be more than a few hundred meters. The eastern contact between Ivanpah granite and New Trail Canyon sedimentary rocks appears to be thrust controlled as discrete units of sheared calc-silicates define the contact. All

structures in the New Trail Canyon structural block pre-date emplacement of the KMM thrust plate (< 86 Ma) and post-date the Ivanpah granite (>138 Ma).

The Striped Hills structural block contains a complete section of the Mescal slice of the MP thrust plate. Although three thrust slices occur within the MP thrust plate in the Clark Mountains, the other thrust slices of the MP thrust plate are absent in the Ivanpah Mountains. From west to east (structurally highest to lowest) the Mescal slice includes discrete shear zones in Precambrian to Cambrian clastic sedimentary rocks (e.g. Sterling thrust), the Striped Hills syncline and the Mescal thrust (Figure 1.2 and 1.3). It is not possible to correlate sedimentary units east of the Mescal thrust to a particular thrust plate of the Clark Mountain thrust complex because no additional through-going faults are present. This sedimentary package of Bonanza King Formation carbonates contains a series of small satellite folds overturned to the NE and minor discrete thrust faults. All units dip moderately westward, which led Burchfiel and Davis (1971) to conclude that these sedimentary units formed the western limb of the overturned anticline described above. Thus, Burchfiel and Davis (1971) originally mapped this sedimentary sequence as part of the autochthonous platform sedimentary rocks exposed in the New Trail Canyon area, but later reinterpreted the Striped Hill sedimentary units to be part of the allochthonous sedimentary sequence of the MP thrust plate (Burchfiel & Davis, 1988). Either interpretation requires the disappearance of the KMM thrust plate north of the Ivanpah Mountains. The Striped Hills granodiorite and Ivanpah granite intruded the sedimentary sequence in the eastern Striped Hills area forming a series of mineralized skarns. These intrusive phases are Jurassic in age and do not exhibit significant thrust deformation alomg the western contact. The field evidence argues for the lack of KMM thrusting in the Ivanpah Mountains or a much older age for KMM thrusting if it was obliterated by intrusion of Jurassic Ivanpah and Striped Hills plutons.

The final structural block in the Ivanpah Mountains consists of structures within the Jurassic Ivanpah granite. Thrusting occurs within the Ivanpah granite along the Morning Star fault system (described in Chapter 2) and along the eastern margin of the Ivanpah granite. The Morning Star fault system, which includes the Morning Star and Sunnyside thrust faults, cuts the central portions of the Ivanpah granite (Figure 1.2 and 1.3), but has yet to be traced completely through the granite. A porphyritic pluton similar to the Kessler Springs adamellite cuts the Morning Star fault system in the northern portion of the Ivanpah Mountains (Figure 1.3). Weisenberg (1973) and Robinson (1979) describe a magmatic foliation, composed of aligned feldspar and phyllosilicate minerals, in the Ivanpah granite which they attribute to syntectonic emplacement of the pluton. This foliation is absent to the east of the Morning Star fault complex. Within the fault complex all foliation is due to movement on the subparallel Morning Star and Sunnyside thrust faults. Minor foliation of the granite west of the Morning Star fault complex is likely due to post-tectonic deformation of the Ivanpah granite during thrusting. Because the Morning Star fault complex can not be traced through the Ivanpah Mountains, it is not possible to correlate the Morning Star fault system with thrusting in the Clark Mountain thrust complex to the north. Beckerman et al. (1982), however, correlated the Morning Star thrust to the New York Mountain thrust which cuts Mid Hills adamellite in the New York Mountain–Mid Hills area (Figure 1.2).

Mineralization of the Ivanpah Mountains

Two distinct mineralization styles occur around the Ivanpah Mountains. These include (1) contact metasomatic Pb-Zn-Ag deposits, and Sn-W and Cu skarn deposits

related to igneous intrusion, and (2) epithermal, fault zone-hosted, precious-metal deposits.

Contact metasomatic Pb-Zn-Ag and Cu skarn deposits occur in the northeastern Ivanpah Mountains throughout the New Trail Canyon and Oro Wash areas (Figure 1.3). These deposits are hosted by Cambrian Bonanza King Formation dolomite at or structurally above the contacts between dolomite and various igneous intrusions. Contact metasomatic Pb-Zn-Ag and Cu skarn deposits in the New Trail Canyon area forms part of a continuous belt of metasomatic and skarn deposits throughout the Paleozoic carbonate rocks in the Clark, Ivanpah and New York Mountains. These deposits range from predominately Pb-Zn-Ag in the Clark Mountains, to Pb-Zn-Ag and Cu in the Ivanpah Mountains, and finally to Cu and W-bearing skarns in the New York Mountains. Contact metasomatic Sn-W and Cu skarn deposits also occur at the western granitic margin of the Ivanpah Mountains where the Striped Hills granodiorite intruded the Paleozoic miogeoclinal sedimentary rocks (Figure 1.3). All of these metasomatic and skarn deposits had past production during the early part of this century, but are sub-economic today.

Minor amounts of precious-metal mineralization occurs in contact metasomatic and skarn deposits, but the vast majority of precious-metal mineralization occurs in fault zone-hosted, epithermal deposits within plutonic rocks of the Ivanpah Mountains. The largest and only significant metal producer in the Ivanpah Mountains is the Morning Star mine (Chapter 3 and 4) which is hosted by the Ivanpah granite in the upper-plate of the Morning Star thrust fault. Mineralization consists of electrum, silver sulfides and silver-gold sulfides with base metal sulfides in a quartz±carbonate stockwork vein system that forms a tabular orebody along the fault plane. Precious-metal mineralization postdates intrusion of the Ivanpah granite, but early mineralization is contemporaneous with

thrusting on the Morning Star fault (Chapter 3). Additional sub-economic, fault zone-hosted precious-metal mineralization occurs in Teutonia Batholith intrusions west of the correlated Morning Star and New York Mountain thrust faults.

Sub-economic porphyry Mo-Cu mineralization occurs in the central New York Mountains east of the New York Mountain thrust fault (Hewett, 1956). Mineralization consists of a central core of Mo-Cu mineralization associated with phyllic and argillic alteration surrounded by Pb-Zn mineralization in a series of small prospects (Ntiamoah-Agyakwa, 1987). The central porphyry mineralization occupies in a 4 square km area that is cut on the southwest corner by the New York Mountain thrust fault, although Ntiamoah-Agyakwa (1987) argues for normal fault re-activation of the New York Mountain fault in this area. The peripheral Pb-Zn mineralization occurs up to 3 km away from the periphery of the porphyry Mo-Cu mineralization (Ntiamoah-Agyakwa, 1987).

Summary of Geochronology

Geochronology of plutonic rocks, hydrothermal alteration and tectonic activity in the Ivanpah Mountains and surrounding areas is summarized in Figure 1.4. Age determinations for plutonism, metamorphism and tectonism of the Precambrian intrusive series, Sierra Nevada batholith, Death Valley and northeastern and eastern Mojave Desert regions are also plotted on Figure 1.4 for comparison. Due to the complex plutonic and tectonic history of the area, all K-Ar and Ar-Ar age determinations record only minimum ages, cooling ages or reset ages.

Undifferentiated granitic plutons in the Silurian Hills (DeWitt et al., 1984) and the Oro Wash/Breccia pluton suite in the Ivanpah Mountains (Sutter, 1968) were intruded at greater than 190 Ma. The Rock Springs monzodiorite has a minimum age of 168 Ma

Figure 1.4. Compilation of age dates for the Teutonia Batholith and surrounding areas of central and southern California. References are 1.) Adams et al. (1967), 2.) Armstrong (1968), 3.) Bateman (1981), 4.) Beckerman (1982), 5.) Beckerman et al. (1982), 6.) Burchfiel and Davis (1971), 7.) Burchfiel and Davis (1977), 8.) Burchfiel and Davis (1981), 9.) Chen and Moore (1979), 10.) DeWitt (1980), 11.) DeWitt et al. (1984), 12.) Everndon and Kistler (1970), 13.) Fleck (1970), 14.) Foster et al. (1989), 15.) Foster et al. (in press), 16.) Hewett et al. (1969), 17.) Hoisch et al. (1988), 18.) Jaffe et al. (1959), 19.) Kistler et al. (1971), 20.) Labotka et al. (1980), 21.) Lanphere (1964), 22.) Martin et al. (1982), 23.) Ntiamoah-Agyakwa (1987), 24.) Suppe (1985), and 25.) Sutter (1968).

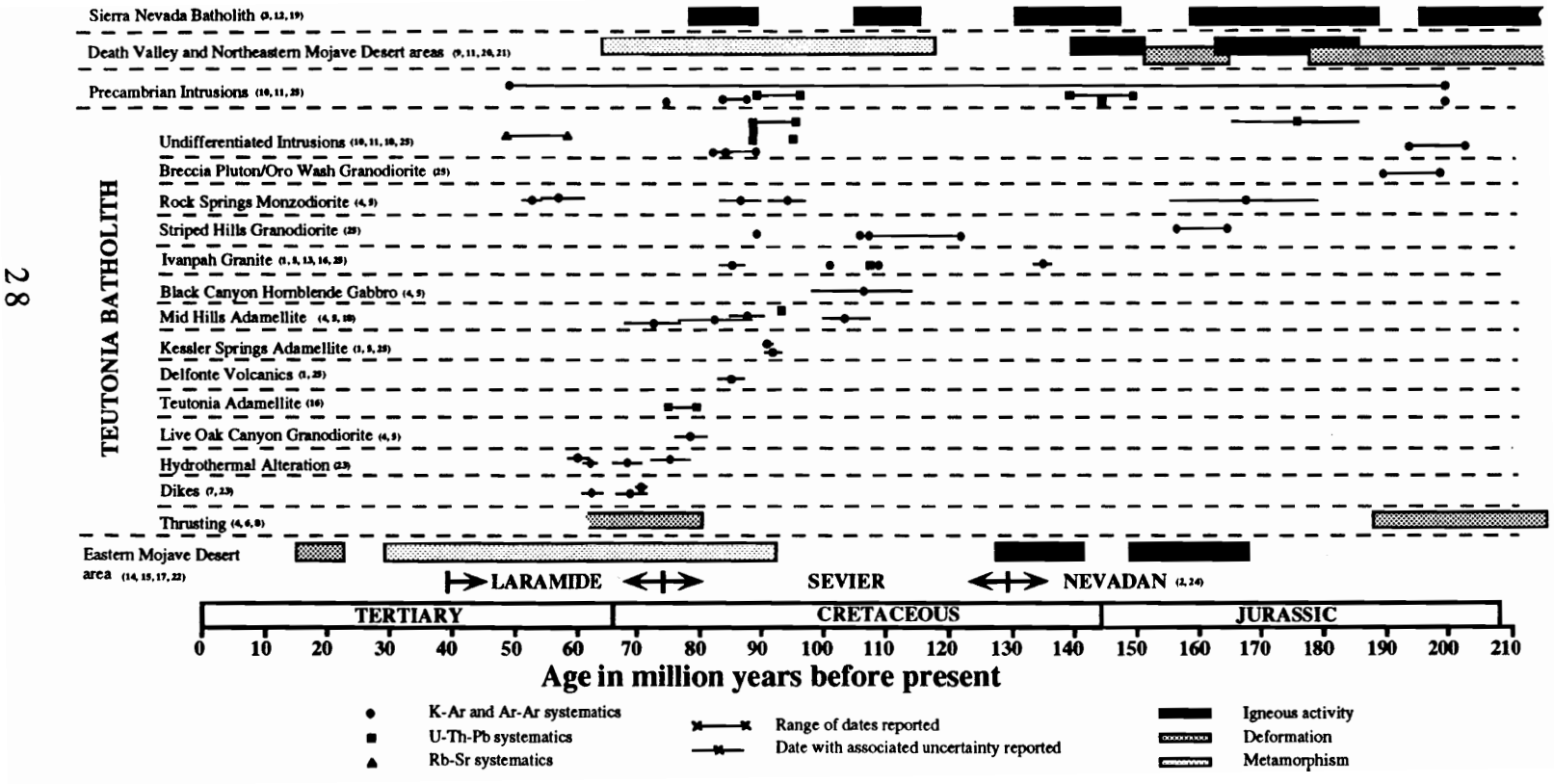
Sierra Nevada Batholith (9, 12, 19)
Death Valley and Northeastern Mojave Desert areas (9, 11, 20, 21)
Precambrian Intrusions (10, 11, 25)
TEUTONIA BATHOLITH
Undifferentiated Intrusions (10, 11, 18, 25)
Breccia Pluton/Oro Wash Granodiorite (25)
Rock Springs Monzodiorite (4, 5)
Striped Hills Granodiorite (25)
Ivanpah Granite (1, 3, 13, 16, 25)
Black Canyon Hornblende Gabbro (4, 5)
Mid Hills Adamellite (4, 5, 16)
Kessler Springs Adamellite (1, 5, 25)
Delfonte Volcanics (1, 25)
Teutonia Adamellite (16)
Live Oak Canyon Granodiorite (4, 5)
Hydrothermal Alteration (23)
Dikes (7, 23)
Thrusting (4, 6, 8)
Eastern Mojave Desert area (14, 15, 17, 22)
LARAMIDE
SEVIER
NEVADAN (2, 24)
TERTIARY
CRETACEOUS
JURASSIC
0 10 20 30 40 50 60 70 80 90 100 110 120 130 140 150 160 170 180 190 200 210
Age in million years before present
K-Ar and Ar-Ar systematics
U-Th-Pb systematics
Rb-Sr systematics
Range of dates reported
Date with associated uncertainty reported
Igneous activity
Deformation
Metamorphism

(Beckerman et al., 1982) and exhibits a similar isotopic resetting history as the Silurian Hills undifferentiated granitoids (Figure 1.4). The Striped Hills granodiorite and Ivanpah granite were the next to intrude at 155-165 and 135 Ma, respectively (Sutter, 1968). The Mid Hills adamellite and Black Canyon gabbro intruded synchronously with minimum ages between 104 to 107 Ma (Beckerman et al., 1982). The remaining phases of the Teutonia batholith (Live Oak Canyon granodiorite, Teutonia adamellite and Kessler Springs adamellite) intruded between 75 and 92 Ma (Beckerman et al., 1982). This major episode of plutonic activity may account for the regional resetting of K-Ar and Ar-Ar geochronology for older batholithic phases and Precambrian rocks (Figure 1.4). Ntiamoah-Agyakwa (1987) dated a series of "intermineral" porphyritic adamellite dikes and related hydrothermal alteration related to porphyry mineralization in the New York Mountains at 60 to 80 Ma. This is the last recorded thermal event in the area until the less than 26 Ma volcanic episode (Katz & Boettcher, 1980; McCurry, 1980; Glazner, 1990; Hazlett, 1990; Buesch, 1991; Smith et al., 1991). The Late Tertiary volcanic event may also account for reset ages younger than those recorded for plutonic and hydrothermal activity associated with the Teutonia Batholith. This Late Tertiary resetting of age determinations is particularly prominent for the undifferentiated plutons of the Silurian Hills area (DeWitt et al., 1984) because large amounts of Miocene volcanics occur in the Silurian Hills area.

Geologic History of the Ivanpah Mountains

The Mesozoic foreland fold and thrust belt extends from Utah to southeastern California where it is intruded by the Teutonia Batholith (Burchfiel & Davis, 1972; Burchfiel & Davis, 1975; 1977; 1982). Previous mapping and geochronology defined

two episodes of compressional tectonic activity within the Mesozoic foreland fold and thrust belt in the Clark, Ivanpah and New York Mountains (Burchfiel & Davis, 1981; 1988). Using cross-cutting plutons to constrain the ages of deformation, Adams et al. (1967) and Sutter (1968) concluded that the early episode of thrusting along the MP and WP thrust plates took place prior to 190 Ma and the KMM thrusting episode occurred less than 86 Ma. Previously the structures within the Ivanpah Mountains were included in this later episode of deformation (Burchfiel & Davis, 1971). Recent mapping and reinterpretation of magmatic and tectonic features of the northeastern Mojave Desert suggests that a third episode of Mesozoic thrusting occurred in the Ivanpah and New York Mountains. This third episode of thrusting appears to be absent in the Clark Mountains. Structures belonging to this third episode of eastward directed thrusting include the Morning Star fault system and parautochthonous thrust slices in the New Trail Canyon structural block for the Ivanpah Mountains. The New York Mountain thrust (Beckerman et al., 1982) and parautochthonous thrusts in the Sagamore Canyon-Slaughterhouse Springs (Burchfiel & Davis, 1977) area of the New York Mountains, to the south of the Ivanpah Mountains, probably also represent this newly defined episode of thrusting.

In the New York Mountains the New York Mountain thrust fault cuts the 105 Ma Mid Hills adamellite. All folding and parautochthonous thrusting in the Sagamore Canyon-Slaughterhouse Springs area are cut by a late-stage porphyritic dike which was dated at 72 Ma (Burchfiel & Davis, 1977). These dates confine movement of the third episode of thrusting on the Mesozoic foreland fold and thrust belt to be between 105 and 72 Ma in the New York Mountains. Beckerman et al. (1982) obtained minimum ages for movement on the New York Mountain thrust fault of between 73 and 88 Ma, which corresponds to the 75 to 90 Ma ages Sutter (1968) obtained for syntectonic

metamorphism along the Pachulka thrust. The New York Mountain thrust has also been correlated with the Morning Star thrust (Burchfiel & Davis, 1971; Beckerman et al., 1982). Structures within the New Trail Canyon and Sagamore Canyon-Slaughterhouse Springs areas have also been correlated across the Ivanpah Valley (Burchfiel & Davis, 1977). Given recent radiometric geochronology and these structural correlations, the third episode of Mesozoic thrusting occurred between 105 and 88 Ma.

In the Ivanpah Mountains, the 138 Ma Ivanpah granite is cut by the Morning Star fault complex and parautochthonous thrusts of the New Trail Canyon contain slivers of Ivanpah granite in the upper-plate. The northern extension of the Morning Star fault complex is intruded by a pluton that is tentatively mapped as the Kessler Springs adamellite. If this correlation is correct, then movement of the Morning Star fault system pre-dates intrusion of the adamellite, which has a minimum age of 92 Ma (Adams et al., 1967; Sutter, 1968; Beckerman et al., 1982). Therefore, the third episode of thrusting on the Mesozoic foreland fold and thrust belt occurred between 138 and 92 Ma in the Ivanpah Mountains.

The Pachulka, Morning Star and New York Mountain thrusts have similar ductile deformation styles and formed at similar structural levels. These thrust faults are the only exposures of mylonite in the Clark Mountain thrust complex, the Morning Star fault system and the New York Mountains, Mid Hills and Sagamore Canyon-Slaughterhouse Springs areas. Adams et al. (1967) and Sutter (1968) obtained K-Ar whole rock and biotite ages for syntectonic recrystallization and mylonite formation on the Pachulka thrust and Winter Pass thrust of 75 to 90 Ma. Movement on the Morning Star and New York Mountain thrust occurred between 90 and 105 Ma using cross cutting plutons to bracket deformation ages. The discrepancy in the age of movement between the Winter Pass thrust plate and the correlated Morning Star-New York Mountain fault system may be due

Figure 1.5. Schematic cross section illustrating the tectonomagmatic evolution of the Ivanpah Mountains area. Cross section approximately across the Striped Hills area to the New Trail Canyon area of the Northern Ivanpah Mountains. A.) Undeformed platform (shaded) and miogeoclinal (white) sedimentary sequences laid down during Paleozoic time. B.) Prior to 190 Ma the Winter Pass (WP) sheet and the three thrust slices of the Mesquite Pass (MP) thrust sheet moved from west to east putting miogeoclinal sediments (white) over folded platform sediments (shaded). After thrusting the Oro Wash pluton intruded near the base of the MP thrust sheet at a depth of 6.5 to 8.5 km. C.) By Late Jurassic time the Ivanpah granite and Striped Hills pluton suite intruded to mid crustal depth. D.) in Early Cretaceous time, while magmatic activity occurred in other portions of the Teutonia Batholith the Ivanpah Mountains underwent an episode of eastward directed thrust faulting on the Morning Star thrust and parautochthonous thrusts in the new Trail Canyon. E.) By Late Cretaceous time the final episode of magmatic activity occurred in the Teutonia Batholith which formed the Kessler Springs and Teutonia plutons in the Ivanpah Mountains and cause a regional doming event that was overridden by the Keaney/Mollusk Mine (KMM) thrust sheet.

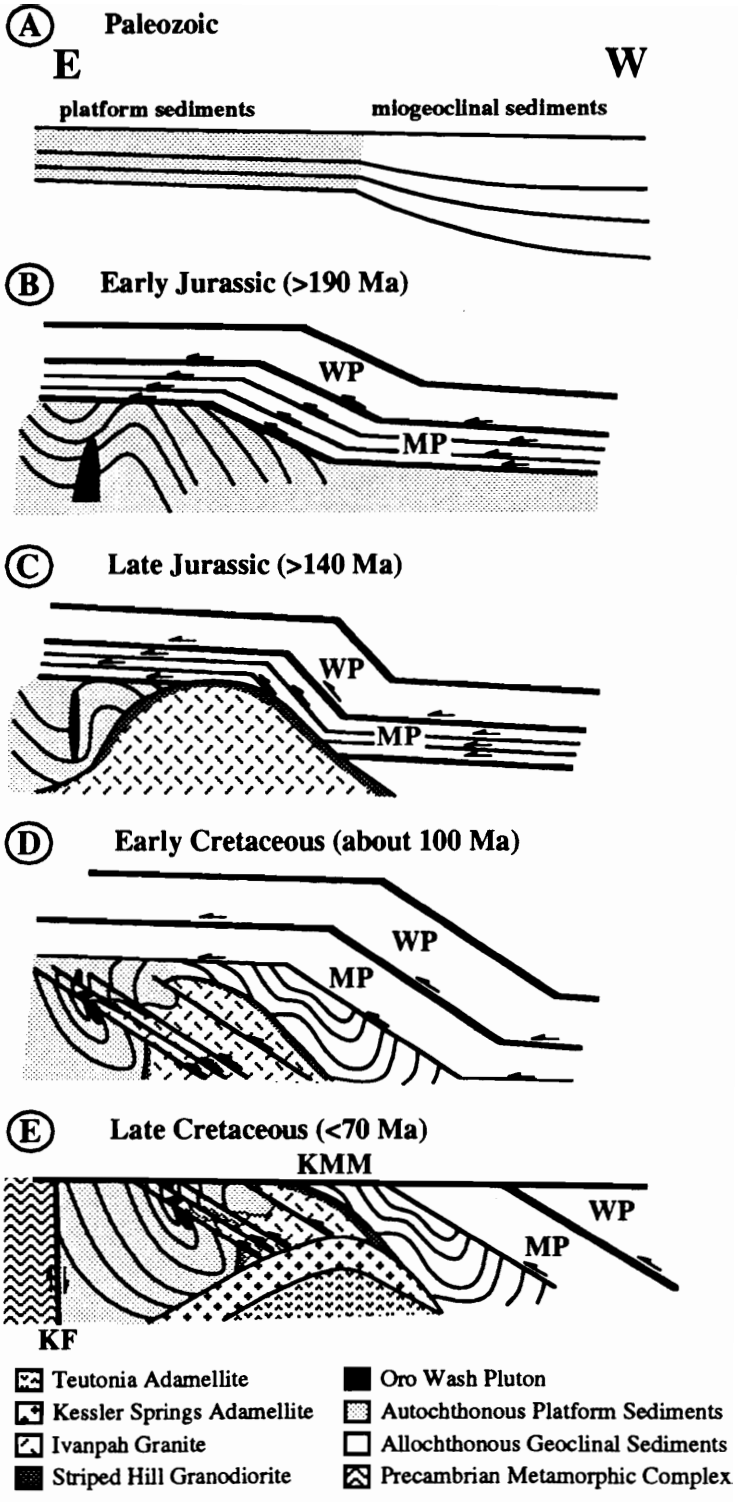
A
Paleozoic
E
W
platform sediments
miogeoclinal sediments
B
Early Jurassic (>190 Ma)
WP
MP
C
Late Jurassic (>140 Ma)
WP
MP
D
Early Cretaceous (about 100 Ma)
WP
MP
E
Late Cretaceous (<70 Ma)
KMM
WP
MP
KF
Teutonia Adamellite
Kessler Springs Adamellite
Ivanpah Granite
Striped Hill Granodiorite
Oro Wash Pluton
Autochthonous Platform Sediments
Allochthonous Geoclinal Sediments
Precambrian Metamorphic Complex

to isotopic resetting caused by extensive Late Cretaceous plutonism. Alternatively, the 90 Ma age may be the minimum age of movement on the Pachulka thrust with the younger ages representing cooling ages. In either case it appears that ductile deformation on the Morning Star–New York Mountains thrust faults corresponds to reactivation along the Winter Pass thrust in the Clark Mountain thrust complex.

Therefore, the Mesozoic foreland fold and thrust complex in the northeastern Mojave Desert consists of three discrete episodes of thrusting separated by intrusion of different portions of the Teutonia batholith. The structural and magmatic history of the Ivanpah Mountains is illustrated schematically in Figure 1.5. Initial eastward directed thrusting of miogeoclinal sedimentary rocks took place prior to 190 Ma (Figure 1.5B) (Burchfiel & Davis, 1971; 1981; 1988). This Triassic event initiated as ductile deformation on the basal WP thrust which caused syntectonic folding of the underlying miogeoclinal and platform sedimentary sequences. Thrusting progressed eastward into brittle deformation within the various thrust slices of the MP thrust plate. Final movement of the early episode of thrusting occurred on the imbricate series of thrust faults that constitute the MP basal bounding fault.

Sporadic intrusion of Jurassic and Early Cretaceous phases of the Teutonia batholith followed the initial episode of thrusting in the Silurian Hills, Ivanpah Mountains and New York Mountains (Figure 1.5C). Crustal thickening due to early thrusting may have caused melting of lower crustal sedimentary rocks and Precambrian basement to give rise to Mesozoic plutonism. The Early Jurassic to Triassic Oro Wash granodiorite-Breccia Pluton suite, and possibly other Triassic granodioritic plutons in the Clark Mountains (Sutter, 1968; Burchfiel & Davis, 1971), were emplaced following thrusting. The Breccia Pluton intruded to the base of the Mesquite Pass thrust plate which was overlain by the Winter Pass thrust plate at the time of pluton emplacement (Burchfiel &

Davis, 1971; 1988). The Oro Wash pluton intruded autochthonous sedimentary rocks that were overlain by both MP and WP thrust plates. The two thrust blocks and the autochthonous sedimentary sequences combine for 5.0 to 9.0 kilometers of preserved pre-Triassic sedimentary stratigraphy, suggesting pluton emplacement depth of at least 5 kilometers for the Jurassic and Early Cretaceous phases of the Teutonia batholith.

The Middle Jurassic Rock Springs monzodiorite intruded the southeastern end of the New York Mountains at a slightly later time and a depth of 8.5 to 10 km (Anderson et al., 1989). The deeper emplacement depth for the Rock Springs monzodiorite is probably due to thickening of the foreland fold and thrust complex in southern portions of the Mojave Desert. Evidence for structural thickening includes an increased abundance of ductile deformation and nappe formation in the New York Mountains, Old Woman Mountains and Piute Mountains (Hoisch et al., 1988). Other plutons in the area, particularly the Bristol Mountain, southern Providence Mountains and Granite Mountain II, which all crop out 20 km south of the New York Mountain-Mid Hills area, are composed of Late Jurassic plutons emplaced at 11 to 13 km depths (Young & Wooden, 1988; Fox & Miller, 1990). Burchfiel and Davis (1981) and Hoisch et al. (1988) have also calculated 9 to 12 kilometers of post-Cretaceous uplift south of the New York Mountains based on regional geologic reconstruction which confirm these pluton emplacement depths.

The Striped Hills granodiorite and Ivanpah granite intruded as a cogenetic magmatic suite differentiated by chemical reaction with the host carbonate rocks (Appendix A) contemporaneously with the Rock Springs monzodiorite. Jurassic plutonism throughout the Mojave and Sonoran deserts of southeastern California and southwestern Arizona are thought to be epizonal compared to deeper levels of emplacement for Cretaceous plutons (Allen et al., 1983; Barton et al., 1988; Tosdal et al.,

1989). Recent work, however, has uncovered mid-crustal level (10 to 30 kilometers depth) Jurassic plutonism in the Old Women, Chemehuevi and Granite Mountains (Howard et al., 1987; Young & Wooden, 1988; Anderson et al., 1989; John & Wooden, 1990). Similar results are indicated here for the Ivanpah and New York Mountains.

Jurassic magmatism was followed by Early Cretaceous magmatic activity after a short hiatus. Cretaceous plutons of the Teutonia batholith intruded between 70 and 110 Ma at epizonal crustal depths (<6 kbars) (Anderson et al., 1989). Thermobarometry and K-Ar age dates indicate a rapid succession of shallower emplacement depths from older plutons (e.g. 105 Ma Mid Hills pluton was emplaced at 3.5-6.5 km depth) to younger plutons (92 Ma Kessler Springs pluton was emplaced at 0.5 to 1.5 km depth) (Anderson et al., 1989). Depth of emplacement for ≤70 Ma plutons have not been determined. Regional uplift and unroofing south to southwest of the Ivanpah Mountains would account for these observations.

A second episode of ductile thrusting followed soon after the Jurassic and Early Cretaceous intrusions (Figure 1.5D). Ductile thrusting occurred along the Morning Star fault complex and the New York Mountain thrust fault between 90 and 105 Ma. This ductile episode of thrusting is probably related to the increased heat flow caused by Early Cretaceous magmatic activity and may have reactivated the Winter Pass thrust in the Clark Mountains. Thrusting also took place on the contact between Ivanpah granite and sedimentary rocks of the New Trail Canyon area. Movement along the faulted contact coupled with thrusting on the Morning Star fault system formed the tabular like outcrop pattern of the Ivanpah granite. Brittle deformation occurred throughout the autochthonous sedimentary sequence of the New Trail Canyon and Sagamore Canyon-Slaughterhouse Springs areas during this second episode of thrusting.

Plutonism followed the second episode of thrusting and included the epizonal Late Cretaceous members of the Teutonia batholith in the Ivanpah Mountains, New York Mountains, Cima Dome and Mid Hills areas (Beckerman et al., 1982; Anderson et al., 1989). Restoration of fault blocks along the strike-slip fault in the Ivanpah Valley places all Late Cretaceous plutonism to the south and west of the present day location of the Ivanpah Mountains.

High angle left-lateral normal faulting along the South Mountain, Kokoweef and Slaughterhouse faults followed Late Cretaceous plutonism and brought Precambrian crystalline basement adjacent to Paleozoic platform sedimentary rocks. The final episode of thrusting occurred with near surface transport of the KMM thrust plate and followed normal faulting (Figure 1.5E). Emplacement of numerous plutons to the south and southwest of the Ivanpah Mountains may have created the stress system necessary to reactivate thrusting in the area. The KMM thrust is not present in the Ivanpah Mountains or to the south. In the southern Clark Mountains the KMM thrust rides over a syntectonic gravel (Burchfiel & Davis, 1988) which suggests near surface transport. Because there is no outcrop of the KMM thrust, or correlative thrust faults in the Ivanpah Mountains, either the fault predates emplacement of the Ivanpah granite or the KMM thrust switched from structurally lower than the WP and MP thrust plates in the Clark Mountains to structurally higher in the Ivanpah Mountains. It is unlikely that the age of movement on the KMM thrust plate could pre-date the 138 Ma Ivanpah granite because the KMM thrust plate over rides the high angle normal faults on the eastern side of the Clark Mountains. Burchfiel and Davis (1971) show the KMM thrust cutting down below the MP and WP thrust blocks in the Clark Mountains. In the Ivanpah Mountains the structurally highest levels of the MP and lower portions of the WP thrust blocks are present in the Striped Hills area. If the KMM thrust had occurred within the Ivanpah Mountains, outcrops of

the KMM basal bounding fault should be present west of Striped Hills. Alternatively, the KMM thrust may have moved over top of the WP and MP thrust blocks in the Striped Hills area. All indications are that Late Cretaceous thrusting along the Mesozoic foreland fold and thrust complex did not affect the Ivanpah and New York Mountains. Rapid uplift of the southern Ivanpah Mountains to near surface conditions would account for the lack of Keaney-Mollusk Mine thrusting in the Ivanpah Mountains and further south. Near surface transport of the Keaney-Mollusk Mine thrust plate would have ridden over the Ivanpah Mountains area, which explains the lack of exposures of this third episode of thrusting.

The Cretaceous episode of rapid uplift could also be responsible for both ductile and brittle deformation along the Morning Star and New York Mountains thrust faults, as well as for the parautochthonous thrusts in New Trail Canyon and Sagamore Canyon-Slaughterhouse Springs areas. The extensive igneous activity combined with rapid uplift to the south-southwest could have given rise to eastward directed thrusting during Late Cretaceous (90 to 105 Ma) time. Fluid infiltration and thermal heating of the region caused by igneous activity may have induced mylonite formation which converted to brittle deformation as either shallower crustal levels were obtained or thermal dissipation occurred. The ductile deformation on the Morning Star and New York Mountain thrust faults contrasts with brittle deformation along the KMM thrust which rode close to the surface. Spatial distribution of these structural features with respect to the Late Cretaceous igneous activity would suggest a decrease in ductile deformation away from the area of uplift, which is consistent with field evidence.

Implications for Mineralization

Mineralization in the northeastern Mojave Desert appears to be either genetically or indirectly related to intrusion of various phases of the Teutonia batholith. The batholith corps out as an elongated ellipse, with its long axis trending NW-SE, centered around Cima Dome (Figure 1.2). The older (Jurassic and Early Cretaceous), mesozonal intrusions form a crescent around the margins of the batholith to the northwest, northeast and east, with the younger (Late Cretaceous), epizonal plutons forming the core of the ellipse. Mineralization includes metasomatic and skarn deposits which occur in parautochthonous and allochthonous sedimentary rocks either above or at the contact with batholithic intrusions to the north and east, and precious- and base-metal mineralization within the intrusive phases of the batholith.

Skarn and metasomatic mineralization is genetically related to intrusion of the older members of the batholith. These deposits range from Ag-Pb-Zn dominated in the north (Clark Mountains) where the early thrusting is thickest, to Ag-Pb-Zn and Cu deposits in the New Trail Canyon area and Cu- and W-bearing skarns in the New York Mountains, where remnants of the early thrust plates are absent. The change in mineralogy of skarn deposits to the south implies formation of the southern deposits at higher temperatures and pressures, which is consistent with deeper pluton emplacement depths (Anderson et al., 1989) and larger amounts of post-Cretaceous uplift (Burchfiel and Davis, 1981; Hoisch et al., 1988). The only skarn deposits which do not fit this zonation are the Sn-W and Cu skarns in the Striped Hills and Evening Star areas of the Ivanpah Mountains. These skarn deposits in the Ivanpah Mountains occur at the contact between miogeoclinal and platform sedimentary rocks and the mid-crustal level Striped Hills granodiorite.

Precious-metal mineralization occurs in fault rocks within plutonic phases of the Ivanpah and New York Mountains. This fault zone-hosted, precious-metal mineralization only occurs west of the correlated Morning Star and New York Mountain thrust faults

and east of the batholith's central core of Late Cretaceous intrusions. Epithermal mineralization post-dates the second episode of faulting (≤90 Ma), which correspond to regional uplift and epizonal Late Cretaceous intrusions. The zone of precious-metal mineralization forms an elliptical-shaped crescent around the late plutonic phases, particularly the Kessler Springs adamellite, which were likely responsible for renewed deformation along the Mesozoic foreland fold and thrust belt (see above). It is also likely that this final episode of plutonic activity provided the thermal input required to form hydrothermal mineralization. The 60 to 80 Ma sub-economic porphyry Mo-Cu mineralization in the central New York Mountains (Hewett, 1956; Ntiamoah-Agyakwa, 1987) probably result from this final plutonic episode within the Teutonia batholith.

Hydrothermal mineralization appears to be concentrated to the north and east of the Teutonia batholith because of the pre-existing structural fabric established by the Mesozoic foreland fold and thrust belt and the succession on shallower levels of pluton emplacement to the southwest. Hewett (1956) originally noticed the lack of mineralization in the area southwest of the batholith's axis, which runs through the Cima Dome area, and attributed this absence of mineralization to deeper levels of erosion within the batholith. New estimates for depth of pluton emplacement and regional uplift (Anderson et al., 1989; Burchfiel and Davis, 1981; Hoisch et al., 1988) indicate the southwestern portion of the batholith represents shallow pluton emplacement and lesser amounts of erosion. Thus the lack of mineralization appears to be caused by the Late Cretaceous episode of pluton activity.

Summary and Conclusions

Three episodes of Mesozoic thrusting occurred along the Foreland fold and thrust belt: prior to 190 Ma, between 90 and 105 Ma and post-80 Ma. Each episode of deformation is interrupted by magmatic activity. In the Clark Mountains only the first and third episodes of thrusting occur, but reactivation of early thrusts during the second episode of deformation is probable. In the Ivanpah Mountains only the first and second episodes are observed, and in the New York Mountains only the second episode is present. The third episode of thrusting is absent in the Ivanpah and New York Mountains due to shallowing of the near surface KMM thrust block south of the Clark Mountain thrust complex. Skarn mineralization is related to early plutonic activity, and deformation and magmatism during and shortly after the secondary episode of Mesozoic thrusting led to the formation of the hydrothermal precious-metal mineralization.

Chapter 2

Structural Petrology and Alteration of the Morning Star Fault System.

Introduction

Structurally-controlled mineral deposits typically exhibit evidence of hydrothermal fluid infiltration and alteration of fault-generated rocks. The type of fault rocks formed at various times during the evolution of structurally-controlled mineral deposits may have a pronounced effect upon the style of deformation and physical and chemical conditions of ore formation. For example, the development of a syntectonic clay-bearing fault gouge results in steady-state frictional behavior which produces stable sliding (Scholz et al. 1972; Byerlee & Summers 1976). The early formation of a clay gouge, at low confining pressures, decreases cataclastic deformation required to form dilatant zones for fluid migration and subsequent mineralization (Logan et al. 1979). Therefore, it is important to differentiate between syntectonic and post-tectonic mineralization and alteration in structurally-controlled deposits.

The Ivanpah Mountains of the eastern Mojave Desert formed in response to tectonic and magmatic activity along the Mesozoic foreland fold and thrust belt (Chapter 1). Structurally-controlled mineralization occurs throughout the Ivanpah Mountains and in particular along the Morning Star fault system (MSFS) at the Morning Star deposit and a series of sub-economic historic workings. The evolution of structurally-controlled mineralization and metallogeny in the Ivanpah Mountains are related to the structural

evolution of the area, and more specifically the evolution of the MSFS. This paper describes the various fault rocks within the MSFS. A structural analysis of these fault rocks was conducted to establish sense of fault displacement, style and physicochemical conditions of deformation, and timing of tectonic and hydrothermal activity.

Geological Setting

The Mesozoic foreland fold and thrust belt forms a continuous structural belt which extends across the western United States to the New York Mountains in the northeastern Mojave Desert, California (Burchfiel and Davis 1972; 1975; 1977). The Early and Late Mesozoic structural fronts of the Mesozoic foreland fold and thrust belt converge into essentially a single front at the Clark Mountains of the northeastern Mojave Desert (Figure 2.1) (Burchfiel and Davis 1971; 1972; 1975). Continuation of the foreland fold and thrust belt to the south of the Clark Mountains, where deformation shifts eastward from Paleozoic miogeoclinal sedimentary rocks to platform sedimentary rocks and Precambrian crystalline basement, is disrupted by the emplacement of the Jurassic-Cretaceous Teutonia batholith (Beckerman et al. 1982; Chapter 1). Three episodes of thrusting (pre-190 Ma, 90 to 105 Ma and post-80 Ma) occurred in the northeastern Mojave Desert (Chapter 1; Burchfiel and Davis 1971; 1988). Thrusting only cuts batholithic rocks along the MSFS in the Ivanpah Mountains (Chapter 1) and the New York Mountain thrust fault of the New York Mountains (Beckerman et al. 1982). Burchfiel and Davis (1971; 1977) and Beckerman et al. (1982) have correlated the New York Mountain thrust to the MSFS and thrust movement occurred on both fault systems between 90 and 105 Ma (Chapter 1).

Figure 2.1 Generalized geologic map of the Teutonia batholith and surrounding areas. Modified after Beckerman et al. (1982) with additional geology from Evans (1971; 1974), Burchfiel and Davis (1971; 1988), DeWitt et al. (1984) and this study. A detailed map of the area around the Morning Star fault system (outlined) is shown in Figure 2.2. Faults shown on the map, listed from north to south, include Pachulka thrust (PT), Mesquite Pass thrust (MP), Mollusk Mine thrust (MMT), South fault (SF), Sterling thrust (ST), Mescal thrust (MT), Kokoweef fault (KF), Morning Star thrust (MS), Slaughterhouse fault (SHF), and New York thrust (NYM). Sample Law-89-04 on the Pachulka thrust and Law-89-03 on the Sterling thrust were studied for comparison to structures along the Morning Star fault system (Figure 2.2).

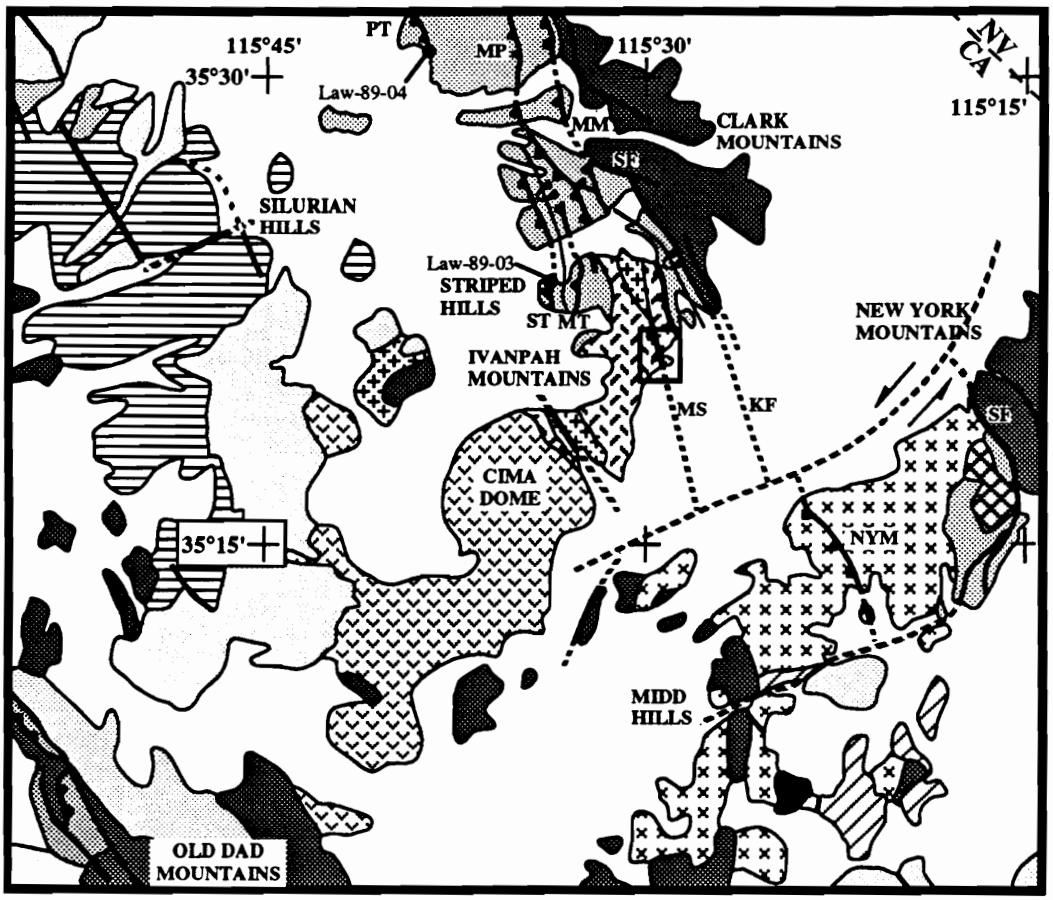

Quaternary Alluvium

Cenozoic Volcanics and Sediments

TEUTONIA BATHOLITH

CRETACEOUS

- Live Oak Canyon Granodiorite
- Teutonia Adamellite
- Kessler Springs Adamellite
- Mid Hills Adamellite
- Black Canyon Gabbro

JURASSIC

- Ivanpah Granite
- Rock Spring Monzodiorite
- Undifferentiated Granitic Rocks

Paleozoic and Mesozoic Sediments

Precambrian Metamorphic Rocks

0 5 10 miles

0 5 10 15 km

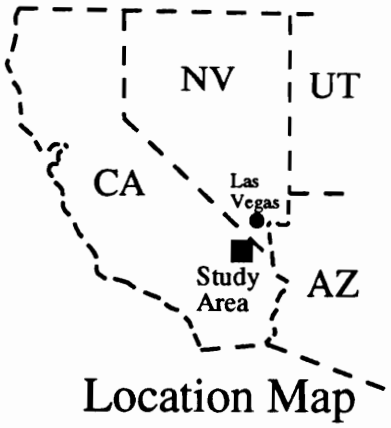

Location Map

Ductile deformation, outside the Ivanpah and New York Mountains, only occurs on the basal fault of the Winter Pass thrust plate, which has been mapped as the correlated Winter Pass, Pachulka and Sterling thrust faults, in the Clark Mountains (Figure 2.1). All other thrusts in the Clark Mountain thrust complex exhibit only brittle deformation. The Pachulka thrust is marked by a 1 to 4 cm ultramylonite which separates 100 m of Precambrian mylonitic gneiss in the upper-plate from 5 m of mylonitic quartzite of the Mesquite Pass thrust plate in the lower-plate (Burchfiel and Davis 1988). Deformed rocks form L and L-S mylonites with a shallow dipping mylonitic foliation and a stretching lineation which plunges S80°W (Burchfiel and Davis 1988). The S-C fabric and other shear sense indicators are consistent with eastward directed thrusting along the Pachulka thrust (Burchfiel and Davis 1988).

The Ivanpah Mountains form the southern continuation of the structurally complex Clark Mountains. Early (>190 Ma) eastward directed thrusting of the Mesozoic foreland fold and thrust belt dissects the miogeoclinal sedimentary rocks of the Striped Hills area on the northwestern flank of the Ivanpah Mountains (Figure 2.1). All thrusts in the Striped Hills area contain brittle deformation except for the Sterling thrust. The Sterling thrust consists of a series of discrete S-C mylonitic shear zones where the mylonitic fabric becomes more penetrative at structurally higher levels. Burchfiel and Davis (1971) originally correlated the Sterling thrust with the basal Winter Pass and Pachulka thrust faults, but later (Burchfiel and Davis 1988) assigned the Sterling thrust to the uppermost levels of the Mesquite thrust plate. S-C mylonitic foliation and lineation have similar trends to those on the Pachulka thrust and indicate eastward directed thrusting (Burchfiel and Davis 1971; 1988).

Intermediate age (90-105 Ma) thrusting occurs along the MSFS and within autochthonous and parautochthonous platform sedimentary rocks of New Trail Canyon

(Chapter 1). The MSFS has been interpreted as a continuation of Mesozoic foreland thrusting (Burchfiel and Davis 1971) that displaces the Ivanpah pluton – an early member of the Teutonia batholith (Beckerman et al. 1982; Chapter 1) – on both sides of the fault. Both ductile and brittle deformation occurred along the Morning Star and Sunnyside faults – the two principal structures within the Morning Star fault system (Figure 2.2). Deformation along the Morning Star fault system is described below in detail. Ductile deformation also occurs on the New York Mountains thrust fault in the New York Mountains (Beckerman et al. 1982).

The Ivanpah Mountains are underlain by the Jurassic Ivanpah granite and Striped Hills granodiorite of the Teutonia batholith. The Teutonia batholith is a complex series of Jurassic and Cretaceous plutons derived from partial melting of the Precambrian basement complex following early stages of Mesozoic thrusting (Beckerman et al 1982; Wooden et al. 1988; Wooden et al. 1990). Batholithic rocks intruded the Precambrian crystalline complex and Paleozoic allochthonous miogeoclinal and autochthonous platform sedimentary sequences. Numerous late stage granite and diorite dikes genetically related to the Teutonia batholith cut the Ivanpah Mountains (Appendix A). Cretaceous plutonism of the batholith is unaffected by thrusting in the Ivanpah Mountains, but the 105 Ma Mid Hills adamellite is cut by the New York Mountains thrust in the New York Mountains.

Previous Work

During a regional geology and mineral resource reconnaissance study of the northeastern Mojave Desert, Hewett (1956) designated all foliated rocks along the MSFS and New York Mountain thrust fault as Precambrian gneiss that was thrust over portions of the Teutonia Quartz monzonite (later renamed Teutonia Batholith). Following

Figure 2.2 Generalized geologic map around the area containing the Morning Star fault system. Location of mylonite samples used in petrofabric analyses are given on the map.

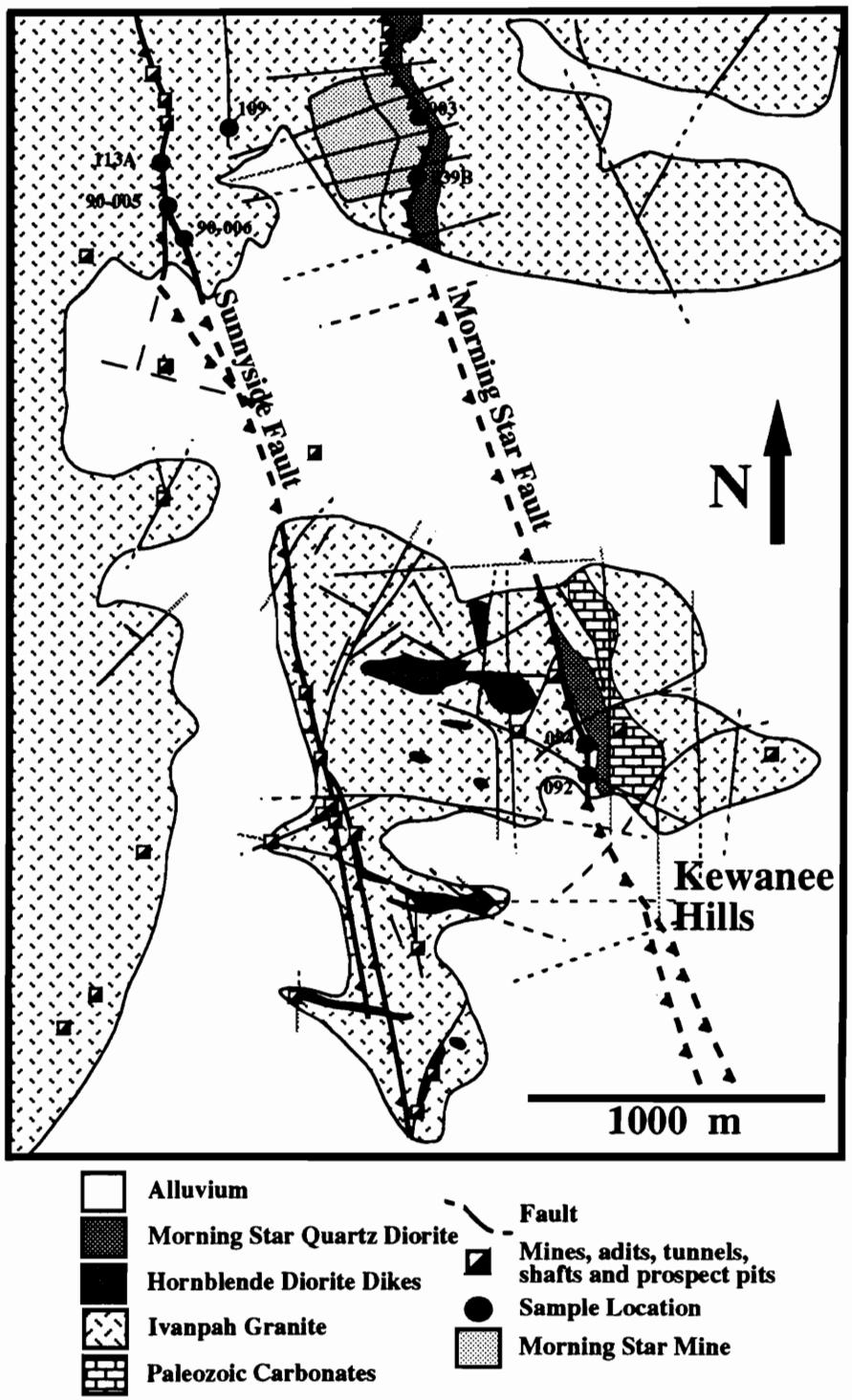
109
113A
90-005
90-006
103
39B
Sunnyside Fault
Morning Star Fault
N
084
092
Kewanee
Hills
1000 m
Alluvium
Morning Star Quartz Diorite
Hornblende Diorite Dikes
Ivanpah Granite
Paleozoic Carbonates
Fault
Mines, adits, tunnels, shafts and prospect pits
Sample Location
Morning Star Mine

Hewett's work, Evans (1958; 1971; 1974) and Thompson (1978) remapped structures of the western Ivanpah Mountains, but kept with Hewett's interpretation. Regional structures and tectonic evolution of the eastern Mojave Desert have been worked out by Burchfiel and Davis (1972; 1975; 1977; 1981); the regionis summarized in Chapter 1 and shown in Figure 2.1. In an attempt to bracket the timing of regional thrusting Sutter (1968) and Weisenberg (1973) described the geochronology and igneous petrology, respectively, of the Ivanpah Mountains and adjacent areas. Burchfiel and Davis (1972; 1975; 1977; 1981), Sutter (1968) and Weisenberg (1973) mapped the MSFS as a thrust fault and related eastward directed thrusting to the final episode of movement (post-80 Ma) on the Mesozoic foreland fold and thrust belt of the Clark Mountains. Nelson and Burchfiel (1979) showed that Mesozoic sub-horizontal shortening in the New Trail Canyon area of the Ivanpah Mountains was accomplished by large scale folding and parautochthonous thrusting of Paleozoic platform sedimentary rocks, and penetrative shearing in the crystalline basement. The MSFS and parautochthonous thrusts in the New Trail Canyon have been reinterpreted to be part of a intermediate age episode of thrusting (105 to 90 Ma) along the Mesozoic foreland fold and thrust belt (Chapter 1).

Precious-metal mineralization at the Morning Star deposit occurs as a tabular zone of high grade ore which lies directly above the fault plane in the upper-plate of the Morning Star fault (Chapter 3, 4). Early mineralization exhibits deformation textures consistent with post-depositional fault displacement. Additional sub-economic mineralization occurs along the subparallel Sunnyside fault and the southern extent of the Morning Star fault (Figure 2.2). Ausburn (1988) and Sheets et al. (1989) argued for thrust displacement on the Morning Star fault within the Morning Star deposit, because ductile deformation overlies brittle deformation. However, Byington (1988; 1989) re-interpreted movement on the Morning Star fault to be right-lateral normal oblique slip

based on an Andersonian-type construction from conjugate fracture and vein sets in the Morning Star open pit.

A detailed study of the fault rocks along the MSFS has been instituted to determine shear sense during brittle and ductile deformation and the relationship between deformation and mineralization at the Morning Star deposit. The details concerning sample selection and analytical techniques used in this study are given in Appendix 2.1.

The Morning Star Fault System

The Morning Star fault system consists of the Morning Star fault, the Sunnyside fault and a complex set of structures between these two bounding faults (Figure 2.2). The Morning Star fault trends N20°W and dips 35°SW, while the Sunnyside fault has a parallel trend but dips between 35 and 45°SW. Both faults contain equigranular to porphyritic Ivanpah granite in both the upper and lower plates. The Ivanpah granite is an equigranular to porphyritic guartzofeldspathic granite with minor biotite and hornblende (Appendix A). The pre-tectonic Morning Star quartz diorite dike crops out locally along the Morning Star fault directly below the fault, and minor remnants of hornblende diorite dikes occur along the Sunnyside structure (Figure 2.2). Numerous fine-grained dikes occur throughout the area of deformation.

The Morning Star fault crops out as a 0.3 to 2.4 meters thick fault gouge zone (described below) which truncates the Morning Star dike. The Morning Star and Sunnyside faults are also marked by a 3 to 6 meters thick zone of foliated granite. The mylonite along the Morning Star fault grades upward into a discrete protomylonite zone, while mylonites on the Sunnyside fault resemble those along the Morning Star fault except protomylonites are more abundant.

The Morning Star fault mylonite unit lies immediately on top of the fault gouge zone and clasts of foliated rocks have been found in the gouge zone near this sharp contact. The zone of ductile deformation (mylonite and protomylonite) has been displaced over the zone of brittle deformation (fault gouge), and is indicative of eastward directed thrust displacement during brittle deformation along the Morning Star fault. The lower portion of the mylonite is sericitically and argillically altered, and typically brecciated. Mylonitic foliation is manifest by stretched quartz ribbons and elongated pods of cataclastically deformed feldspar. No variation in the orientation of mylonite foliation was observed during the transition from undeformed to protomylonite or from protomylonite to mylonite. Only a change in the penetrative nature of the foliation was observed between the protomylonite and mylonite, which is suggestive of a strain gradient.

The Sunnyside structure is marked by a mylonite unit with a thin (<0.3 meter thick) fault gouge that cuts the mylonite approximately in half. At the structurally highest levels of the Sunnyside mylonite zone, in the area of sample 90-005 (Figure 2.2), the mylonitic fabric is folded into a synform which is asymmetrically overturned to the southwest (Figure 2.3). Erosional features and alluvium cover west of the folded mylonite obscure the structural elements which caused this folding. However, the asymmetry of the synform is indicative of eastward directed thrusting following mylonite formation on the Sunnyside fault.

The area between the Morning Star and Sunnyside faults contains a series of discrete mylonite and protomylonite units oriented sub-parallel to the Morning Star and Sunnyside faults. These mylonite units are typically truncated by quartz-filled breccia

Figure 2.3 Asymmetrically overturned synform in the upper portion of the Sunnyside mylonite zone near the Sunnyside mine decline (at location 90-005 on Figure 2.2). Photograph taken looking northwest and mechanical pencils define the mylonitic foliation on each folded limb of the synform. The asymmetry is indicative of dextral or eastward directed thrusting following mylonitic fabric development.

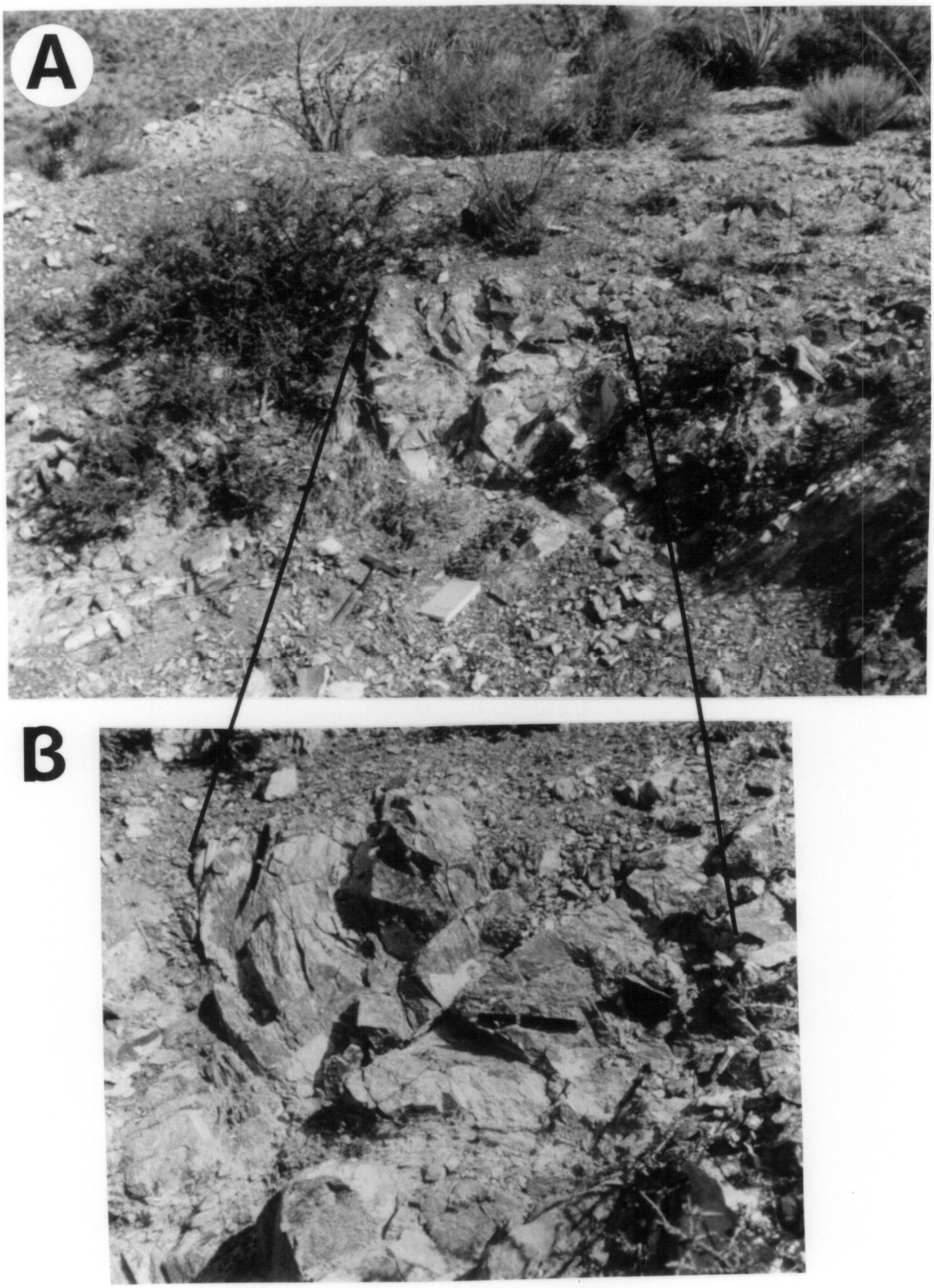
A
B

veins and are commonly thinner than the mylonite zone that marks the Morning Star and Sunnyside faults. No strain transition or rotation of pre-existing fabrics were detected along any of these sub-parallel mylonite units. All other features of these intermediate mylonitic units are similar to the mylonites found on the Morning Star and Sunnyside faults.

Brittle structures in the MSFS are manifest by thin fractures and veins, cataclastic deformation of the mylonite, brecciation of the granite and fault gouge formation. These brittle structures have overprinted the ductile deformation along the MSFS. Faults and fractures of various orientations cut the upper-plate and, to a lesser extent, lower-plate rocks along the Morning Star fault (Figure 2.2). These brittle structures are less well developed along the Sunnyside structure, but alluvium covers the upper-plate of the Sunnyside structure. Brittle structures at the Morning Star mine site include a series of E-W to ENE-WSW trending steeply dipping unmineralized structures, and mineralized stockwork veins, breccia zones and low angle structures. Two sets of mineralized structures, confined to the upper-plate of the Morning Star fault, have been identified (Chapter 3). One set strikes N to NW and dips vary from sub-parallel to the Morning Star fault (35°SW), moderately dipping (50 to 25°) in the same direction as the Morning Star fault (SW) – some of these structures asymptotically approach the fault with depth –, and dipping back (NE) at a high angle (60 to 85°) into the Morning Star fault. The second set of mineralized veins varies in strike from NE to E-W and dip at a moderate to high angle (from 60°N to 60°S). Intersection of the two principal mineralization vein sets creates oreshoots trending S84°W and plunging 62°SW (Byington 1988; 1989). Mineralized quartz±carbonate stockwork veins and silica-cemented breccias form a tabular-like orebody within and above the mylonite zone along the Morning Star fault.

The unmineralized E-W structures are vertical to steeply north dipping (90 to 60°) and cut the Morning Star orebody, Morning Star fault and Morning Star dike. Displacement on the E-W structures appears to be left-lateral normal oblique-slip with the northern side moving down and westerly relative to the southern side. Maximum throw of up to 4.5 m occurs on each E-W structure. Similar E-W structures have been postulated under the alluvial cover between the Morning Star deposit and the Kewanee Hills area (Figure 2.2) based on structural contour mapping of the Morning Star fault surface in 140 exploration drill holes. Similar E-W structures could not be mapped through to the Sunnyside fault due to alluvial cover and lack of exploration drilling, but some E-W structures were observed in prospect pits and tunnels along the Sunnyside structure. The E-W structures form an en echelon left-lateral array of fractures which accounts for the eastward displacement of the Morning Star and Sunnyside faults in the Kewanee Hills area (Figure 2.2). In the Morning Star deposit, the unmineralized E-W structures are filled with a white clay-bearing gouge which differ from gouge along the Morning Star fault in that granite fragments are angular and the matrix is not foliated.

Pervasive to weak propylitic alteration occurs in both the upper- and lower-plates of the Morning Star fault and envelops the area of mineralization. The intensity of the propylitic alteration decreases rapidly away from the Morning Star mine site and is truncated to the north by an E-W high angle structure. Argillic + sericitic alteration occurs only in the mineralized upper-plate adjacent to the stockwork vein system and silica-flooded breccias. Alteration of the Morning Star fault gouge and unmineralized E-W structures is also believed to be related to the argillic + sericitic alteration episode. Silicification is prevalent around the tabular ore horizon and at a structurally higher level in the upper-plate of the Morning Star fault where the principal fracture sets intersect.

Ductile Fault Rocks

Macrostructures

Ductiley deformed granite along the Morning Star and Sunnyside faults form mylonites with a well developed mylonitic foliation and a weak down dip mineral lineation. The mineral lineation was observed on only 36% of the mylonite outcrops and hand specimens. Foliation (S) surfaces in the Morning Star mylonites trend S16°E and dip 39°SW and those in the Sunnyside mylonites trend S13°E and dip 43°SW (Figure 2.4). The mineral stretching lineations trend S86°W and plunges 43°SW for the Morning Star mylonites, and trend S78°W and plunge 42°SW for the Sunnyside structures (Figure 2.4). The stretching lineation for both structures is at a high angle (102° and 91° for the Morning Star and Sunnyside structures, respectively) to the mylonitic foliation, which indicates essentially dip slip movement during ductile deformation on both structures. The mylonite stretching lineation has essentially the same trend as oreshoots in the Morning Star deposit (S84°W, 62°SW), although the oreshoots have a steeper plunge.

In slabs and thin sections cut parallel to the XZ plane, the mylonites form Type I S-C mylonites according to the classification of Lister and Snoke (1984) with well defined S surfaces (mylonitic foliation) but only weakly developed C surfaces (Figure 2.5). Occasionally the S surfaces are folded or crenulated with asymmetric fold axial planes aligned approximately parallel to the C surfaces (Figure 2.5C). Heterogeneity in the original granite composition also causes differences in the textural development of the resulting mylonite. For example, slight changes in the modal abundance of feldspars and mica, relative to quartz, causes islands of cataclastically deformed feldspar in quartz

Figure 2.4 Field orientations of poles to foliation and lineations in the Morning Star fault system. Both structures are plotted on stereonet A and only the Morning Star mylonites and Sunnyside mylonites are plotted on stereonets B and C, respectively. The number of data points (N), contour intervals (C.I.) and the orientation of the point maxima for each stereographic projection are given below the respective net.

POLES TO FOLIATION

LINEATIONS

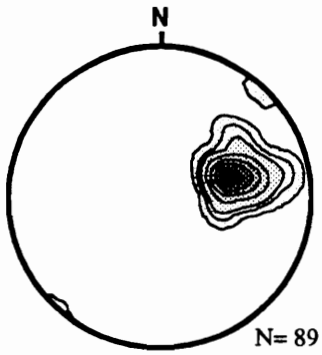

N= 89
C.I.=1, 3, 5,10,15, 20, 25, 27
Maxima 163°, 43°SW

A

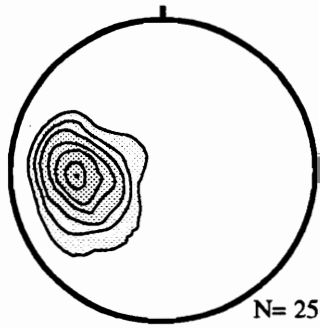

N= 25
C.I.=1, 3, 5, 8, 10, 13, 15
Maxima 266°, 42°SW

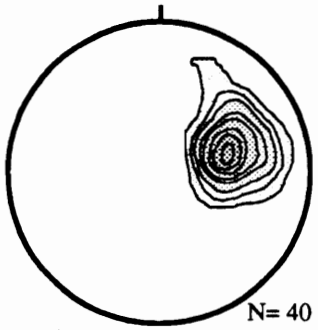

N= 40
C.I.=1, 3, 5, 8,10,13,15,17
Maxima 164°, 39°SW

B

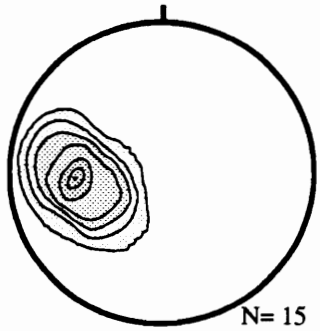

N= 15
C.I.=1, 3, 5, 7, 10, 12
Maxima 266°, 43°SW

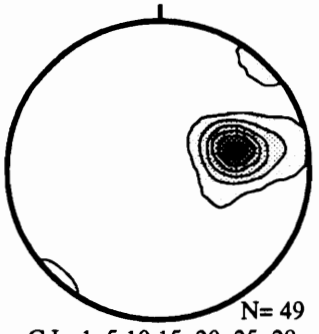

N= 49
C.I.=1, 5,10,15, 20, 25, 28
Maxima 167°, 43°SW

C

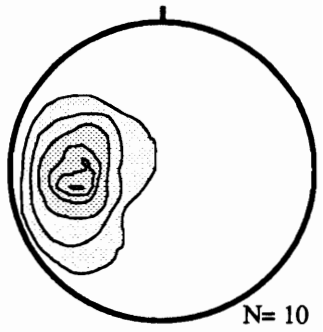

N= 10
C.I.=1, 3, 5, 7, 8, 9
Maxima 258°, 42°SW

Figure 2.5 Photographs of mylonites. All samples are cut parallel to the mineral lineation and perpendicular to the mylonite foliation. Samples shown in photographs A, C and D are from the Morning Star fault and sample in figure B is from the Sunnyside fault. Samples A, B and D are oriented looking north along the fault - mineral lineation plunges and foliation dips to the left. Sample C is oriented looking south along the fault - mineral lineation plunges and foliation dips to the right. All samples illustrate macrostructures which indicate thrusting along both faults. See text for further discussion.

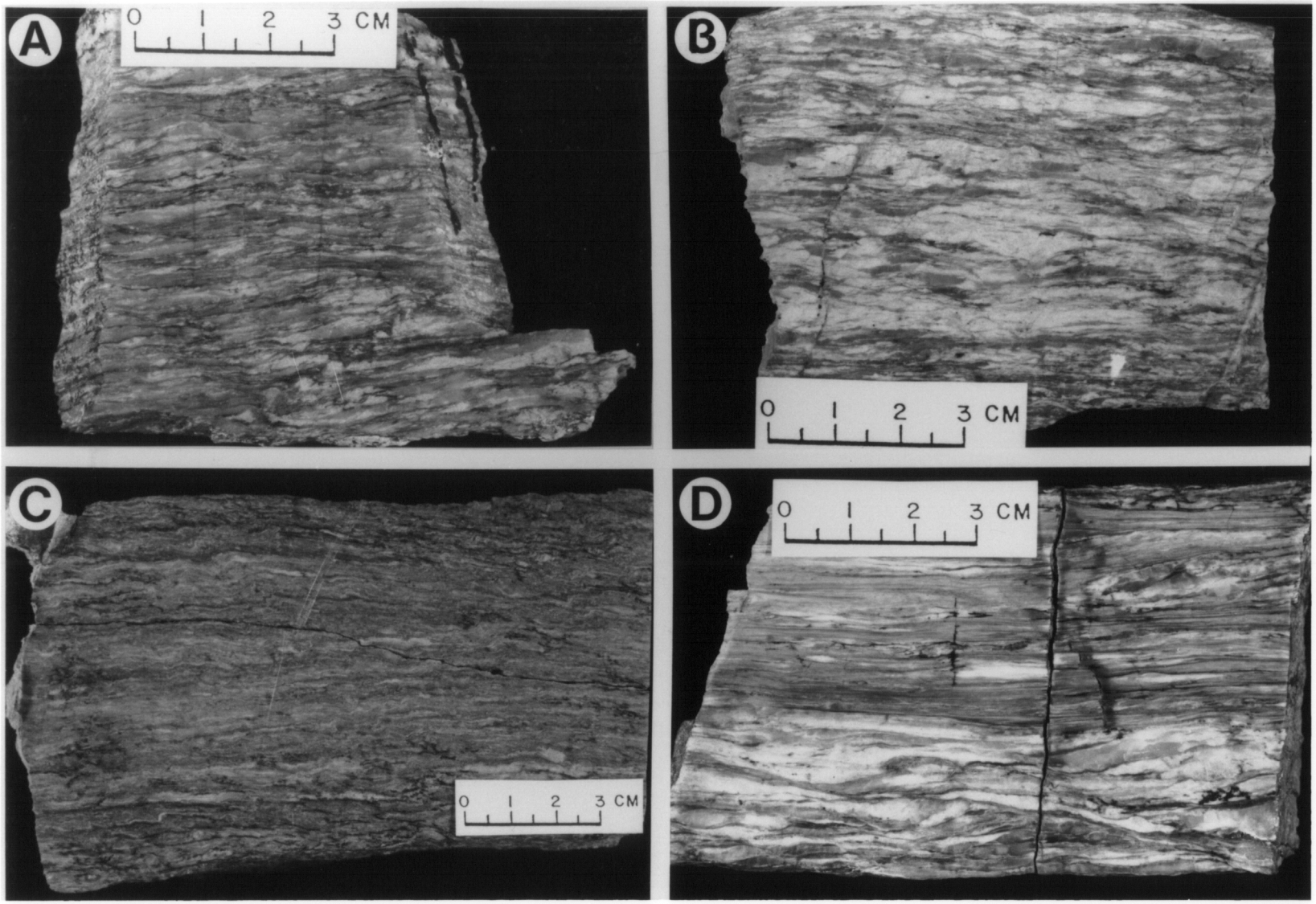
A
0 1 2 3 CM
B
0 1 2 3 CM
C
0 1 2 3 CM
D
0 1 2 3 CM

ribbons (Figure 2.5A), while quartz-rich portions are dominated by ribbon development for both quartz and feldspar (Figure 2.4D). Also, some feldspar-rich zones form asymmetrical shear bands (lower portion of Figure 2.5D) which occur more sporadically and form less continuous C surfaces. Hanmer and Passchiev (1991) suggest asymmetrical shear bands develop due to noncoaxial flow along zones of initial anisotropy, but in the Morning Star fault zone the asymmetrical, feldspar-rich shear bands exhibit the same shear sense as the S-C structures.

These kinematic indicators are better developed along the Sunnyside structure where mylonites exhibit less hydrothermal alteration or cataclastic deformation than structures along the Morning Star fault. Morning Star mylonites are typically altered to quartz-sericite and cut by quartz-cemented breccias. The mylonitic foliation appears to change orientation as shear strain increases, but brecciation obscures the transition zone and may cause local rotation of some mylonite blocks so that shear sense indicators and stain gradients could not be determined for brecciated samples. Mafic dikes in the Kewanee Hills area also exhibit S-C mylonitic fabrics. These mafic mylonites exhibit the same fabric development described above for granitic mylonites.

The S-C fabric development, asymmetrical folding of mylonitic foliation, asymmetrical shear bands and other shear sense indicators all support eastward directed thrusting during ductile deformation along the Morning Star, Sunnyside and intervening faults. Late normal fault movement is indicated by minor (millimeter scale) offsets on open joints, fractures and late veins (e.g. Figure 2.5B). These normal slip offsets may represent a relaxation feature following thrust movement.

Microstructures

Microscopically the mylonite fabric is composed of large ribbon quartz grains surrounded by bands of totally recrystallized quartz that alternate with cataclastically deformed bands of feldspar and micaceous layers. Thin micaceous layers range up to 50 μm thick and typically separate bands of quartz and feldspars. Quartz ribbons range from 500 μm to 1 mm wide and exhibit irregularly spaced subgrain development and dynamic recrystallization into finer grain sizes (up to 10 μm long). Most quartz ribbons are composed of multiple grains, but single grained ribbons were observed. The recrystallized grains have sharp, high angle grain boundaries. Also present in some larger quartz ribbons are conjugate bands containing recrystallized quartz grains (Domain A) that form angles up to 35° to the long axis of the quartz ribbon. Domain A recrystallization structures are indicative of nucleation recrystallization in regions of highest strain. Core and mantle structures also occur in some quartz ribbons, but these textures are rare. Thick quartz ribbons (1 mm thick) are commonly separated by thin bands (few 10s of μm) of totally recrystallized quartz (Domain B) or lie within zones of totally recrystallized quartz.

Zones of totally recrystallization quartz (Domain B) contain uniform sized quartz crystals which are elongated about 22° to the mylonitic foliation (S_A). This quartz grain shape alignment (S_B), relative to S_A, defines a dextral shear sense which is consistent with eastward directed thrust movement. Individual quartz grains have serrated grain boundaries. Two domains are recognized in the zones of totally recrystallized quartz grains. The first domain (B1) has quartz c-axes oriented approximately parallel to the elongation direction and in the second domain (B2) the c-axes are at a high angle to the elongation direction.

Feldspars typically exhibit brittle behavior in a ductile matrix of quartz and mica. Mechanical twinning is common in feldspars, but hydrothermal alteration destroys these

structures by preferential alteration along twin lamellae. Subgrain development occasionally occurs in highly strained samples which contain large feldspar grains. In samples with greater than 90% recrystallized quartz, the deformed feldspar aggregates exhibit recrystallization around the feldspar fragments to form a core and mantle structure.

Crystallographic Fabrics

Quartz c-axis fabrics were measured on three samples from each (Sunnyside and Morning Star) structure and one additional sample from a mylonite between the two bounding faults (Figure 2.2 and 2.6). All fabric patterns exhibit essentially a disrupted small circle distribution around the poles to foliation (Z). This is best developed in sample SS113A (Figure 2.6). Samples SS005-2, SS109-1 and MS039-B have small c-axes intervals that plot near the center of the diagram (Y) which suggests a trend towards Type I cross girdle patterns using the classification of (Lister, 1977). Sample SS006-1 and MS092-B have unusual petrofabric development with SS006-1 having essentially four point maximas distributed around the pole to foliation (Z) and lineation (X), and MS092-B exhibits a discontinuous single girdle fabric containing the specimen Y axis and passing through the XZ plane.

Crystallographic fabrics for the Morning Star and Sunnyside faults are asymmetric with respect to the poles to foliation, with samples SS006-1 and MS039-B approaching symmetrical (Figure 2.6). Sample SS109-1, which was an intermediate fault between the Sunnyside and Morning Star structures, has a nearly symmetric shaped fabric (Figure 2.6). External and internal symmetry parameters are presented in Table 2.1 to better illustrate the asymmetry where each parameter is defined by Law (1990) and shown diagramatically in Figure 2.6. The asymmetry of the petrofabric diagrams indicates

Figure 2.6 Quartz crystallographic fabrics for samples along the Sunnyside structure, the Morning Star structure and a small intervening fault between these two structures. See inserted stereographic projection for orientation and definition of external and internal symmetry parameters. All fabric diagrams are plotted with lineation down dip to the left. Therefore, all fabric diagrams are plotted with a view looking to the north along the fault. See text for discussion of individual fabric diagrams.

Sunnyside Structure

SS113A

500 data
CI=1 2 3 4 5 6 7 X uniform

SS005-2

400 data
CI=1 2 3 4 5 6 7 X uniform

SS109-1

400 data
CI=1 2 3 4 X uniform

SS006-1

625 data
CI=1 2 3 4 5 6 X uniform

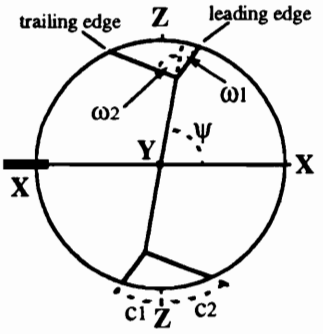

Morning Star Structure

MS039-B

300 data
CI=1 2 3 4 5 6 X uniform

MS094

500 data
CI=1 2 3 4 5 X uniform

MS092-B

300 data
CI=1 2 3 4 5 6 7 X uniform

Table 2.1 External and internal symmetry elements for crystallographic fabric diagrams.

Morning Star fault system

Sample	angle C_1	angle C_2	angle ω_1	angle ω_2	angle ψ
SS113A	23°	39°	42°	73°	74°
SS005-2	28°	34°	38°	76°	72°
SS006-1	41°	44°	NA	NA	NA
SS109-1	36°	37°	67°	72°	88°
MS039-B	36°	37°	51°	66°	84°
MS094	36°	38°	NA	NA	NA
MS092-B	NA	30°	NA	NA	58°

Pachulka thrust in the Clark Mountains

Sample	angle C_1	angle C_2	angle ω_1	angle ω_2	angle ψ
Law-89-04	38°	41°	48°	52°	88°

Sterling thrust in the western Ivanpah Mountains

Sample	angle C_1	angle C_2	angle ω_1	angle ω_2	angle ψ
Law-89-03	35°	44°	40°	89°	70°

dextral shear sense or eastward directed thrusting with the exception of SS006-1.

Petrofabric diagrams for individual domains are shown in Figure 2.7. In sample SS006-1 (Figure 2.7A) quartz ribbons occur in micaceous layers (Quartz Ribbons 1) and in layers of recrystallized quartz grains (Quartz Ribbons 2). Quartz crystallographic fabrics for each type of quartz ribbons plot as a single or double maxima stretched out along the outer perimeter of the XZ plane of the stereonet. Ribbons in micaceous bands (Quartz Ribbons 1) have maxima which plot approximately 90° from the maxima of quartz ribbons in recrystallized zones (Quartz Ribbons 2). This arrangement can be interpreted as formation during extension for quartz ribbons in micaceous layers (Quartz Ribbons 1) and during compression for quartz ribbons in recrystallized layers (Quartz Ribbons 2). Quartz ribbons typically result from elongation of original quartz grains or by selective grain boundary migration from a fine-grained recrystallized aggregate. Either mechanism should record the shear sense during ribbon formation. The opposite sense of shear recorded by the two sets of quartz ribbons may relate to the rheological properties of the surrounding layer if the ribbon developed by elongation of original grains, or may result from the orientation of recrystallized grains if grain boundary migration was the principal deformation mechanism. Alternatively, the high angle between recrystallized ribbons may result from initial kink development of quartz which was later recrystallized during increasing strain. Bands of recrystallized quartz grains within both types of quartz ribbons (Domain A) and zones of totally recrystallized quartz grains (Domain B) have asymmetrical fabrics with point maxima on the outer XZ perimeter and the total fabric consist of four point maxima stretched out along the outer perimeter. Crystallographic fabric development for sample SS005-2 (Figure 2.7B) contain the same domains seen in sample SS006-1 (Figure 2.7A). Only type 2 quartz ribbons occur in sample SS005-2 because the sample is essentially mica free, and the

Figure 2.7 Quartz crystallographic fabric diagrams plotted for different domains within samples SS006-1 (A.) and SS005-2 (B.). The different domains include quartz ribbons, recrystallized quartz grains and trails of recrystallized grains within quartz ribbons (Domain A) and zone of totally recrystallized quartz grains (Domain B). For sample SS006-1 the quartz ribbons are divided into ribbons in micaceous bands (Quartz Ribbons 1) and ribbons in zones of totally recrystallized quartz (Quartz Ribbons 2). For sample SS005-2 the zone of totally recrystallized quartz grains is divided into two groups based on orientation of quartz c-axis (Domains B1 and B2). Total fabric diagrams include all data from each of the individual fabric diagrams plus additional c-axis orientations measured in traverses perpendicular to the mylonitic fabric. Orientation of all stereonets is the same as in Figure 2.6.

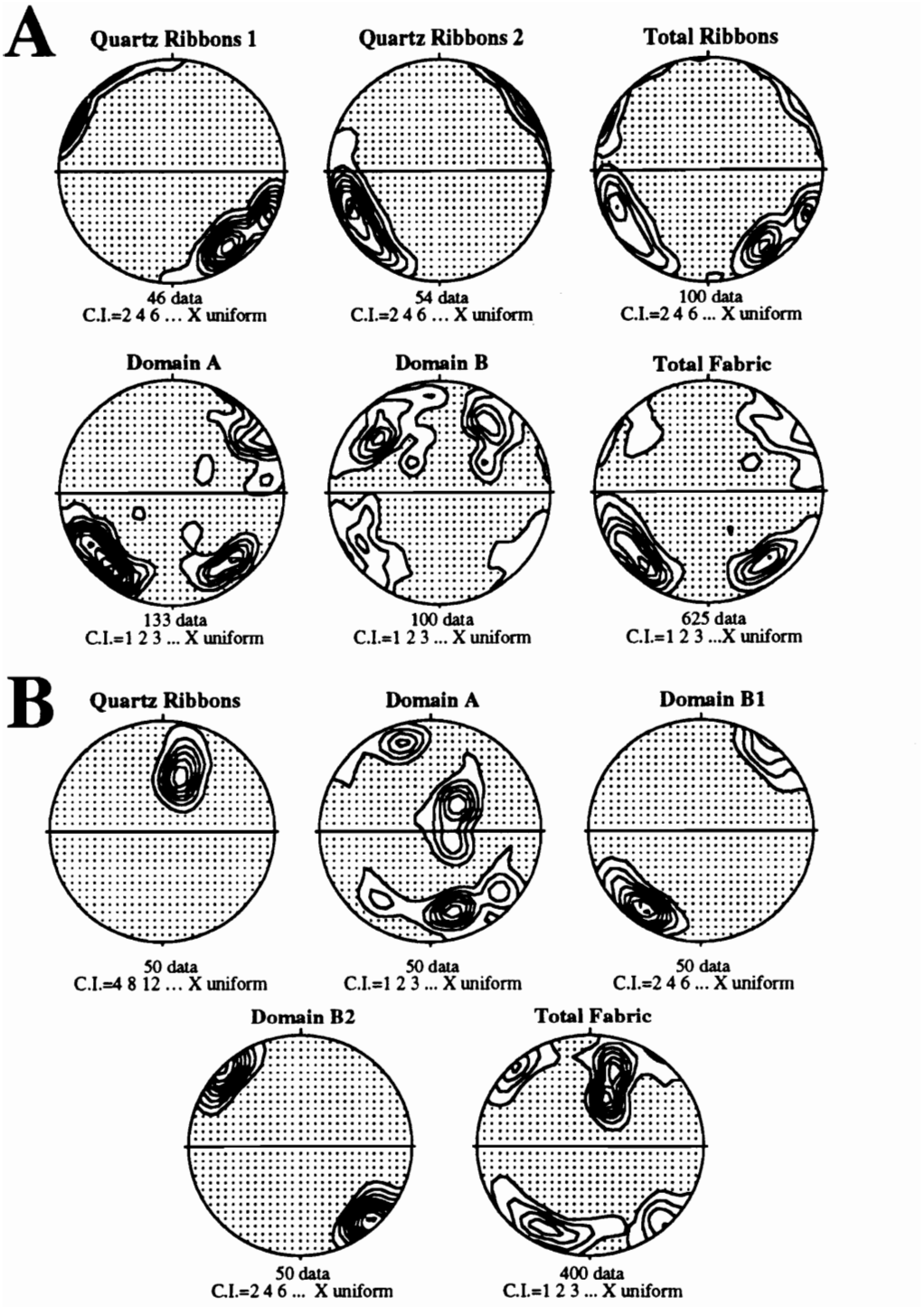
A
Quartz Ribbons 1
46 data
C.I.=2 4 6 ... X uniform
Quartz Ribbons 2
54 data
C.I.=2 4 6 ... X uniform
Total Ribbons
100 data
C.I.=2 4 6 ... X uniform
Domain A
133 data
C.I.=1 2 3 ... X uniform
Domain B
100 data
C.I.=1 2 3 ... X uniform
Total Fabric
625 data
C.I.=1 2 3 ...X uniform
B
Quartz Ribbons
50 data
C.I.=4 8 12 ... X uniform
Domain A
50 data
C.I.=1 2 3 ... X uniform
Domain B1
50 data
C.I.=2 4 6 ... X uniform
Domain B2
50 data
C.I.=2 4 6 ... X uniform
Total Fabric
400 data
C.I.=1 2 3 ... X uniform

quartz ribbons plot as a single point maxima inclined at 30° to the specimen Y axis. Two domains of totally recrystallized quartz grains occur (Domain B1 and B2) which have single point maxima at essentially 90° to each other. The total fabric development defines a small circle distribution around the pole to foliation.

Quartz c-axis orientation was also measured on sample Law-89-04 from the Pachulka thrust and Law-89-03 from the Sterling thrust (Figure 2.1 for location and Figure 2.8 for petrofabric diagrams). Both thrusts have asymmetrical and discontinuous cross girdle crystallographic c-axis patterns, where the degree of asymmetry is shown by the external and internal symmetry parameters (Table 2.1). Asymmetry is consistent with eastward directed thrusting as mapped by Burchfiel and Davis (1971; 1988). The crystallographic c-axis pattern for sample Law-89-04 from the Pachulka thrust appears to be a Type II cross girdle pattern and sample Law-89-03 from the Sterling thrust resembles a Type I cross girdle pattern using the classification of (Lister 1977). The change from Type II to Type I cross girdle crystallographic c-axis pattern suggests higher mylonite formation temperatures for the Pachulka thrust than the Sterling thrust. The cross girdle petrofabric diagrams differs from the small circle or single girdle patterns observed along the Morning Star fault system.

Brittle Fault Rocks

Within the Morning Star mine, the Morning Star fault gouge zone consists of an upper Fe-stained layer (brown gouge) and a lower unoxidized blue-gray layer (Figure 2.9A). The brown and blue-gray gouge layers generally constitute 20 and 80 percent, respectively, of the fault zone. The physical appearance of each gouge layer is identical except for the color difference, which was used during mapping to divide the gouge zone.

Figure 2.8 Quartz crystallographic fabric diagrams for the Pachulka thrust in the Clark Mountains and the Sterling thrust in the western Ivanpah Mountains. Sample locations are given on Figure 2.1. Stereonets are plotted using the conventions given for Figure 2.6.

Pachulka Thrust
sample Law-89-04

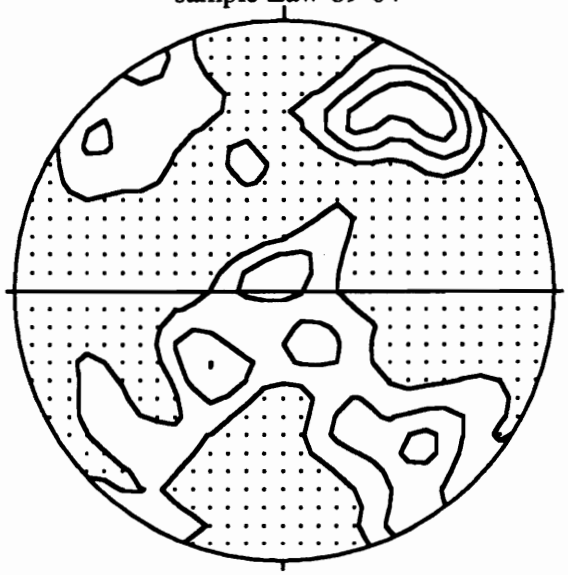

305 data
C.I.=1 2 3 X uniform

Sterling Thrust
sample Law-89-03

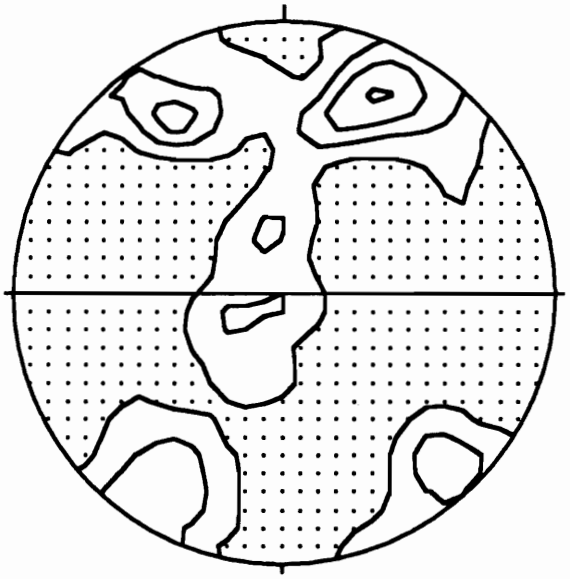

300 data
C.I.=1 2 3 4 X uniform

Figure 2.9. Photographs of the gouge layer along the Morning Star fault.

A.) Close up view of the fault gouge (brown and light blue-gray areas) that decorates the Morning star fault and altered Morning Star diorite dike (dark gray area) which underlies the fault on the 4700 bench of the Morning Star mine. Photo taken looking east into the fault zone, so the fault dips out of the photo at about 35°. Sample 003 was taken from the contact between the brown and blue-gray gouge layers in the upper central portion of the broken area of the photograph. For scale, the broken area is approximately 10 meters high.

B.) Contact of the upper gouge zone and the overlying altered Ivanpah granite (at hammer head) from the northeast corner of bench 4600 in the Morning Star mine. The upper contact is sharp and the gouge zone contains fewer coarse rock fragments.

C.) Close-up photograph of the blue-gray gouge along the Morning Star fault from the 4600 foot bench of the Morning Star mine. Oriented, rounded and elongated, bleached, gravel sized (>4 mm) granite fragments surrounded by anastomosing clay selvages occur in the blue-gray portion of the fault gouge. Note the foliated nature of the gouge in this area as compared to the area shown in Figure 2.11B. Photograph is of the area in the center of the broken away zone shown in Figure 2.9A. Sample RWS-003 is taken from the contact about 1.5 meters above the area shown.

D.) Photograph of the fault gouge that decorates the Morning Star fault outside of the Morning star mine. This gouge zone constitutes the entire width of the Morning Star fault, between the knife and the hammer head (lowermost left), from an old mine adit 300 meters north of the Morning Star mine. The photograph shows the fine grained nature and thin laminations of the gouge zone. The different colored layers (dark layers are brown gouge and light layers are blue-gray gouge) of the gouge zone are now interlayered compared to gouge found in the mine (Figure 2.9A). Above the knife is bleached Ivanpah granite and the hammer is laying on rubble on the adit floor.

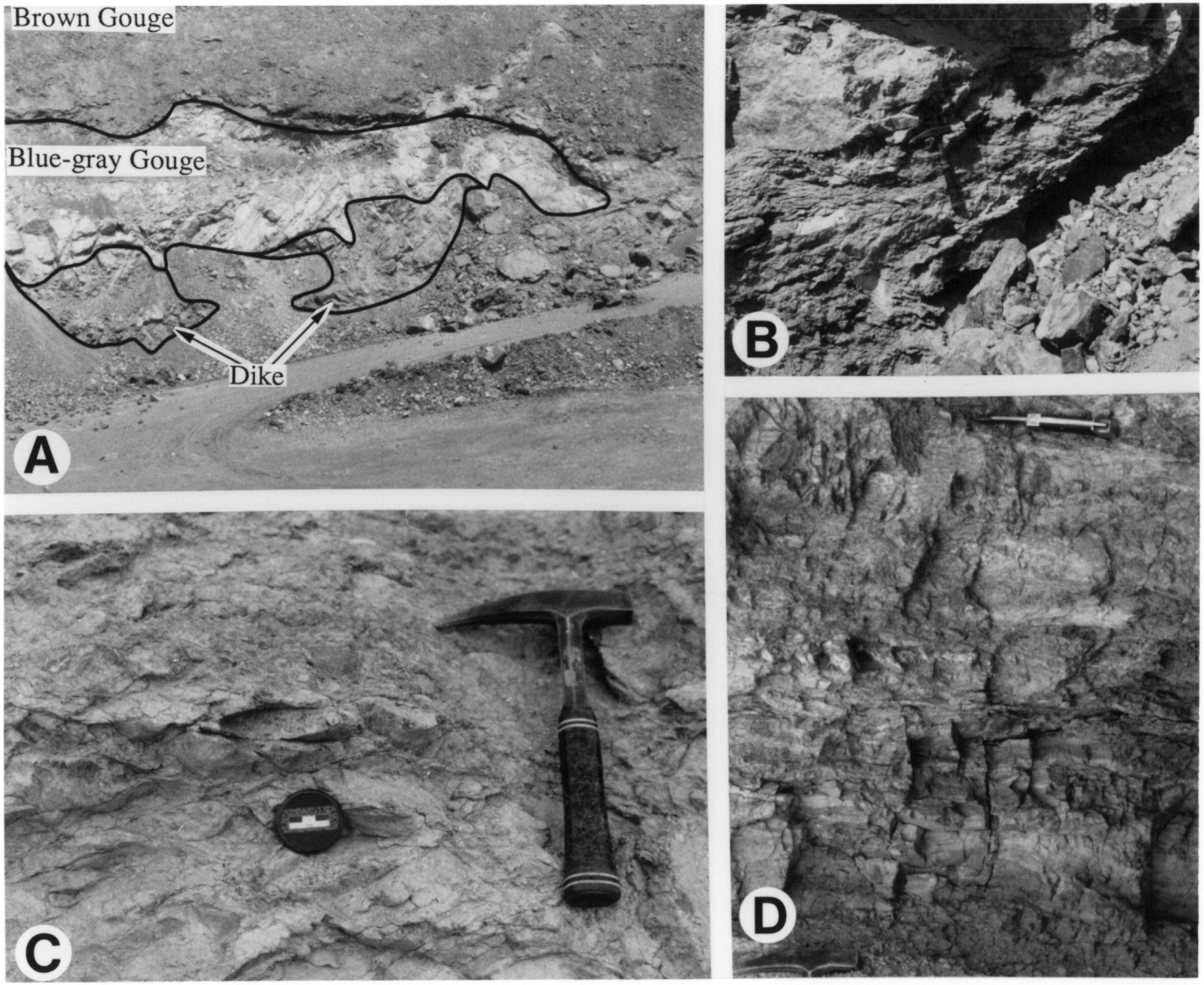
Brown Gouge
Blue-gray Gouge
Dike
A
B
C
D

The average chemical and modal analyses of the various gouge types and intrusions are given in Table 2.2. The upper contact of the gouge with the mylonitized Ivanpah granite is sharp and gouge in this upper zone contains few coarse grained rock fragments (Figure 2.9B). The remaining gouge generally consists of between 5 and 55 percent gravel-size (>4 mm) rock fragments in a matrix of sand-size and fine-grain minerals and rock fragments (Figure 2.9). The geometry of the coarse-grained fragments ranges from well rounded to elongated (Figure 2.9C). The coarse-grained fragments are composed of altered Ivanpah granite, Morning Star quartz diorite, ductiley deformed rocks, and quartz grains. Elongated fragments are commonly surrounded by anastomosing selvages of clay minerals that impart a foliated texture to the gouge zone (Figure 2.9C). Slickensides are common on these clay selvages. These slickensides have a fairly consistent orientation on individual foliation surfaces, but the slickenside orientation varies from surface to surface. The variable orientations of slickensides may have resulted from a complex fault displacement history or may be an artifact of the mining operation.

A series of discontinuous blue gouge layers typically occurs between the brown and blue-gray gouge or within the upper portion of the blue-gray gouge. These blue gouge layers, which are never greater than a few centimeters thick and usually less than two meters long, contain few visible rock fragments and have high internal cohesion. Slickensides are common and exhibit the random orientations on different foliation surfaces which is similar to slickensides observed in the brown and blue-gray gouge layers.

Within the mine, the lower contact of the gouge zone grades into either a highly altered apple green gouge zone, apple green quartz altered diorite (?) or an altered quartz diorite dike (Figure 2.9, 2.10). Pervasive propylitic alteration of the diorite dike resulted in the apple green coloration of the lower gouge and underlying diorite. Epidote and

Table 2.2. Major element oxide geochemisty and modal analysis of rocks, alteration assembleges and gouge across the Morning Star fault zone in the Morning Star deposit.

Major Element Chemistry

Rock Unit	Ivanpah Granite	Morning Star Diorite	Altered M. S. Diorite	Altered Mylonite	Apple Green Granite	Apple Green Gouge	Brown Gouge	Blue Gouge	Blue-gray Gouge	E-W Gouge
Number of Analysis	9	7	5	1	4	1	3	1	3	4
SiO2	71.08±4.09	51.40±1.43	48.75±9.23	48.71	61.95±10.48	64.24	53.15±8.93	60.60	49.84±12.49	63.23±14.75
TiO2	0.30±0.21	1.89±1.43	1.35±0.66	1.00	0.52±0.52	0.40	1.27±0.81	0.52	1.33±0.75	0.70±0.98
Al2O3	14.15±1.52	14.73±0.25	15.12±1.40	15.85	13.03±0.90	13.84	13.80±0.40	13.60	13.91±0.72	11.15±3.38
FeO*	2.06±1.24	9.26±0.80	7.95±2.96	9.31	4.11±2.53	3.17	5.34±1.53	3.18	5.10±2.16	3.66±3.43
MgO	0.4.±0.32	3.92±0.56	4.71±2.22	3.31	2.04±1.47	1.42	0.79±0.21	1.68	2.04±1.15	1.33±1.30
MnO	0.03±0.02	0.14±0.02	0.11±0.04	0.19	0.07±0.03	0.05	0.05±0.03	0.07	0.13±0.06	0.07±0.08
CaO	0.98±0.71	5.54±0.51	6.13±1.88	5.03	3.60±1.49	3.04	8.24±3.77	4.78	8.15±5.31	5.31±8.78
BaO	0.05±0.04	0.05±0.02	0.02±0.01	0.04	0.07±0.04	0.07	0.02±0.00	0.04	0.03±0.03	0.13±0.19
K2O	5.66±0.75	2.26±0.48	2.63±1.09	4.64	3.72±0.78	3.60	3.34±0.25	3.64	4.10±0.82	3.63±1.82
Na2O	3.34±0.56	3.45±0.33	2.86±0.50	1.11	2.42±0.54	3.24	0.08±0.05	0.01	1.24±1.52	0.35±0.21
P2O5	0.09±0.06	0.31±0.02	0.24±0.14	0.29	0.14±0.10	0.14	0.25±0.08	0.19	0.29±0.10	0.14±0.13
L.O.I.	1.00±0.39	5.50±1.15	8.70±4.29	10.05	7.16±3.92	6.05	12.23±2.95	10.11	12.80±6.24	9.12±6.61
Total	99.14	98.45	98.57	99.54	98.83	99.25	98.56	98.42	98.96	98.82
Reference	Chapter 1, Robinson,1979									

Average Modal Analysis

	Ivanpah Granite	Morning Star Diorite
	23	8
Quartz	27.8±4.7	9.7±2.2
Orthoclase	42.4±7.8	7.9±2.5
Plagioclase	19.2±4.9	39.5±8.2
Biotite	5.2±3.4	6.4±5.6
Hornblende	0.5±0.9	5.2±4.5
Opaques	2.1±1.1	8.3±3.1
Apatite	0.6±0.6	0.4±0.3
Sphene	0.5±0.8	0.2±0.3
Allanite	0.6±0.8	NP
Zircon	0.4±0.4	0.4±0.6
Chlorite	1.0±1.5	12.0±4.0
Epidote	0.3±0.5	7.8±4.0
Calcite	NP	1.0±1.9
Muscovite	0.4±0.7	1.2±1.6
Garnet	0.1±0.2	NP
Reference	Chapter 1, Robinson,1979	Chapter 1

chlorite are the principal mineral components in these apple green rocks and gouge. At the contact between green gouge and altered quartz diorite, the gouge contains abundant coarse-grained angular fragments of altered dike. The apple green quartz diorite is texturally identical to the Morning Star dike with all feldspars and mafic minerals replaced by chlorite, epidote and calcite. Locally the apple green quartz diorite is silicified.

Gouge along the Morning Star fault outside of the mine resembles the gouge observed within the mine, except outside the mine the gouge contains fewer coarse-grained rock fragments, lacks the apple green gouge layer and has a finer-grained, more cohesive matrix. Clasts and rock fragments in gouge encountered outside the Morning Star mine are similar to those described within the mine. Typically gouge outside the mine is thinly laminated (Figure 2.9D), and the laminated gouge forms sharp contacts at the upper and lower boundaries of the fault zone. Slickensides are generally absent in the laminated gouge. Brown and blue-gray colored gouge types are interlayered to form the laminated texture (Figure 2.9D). The thinly laminated gouge also exhibit asymmetrical folds with fold axes overturned to the east, which is consistent with thrust movement during brittle deformation on the Morning Star fault (Figure 2.10). Byington (1988; 1989) argued for right lateral normal oblique slip during brittle deformation, but the observation presented above contradict his interpretation. At shallow crustal levels where the confining pressure is low, post-thrusting relaxation of the fault may have caused minor amounts of normal fault displacement, but no evidence of strike-slip movement on the Morning Star fault was observed during this study.

High angle E-W structures are also gouge filled. These structures range from a few centimeters to a few meters wide and generally narrow with depth (Figure 2.11A). Gouge in E-W structures consists of angular rock fragments randomly distributed in an unfoliated, loosely consolidated matrix of white clay minerals (figure 2.11B). Rock

Figure 2.10. Photograph and sketch of folded fault gouge outside of the Morning Star mine. Folding (directly above the hammer) in the upper portion of the laminated gouge was seen in an abandoned mine adit 1000 meters south of the Morning Star mine. The upper left portion of the photograph shows the Fe-stained, foliated Ivanpah granite. Asymmetrically overturned to the NE folds and associated fracturing indicate thrust movement during brittle deformation postdating gouge formation.

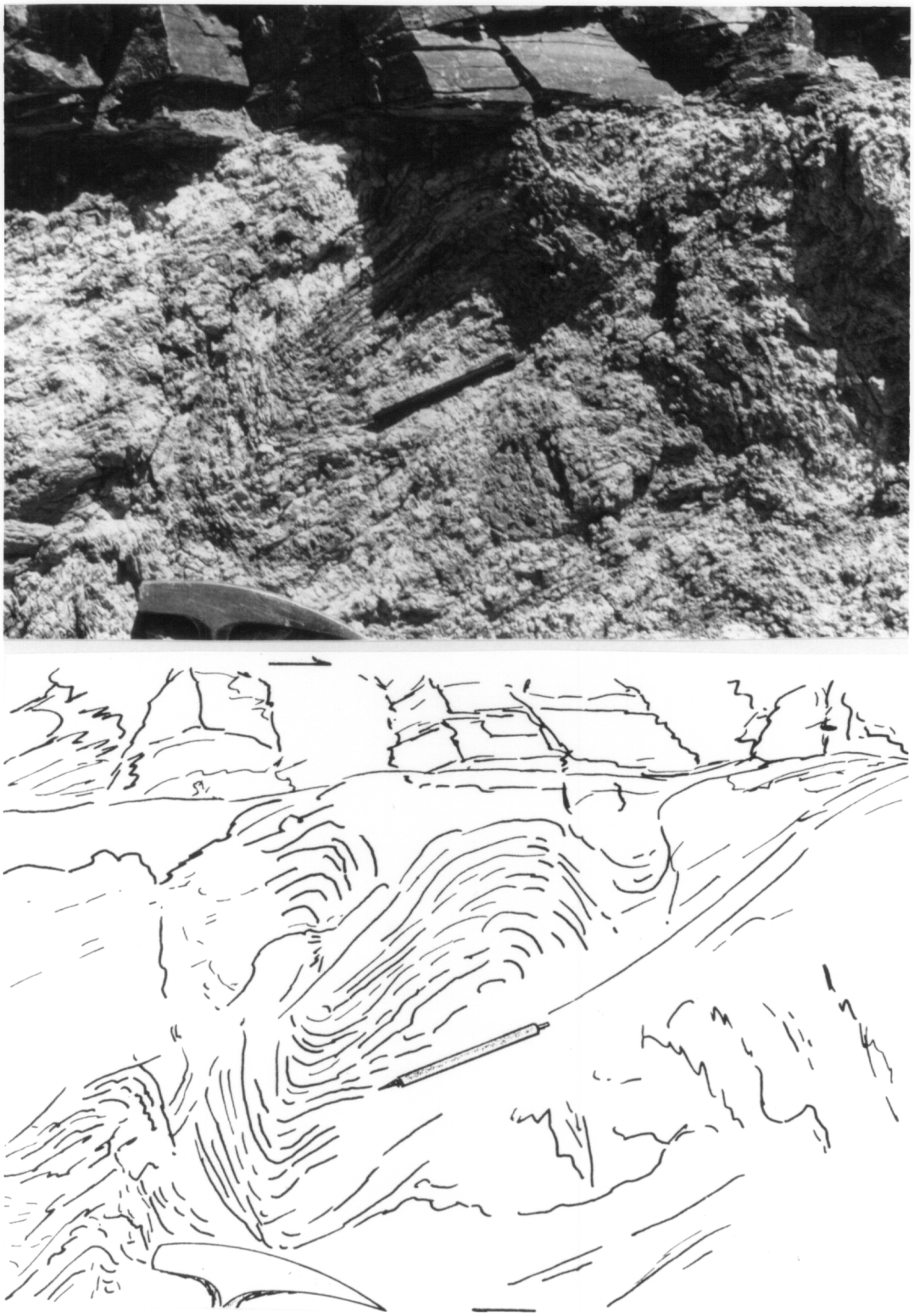

Figure 2.11. Photographs of the gouge filled E-W structures from the Morning Star mine.

A.) Typical E-W structure. The photograph was taken at the southwestern extreme of the mine on the 4600 foot bench and is looking due west. Field notebook (left) and camera case (right) are placed at the edge of the E-W structure and are 20 centimeters each for scale.

B.) Close-up photograph of gouge from E-W structures. Randomly oriented, angular, bleached, gravel sized granite fragments in a fine grained white clay-bearing matrix constitute gouge from the E-W structures. The photograph is looking due west and is a close-up of gouge from the structure in Figure 2.11A. Mechanical pencil for scale is 6 centimeters.

B
A

fragments consist entirely of quartz and altered granite and generally range from 10 to 70 percent of the gravel-size fraction.

Chemistry Across the Fault Zone

Geochemistry of host rocks and brittle fault rocks were determined for samples across the Morning Star fault zone (Table 2). A schematic cross section of the Morning Star fault zone within the Morning Star mine is illustrated on Figure 2.12 along with a transect of the geochemistry across the gouge and alteration zones. For the Ivanpah granite (left) and Morning Star diorite (right) the average composition of unaltered samples has been plotted on Figure 2.12 and the dashed lines represents a simple linear trend between these two averages.

The most striking feature of Figure 2.12 is the strong Na_2O depletion within the gouge and altered granite of the upper-plate. Only minor Na_2O depletion occurs in the altered dioritic rocks. CaO is strongly enriched in the gouge zone, with the exception of the blue gouge layer, and unchanged throughout the rest of the altered zones. Al_2O_3 and K_2O exhibit little or no change across the altered zone except for one sample of altered granite. The altered granite sample which exhibits the strong Al_2O_3 and minor K_2O depletion is completely bleached and silicified. MgO also exhibits little or no change across the alteration zone except for the altered mylonite and two altered diorite samples. All other major element oxide plots exhibit erratic trends across the alteration zone with TiO_2, total Fe, P_2O_5, MnO, and loss on ignition (L.O.I.) having very similar trends. All of these oxides have a generally depleted or weakly enriched behavior for altered dioritic rocks and a stronger enrichment across the gouge zone. SiO_2 has the most erratic behavior and its trends are opposite those mentioned above. Silica is enriched in the

Figure 2.12. Schematic cross section from unaltered Ivanpah granite through the fault zone and alteration assemblage into unaltered Morning Star diorite dike showing the major element oxide trends across the fault and altered zones. Ivanpah granite and Morning Star diorite are plotted as the average of all chemical analyses for these rock types (see Chapter 1). Altered rock are plotted as individual analyses projected onto the cross section based on distance from the mylonite-fault gouge contact. L.O.I. represents loss on ignition and gives an estimate of the extent of alteration.

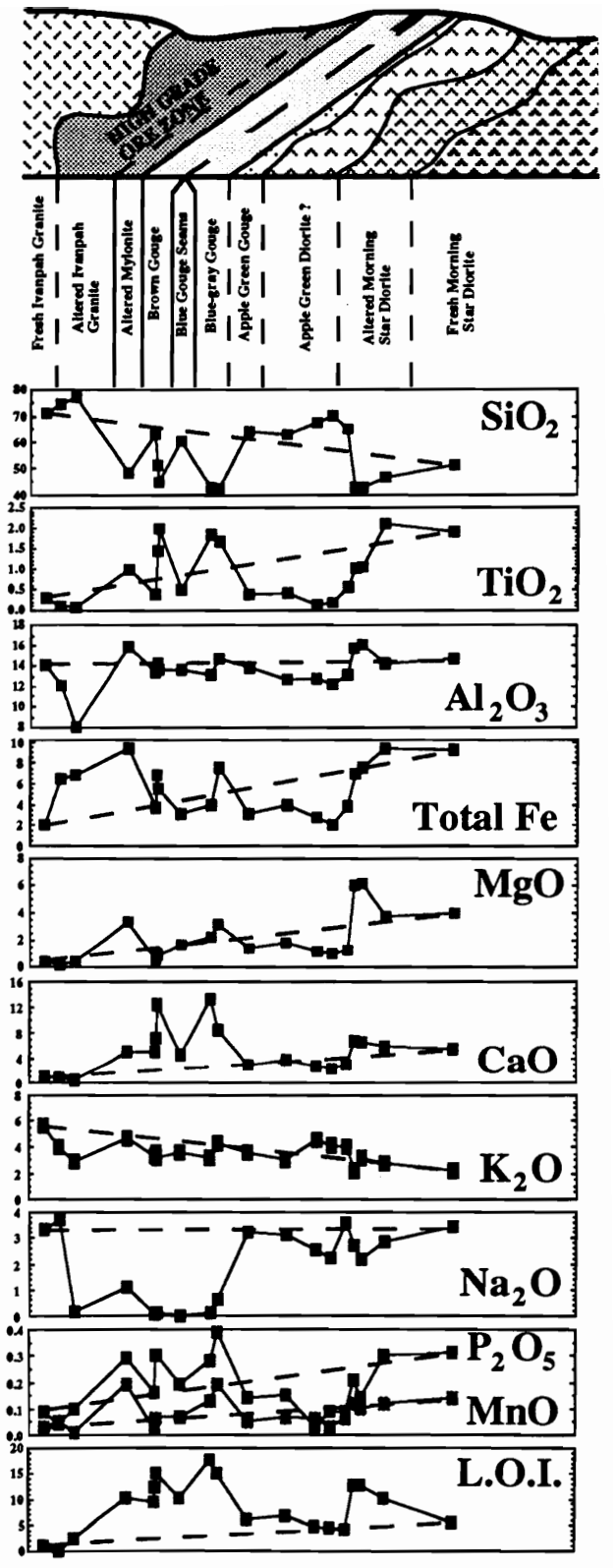
Fresh Ivanpah Granite
Altered Ivanpah Granite
Altered Mylonite
Brown Gouge
Blue Gouge Seams
Blue-gray Gouge
Apple Green Gouge
Apple Green Diorite ?
Altered Morning Star Diorite
Fresh Morning Star Diorite
SiO2
TiO2
Al2O3
Total Fe
MgO
CaO
K2O
Na2O
P2O5
MnO
L.O.I.

dioritic rocks and depleted across the gouge zone. The increased loss on ignition for fault gouge samples, above the baseline, represents increased alteration of cataclastically deformed fault rocks to clay and carbonate minerals. Chemical features of the fault zone are consistent with the gouge zone acting as a conduit for hydrothermal fluids.

Grain-Size Distribution

The grain-size distribution of gouge samples is a complex function of cataclastic (deformation) and hydrothermal (alteration) processes. If distinctions between tectonic and hydrothermal processes are possible, investigation of the grain-size distribution of gouge may map fluid flow pathways. A comparison of the grain-size distribution for gouge samples from the Sunnyside fault, E-W structures in the Morning Star mine and the Morning Star fault is shown in Figure 2.13 and 2.14. Each sample is plotted as the cumulative weight percentage of material finer than a given grain-size. Other natural and experimental gouges are plotted in Figure 2.13D and these studies were chosen because of the mineralogical and textural similarities between the host rocks in these studies and the undeformed and ductiley deformed Ivanpah granite. The range for natural gouge samples from Lake Hughes drill core and the experimental studies are for different confining pressures. An increase in confining pressure correlates with an increased percentage of fine-grain material in the fault gouge. Thus, in Figure 2.13D, the lower curves are for low confining pressures and the upper curves are for higher confining pressures.

The distribution of grain sizes for gouge samples along the Sunnyside fault (Figure 2.13A) and E-W structures in the Morning Star mine (Figure 2.13B) are similar to one another. Gouge from each of these structures consist of 20 to 30% clay-size material and

Figure 2.13. Grain size distribution of gouge samples along the Sunnyside structure (A), E-W structures in the Morning Star deposit (B), and the Morning Star fault (C). Experimentally generated gouge and other natural fault gouge produced from granitic and foliated rocks (D) are shown for comparison. The four digit designation for samples from the Morning Star study represent elevation of the sample based on a bench system in the mine; the higher numbers represent higher elevations with 4725 being the approximate elevation of the surface at the mine site. Therefore, Figure 2.13C compares the grain size distribution for brown, blue-gray and green gouge samples from different depths within the Morning Star deposit. Samples of natural gouge in Figure 2.13D are from the San Andreas fault, California, from Anderson et al. (1980). The range of grain sizes for the Lake Hughes drill core represents gouge from 213.7 meters (lower curve) to 372.5 (upper curve) meters deep along the fault. Experimentally generated fault gouge was conducted using Sierran granodiorite and Pelona schist (data from Sammis et al. 1986). Confining pressures of experiments range from 0.0 MPa (lower curve) to 13.8 MPa (upper curve) for the granodiorite and from 0.0 MPa (lower curve) to 12.4 MPa (upper curves) for the schist.

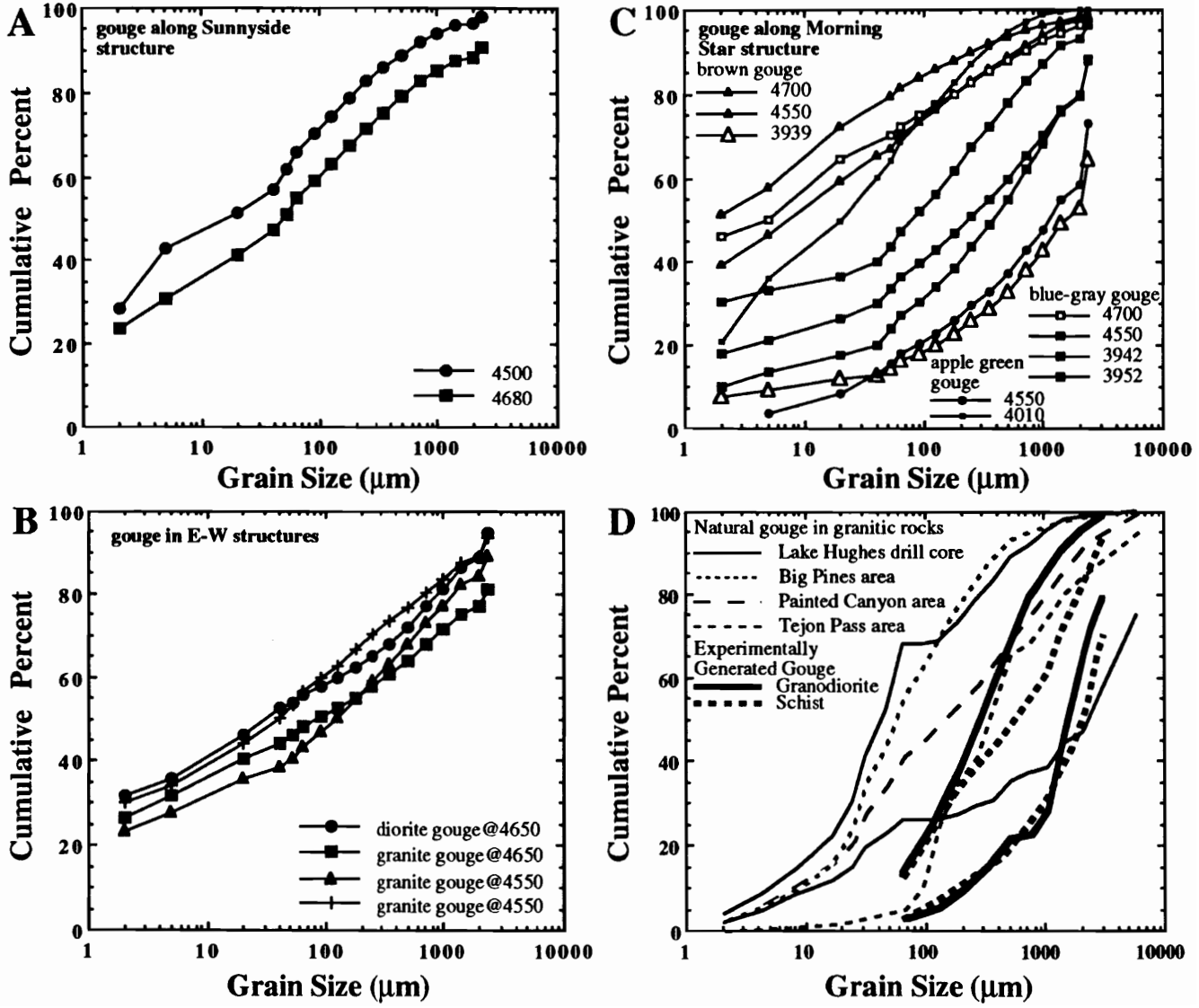
A
gouge along Sunnyside structure
4500
4680
Cumulative Percent
Grain Size (μm)
B
gouge in E-W structures
diorite gouge@4650
granite gouge@4650
granite gouge@4550
granite gouge@4550
Cumulative Percent
Grain Size (μm)
C
gouge along Morning Star structure
brown gouge
4700
4550
3939
blue-gray gouge
4700
4550
3942
3952
apple green gouge
4550
4010
Cumulative Percent
Grain Size (μm)
D
Natural gouge in granitic rocks
Lake Hughes drill core
Big Pines area
Painted Canyon area
Tejon Pass area
Experimentally Generated Gouge
Granodiorite
Schist
Cumulative Percent
Grain Size (μm)

Figure 2.14. Grain size distribution of gouge samples across the Morning Star fault on bench 4550 in the Morning Star mine.

A.) Line drawing from photographs illustrating the gouge types encountered in the Morning Star fault on bench 4550. The gouge zone is approximately 2 meters wide from granite to diorite dike in the drawing. Sample locations are designated by the dots.

B.) Grain size distribution of gouge samples illustrated in Figure 2.14A. See text for discussion of changes in grain size distribution across the fault zone.

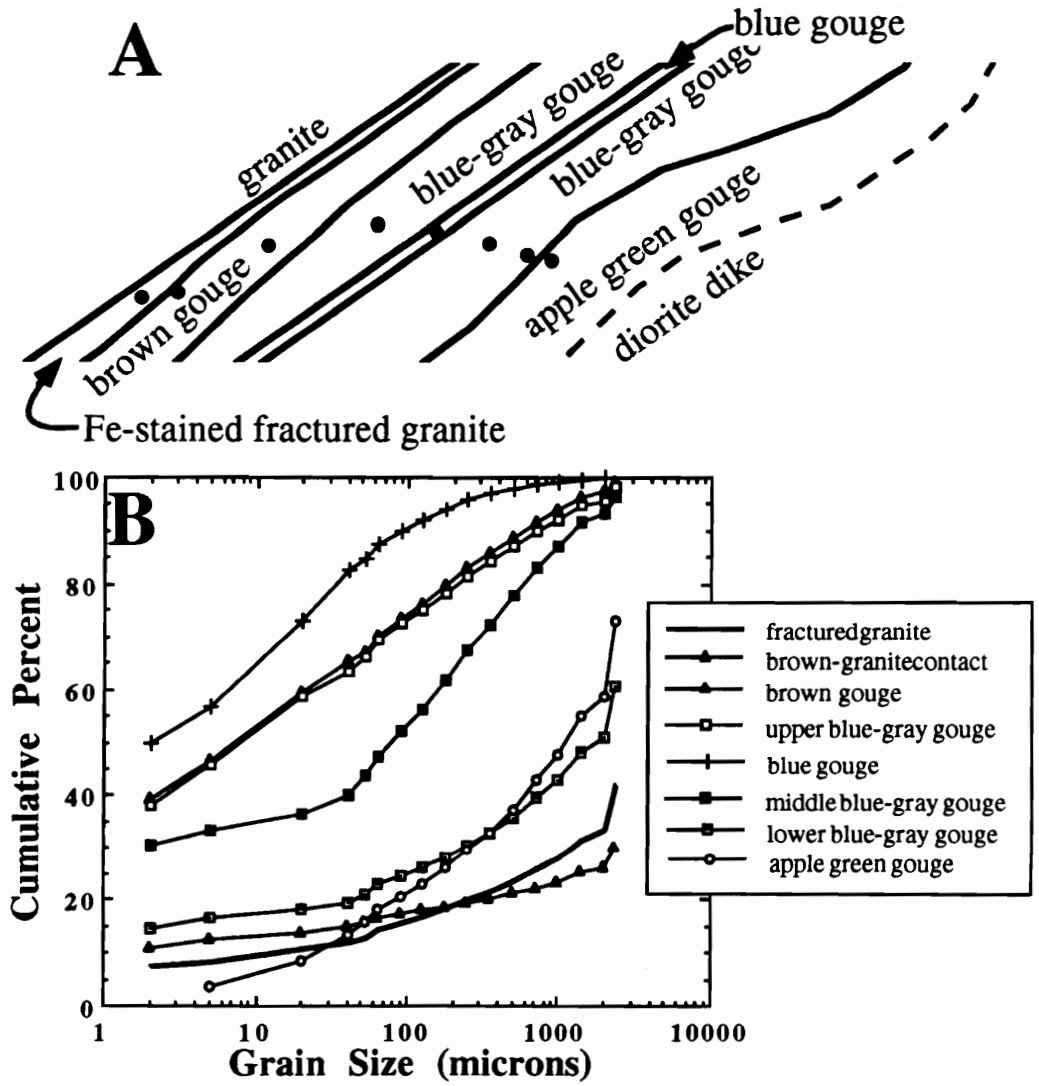
A
blue gouge
granite
blue-gray gouge
blue-gray gouge
brown gouge
apple green gouge
diorite dike
Fe-stained fractured granite
B
Cumulative Percent
100
80
60
40
20
0
1
10
100
1000
10000
Grain Size (microns)
fracturedgranite
brown-granitecontact
brown gouge
upper blue-gray gouge
blue gouge
middle blue-gray gouge
lower blue-gray gouge
apple green gouge

up to 35 to 55% silt-size material. Gouge along both structures differ considerably in the amount of clay- and silt-size material from gouge in other granitic terranes and experimentally generated fault gouge in granitic and foliated rocks (Figure 2.13D) (Wahlstom et al. 1968; Anderson et al. 1980; Chester & Logan 1986; Sammis et al. 1986). Experimentally deformed granite and foliated rock (schist) generate gouge with less than 10% of the material smaller than 63 μm (clay and silt sizes) (Sammis et al. 1986), while natural gouge in granitic rocks typically contain less than 25% clay- and silt-size materials at low confining pressures (Anderson et al. 1980). The sand-size and larger size fractions for the Sunnyside fault (Figure 2.13A) and E-W structures in the Morning Star mine (Figure 2.13B) are consistent with the trends observed in gouge from other granitic terranes and experimentally generated gouge in granite and foliated rocks (Figure 2.13D).

The distribution of grain sizes for gouge along the Morning Star fault has a more complex pattern (Figure 2.13C and 2.14) than gouge from other structures in the area (Figure 2.13). Brown and blue-gray gouge at near surface levels of the fault (4700 bench) contain ≥45% clay-size material and ≥65% clay- and silt-size material which is much larger than the 25% clay and silt sized material generated in dry faults and fault experiments (Anderson et al. 1980; Sammis et al. 1986). Brown and blue-gray gouge at deeper levels (4500 and ≈3940 bench) along the Morning Star fault contain smaller amounts of clay-, silt- and sand-size material, and larger amounts of coarse-grained fractured host rocks than near surface samples. The deeper level samples have grain-size distributions more consistent with experimentally generated and other natural gouges (Figure 2.13 C and D).

The variation in grain-size observed between gouge samples with depth can also be seen in a cross section of gouge on the 4550 level within the Morning Star mine (Figure

2.14). Fractured granite and brown gouge at the upper fault zone contact and blue-gray and apple green gouge at the lower fault zone contact have similar grain-size distributions (Figure 2.14B). These highly fractured zones contain more abundant coarse-grained material and smaller amounts of fine-grained materials compared to gouge in the central portions of the fault zone (Figure 2.14B). Larger amounts of clay-size material occur in gouge samples that are closer to the center of the fault zone. Although much of the clay-size material probably resulted from hydrothermal alteration of cataclastic fault rocks, the increase in finer grained material towards the center of the fault zone implies a strain gradient. Alternatively, focused fluid flow within the fault zone along areas of increased permeability due to cataclastic deformation may have produced increased amounts of finer-grained material in the center of the fault zone.

Mineralogy

Mineralogy and quantification for the clay-size fraction of gouge samples is given in Table 2.3. Analytical procedures for XRD mineral analyses and quantification are given in Appendix 2.1. An example of a set of XRD patterns for the clay-size fraction of gouge samples 003B and 003BG are given in Figure 2.15. Only the mineralogy of the clay-size fraction was quantified because a quantification scheme was not available for coarser materials, but semi-quantitative abundances are available for silt-size material by comparing the areas under selected X-ray peaks.

Mineralogy of the clay-size fraction of gouge samples consists of randomly interstratified clay, montmorillonite, muscovite (sericite and illite), kaolinite, quartz and chlorite with lesser amounts of calcite, dolomite, goethite and episode (Table 2.3). The individual mineral components that are interlayered to form the randomly

Table 2.3. Mineralogy of clay-size fractions for gouge samples.

	Morning Star fault gouge							
sample	003B	003BG	027A	027B	027E	025	MSE-88-1*	MSE-88-1*
type of gouge	brown	blue-gray	brown	blue	blue-gray	apple green	brown	blue-gray
bench	4700	4700	4550	4550	4550	4550	3942	3939
Minerals								
Random Interstratified	38	32	11	6	3	trace?	NP	NP
Montmorillonite	NP	NP	5	3	3	1	8	4
Chlorite	NP	NP	trace	7	9	12	trace	trace
Muscovite	28	33	31	36	41	23	46	50
Kaolinite	23	25	28	23	14	6	7	5
Quartz	8	8	16	20	25	19	29	34
Feldspar	1	trace	1	1	trace	29	6	5
Calcite	1	1	7	6	1	NP	3	1
Dolomite	NP	1	NP	2	4	6	NP	1
Geothite	1	NP	1	NP	NP	NP	1	NP
Epidote	NP	NP	NP	trace	trace	4	NP	NP

	E-W structures		Sunnyside fault
sample	037B	036C	90-007
type of gouge	white	white	
elevation	4550	4550	4680
Minerals			
Random Interstratified	1	trace	34
Montmorillonite	6	5	NP
Chlorite	trace	4	trace
Muscovite	36 (illite)	29 (illite)	30
Kaolinite	4	5	24
Quartz	30	32	9
Feldspar	22	24	2
Calcite	trace	1	1
Dolomite	NP	NP	NP
Geothite	NP	NP	NP
Epidote	NP	NP	NP

all abundances reported in weight percent and determined by quantitative XRD (see Appendix 2.1)
* MSE-88-01 is from drill hole outside the extent of the open pit mine
NP = mineral not present or not observed by XRD

Figure 2.15. X-ray diffraction patterns for the clay-size (<2 μm) fraction of samples 003B (brown gouge) and 003BG (blue-gray gouge) which occur along the Morning Star fault on the 4700 bench of the Morning Star mine. Each clay sample was saturated with either Mg-glycerol (Mg-gly) and KCl and X-rayed at room temperature (25°C) and 110°C (see Appendix 2.1 for analytical procedures). The following abbreviations are used: RI - randomly interstratified clay; M - muscovite (sericite) (001); K - kaolinite (001); M,2° - muscovite second order peak (002); Q - quartz; G - goethite; K,2° - kaolinite second order peak (002); A - anatase (see text); C - calcite; D - dolomite; Ksp - potassium feldspar.

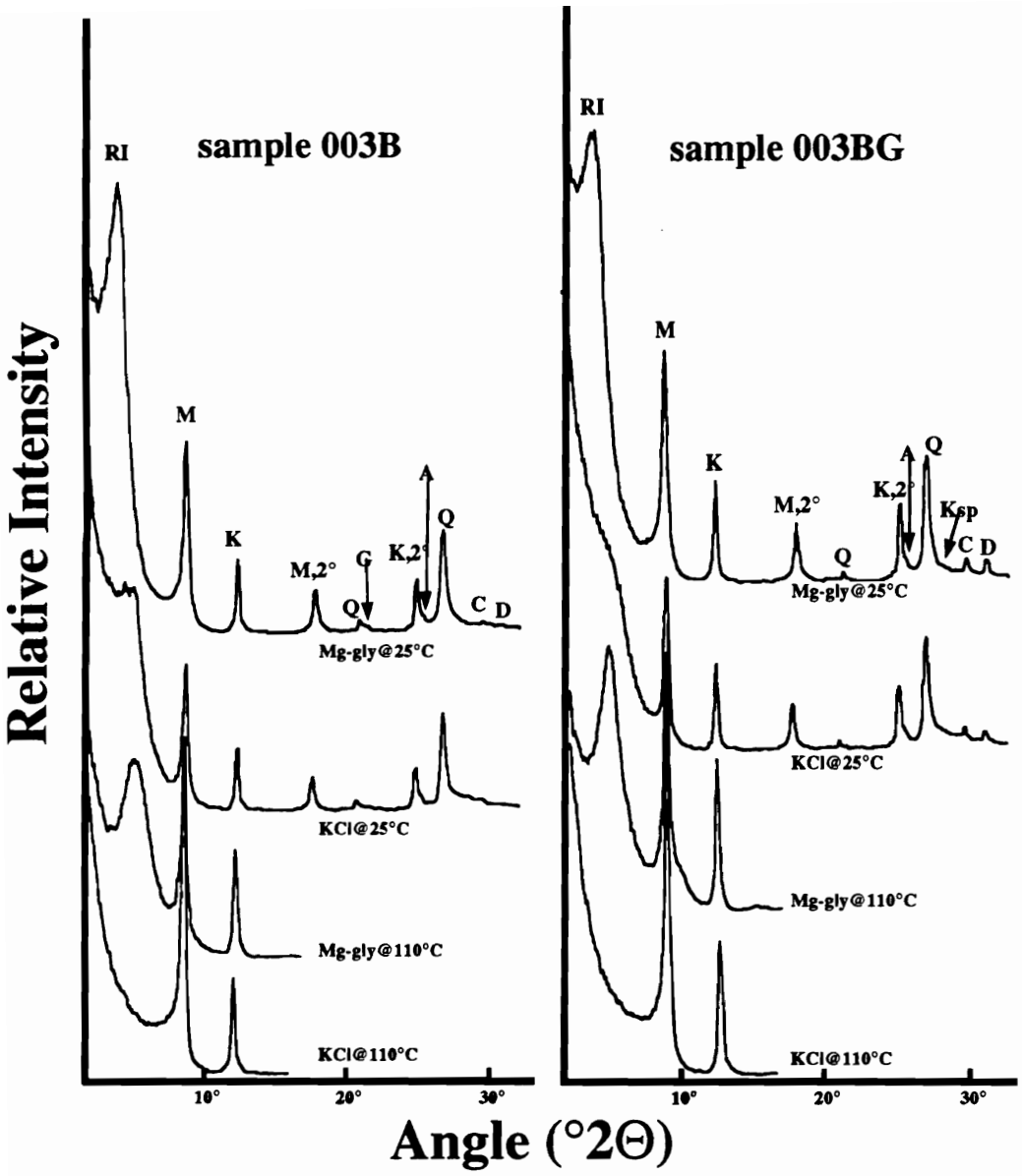
sample 003B
sample 003BG
RI
M
K
M,2°
G
K,2°
Q
C
D
Ksp
Mg-gly@25°C
KCl@25°C
Mg-gly@110°C
KCl@110°C
10°
20°
30°
Relative Intensity
Angle (°2Θ)

interstratified clays are ambiguous, but the most likely candidates include muscovite (illite) and smectites (see appendix 2.1). Randomly interstratified clay minerals are generally poorly crystalline, using the "valley"/"peak" height ratio technique (Thorez 1975). The abundance of randomly interstratified clay minerals decreases with depth along the Morning Star fault as the abundance of smectites increases. The montmorillonite becomes more crystalline with depth along the fault. Traverses across the fault zone on a given level show that more randomly interstratified clay and montmorillonite occur in the upper portions of the gouge (brown gouge), and the abundances of these minerals decreases across the fault zone (i.e. brown>blue>blue-gray>apple green). Quartz and feldspar, generally potassium feldspar, occur in all gouge samples with the abundance of both quartz and feldspar increasing with depth along the fault, but no substantial change in abundance occurs across the fault zone. Muscovite occurs in all gouge samples but is more abundant in the lower portions of the fault zone on a single level and increases in abundance with depth along the fault. Kaolinite exhibits a trend opposite that of muscovite. The muscovite and kaolinite diffraction peaks are generally strong and symmetrical which indicates well crystalline materials. DSC patterns confirm the highly ordered, well crystalline nature of the kaolinite. Calcite occurs in the brown gouge while the other gouge types contain both calcite and dolomite and the calcite-to-dolomite ratio decreases across the gouge zone (i.e. brown>blue>blue-gray>apple green). Minor amounts of goethite were observed in the brown gouge and probably caused the brown coloration. Fault gouge along the Sunnyside structure (one sample) has the same minerals in abundances similar to gouge at the highest levels of the Morning Star fault.

Gouge in the E-W structures contains essentially quartz, sericite and feldspar with lesser amounts of montmorillonite, randomly interstratified clays and kaolinite. Samples

of gouge from the E-W structures have broad, asymmetrical 10.10 Å peaks which are indicative of illite. The illite appears poorly crystalline because the (001) peak is skewed on the low angle (2Θ) side and the (003) peak is skewed on the high angle side.

X-ray diffraction patterns for the silt-size fractions contain the same minerals observed in the clay-size fraction except for the absence of randomly interstratified clay minerals and montmorillonite. Muscovite and kaolinite are present only in the fine (2 to 5 μm) and medium (5 to 20 μm) silt-size fractions. Calcite and dolomite, which are more abundant in the silt- and sand-size fractions, are present in blue-gray gouge samples, but only calcite is present in brown gouge samples. In all gouge samples the quartz-to-carbonate ratios increases with increasing grain-size. The abundances of quartz and feldspar also increase with depth along the fault. Epidote group minerals and chlorite, which cause the green coloration of the altered host rocks and lowermost gouge unit and form the principal constituents of the surrounding propylitic alteration, are more abundant in the silt-size material than the clay-size materials.

The sand-size fractions contain the same mineralogy as the silt- and clay-size fractions. Quartz, carbonate minerals, and altered rock fragments constitute the majority of the optically examined sand-size fraction. Rock fragments consist of quartz, altered feldspars, opaques and minor amounts of sphene, apatite, or allanite(?). Many of the samples contain subtranslucent minerals that resemble rutile. Mylonite and sheared granite fragments are also present. Larger grain-size fragments of quartz and host rock may also contain fine fractures filled with clay minerals. Optical examination also reveals the presence of pyrite, galena and chalcopyrite in gouge samples from the upper levels of the Morning Star fault, but these minerals are in quantities too small to be detected using XRD for fine-grained materials. Pyrite is typically euhedral and disseminated throughout quartz and rock fragments, and shows no sign of deformation. Galena and chalcopyrite

occur as anhedral masses in quartz, isolated grains or cleavage fragments. These minerals are the principal sulfide phases of mineralization in the Morning Star deposit.

The principal mineralogical differences between gouge types (on a single level) include the presence of more randomly interstratified clays, montmorillonite, kaolinite and Fe-oxide minerals in the upper portion of the fault zone (brown gouge) and the presence of dolomite and increased abundances of muscovite in the lower portions of the gouge zone (blue-gray). The lowest portions of the gouge zone (apple green gouge) contains increased abundances of chlorite and epidote.

The Fe-oxide minerals were probably produced by supergene oxidation of sulfide minerals in the upper-plate of the Morning Star fault. Descending supergene fluids would increase the abundance of Fe-oxide minerals in the fractured granites of the upper-plate and the upper portion of the gouge (brown layer). The chemical profile across the fault (Figure 2.12) supports this interpretation because the granitic rocks and upper brown gouge zone are enriched in total Fe relative to the lower gouge zones and altered dike rocks. Ore petrology of the Morning Star deposit has also identified secondary iron-, copper- and precious-metal-bearing phases formed in the upper levels of the deposit by supergene processes (Chapter 4).

Randomly interstratified clays occur in the upper levels of the fault and in the upper portions of the fault zone. In the lower portions of the fault zone and deeper along the fault, the randomly interstratified clays convert to montmorillonite which becomes more crystalline with depth. MacEwan and Ruiz-Amil (1975), who reviewed the literature on interstratified clay minerals, reported hypogene interstratified clay minerals to be regular, well ordered mixtures of specific clay minerals. Therefore, the randomly interstratified clay minerals observed probably formed by supergene processes. The occurrence of randomly interstratified clay in near surface gouge which decreases in abundance with

depth suggest supergene fluids migrated along the fault parallel to the gouge foliation because fluid migration perpendicular to the fault zone is generally prohibited by the foliated, clay-rich gouge (Logan and Decker 1994).

Most of the quartz, carbonates, kaolinite and muscovite were probably formed by hydrothermal processes. Alternatively, feldspar in the upper levels of the fault may represent remnants of cataclastically deformed host rock, but in deeper potions of the fault where feldspars are abundant, hydrothermal alteration of the host rocks may precipitate fine-grained feldspar. Quartz and carbonate are the chief gangue minerals in the ore deposit and muscovite (sericite) and kaolinite are the principal clay minerals of the alteration assemblages (Chapter 3). A hydrothermal origin for these minerals requires mineralizing fluids to move up the fault zone and deposit the ore in open spaces in the upper-plate. This theory is consistent with the structure of the ore deposit (Figure 2.2B) and the geochemistry across the fault zone (Figure 2.12). The presence of pyrite, galena and chalcopyrite in the fault gouge also supports such a model. The model also accounts for the larger percentage of clay-size materials at the Morning Star deposit compared to other natural and experimental generated fault gouge in similar rock types (Figure 2.13 and 2.14), because chemical alteration of cataclastically deformed fault rocks would be accelerated by the grain-size reduction to form increased amounts of fine-grained material. Focused fluid flow within the gouge zone will also explain increased abundances of clay-size material in the center of the fault zone compared to the gouge-host rock contacts that have grain-size distributions that resemble other natural and experimental generated fault rocks (Figure 2.13 and 2.14).

The presence of dolomite in the blue-gray gouge requires derivation of this portion of the gouge from a Mg-rich rock, interaction with Mg-bearing fluids or dolomite leaching from the overlying brown gouge. The latter does not seem possible because

calcite, which is generally more chemically reactive than dolomite, is retained by the brown gouge. Differentiation between the other interpretations is difficult without further study. Derivation of the blue-gray gouge from the Morning Star dike or from fluids which interacted with the dike would account for the occurrence of dolomite. Geochemistry across the fault zone show similarities between the blue-gray gouge and the underlying dike rocks (Figure 2.12). This does not, however, preclude the formation of the blue-gray gouge from Mg-rich fluids.

Discussion

The Morning Star fault was originally mapped as a thrust fault (Hewett 1956; Burchfiel and Davis 1971), but later reinterpreted as a right-lateral fault with a weak normal slip component (Byington 1988; 1989). Kinematic indicators such as asymmetric folds of foliation surfaces, S-C structures and asymmetric petrofabric patterns for the mylonites on the Morning Star and Sunnyside faults indicate thrust movement during ductile deformation. Microstructures are also consistent with eastward directed thrust movement during ductile deformation. Similar macrostructures, microstructures and petrofabric patterns occur along the Sunnyside and Morning Star structures which is consistent with both structures being subjected to similar deformation conditions.

The small circle or near small circle distribution of quartz c-axes patterns along the Morning Star fault system suggests essentially a pure flattening ($K=0$) or a major flattening ($K>0$ and $K<1$) component to mylonite foliation development (Schmid & Casey 1986). Flattening is also suggested by the absence of a stretching lineation on many mylonite samples and outcrops. A quantification of strain is not possible because no strain markers have been detected, but experimental deformation studies require 30%

shortening to form recognizable patterns on petrofabric diagrams (Lister and Hobbs 1980).

Quartz crystallographic patterns for individual domains suggest a complex deformation history during mylonite formation along the MSFS. Part of the complex c-axis fabric patterns may be due to initial heterogeneities in the Ivanpah granite. The Ivanpah granite ranges in texture from equigranular to porphyritic, and the mineral compositions vary from essentially quartz-feldspar to quartz-feldspar-mica. The abundance of micas and development of micaceous foliation surfaces causes different quartz c-axis orientations for ribbon quartz (Figure 2.7A). Also different c-axis fabric patterns occur for different zones of dynamically recrystallized quartz. Initial quartz grains from the host granite may have been elongated by a dislocation creep mechanism during early ductile deformation. Sub-grain development occurred and work-hardening probably limited by the ability of dislocations to climb (climb-accommodated dislocation creep) (Yund & Tullis 1991). Recrystallization of subgrains into bands of polygonal quartz probably resulted from high-angle grain boundaries as dislocations climb into the grain boundaries. The resulting crystallographic fabric would have recrystallized grains with a similar orientation as ribbon grains. Minerals such as feldspars, which have relatively slow diffusion rates, thereby limiting dislocation climb, deform by dynamic recrystallization during grain boundary migration which results in fine-grained aggregates of strain free grains. This process may account for recrystallization of some feldspar grains, however other feldspar may have deformed by cataclastic flow or been precipitated by the influx of minor quantities of fluids.

The small circle or near small circle distribution of quartz c-axes allows for direct correlation of the MSFS samples to experimental studies. Small circle petrofabric development around the pole to mylonite foliation are favored over single point maxima

by either higher temperatures or slower strain rates (Tullis et al. 1973). The diffuse nature of some of the crystallographic fabric patterns also suggests relatively low strain (Price 1985). Thus, ductile deformation along the MSFS appears to have occurred at relatively high temperatures or slow strain rates over an extended period of time. Climb-accommodated dislocation creep is indicated by sub-grain structures in ribbon quartz and development of new grains by dynamic recrystallization. No estimation of temperature or strain rate is available because climb-accommodated dislocation creep may occur over a large range of geological conditions (White 1976). Recrystallization-accommodated dislocation creep of feldspars occurs for natural strain rates between about 450 and 650°C (Simpson 1985). Microstructures from mylonites in the MSFS are consist with fabric development in this temperature range, and although no measure of the strain rate or degree of shortening were obtained form the fault rocks, a minimum estimate of 30% shortening is indicated by the petrofabric diagrams (Lister and Hobbs 1980).

At some point the Morning Star fault system converted from aseismic crystal plastic deformation (mylonite) to seismic brittle deformation (gouge and fracturing of the upper-plate). This transition was probably gradual and consisted of multiple episodes of seismic faulting instead of an single instantaneous event. The Morning Star fault system, and correlative New York Mountain thrust fault, is cut the 105 Ma Mid Hills adamellite which was emplaced at a depth of 3.5 to 6.5 km and is cut by a plug from the 92 Ma Kessler Springs adamellite which was emplaced at a depth of 0.5 to 1.5 km (Chapter 1; Anderson et al., 1989). Crystal plastic deformation occurred above 450°C and the main stage of mineralization at the Morning Star deposit, which precipitated after cataclastic deformation of the early mineralization, occurred at approximately 300°C (Chapter 4). This episode of uplift (decrease in confining pressure) and decrease in temperature favors

brittle deformation relative to ductile deformation and probably accounts for the transition between deformation styles along the Morning Star fault system.

Brittle deformation textures are consistent with eastward directed thrusting on the Morning Star fault system. Evidence to support thrusting during brittle deformation includes ductile deformation overlying brittle deformation, folded mylonite (Figure 2.3) and folded fault gouge (Figure 2.10). Ductile deformation overlying brittle deformation supports thrust movement because foliated gouge typically forms at shallow crustal levels and mylonites typically form at deeper crustal levels (Sibson 1977). Initial brittle deformation probably caused folding of the early mylonite along the Sunnyside structure and gouge formed during alteration of the cataclastic fault rocks. Subsequent episodes of fault movement converted the initially randomly oriented phyllosilicates into foliated gouge. Later folding of the laminated gouge implies continued episodes of thrust displacement on the Morning Star fault system. No evidence of normal or strike-slip fault displacement was found during this study in contrast to the findings of Byington (1988; 1989).

Hydrothermal fluids probably migrated into dilatant zones formed by brittle faulting. Initial cataclastic deformation would cause grain-size reduction, but this initial brittle deformation would create a total volume increase as microcracks open within individual grains and rock fragments. Any hydrothermal fluids present during the initial brittle deformation would flow into the cataclastic zone and migrate along the fault. If these fluids were out of equilibrium with the host rocks (principally quartz+orthoclase+albite±biotite), chemical reactions would produce muscovite and kaolinite to reestablish chemical equilibrium. Reactions would be of the form:

$$3\ \text{K-feldspar} + 2\ H^{+}(aq) = \text{muscovite} + 6\ \text{quartz} + 2\ K^{+}(aq)$$

Repeated fracturing and the influx of fluids during brittle deformation would lead to the complete replacement of feldspar by muscovite and possibly kaolinite. Because rock strength decreases with increasing phyllosilicate content (Shea & Kronenberg 1993), the resulting phyllosilicate-rich fault zone would be much weaker than the unaltered protolith. Brecciation and fracturing of the upper-plate would be reduced by early formation of foliated gouge, and thus fewer dilatant zones would form in the upper-plate. Early formed quartz and pyrite veins are deformed which also indicate syntectonic fluid migration into the fault during early brittle deformation.

The intrusion of fluids into the fault zones would be aided by seismic pumping and would occur in rocks deformed by seismic events which create porosity. During early cataclastic deformation alteration of fault rocks would produce randomly oriented phyllosilicates, similar to the gouge in the E-W structures. Continued fault movement would shear the newly formed phyllosilicates into foliation surfaces parallel to the shear zone boundaries. Repeated episodes of seismic activity along the fault favors repeated episodes of grain-size reduction, shearing of phyllosilicates into foliation surfaces and alteration of the fault rocks. Mineralogy, grain-size distribution and textures of the Morning Star gouge are consistent with multiple episodes of cataclastic deformation. The sequence of events which produced folded mylonite, formation of fault gouge, foliation of gouge and later folding of that gouge also indicate multiple episodes of brittle deformation. The randomly oriented, unfoliated gouge in the E-W structures is more consistent with post-tectonic, fluid-dominated alteration of cataclastic fault rocks.

Increased cohesion of fault gouge due to syntectonic alteration and foliation development, would restrict fluid migration at high angles to the fault zone. However, some fluid migration may continue along the fault zone between foliation surfaces due to variations in grain size (Logan & Decker 1994). The migration of fluids within the gouge

zone would continue to alter rock fragments and coarser grain-size materials to produce large quantities of fine-grained material in the fluid channelways. The hydrothermal fluids deposited mineralization in open fractures at the top of the fault gouge zone and in the upper-plate rocks, but mineralization in the fault zone and lower-plate is essentially absent. The absence of extensive mineralization in the fault gouge is consistent with post-tectonic fluid migration being restricted to the fractured upper-plate rocks above the foliated gouge zone. The cyclic nature of rupture, fluid infiltration and mineralization is consistent with structures and textures within the gouge zone and suggests a steady-state was not achieved until late in the deformation history. Repeated rupturing due to fault movement should be sufficient to form brecciation and dilatant zones in the upper-plate rocks. Thus, fluids derived south and west of the Morning Star fault would initially be channeled up the cataclastically deformed fault zone and later restricted to the fractured upper-plate rocks by the formation of foliated fault gouge. This model is consistent with the minor amounts of initial syntectonic mineralization and the bulk of the mineralization being post-tectonic and occupying open spaces in the upper-plate of the Morning Star thrust (Chapter 3). The E-W structures formed late, because they cut the Morning Star ore body, Morning Star fault and Morning Star dike. These E-W structures produced open brecciated zones which were altered during fluid-dominated, hydrothermal activity. This interpretation is consistent with the angular rock fragments and unfoliated gouge which occupies these structures and lack of mineralization.

Late supergene fluids interacted with the upper-plate ore zone to form Fe-oxide and randomly interstratified clay minerals in the gouge zone. These supergene fluids acted to enhanced ore grades, at least on a local scale, within the deposit (Chapter 4).

Relationship to the Mesozoic Foreland Fold and Thrust Belt

Ductile deformation only occurs in the Mesozoic foreland fold and thrust belt along the Winter Pass thrust plate (Pachulka and Sterling thrusts) and the Morning Star fault system. All these mylonites have similarly oriented lineations and foliations, but the Winter Pass faults contain principally L- and L-S tectonites while the Morning Star fault system contains principally L-S and S-tectonites. Crystallographic c-axis patterns change from a Type II cross girdle pattern along the Pachulka thrust (Figure 2.8A) to a Type I cross girdle pattern on the Sterling thrust (Figure 2.8A), and finally to small circle or single girdle patterns along the Morning Star fault system (Figure 2.6). The variations in the types of ductile fault rocks and petrofabric patterns suggests a conversion from high temperature, non-coaxial plane strain in the Clark Mountains to lower temperature, non-coaxial shortening in the Ivanpah Mountains. This apparent change in the style of deformation may be related to the type of country rock involved during ductile deformation, since the Winter pass thrust plate involves quartzites thrust over gneisses and the Morning Star fault system is confined to granite. The Ivanpah granite may have acted as a resistant plug emplaced in a pre-existing thrust complex (Clark Mountain thrusts). The resistant plug sustained considerable amounts of shortening, which resulted in noncoaxial flattening to produce the mylonites on the Morning Star fault system, prior to seismic rupturing, that produced the fault gouge and brecciation. Deformation along the fault complex reactivated pre-existing faults.

The Winter Pass thrust plate was emplaced prior to 190 Ma (Burchfiel and Davis 1971), however Burchfiel and Davis (1988) describe emplacement of the Winter Pass thrust plate as follows:

> "... some field relationships in the Pachulka Springs area can be interpreted as circumstantial evidence that the Pachulka thrust plate (=Winter Pass?) was not

emplaced until the Cretaceous. We are uncomfortable with such a young age of thrusting for this highest sheet in the complex."

Deformation on the Morning Star thrust occurred between 90 and 105 Ma (Chapter 1). Because both structures contain ductile deformation, thrusting which formed the Morning Star fault system may have reactivated the thrusts at the base of the Winter Pass thrust plate. Late Cretaceous compression may have been accommodated in the Clark Mountains by reactivation of existing thrust faults, but may only have been accomplished within the igneous rocks of the Teutonia batholith (Ivanpah granite and Mid Hills adamellite) by discrete zones of shortening (Morning Star, Sunnyside and New York Mountain thrusts). This interpretation is consistent with the observations of Nelson and Burchfiel (1979) for the New Trail Canyon area where sub-parallel shortening was accommodated in the autochthonous platform sedimentary rocks by large scale folding and in the crystalline basement by penetrative shear zones.

Increased crustal shortening ultimately caused brittle failure along the Morning Star fault system, but similar brittle deformation is absent at the base of the Winter Pass thrust plate. Regional uplift southwest of the Ivanpah Mountains and decreasing temperatures may have facilitated the transition from ductile to brittle deformation along the Morning Star fault system. The Morning Star fault contains syntectonic clay minerals which are absent on other thrusts of the Mesozoic foreland fold and thrust belt. Introduction of fluids during crustal shortening may also have promoted brittle failure along the Morning Star fault system. The lack of episodic brittle deformation and focused fluid flow on other structures in the Mesozoic foreland fold and thrust belt may also explain the lack of economic mineralization along these structures.

Appendix 2.1

Analytical Techniques

The MSFS was mapped during the summer of 1988 and 1989. The results of this mapping are presented in Figure 2.2. Fieldwork concentrated on measuring mylonite fabrics, evaluating macroscopic kinematic indicators and sampling fault rocks for structural petrology and petrofabric analysis. Thirty nine polished slabs and 31 thin sections were studied petrographically for microstructures and kinematic indicators. Seven mylonite samples were selected for quartz crystal fabric analyses using a 4-axis Lietz universal stage with data analyses conducted using the computer programs FABRIC (Starkey 1989) and STEREOPLOT (Mancktelow 1991). Two additional samples of mylonites associated with the Clark Mountain thrust complex were studied for petrofabric analysis to compare structural styles: sample Law-89-04 is from the Pachulka thrust and Law-89-03 is from the Sterling thrust (Figure 2.1). All slabs and thin sections were cut parallel to the stretching lineation (X), or the regional orientation of the stretching lineation if no lineation was observed on the specimen, and perpendicular to the mylonite foliation. The orientation of 300 to 625 quartz c-axis orientations were measured for each mylonite and all petrofabric data is presented on contoured equal-area upper-hemisphere stereographic projections using STEREOPLOT (Mancktelow 1991). The plane of each stereonet contains the specimen lineation (X) and poles to foliation (Z). In all stereographic projections the foliation is horizontal and the lineation, which lies within the plane of foliation, is horizontal and dipping to the left (i.e. viewing direction is always looking north). The orthogonal axis system used in this paper defines Z as the perpendicular to foliation and Y lies within the plane of foliation and is perpendicular to the lineation (X). No relationship between X, Y and Z and the axes of the finite strain

ellipse is intended. For complex mylonite samples containing different quartz domains petrofabric data was measured for each visibly distinct domain or structure.

Major element chemistry was determined for host rock and brittle fault rock samples. All gouge samples submitted for chemical analysis were mechanically disaggregated and then sieved to remove the gravel-size fraction. Thirty eight samples were analyzed by Chemex Labs Ltd. (Spark, Nevada) using ICP-AES (Table 2.2 for summary table and Appendix 2.2 for the complete data set). Detection limits are 0.01 weight percent per oxide. Duplicate samples and well characterized secondary standards were analyzed for precision and accuracy.

Fault gouge samples were completely dispersed in an ultrasonic bath using distilled water treated with 1.0 N sodium carbonate to obtain a pH of 10. The suspension was filtered through a 300 mesh (50 μm) wet sieve. Distilled water of pH 10 was added and this procedure was repeated until the supernatant liquid became clear. The sand-size fraction was washed to remove the remaining fine-grained particles and then oven dried. The sand was sieved and mineralogy was determined by XRD and optical techniques.

The -300 mesh (<50 μm) materials were further separated into coarse (50 to 20 μm), medium (20 to 5 μm) and fine (5 to 2 μm) silt-size and a clay-size (less than 2 μm) fractions using gravitational and centrifugal techniques (Jackson et al. 1949; Tanner and Jackson 1947; Day 1965). Each size fraction was x-rayed for mineral identification.

Mineralogical analyses was conducted by X-ray diffraction (XRD), differential scanning calorimetry (DSC) and optical examination. XRD was used to quantify clay-size fractions using integrated peak intensities and iterating a series of binary standard equations (from Dr. L. Zelazny, Crop and Soil Environmental Sciences Department at VPI&SU) where kaolinite content was determined from DSC. The coarser materials were examined optically. Clay-size fractions were X-rayed, in the Crop and Soil

Environmental Sciences Department at VPI&SU, using a DIANO-XRD 8300AD diffractometer utilizing Cu Kα radiation and run at 40 KV, 20 mA with a stepping interval of 0.025° 2θ at 1.3 seconds per step. All silt- and sand-size separates were X-rayed, in the Department of Geological Sciences at VPI&SU, using a SCINTAG 2000XRD diffractometer utilizing Cu $K\alpha_1$ radiation and run at 45 KV, 35 mA with a 2° 2θ per minute scan and a 0.01° 2θ stepping interval. DSC analyses were conducted, in the Crop and Soil Environmental Sciences Department, using a DuPont DSC 2910 differential scanning calorimeter run between 50 and 630°C at 20°C per minute in a N_2 atmosphere. Only the mineralogy of the clay-size fraction was quantified (Table 2.3) as a standardization scheme has not been determined for the SCINTAG 2000XRD.

The clay-size fraction (<2 μm) was prepared for X-ray diffraction analysis by vacuum settling onto clay tile (Gibbs, 1971; Rich & Barnhisel, 1977). Clay tile mounts were prepared using magnesium saturated glycerol solvated (Mg-gly) and potassium saturated (KCl) samples and X-ray patterns were run at room temperature and after heat treatment overnight at 110°, 300° and 550°C. X-ray diffraction patterns for samples 003BG and 003B are given in Figure 2.15 to illustrate changes in basal (00l) diffraction peaks during some of the various solution and heat treatments.

Silt- and sand-size separates were prepared for XRD using the standard powder techniques (Gibbs, 1971). All sand-size fractions less than 500 μm were X-rayed for mineralogy. Coarser fractions were only examined optically.

Interstratified clay was identified by the 22 Å peak on Mg-gly. X-ray pattern that forms the series of peaks between 16 and 27 Å upon KCl saturation (Figure 2.15). The 22 Å Mg-gly. peak collapses to 18.5 Å upon heating to 110°C. No higher order basal peaks were observed for the interstratified clay which suggests this clay mineral is randomly interstratified. The exact mineral components of the interstratified clay are

ambiguous because of the 22 Å Mg-gly peak and the lack of higher order peaks. The randomly interstratified clay most likely contains a muscovite (illite) component. Collapse of the 22 Å Mg-gly. peak under KCl saturation and heating to 110°C indicates that likely candidates for the other component are smectites, vermiculites or hydroxy-interlayered vermiculites. Montmorillonite was identified by a 17-18 Å Mg-gly peak which collapses to 14 Å at 110°C or 12-13 Å for KCl saturation.

Muscovite, kaolinite, and quartz were identified by the 10.10, 7.15, and 4.26 and 3.34 Å peaks, respectively. Carbonate minerals were identified by the 3.04 Å and 2.88 Å peaks for calcite and dolomite, respectively. Goethite is detected by the high angle shoulder peak on the 4.26 Å quartz peak. The only X-ray peaks not accounted for are the high and low angle shoulder on the second order (002) muscovite peak (best seen in the KCl saturated patterns in Figure 2.15) and the high angle shoulder on the second order kaolinite peak. The origin of the second order muscovite shoulder peaks is unknown. The high angle kaolinite shoulder peak occurs at a d-spacing of 3.51±0.03 Å. This is probably not the third order (003) muscovite peak because this third order peak should occur at 3.37 Å. The prominent peak for the mineral anatase (TiO_2) occurs at 3.52 Å which is consistent with the second order kaolinite shoulder peak. The 3.52 Å peak also appears in X-ray diffraction patterns of coarser materials which contain no clay mineral peaks, which implyes the presence of anatase in the clay-size fraction is likely. A series of small irregular diffraction peaks occur between 31 and 36° 2θ in some clay- and silt-size separates. The minerals that form these peaks have not been positively identified, but they resemble the diffraction lines for epidote group minerals.

Appendix 2.2

Major Element Chemistry

Major element chemical analyses of Ivanpah granite, Morning Star dike, and gouge zones.

Sample	RWS-078	RWS-095	RWS-90-009A	RWS-90-012
Rock Unit	Ivanpah	Ivanpah	Ivanpah	Ivanpah
SiO2	76.57	69.53	71.34	74.43
TiO2	0.04	0.34	0.47	0.11
Al2O3	12.31	15.46	12.93	12.16
FeO*	0.73	1.56	3.61	6.53
MgO	0.06	0.22	0.63	0.15
MnO	0.01	0.01	0.06	0.05
CaO	0.46	0.46	1.68	0.95
BaO	0.01	0.07	0.02	0.01
K2O	5.16	5.89	4.52	3.94
Na2O	3.44	3.92	3.15	3.70
P2O5	0.02	0.05	0.11	0.04
L.O.I.	0.68	1.27	0.51	0.01
Total	99.51	98.79	99.02	99.08
K2O+Na2O	8.60	9.81	7.67	7.64
FeO*/FeO*+MgO	0.92	0.88	0.85	0.98
moles A/CNK	1.36	1.51	1.38	1.42
K2O/Na2O	1.50	1.50	1.43	1.06

Sample	RWS-097	RWS-89-012	RWS-075	RWS-011
Rock Unit	Ivanpah	Altered Ivanpah	Ivanpah	Altered Ivanpah
SiO2	66.56	71.70	72.70	77.17
TiO2	0.56	0.22	0.25	0.84
Al2O3	14.83	13.93	13.55	7.98
FeO*	3.55	2.23	1.65	6.87
MgO	1.09	0.29	0.41	0.42
MnO	0.05	0.02	0.03	0.01
CaO	2.45	0.78	0.77	0.35
BaO	0.09	0.04	0.01	0.01
K2O	5.26	6.11	5.08	2.92
Na2O	3.11	2.95	2.90	0.13
P2O5	0.17	0.06	0.02	0.10
L.O.I.	0.97	0.61	1.63	2.26
Total	98.67	98.93	99.09	99.06
K2O+Na2O	8.37	9.06	7.98	3.05
FeO*/FeO*+MgO	0.77	0.88	0.80	0.94
moles A/CNK	1.37	1.42	1.55	2.35
K2O/Na2O	1.69	2.07	1.75	22.46

Sample	RWS-89-030C	RWS-89-063	RWS-89-010	RWS-006
Rock Unit	Ivanpah	Ivanpah	Ivanpah	M.S. Dike
SiO2	69.26	64.91	77.11	53.06
TiO2	0.13	0.60	0.06	2.07
Al2O3	15.58	16.49	12.28	15.07
FeO*	1.13	3.54	0.51	8.69
MgO	0.25	0.56	0.12	4.17
MnO	0.01	0.06	0.01	0.15
CaO	0.90	1.20	0.11	5.61
BaO	0.08	0.13	0.02	0.03
K2O	7.09	5.85	5.96	1.89
Na2O	3.57	4.41	2.59	3.97
P2O5	0.09	0.20	0.05	0.33
L.O.I.	1.45	1.10	0.75	4.07
Total	99.52	99.04	99.57	99.09
K2O+Na2O	10.66	10.26	8.55	5.86
FeO*/FeO*+MgO	0.82	0.86	0.81	0.68
moles A/CNK	1.35	1.44	1.42	1.31
K2O/Na2O	1.99	1.33	2.30	0.48

Sample	RWS-103-1	RWS-90-021	RWS-103-2	RWS-104-1
Rock Unit	M.S. Dike	M.S. Dike	M.S. Dike	M.S. Dike
SiO2	52.37	50.50	52.56	50.01
TiO2	1.95	1.38	2.01	2.06
Al2O3	14.94	14.63	14.94	14.49
FeO*	9.48	8.15	9.27	10.11
MgO	3.42	4.96	3.28	3.67
MnO	0.13	0.11	0.13	0.15
CaO	4.89	5.58	4.87	6.15
BaO	0.08	0.02	0.07	0.04
K2O	2.84	1.50	2.77	2.13
Na2O	3.60	3.04	3.65	3.40
P2O5	0.31	0.32	0.32	0.29
L.O.I.	4.93	7.54	5.30	5.61
Total	98.94	97.74	99.15	98.12
K2O+Na2O	6.44	4.54	6.42	5.53
FeO*/FeO*+MgO	0.73	0.62	0.74	0.73
moles A/CNK	1.32	1.45	1.32	1.24
K2O/Na2O	0.79	0.49	0.76	0.63

Sample	RWS-104-2	RWS-89-019	RWS-90-020	RWS-118A
Rock Unit	M.S. Dike	M.S. Dike	Altered M.S. Dike	Altered M.S. Dike
SiO2	49.36	51.93	43.06	45.70
TiO2	2.12	1.62	1.03	1.98
Al2O3	14.60	14.42	15.82	16.36
FeO*	10.38	8.75	7.02	11.90
MgO	4.02	3.91	5.99	6.43
MnO	0.15	0.13	0.12	0.17
CaO	6.08	5.63	6.77	8.13
BaO	0.04	0.06	0.01	0.03
K2O	2.18	2.50	2.26	1.04
Na2O	3.43	3.08	2.72	2.99
P2O5	0.29	0.32	0.21	0.45
L.O.I.	5.28	5.48	12.67	2.66
Total	97.93	97.83	97.67	97.84
K2O+Na2O	5.61	5.58	4.98	4.03
FeO*/FeO*+MgO	0.72	0.69	0.54	0.65
moles A/CNK	1.25	1.29	1.35	1.35
K2O/Na2O	0.64	0.81	0.83	0.35

SAMPLE	RWS-018	RSW-89-002	RWS-89-021A	RWS-012
Rock Unit	Altered M.S. Dike	Altered M.S. Dike	Altered M.S. Dike	Propylitically Altered Mylonite
SiO2	43.10	65.00	46.90	48.71
TiO2	1.05	0.58	2.10	1.00
Al2O3	16.09	13.13	14.18	15.85
FeO*	7.56	3.90	9.39	9.31
MgO	6.17	1.23	3.74	3.31
MnO	0.10	0.06	0.12	0.19
CaO	6.72	3.08	5.96	5.03
BaO	0.02	0.03	0.03	0.04
K2O	3.19	3.96	2.70	4.64
Na2O	2.17	3.57	2.87	1.11
P2O5	0.14	0.09	0.30	0.29
L.O.I.	12.60	4.14	10.08	10.05
Total	98.91	98.77	98.37	99.54
K2O+Na2O	5.36	7.53	5.57	5.75
FeO*/FeO*+MgO	0.55	0.76	0.72	0.74
moles A/CNK	1.33	1.24	1.23	1.47
K2O/Na2O	1.47	1.11	0.94	4.18

SAMPLE	RWS-89-017C	RWS-89-001A	RWS-90-022	RWS-90-024
Rock Unit	Apple Green Granite	Apple Green Granite	Apple Green Granite	Apple Green Granite
SiO2	62.82	67.68	46.94	70.36
TiO2	0.44	0.15	1.28	0.20
Al2O3	12.70	12.80	14.33	12.27
FeO*	3.91	2.74	7.73	2.06
MgO	1.82	1.16	4.18	1.00
MnO	0.07	0.06	0.11	0.03
CaO	3.90	2.69	5.57	2.25
BaO	0.06	0.10	0.01	0.09
K2O	3.10	4.56	3.01	4.20
Na2O	3.12	2.52	1.83	2.22
P2O5	0.15	0.03	0.27	0.09
L.O.I.	6.64	4.59	12.85	4.54
Total	98.74	99.07	98.11	99.30
K2O+Na2O	6.22	7.08	4.84	6.42
FeO*/FeO*+MgO	0.68	0.70	0.65	0.67
moles A/CNK	1.25	1.31	1.38	1.42
K2O/Na2O	0.99	1.81	1.64	1.89

SAMPLE	RWS-002	RWS-003B	RWS-90-027A	RWS-003BG
Rock Unit	Brown Gouge	Brown Gouge	Brown Gouge	Blue-gray Gouge
SiO2	51.41	45.22	62.83	42.84
TiO2	1.46	2.00	0.40	1.84
Al2O3	14.24	13.69	13.47	13.22
FeO*	6.80	5.47	3.75	3.93
MgO	0.97	0.83	0.56	2.19
MnO	0.06	0.07	0.02	0.13
CaO	7.24	12.41	5.08	13.22
BaO	0.02	0.02	0.02	0.01
K2O	3.61	3.11	3.31	3.21
Na2O	0.08	0.12	0.03	0.12
P2O5	0.30	0.30	0.16	0.28
L.O.I.	12.24	15.18	9.28	17.56
Total	98.43	98.41	98.91	98.53
K2O+Na2O	3.69	3.23	3.34	3.33
FeO*/FeO*+MgO	0.88	0.87	0.87	0.64
moles A/CNK	1.30	0.88	1.60	0.80
K2O/Na2O	45.13	25.92	110.33	26.75

SAMPLE	RWS-09-027E	RWS-89-018EI	RWS-90-027B	RWS-90-025
Rock Unit	Blue-gray Gouge	Blue-gray Gouge	Blue Gouge	Apple Green Gouge
SiO2	42.41	64.26	60.60	64.24
TiO2	1.68	0.46	0.52	0.40
Al2O3	14.65	13.86	13.60	13.84
FeO*	7.59	3.77	3.18	3.17
MgO	3.11	0.83	1.68	1.42
MnO	0.19	0.08	0.07	0.05
CaO	8.60	2.62	4.78	3.04
BaO	0.02	0.06	0.04	0.07
K2O	4.28	4.81	3.64	3.60
Na2O	0.63	2.98	0.01	3.24
P2O5	0.39	0.20	0.19	0.14
L.O.I.	15.11	5.73	10.11	6.05
Total	98.66	99.65	98.42	99.25
K2O+Na2O	4.91	7.79	3.65	6.84
FeO*/FeO*+MgO	0.71	0.82	0.65	0.69
moles A/CNK	1.08	1.33	1.61	1.40
K2O/Na2O	6.79	1.61	364.00	1.11

SAMPLE	RWS-89-030A	RWS-89-030B	RWS-89-036C	RWS-89-037B
Rock Unit	E-W Structure	E-W Structure	E-W Structure	E-W Structure
SiO2	53.24	47.99	74.77	76.92
TiO2	2.16	0.33	0.17	0.12
Al2O3	14.80	6.99	12.73	10.07
FeO*	8.71	2.93	1.40	1.61
MgO	3.26	0.67	0.48	0.92
MnO	0.05	0.18	0.03	0.01
CaO	2.72	18.34	0.14	0.02
BaO	0.04	0.41	0.05	0.02
K2O	2.90	1.67	5.97	3.98
Na2O	0.19	0.58	0.49	0.15
P2O5	0.34	0.10	0.06	0.07
L.O.I.	10.52	17.86	3.33	4.75
Total	98.95	98.05	99.61	98.63
K2O+Na2O	3.09	2.25	6.46	4.13
FeO*/FeO*+MgO	0.73	0.81	0.74	0.64
moles A/CNK	2.55	0.34	1.93	2.43
K2O/Na2O	15.26	2.88	12.18	26.53

FeO* represents total iron oxide.

Chapter 3

Geology and Mineralization at the Morning Star Precious-metal Deposit

Introduction

In recent years considerable advances in our understanding of the evolution of many major mesothermal and epithermal gold deposits have been made by relating such deposits to their structural setting within fault zones (e.g. Kerrich 1986; Wilkins et al. 1986). Evolutionary models integrating episodes of faulting, fluid pressure cycling and precipitation of ore minerals within dilatant zones have been proposed (e.g. Sibson 1987; Sibson et al. 1988) to explain the observed relationships between ore deposits and structural evolution. Examples include the mineralized shear zones at Yellowknife, Northwest Territories, Canada (Kerrich and Allison 1978) and mineralized detachment faults (Bouley 1986; Wilkins et al. 1986), such as Picacho, California (Drobeck et al. 1986), but little attention has been paid to mineralized low angle thrust faults. The Morning Star deposit clearly constitutes one such natural example of a mineralized low angle thrust fault. This paper describes the relationship between mineralization and thrust faulting at the Morning Star deposit based on data obtained from geological, mineralogical and geochemical studies.

The Morning Star precious-metal deposit is located on the eastern flank of the Ivanpah Mountains near the northeastern edge of the Mojave Desert, California; approximately 100 km southwest of Las Vegas, Nevada (Figure 3.1A). The mine is

Figure 3.1. Generalized geologic map of the area adjacent to the Morning Star deposit. A.) Location of the Morning Star deposit with relationship to the Mesozoic foreland fold and thrust belt of California and Nevada. B.) General geology around the Morning Star deposit including the Kewanee Hills area to the south of the Morning Star open pit mine.

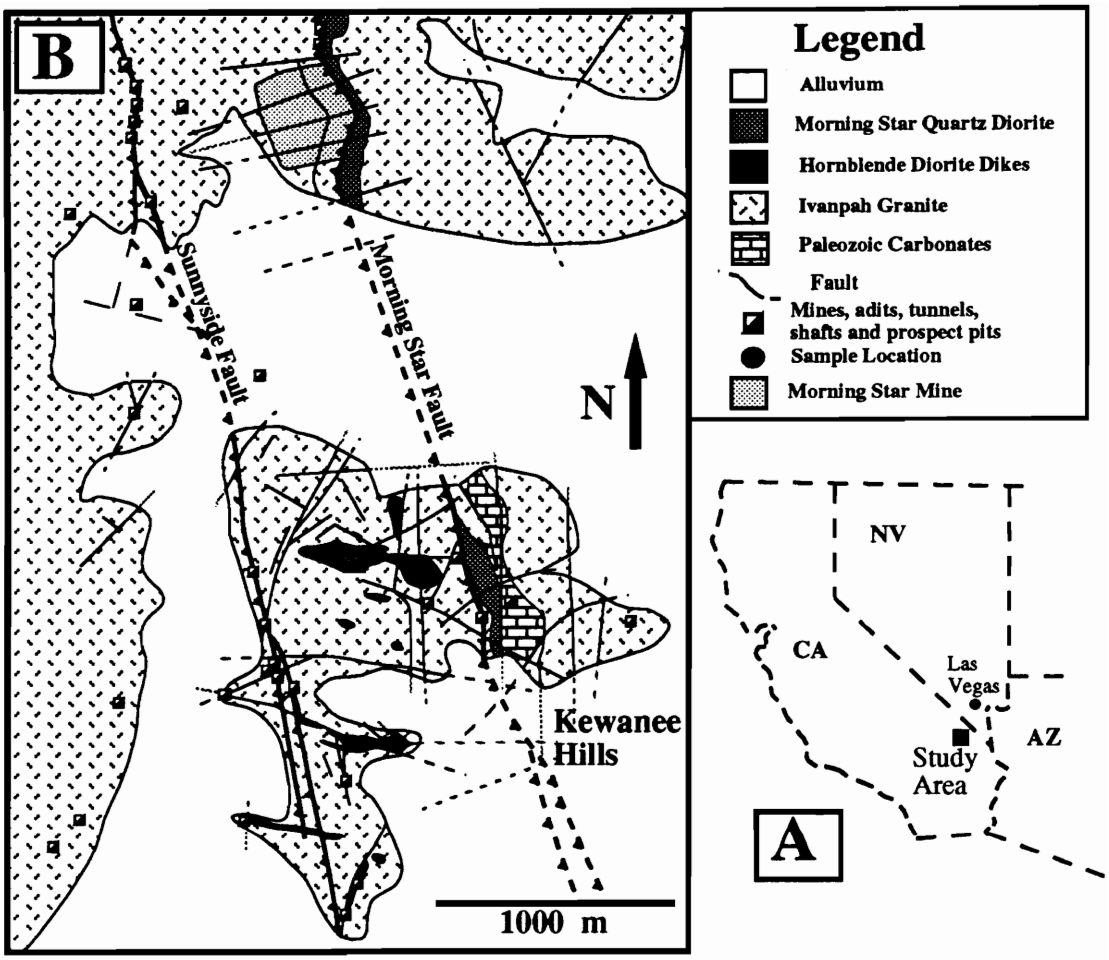
B
Legend
Alluvium
Morning Star Quartz Diorite
Hornblende Diorite Dikes
Ivanpah Granite
Paleozoic Carbonates
Fault
Mines, adits, tunnels, shafts and prospect pits
Sample Location
Morning Star Mine
Sunnyside Fault
Morning Star Fault
N
Kewanee Hills
1000 m
NV
CA
Las Vegas
AZ
Study Area
A

situated at an elevation of roughly 1420 meters (4660 feet at the mine office) above sea level. Gold mineralization was discovered in the Ivanpah Mountains in 1907. The Morning Star mine property was prospected intermittently until the late 1930's when it was acquired by Haliburton Oil Company. During that time Haliburton performed extensive underground exploration which blocked out 2 million tons of gold ore. In 1942 the operation was shut down prior to the onset of gold production due to the War Powers Act. Vanderbilt Gold Corporation, the current owner and operator of the property, acquired the Morning Star in the 1960's and reopened the existing workings and underground exploration. From 1980 to 1982 the mine was developed as an underground operation utilizing trackless mining techniques. In 1986 the mine was converted to an open pit, cyanide heap-leach operation and full scale production of crushed ore began in late 1987. Proven reserves, as of 1988, were approximately 8 million tons of ore averaging 0.06 ounces of gold per ton ore and the mine life was projected at 9 to 10 years with a 40 to 55 thousand ounces of gold per year production schedule (Ausburn 1988). In early 1992 the open pit mining was shut down due to falling gold prices, but heap-leach extraction of metals continued to through 1994.

Geology of the Morning Star Deposit

The Ivanpah Mountains are underlain by Jurassic Ivanpah granite and other Mesozoic plutons of the Teutonia Batholith which intruded a thick section of thrust faulted Paleozoic autochthonous platform and allochthonous miogeoclinal sedimentary rocks (Chapter 1, Appendix A and Chapter 2). The Ivanpah Mountains are cut by the Late Cretaceous Morning Star fault system which juxtaposes Ivanpah granite in both the upper- and lower-plates of the thrust fault (Chapter 2). Mineralization at the Morning Star

deposit is hosted by Ivanpah granite in the upper-plate of the Morning Star thrust fault (Figures 3.1 and 3.2). Surrounding the deposit are numerous fine to medium grained pre-tectonic quartz diorite and hornblende diorite dikes. Locally, especially in the vicinity of the Morning Star mine, the Morning Star quartz diorite dike crops out in the lower-plate immediately below the Morning Star fault (Figure 3.1 and 3.2). Aplite dikes and porphyritic granite dikes and small plugs, believed to be late stage differentiates of Ivanpah granite, also occur throughout the mine and to the west. A detailed description of the geology and igneous petrology of the Ivanpah Mountains is contained in Chapter 1 and Appendix A, and the Morning Star fault system is described in Chapter 2.

The only sedimentary rocks that crop out in the vicinity of mineralization is a roof pendant of Paleozoic Bird Springs Formation dolomite enveloped by Ivanpah granite east of the Morning Star fault in the Kewanee Hills area (Figure 3.1B). Bird Springs Formation is part of the platform sedimentary sequence found in the northeastern Ivanpah Mountains (Chapter 1). The granite-carbonate contact dips 45°SW and the roof pendant pinches out with depth. The dolomite is completely recrystallized but contains no skarn mineralization. Late, unmineralized quartz veins cut the dolomitic roof pendant but no other evidence of hydrothermal activity exists in the roof pendant.

Structural Geology

Mineralization in the area of the Morning Star deposit occurs in foliated to mylonitic Ivanpah granite in the upper-plate of the Morning Star and Sunnyside thrust faults. Economic quantities of mineralization only occur along the Morning Star fault in the area of the mine, but numerous historic mine workings and prospect pits, many of which produced ore earlier this century, occur along the Sunnyside structure and

Figure 3.2. Block diagram outlining the extent of the Morning Star ore horizon in eight E-W cross section through the deposit. The front cross section is at the southern extent of the mine workings and the back cross section is at the northern extent. Dashed lines represent the outline of the 1989 open pit mine and the solid lines represent topography. The cross sections were constructed from mine workings and drill core logs. Structures other than the Morning Star fault have been eliminated from the diagram for clarity.

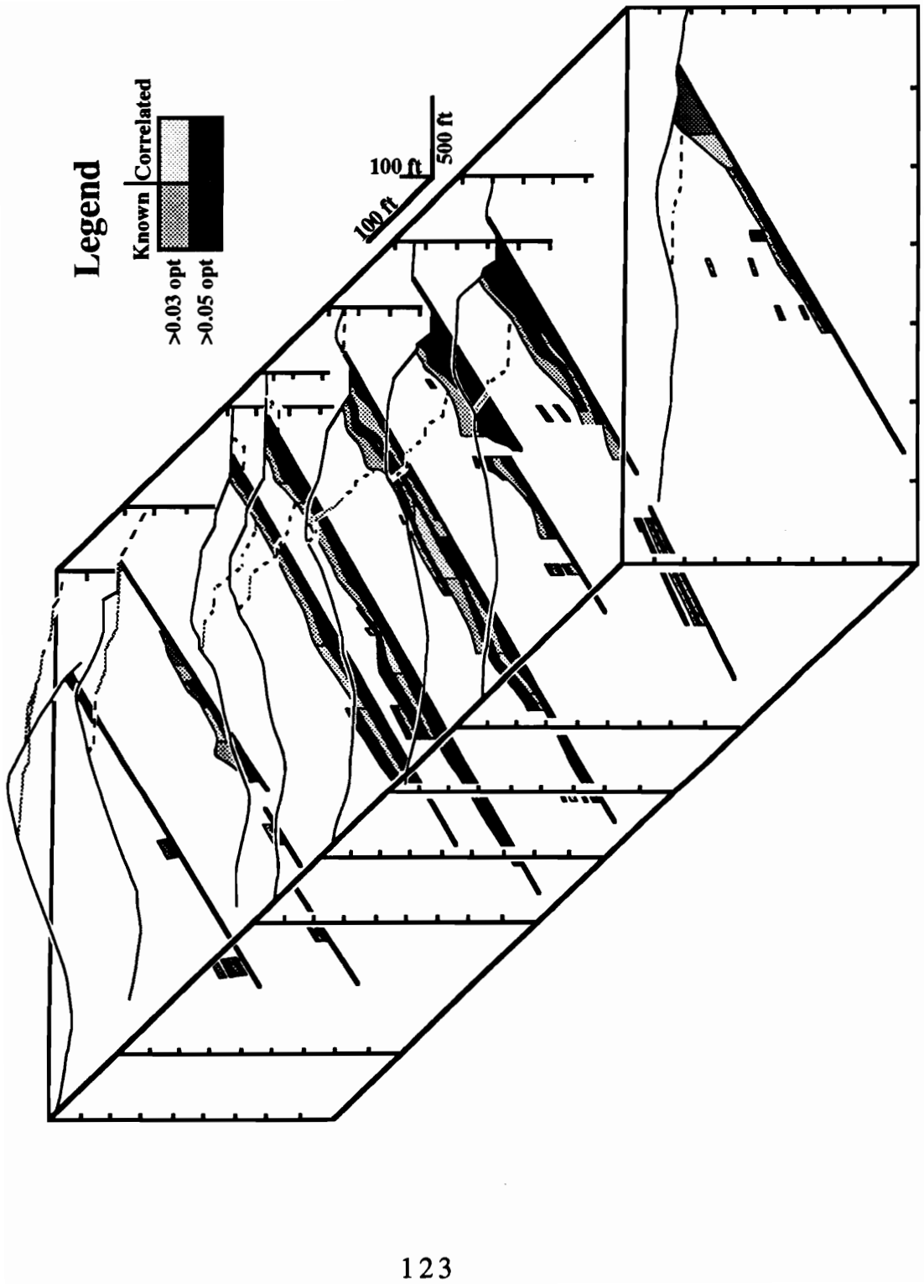
Legend
Known
Correlated
>0.03 opt
>0.05 opt
100 ft
100 ft
500 ft

the southern extent of the Morning Star fault in the Kewanee Hills area (Figure 3.1B). The Morning Star fault trends N20°W and dips 35°SW while the Sunnyside fault has a parallel trend but dips between 35 and 45°SW. Each fault is marked by a 3 to 6 meters (10 to 20 foot) thick zone of mylonite that grades upward into protomylonite. Brittle deformation, manifest by cataclastic deformation of the mylonite, brecciation of the host rocks and fault gouge formation, has overprinted the ductile deformation along the Morning Star structure. All foliated rocks between the Morning Star and Sunnyside thrust faults resulted from tectonic movement along the faults (Chapter 2) in contrast to Hewett (1956) who mapped foliated rocks between these structures as Precambrian gneiss. Deformed granites form S-C mylonites which contain a weak down dip mineral lineation which trends S84°W and dips 43°SW. This mylonitic lineation formed at a high angle to the N20°W trending 35°SW dipping mylonitic foliation. Kinematic indicators and quartz crystal fabric preferred orientation studies indicate thrust movement for ductile deformation on both structures (Chapter 2).

The Morning Star fault crops out at the mine as a 0.3-2.4 meter (1 to 8 foot) thick fault gouge zone which consists of variable-sized bleached and rounded granite fragments surrounded by anastomosing foliated clay selvages. Mineralogy of the clay and fine grained portions of the gouge includes quartz, carbonates, well crystalline kaolinite(±dickite), muscovite (sericite±illite), randomly interstratified clay minerals, montmorillonite, Fe-oxide minerals and feldspars (Chapter 2). Very rare galena and chalcopyrite have been found in fault gouge samples from the upper levels of the mine, but fire-assay analyses of fault gouge samples only found gold and silver at the detection limits for fire-assay techniques on all levels of the mine. The Morning Star dike is truncated by the Morning Star fault and altered dike fragments have been found in fault gouge samples. Kinematic indicators within the fault gouge zone (Chapter 2) indicate

multiple episodes of thrust movement during brittle deformation, in contrast to other workers who argue for variable slip senses over the span of deformation (e.g. Byington 1988; 1989). Asymmetrically folded fault gouge found south of the mine is consistent with thrust movement for the brittle episode of deformation (Chapter 2).

Immediately above the fault gouge zone is mylonitized granite which is truncated by the Morning Star fault at it's lower contact. No disseminated mineralization was found in the mylonite that parallels the fault, except where the mylonite is cut by later veins or brecciated, indicating that mineralization postdates the episode of ductile deformation (Figure 3.3). The zone of ductile deformation which contains vein-hosted mineralization contains mylonite (Figure 3.3A), which grades upward into protomylonite (Figure 3.3B). The zone of ductile deformation (mylonite and protomylonite) has been thrust over the zone of brittle deformation (fault gouge); another indication of thrust displacement during brittle deformation of the Morning Star fault. The upper-plate also contains a series of discrete mylonite units sub-parallel to the Morning Star fault. These subparallel mylonite units crop out throughout the area between the Morning Star and Sunnyside faults. Upper-plate mylonite units are typically truncated by quartz filled breccia veins (Figure 3.3C) and are commonly thinner than the mylonite zone that marks ductile deformation on the Morning Star thrust fault proper.

Faults and fractures of various orientations cut upper-plate and, to a lesser extent, lower-plate rocks (Figure 3.1). Brittle structures at the mine include a series of E-W to ENE-WSW trending steeply dipping unmineralized structures, breccia zones and low angle structures. Two sets of mineralized structures, confined to the upper-plate, have been identified. One set strikes N to NW and dips vary from (1) sub-parallel to the Morning Star fault (35°SW), (2) moderately dipping (50 to 25°) in the same direction as the Morning Star fault (SW) – some of these structures asymptotically approach the fault

Figure 3.3. Photographs of the various foliated rocks at the Morning Star fault and the upper-plate. Tectonic fabrics range from ultramylonite (A and top of C) to protomylonite (B), and both are cut by quartz veins or quartz cemented breccias. The mylonites form gradational contacts with the surrounding granites, but many contacts and strain transitions are obscured by the veins and quartz-cemented breccias (A and C).

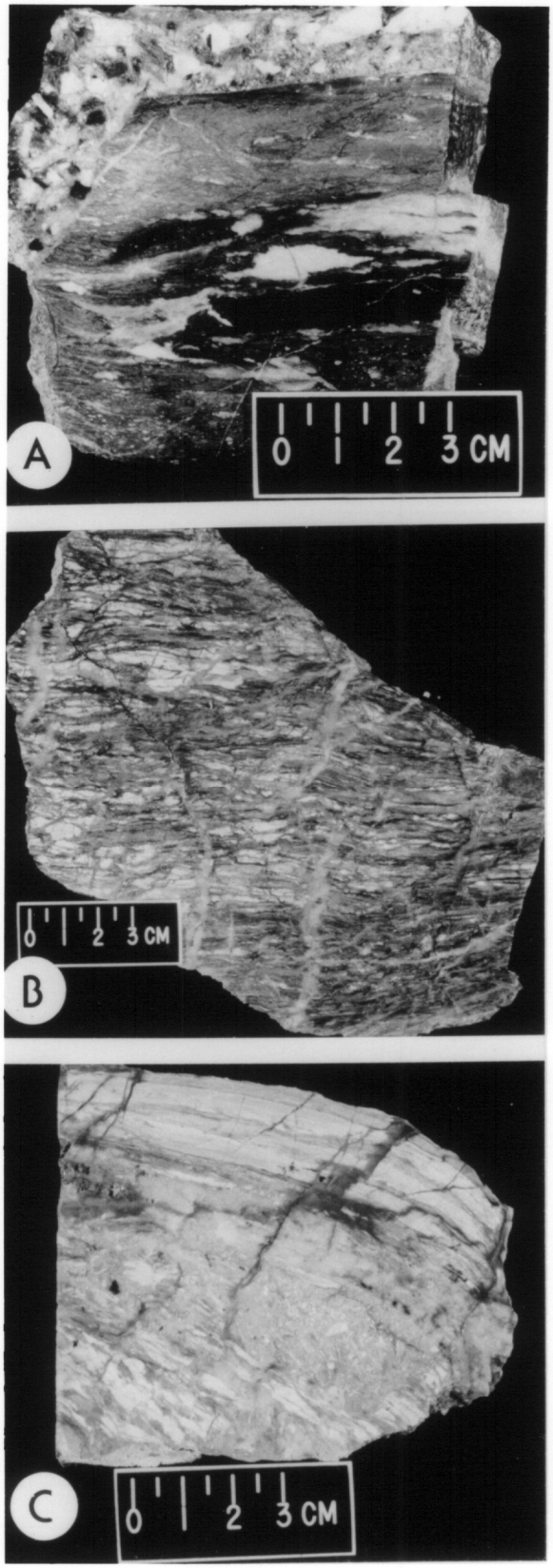
A
0 1 2 3 CM
B
0 1 2 3 CM
C
0 1 2 3 CM

with depth –, and (3) dipping back (NE) at a high angle (60 to 85°) into the Morning Star fault. The second set of mineralized veins varies in strike from NE to E-W and dip at a moderate to high angle (from 60°N to 60°S). Mineralized quartz±carbonate veins and silica-cemented breccias occupy these dilatant zones and are described below.

The unmineralized E-W structures are vertical to steeply north dipping (90 to 60°) and cut the orebody, Morning Star fault and Morning Star dike. Displacement on the E-W structures appears to be left-lateral normal oblique-slip with the northern side moving down and westerly relative to the southern side. Maximum throw is only a 0.3-4.6 meters (1 to 15 feet) on each E-W structure. Similar E-W structures have been postulated under the alluvial cover between the Morning Star deposit and the Kewanee Hills area from structural contour mapping of the Morning Star fault surface in 140 exploration drill holes at the mine and to the south. The E-W structures form an en echelon left-lateral array of fractures that accounts for the eastward displacement of the Morning Star and Sunnyside faults in the Kewanee Hills area (Figure 3.1B). In the Morning Star deposit the unmineralized E-W structures are filled with a white clay-bearing gouge which differs from gouge along the Morning Star fault in that granite fragments are angular and the matrix clay- and fine-grained size materials are not foliated (Chapter 2). Mineralogy of E-W structures is principally illite+quartz+feldspar with lesser amounts of montmorillonite and chlorite (Chapter 2).

Structure of the Ore Horizon

Disseminated base- and precious-metal mineralization at the Morning Star deposit is structurally controlled within an ovoid lens-shaped zone of quartz±calcite stockwork and silica-flooded breccia vein system truncated by the Morning Star thrust fault (Figure

3.2). The orebody has a strike length of about 366 meters (1200 feet), an average vertical thickness of 30 meters (100 feet), and is open ended down dip (Figure 3.2). Economic grade ore pinches out to the northwest and southeast within the ore horizon. Additional mineralization is encountered at structurally higher levels of the upper-plate, above the main ore horizon, at the intersect of prominent vein sets. These structurally higher pockets of mineralization are of limited extent but contain the same mineralogy as the main orebody.

Mineralization is confined to syn- and post-tectonic quartz±carbonate veins, stockwork vein sets and brecciated units (Figure 3.3 and 3.4). Within the orebody and at higher structural levels of the upper-plate, three principal mineralized vein sets are present with numerous secondary or minor quartz±calcite vein and fracture sets. The principal mineralized vein sets trend and dip N68°W, 76°SW; N22°E, 65°NW; and N3°W, 34°NE. Intersection of the first two vein sets controls precious-metal mineralization by creating oreshoots which trend S84°W and dip 62°SW (Byington 1988; 1990). Mineral stretching lineations in mylonitic fault rocks along the Morning Star thrust average S84°W, 43°SW (Chapter 2) and the trend of E-W high angle structures averages S85°W, both which have essentially identical trends as oreshoots. The coincidence in orientation implies brittle structures are controlled by pre-existing ductile fabric development. Numerous secondary vein sets and minor mineralized fractures occur throughout the orebody but no consistent orientation for these minor structures was detected.

Exploration drill holes that cut the high grade ore horizon generally intersect quartz±carbonate stockwork veins (Figure 3.4A) and breccias (Figure 3.3C and 3.4B, D) 5 to 9 meters (15 to 25 feet) vertically above the fault plane (top of the gouge zone). Brecciation occurs in mylonite (Figure 3.3A, C), protomylonite (Figure 3.3B) and quartz veins (Figure 3.4B). Breccias confined to individual quartz veins are also

Figure 3.4. Photographs of veins and breccias within the vicinity of the Morning Star deposit. A. stockwork white coarse-grain quartz veins in slightly sheared, propylitically altered granite from the northern end of the Kewanee Hills area. B. Stockwork veining in silicified granite from the Kewanee Hills area. C. Sheeted veins of sulfide minerals in quartz from the high grade ore horizon on the 4680 bench of the Morning Star open pit mine. D. Argillically altered brecciated mylonite cemented with quartz and minor sulfide minerals from the high grade ore horizon on the 4580 bench of the Morning Star open pit mine. The mylonite in Figure 3.4D was originally propylitically altered which is overprinted by argillic alteration.

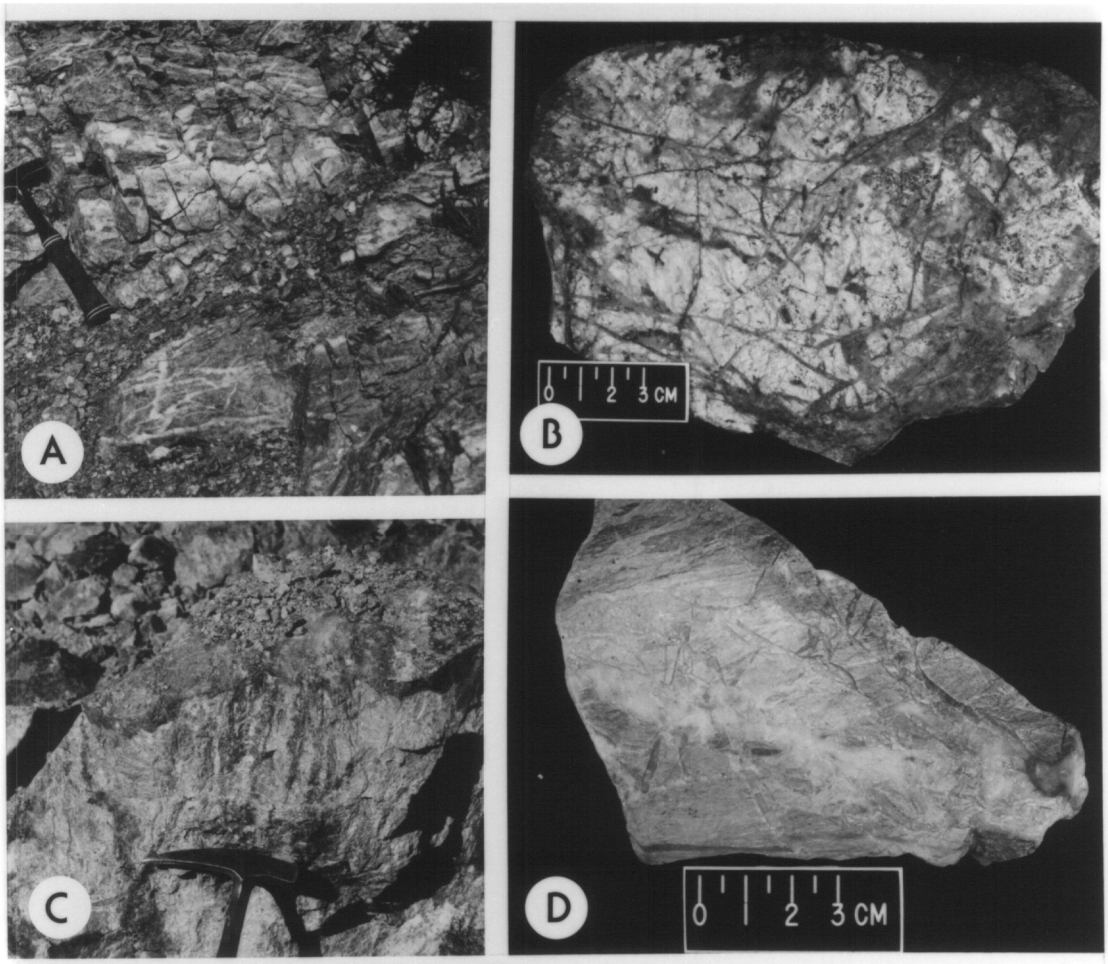

STOCKWORK AND BRECCIAS

found at higher levels of the deposit, but this occurrence is rare. The breccia units usually contain abundant sulfide minerals, electrum, and propylitically and sericitically altered mylonite and protomylonite breccia clasts all cemented by quartz and calcite. Breccia clasts typically show moderate to slight rotational displacement (Figure 3.3C and 3.4D). Stockwork and sheeted vein (Figure 5.4C) zones occur for about 15 to 30 meters (50 to 100 vertical feet) above the zone of intense brecciation. In the Kewanee Hills area a 1.5 meters (5 foot) thick zone of stockwork veined and brecciated silicified granite (Figure 3.4A) is situated directly above the fault plane which is marked by a brecciated quartz vein (Figure 3.4B).

The orebody is oxidized down to the 4400 and 4500 benches throughout the open pit mine. The zone of oxidation corresponds to the present day perched water table which was delineated from exploration drill holes. This occurrence of oxidation corresponding to the elevation of the modern day water table is also observed for other deposits in the eastern Mojave Desert (personal communication, J. Cline). Vertical thickness of the ore horizon increases in the uppermost levels of the open pit mine and thickness increases immediately below the zone of intense supergene oxidation for the central portions of the ore horizon.

Geochemistry

Exploration drill core and underground workings at the Morning Star deposit were assayed (Fire assay) for gold by Vanderbilt Gold Corporation, and mining proceeded utilizing blast hole gold assay maps along mine benches in the open pit. Silver and other trace element geochemistry was determined for only a limited number of mine bench samples and 1.5 meter drill core intervals (Table 3.1). Although the ore horizon forms a

Table 3.1. Trace element geochemistry of the Morning Star deposit.

Sample	HGO-4660	MRO-4660	MSE-27	MSE-27	MSE-27	MSE-27	MSE-24	MSE-24	MSE-24	MSE-24	MSE-24
depth			340-345	410-415	435-440	455-460	3-11	102-112	202-202	339-347	362-367
Ag	102.000	12.600	0.444	5.320	2.790	3.110	0.211	0.341	0.229	0.394	0.028
As	9.040	8.710	0.913	<0.900	<0.900	2.440	1.880	1.250	<0.900	3.820	2.320
Au	78.100	14.500	0.091	2.170	0.305	3.350	0.046	0.073	0.046	0.104	0.046
Bi	57.000	5.580	0.848	6.210	3.770	1.390	<0.235	<0.235	<0.235	0.413	<0.235
Cd	3.720	6.100	0.396	1.320	1.000	2.010	0.666	1.330	1.600	1.110	<0.235
Cu	3089.000	995.000	61.200	461.000	251.000	234.000	84.000	147.000	105.000	54.500	37.000
Ga	<0.480	<0.480	1.900	0.924	0.540	0.554	0.664	0.597	0.764	1.400	8.600
Hg	0.125	<0.100	<0.100	<0.100	<0.100	<0.100	<0.100	<0.100	<0.100	<0.100	<0.100
Mo	10.100	10.000	1.110	2.020	1.830	2.340	1.420	2.090	2.390	2.210	0.541
Pb	2581.000	2529.000	33.500	1149.000	991.000	1564.000	116.000	327.000	338.000	121.000	8.610
Pd	<0.100	<0.100	<0.100	<0.100	<0.100	<0.100	<0.100	<0.100	<0.100	<0.100	<0.100
Pt	<0.250	<0.250	<0.250	<0.250	<0.250	<0.250	<0.250	<0.250	<0.250	<0.250	<0.250
Sb	<0.250	<0.250	<0.250	<0.250	<0.250	<0.250	<0.250	<0.250	<0.250	<0.250	<0.250
Se	1.720	<1.000	<1.000	<1.000	1.240	<1.000	<1.000	<1.000	<1.000	<1.000	<1.000
Sn	<0.450	0.554	0.546	0.780	0.722	0.675	0.613	1.000	1.120	0.640	0.919
Te	<0.500	<0.500	<0.500	<0.500	<0.500	<0.500	<0.500	<0.500	<0.500	<0.500	<0.500
Tl	<0.500	<0.500	<0.500	<0.500	<0.500	<0.500	<0.500	<0.500	<0.500	<0.500	<0.500
Zn	174.000	343.000	48.600	12.400	8.450	21.200	11.500	22.100	31.900	25.900	70.700

Analyses by ICP emission spectroscopy with all concentrations expressed in ppm. MSE-24 and MSE-27 are analyses from drill core at the depths specified (in feet below surface); samples HGO-4660 and MRO-4660 are from the 4660 foot bench of the Morning Star mine.

Trace element geochemistry of mine workings in the Kewanee hills area.

Sample	Au (ppm)	Ag (ppm)	Cu (ppm)	Pb (ppm)	Au/Ag
incline	5.5	11.0	800	>20000	0.50
incline*	13.0	9.4	920	>20000	1.38
dump	48.0	8.2	44	3900	5.85
dump	6.8	9.0	252	3700	0.76
dump	4.0	5.2	300	870	0.77
dump	>15.0	17.0	6200	1550	0.88
shaft	0.1	2.0	263	530	0.05
shaft	1.7	3.4	420	1140	0.50
shaft	9.5	12.0	820	2500	0.79
shaft	0.7	2.0	345	1510	0.35
shaft	0/9	2.6	960	1900	0.35
shaft	4.4	5.7	960	1260	0.77
shaft	1.2	5.9	350	470	0.20

analyses by atomic absorption spectroscopy and reported in Forgerson (1974). *indicates the location of the electrum-bearing sample K-Hills which is analyzed in Chapter 4.

Figure 3.5. Trace element geochemistry verses depth plots at the Morning Star deposit. A. Representative Au and Ag assay values from drill core. Drill hole MSE-23 represents unoxidized ore (not shaded) and Bench 4350 represents both oxidized (shaded) and unoxidized ore (not shaded). B. Trace element geochemistry profiles with respect to depth for Cu, Zn, Pb, Au, Ag, and Bi. Data used to construct this plot are reported in Table 3.1. The Morning Star fault is marked by the arrow in all the plots. See text for discussion of the metal distributions.

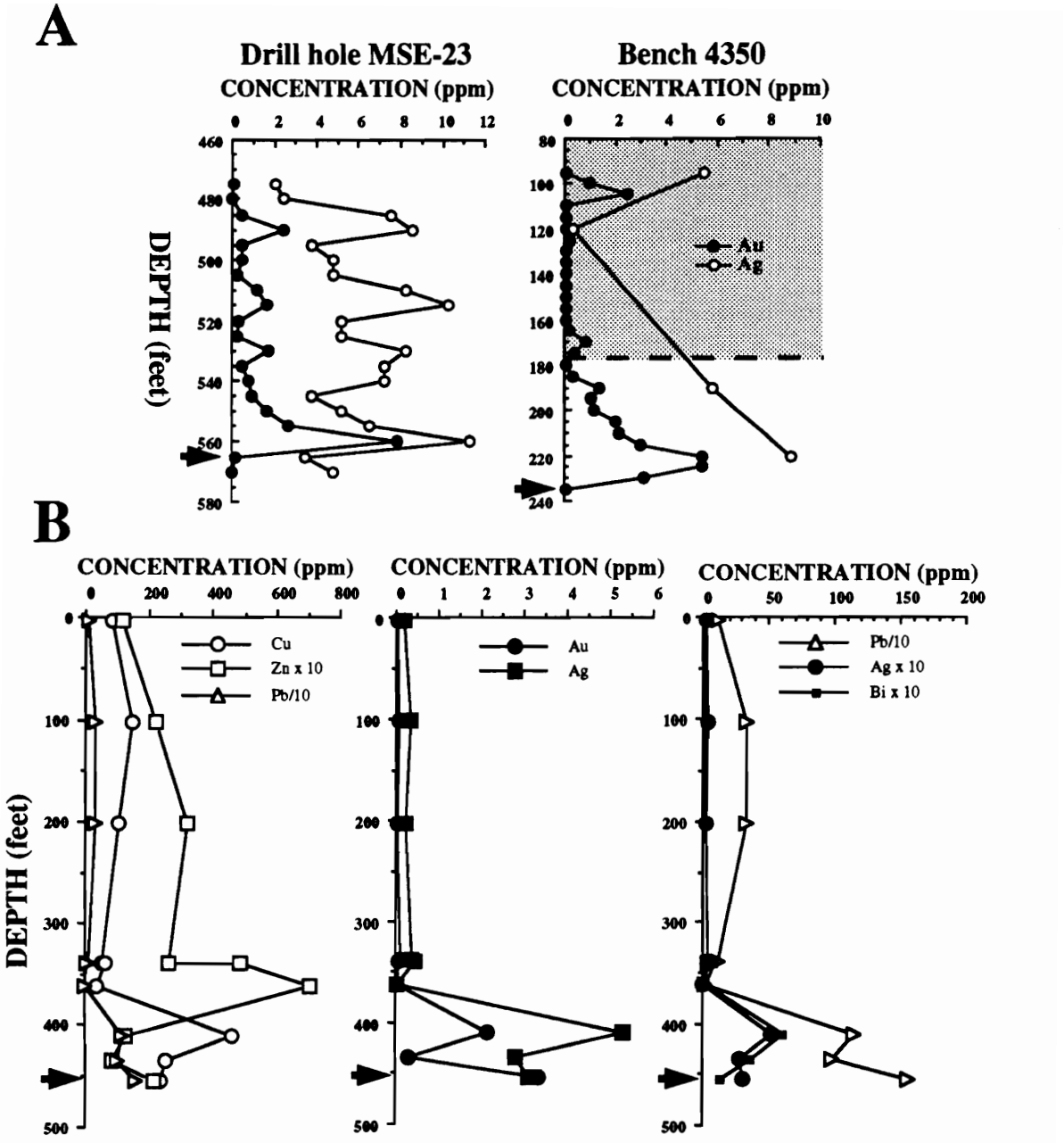
A
Drill hole MSE-23
CONCENTRATION (ppm)
DEPTH (feet)
Bench 4350
CONCENTRATION (ppm)
Au
Ag
B
CONCENTRATION (ppm)
Cu
Zn x 10
Pb/10
CONCENTRATION (ppm)
Au
Ag
CONCENTRATION (ppm)
Pb/10
Ag x 10
Bi x 10
DEPTH (feet)

between Au Sb, As, Pb, and Mo in rock chip and soil samples, and Forgerson (1974) found similar correlations from workings in the Kewanee Hills area (Table 3.1). With the exception of the Mo, As and Sb anomalies, all trace element correlations have been accounted for by minerals associated with gold and silver (see below and Chapter 4). Gold and silver form a strong but nonlinear correlation, with gold abundance increasing with silver abundance (Figure 3.6). Copper and silver also display a slightly wider dispersion halo than gold in soils around the mine (Byington 1988), which is consistent with supergene remobilization of these elements.

A slight zoning of base metals is observed from the limited number of analyses of the high grade ore horizon (Figure 3.5B). Lead is concentrated lower in the ore horizon with copper at intermediate levels and zinc at the highest levels of the ore horizon. Sulfide mineral zonation is consistent with these preliminary geochemical results (see below). A strong correlation also exists between Pb, Ag and Bi from the limited geochemical analyses (Figure 3.5B). A more detailed geochemical survey of the orebody is required to confirm these preliminary results and better define metal zoning.

Hydrothermal Alteration

Hydrothermal alteration is prevalent around the area of mineralization. Propylitic alteration occurs in both the upper- and lower-plates of the Morning Star fault and envelops the Morning Star deposit. The propylitic alteration assemblage contains chlorite+epidote+carbonate±albite. Pervasive propylitic alteration occurs adjacent to the thrust fault and grades to weak propylitic alteration away from the fault. The intensity of the propylitic alteration also decreases rapidly away from the mine site and is essentially

Figure 3.6. Correlation between Au and Ag from all drill core analyses where both metals were assayed throughout the Morning Star deposit.

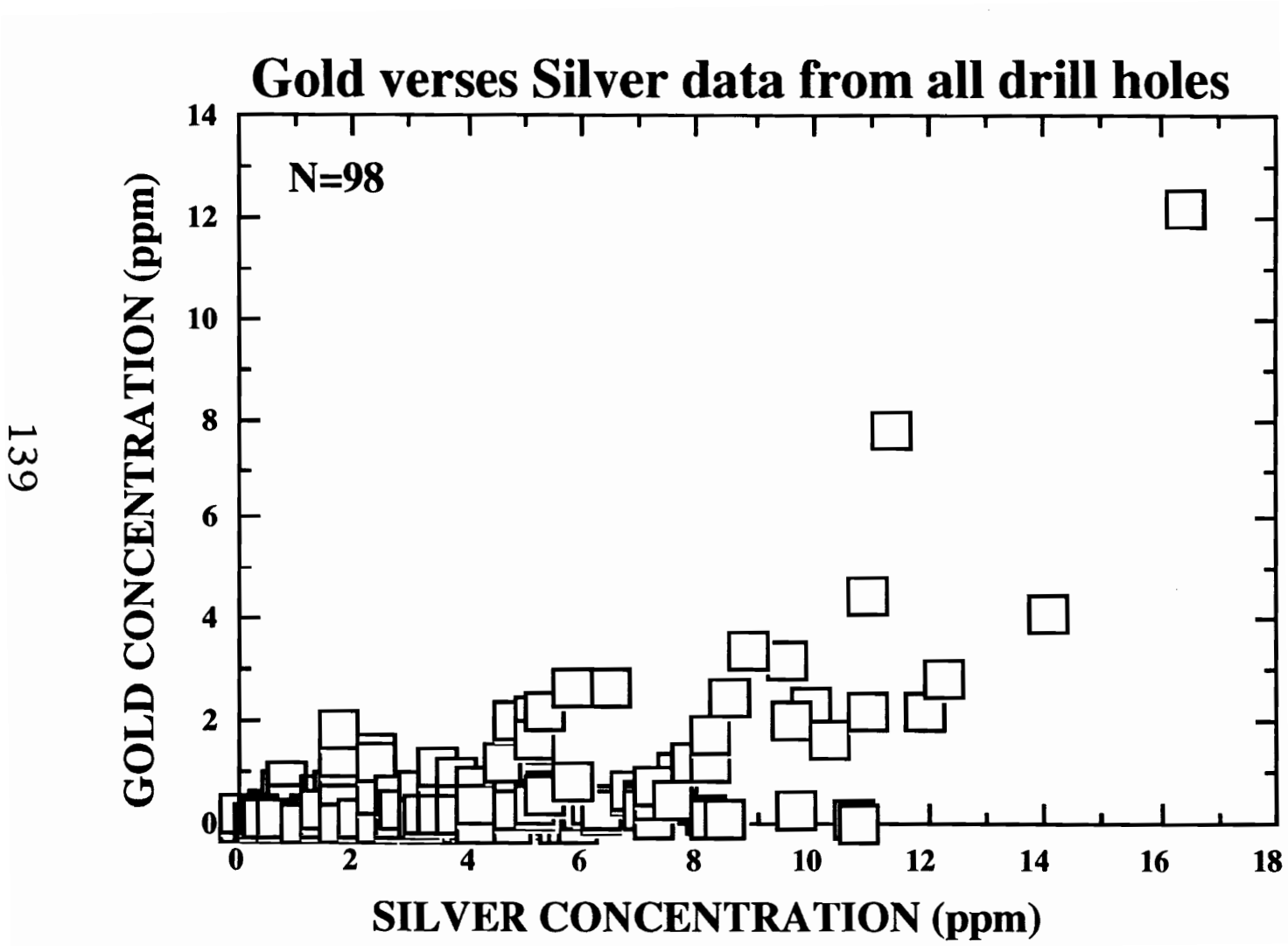
Gold verses Silver data from all drill holes
N=98
GOLD CONCENTRATION (ppm)
SILVER CONCENTRATION (ppm)
0
2
4
6
8
10
12
14
16
18

truncated to the north by an E-W high angle structure. Weak propylitic alteration also surrounds the historic workings in the Kewanee Hills area.

Argillic±sericitic alteration occurs only in the mineralized upper-plate of the Morning Star fault adjacent to the stockwork vein system and silica-flooded breccias. Argillic±sericitic alteration overprints propylitic alteration adjacent to zones of abundant quartz veins in high grade mineralization. Alteration of the Morning Star fault gouge and unmineralized E-W structures is also believed to be related to the episode of argillic±sericitic alteration (Chapter 2). Sericitic alteration occurs at deeper levels along the fault and is though to have formed prior to argillic alteration. Silicification is prevalent around the ore horizon and structurally higher in the upper-plate at the intersection of the principal vein sets. Silicification manifests itself by discrete quartz filled veins, veinlets and breccias. Prior to open-pit mining the orebody was overlain by a wedge shaped silicified caprock which was truncated to the north by an E-W structure and to the east by the Morning Star fault (Forgerson, 1974). The mineralogy of the silicified cap rocks is not known and no samples were available during this study. Silicification, argillic alteration and weak gold and silver mineralization also occur along the Sunnyside structure.

Mineralization

Ore petrography and electron microprobe analyses have identified two episodes of mineralization deposited under differing physical and chemical conditions (Sheets et al., 1988). The two principal episodes of mineralization, designated primary and secondary, are shown on Figure 3.7. An early episode of hypogene (primary mineralization) quartz, carbonate, barite, fluorite, pyrite, chalcopyrite, galena, sphalerite, tetrahedrite, argentite

Figure 3.7. Generalized paragenesis diagram for the Morning Star deposit showing the relative timing of mineralization and wall rock alteration assemblages. Mineralization has been divided into primary and secondary episodes with the primary episode divided into three stages each separated by a deformational events.

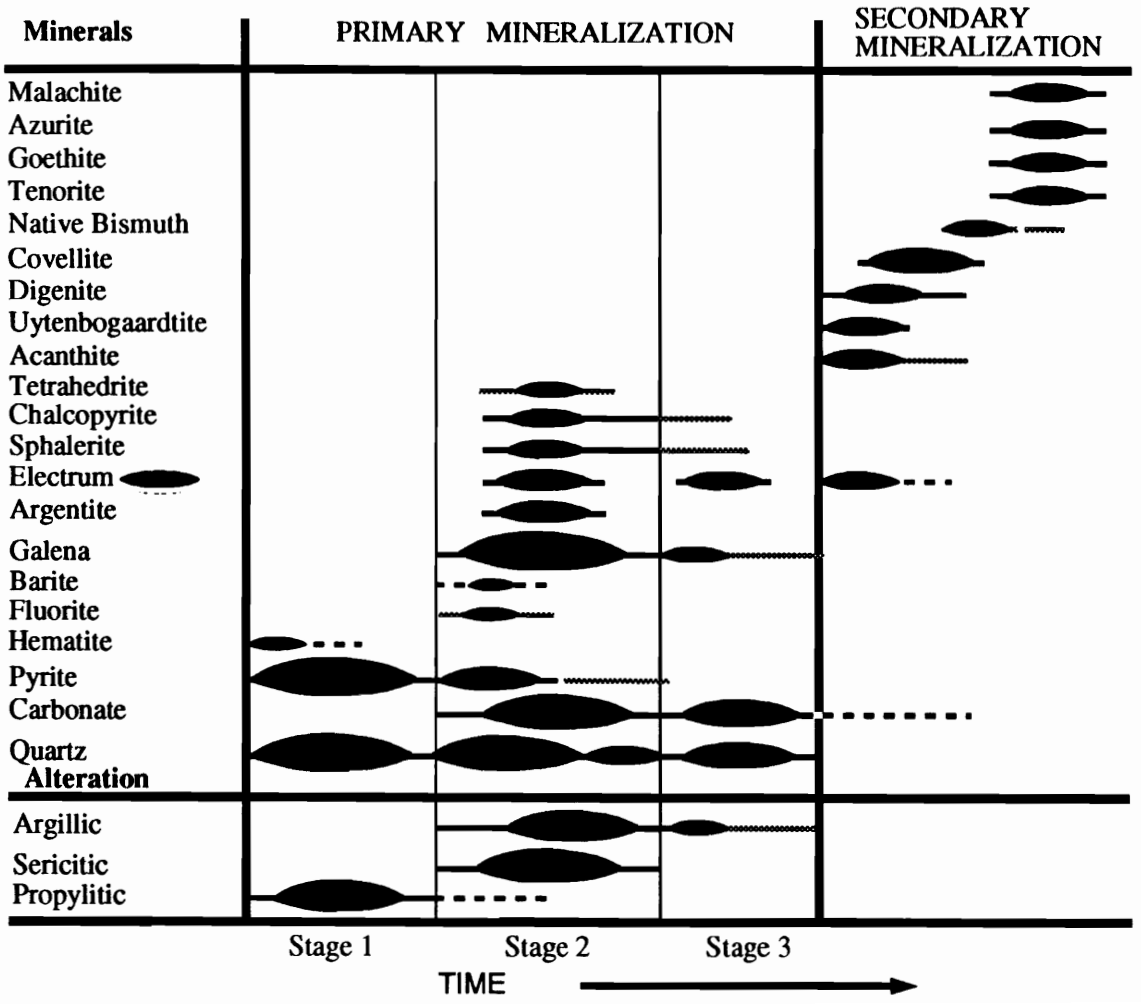
Minerals
PRIMARY MINERALIZATION
SECONDARY MINERALIZATION
Malachite
Azurite
Goethite
Tenorite
Native Bismuth
Covellite
Digenite
Uytenbogaardtite
Acanthite
Tetrahedrite
Chalcopyrite
Sphalerite
Electrum
Argentite
Galena
Barite
Fluorite
Hematite
Pyrite
Carbonate
Quartz
Alteration
Argillic
Sericitic
Propylitic
Stage 1
Stage 2
Stage 3
TIME

and electrum occurs below the zone of oxidation and a later episode of secondary mineralization consists of calcite, covellite, digenite (±chalcocite), goethite, acanthite, uytenbogaardtite (Ag_3AuS_2), native bismuth, electrum, Pb-, Zn- and Cu-carbonates and Cu oxides that occur within the zone of oxidation along with partially oxidized primary minerals. Factors controlling precious-metal mineralization include fracture density, presence of pyrite with galena, sphalerite and chalcopyrite (or the oxidation equivalents), and silicification.

Primary Mineralization

Primary mineralization has been divided into three stages, each stage being separated by an episode of deformation and containing a slightly different mineral assemblage (Figure 3.7). Stage 1 mineralization consists of quartz and pyrite associated with propylitic alteration. Stage 2 mineralization contains the bulk of the base- and precious-metal mineralization in quartz±carbonate stockwork veins and breccias associated with sericitically and argillically altered granite. The third stage of primary mineralization contains minor galena and electrum in late quartz±carbonate veins.

Stage 1 pyrite-bearing quartz veins commonly form subparallel to the regional mylonite foliation and occur in propylitically altered rocks. The early deposited pyrite and quartz exhibit abundant evidence of deformation manifest as brittle fracturing of pyrite and undulatory extinction, subgrain structures and grain-size reduction of the enveloping quartz (Figure 3.8). Some early pyrite-bearing veins contain pyrite fragments cataclastically sheared into bands sub-parallel to the regional mylonitic foliation. Stage 2 base- and precious-metal minerals fill fractures formed in early deformed stage 1 pyrite (Figure 3.8). Minor hematite and ilmenite were observed in propylitically altered host

Figure 3.8. Photomicrograph of early deformed quartz vein containing stage 2 galena and electrum filling fractures in stage 1 or early stage 2 pyrite. Early quartz exhibits undulatory extinction and subgrain structures while pyrite is cataclastically fractured. Scale bar is 250 μm. Photomicrograph A was taken under plane polarized reflected light and photomicrograph B was taken under cross polarized transmitted light.

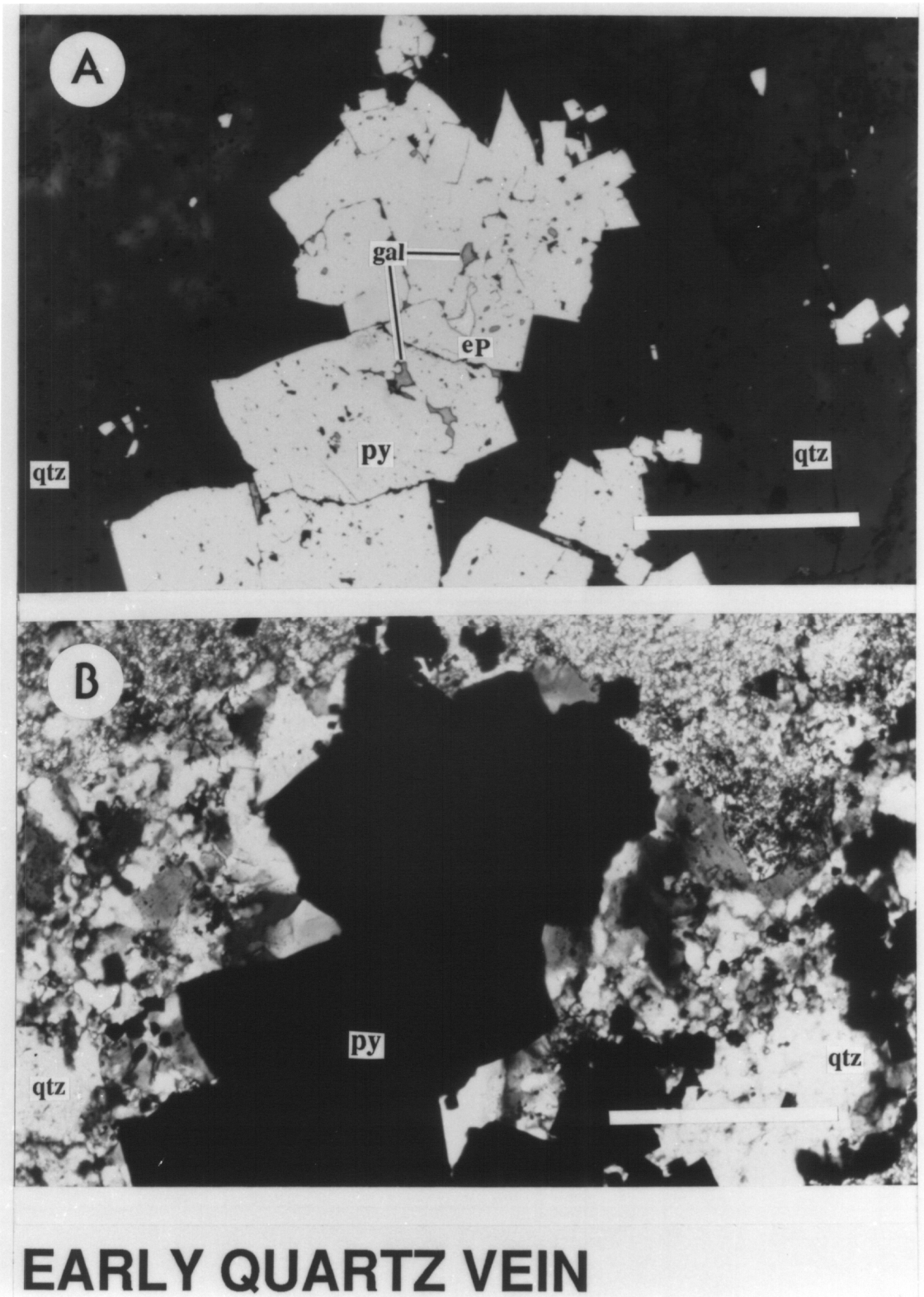

EARLY QUARTZ VEIN

rocks around quartz veins and along the vein-host rock contacts. The oxide minerals were not associated with ore minerals, therefore the oxides appear to have formed early in the paragenesis (stage 1) with pyrite-bearing veins.

During stage 2 mineralization a second generation of quartz and pyrite was precipitated. Base- and precious-metal mineralization typically fills small openings in this second generation of gangue minerals. Minor amounts of fluorite and barite occur early during this second stage of primary mineralization. Neither of these gangue minerals are associated with base- and precious-metal mineralization. Stage 2 mineralization is typified by small cavities and vugs that are lined by euhedral quartz crystals and filled with co-precipitated pyrite, galena, sphalerite, chalcopyrite, tetrahedrite, argentite and electrum (Figure 3.9). Quartz and carbonates are ubiquitous, but monomineralic carbonate veins cut quartz veins indicating that carbonate precipitation continued after quartz ceased. When quartz and carbonate minerals are present in the same veins, coexisting coarse-grained quartz and carbonates were precipitated onto early deposited fine-grained quartz at the vein-wall rock contact. Quartz-absent calcite veins occur later than main stage precious-metal mineralization and typically only contain galena and chalcopyrite. Carbonate only veins occur exclusively in upper levels of the deposit where the Morning Star dike or dike-bearing fault gouge were encountered. Vein textures, such as euhedral growth-zoned quartz crystals, indicate that the majority of the second stage of primary mineralization was deposited in open cavities. Early formed stage 2 mineralization is cataclastically deformed. Deformation manifest itself by grain size reduction of quartz, fracturing of pyrite, folding of galena cleavage pits and development of polysynthetic deformation twins in early carbonate minerals. These deformed vein textures are also associated with cataclastic deformation of the host rocks and deformed veins typically contain base- and precious-metal minerals filling fractures and cataclastic

Figure 3.9. Reflected light photomicrographs of typical primary mineralization at the Morning Star deposit. A. Stage 2 galena (bright white with triangle pits) and chalcopyrite (dull white) filling a vug in quartz (dark). Note the inclusions of sulfide minerals in the euhedral quartz crystals. B. Pyrite (bright white cubes) in quartz (dark) being replaced and embayed by galena (bright white), chalcopyrite (dull white) and sphalerite (gray). C and D. Disseminated stage 2 mineralization in quartz. Scale bars are 250 μm.

A
B
C
D

zones (Figure 3.9B). The occurrence of deformation events between stages 1 and 2 and early in stage 2 implies that the initial precious-metal mineralization took place prior to the final period of fault movement. Textural evidence which includes gold in deformed quartz and pyrite veins (Figure 3.8) confirms syn- or early post-tectonic electrum deposition. The remaining quartz, carbonate, and quartz+carbonate veins and breccia cements exhibit textures indicative of mineral deposition into open spaces. These late textures include 1) little or no internal deformation of individual mineral grains, 2) a gradation inward from the vein walls towards the cavities from anhedral, fine-grained to euhedral, coarse-grained crystals, 3) open vugs of druzzy quartz with later base-metal mineral infillings and 4) randomly oriented euhedral quartz in the centers of some veins. Therefore, the majority of the Morning Star mineralization is post-tectonic and confined to areas of structurally enhanced permeability.

Pyrite, sericite and quartz form the alteration assemblage around most stage 2 veins. Bleaching of fine-grained dikes and argillic alteration also occurs adjacent to the high grade ore horizon in the upper levels of the deposit. Pyrite is typically euhedral and the only sulfide mineral found outside of the veins and breccias. The main episode of pyrite deposition forms euhedral isolated crystals or interpenetrating aggregates of subhedral pyrite which have textures indicative of cataclastic deformation. Stage 2 pyrite is spatially and temporally associated with precipitation of base-metal sulfides. In some samples, stage 2 pyrite is cut by thin, fine-grained quartz veinlets, most likely from stage 3, which are free of base-metal minerals but may contain electrum. Pyrite is also found along vein-wall rock contacts, at the intersections of veins or as disseminated euhedral grains in base metal-poor veins.

Early pyrite is typically fractured and filled with galena, chalcopyrite, sphalerite, argentite (now acanthite), electrum, and gangue minerals (Figure 3.8 and 3.9B). Quartz,

carbonates, and base-metal sulfides also replace and embay pyrite, but inclusion filled grains suggest continued precipitation of pyrite after the onset of base-metal sulfide deposition. This is evidenced by large pyrite crystals in which the inclusion pattern roughly outlines growth zones. Galena, chalcopyrite, sphalerite, and tetrahedrite form the base-metal mineral assemblage occurring as cogenetic anhedral masses that fill open spaces in and around pyrite, carbonate, and quartz or occur as disseminated grains and stringer veinlets within quartz±carbonate veins (Figure 3.9). Galena has been reported to be Ag-bearing (Ausburn, 1988), but the only argentiferous galena observed in this study contains small inclusions of Ag-bearing tetrahedrite (Figure 5.8C). Numerous galena grains were analyzed for Ag and Bi but no evidence of Bi- or Ag-bearing galena was found. Thus the geochemical correlation between Pb, Ag and Bi could not be confirmed for the primary episode of mineralization, except for the minor tetrahedrite inclusions. Electrum and argentite are commonly intergrown with the base-metal sulfide assemblage. Sphalerite contains minor chalcopyrite blebs (chalcopyrite disease) and electron microprobe analysis of sphalerite reveals minor amounts of Fe and Cd (Table 3.2).

A crude mineral zonation, manifest by total sulfide content and specific sulfide mineral assemblages, exists within unoxidized portions of the high grade ore horizon, although the structurally controlled nature of the deposit complicates the zoning pattern. Pervasive propylitic alteration around the ore deposit may contain up to 2% pyrite and pyrite is ubiquitous throughout the deposit. A tabular zone containing greater than 5% total sulfide minerals coincides with the stockwork and breccia vein system, within the high grade ore horizon, directly above the Morning Star fault gouge. This high sulfide zone may locally contain up to 50% disseminated sulfide minerals and generally corresponds to zones of elevated gold values. Structurally above the high sulfide zone is an intermediate sulfide zone containing 2 to 5% sulfide minerals. Narrow zones of 2 to

Table 3.2. Sphalerite Chemistry.

Normalized wt. % elements				Mole %	Mole %	Mole %
Zn	Cd	Fe	S	ZnS	CdS	FeS
64.17	1.81	1.47	32.55	95.7	1.8	2.4
65.30	3.43	0.10	31.17	96.4	3.4	0.2
65.83	1.52	1.43	31.22	96.2	1.5	2.3
64.46	1.93	1.38	32.23	95.8	1.9	2.3
64.03	3.33	0.54	32.11	95.8	3.4	0.9
64.27	2.81	0.96	31.95	95.6	2.8	1.6
64.02	1.72	1.15	33.10	96.3	1.7	1.9
64.73	1.62	1.05	32.60	96.6	1.6	1.7
64.08	1.71	1.59	32.62	95.7	1.7	2.6
62.19	1.76	1.22	34.83	96.1	1.8	2.1
63.01	1.92	1.66	33.41	95.3	2.0	2.8
62.12	1.29	3.68	32.91	92.6	1.3	6.1
64.15	1.57	2.22	32.06	94.8	1.6	3.6
55.91	6.66	2.11	35.32	89.1	7.2	3.7

5% sulfide minerals occur in planes sub-parallel to the Morning Star fault in the upper-plate where structurally higher mineralization occurs. The remainder of the unoxidized ore horizon contains less than 2% disseminated sulfide minerals, which generally consists solely of pyrite related to the propylitic alteration assemblage. The zonation of total sulfide minerals is open-ended down dip but the high sulfide zone (>5%) pinches out or grades down dip into the intermediate sulfide zone (2 to 5%) in the deepest levels of the ore horizon penetrated by exploration drill holes.

Within the tabular ore horizon the sulfide mineral assemblage exhibits a crude zonation that roughly parallels the Morning Star fault, but the lack of geochemical data for the Morning Star deposit prohibits a detailed outline of the metal zonation. Adjacent to the fault, within the high total sulfide and high grade ore zones, the sulfide mineral assemblage is essentially galena+pyrite. Although the galena+pyrite assemblage parallels the Morning Star fault and coincides with elevated ore grades it generally forms small pockets that pinchout both horizontally and down dip. The sulfide mineral assemblage galena+chalcopyrite+pyrite±sphalerite±tetrahedrite forms a tabular zone which contains the pockets of galena+pyrite and persists to higher structural levels and further down dip within the high grade ore horizon. At the highest levels of the high grade ore horizon the sulfide mineral assemblage consists of essentially sphalerite+pyrite±chalcopyrite. The zonation of sulfide mineral assemblages is consistent with metal zonation patterns outlined by the limited geochemistry described above. The zonation from Pb to Pb+Cu±Zn to Zn±Cu with higher structural levels in the Morning Star ore horizon is consistent with geochemistry in the Morning Star mine and from exploration drill holes in the Kewanee Hills area where a more extensive geochemical data set is available (see Byington 1988).

Primary hypogene electrum occurs with quartz and pyrite in unoxidized portions of the orebody. Gold mineralization is restricted to quartz±carbonate veins with abundant pyrite, galena and lesser chalcopyrite, sphalerite and minor argentite and tetrahedrite. Electrum occurs as fracture fill and inclusions with galena in pyrite and disseminated in base-metal sulfide and argentite-bearing quartz vugs (Chapter 4). The fineness of electrum deposited during primary mineralization ranges from 630 to 800 which is lower than the electrum deposited during the secondary stage of mineralization (described below). Electrum from the primary episode of mineralization was deposited during Stage 2 as inclusions and fracture fillings with galena within or on the surface of pyrite and in base-metal and argentite-bearing quartz vugs. Electrum appears to be introduced early in Stage 2 base metal sulfide mineral assemblage. Stage 3 electrum occurs as disseminated grains or filling late fractures and microvugs in quartz. Commonly stage 3 mineralization occurs with disseminated galena, but no other base-metal sulfide minerals are associated with this stage of mineralization.

Secondary Mineralization

Secondary mineralization only occurs within the oxidized upper levels of the Morning Star mine and consists mainly of goethite, digenite (±chalcocite), covellite, cerusite, smithsonite, malachite, azurite, acanthite, uytenbogaardtite and electrum in quartz±carbonate veins. Typically oxidation is not complete, so remnants of primary pyrite and base-metal sulfide minerals persist within various pseudomorphic minerals. Goethite occurs as pseudomorphs after pyrite and with digenite around chalcopyrite. Covellite and digenite (confirmed by x-ray diffraction) also formed as oxidation products of chalcopyrite. Many altered remnants of chalcopyrite are surrounded by course-

grained, bladed covellite aggregates. Digenite occurs with covellite only in pyrite-rich samples. Heavy-metal carbonates either form pseudomorphs after their precursor sulfide minerals or coat open fractures and joints. Goethite and malachite are the most common surface coatings. Covellite also forms surface coatings on open fractures and in quartz veins. These fractures typically crosscut the principal mineralized structures at a high angle. All covellite is blaubleibender (blue-remaining) covellite based on optical identification.

Covellite, digenite, acanthite, uytenbogaardtite and electrum formed during the early part of the secondary mineralization event. Covellite outlines vugs and fractures containing precious-metal mineralization, while covellite and digenite coexist in veins containing base-metal sulfide mineral remnants. Electrum occurs in goethite pseudomorphs after pyrite, in wire-like structures intergrown with acanthite, uytenbogaardtite and covellite, and as rims around primary electrum grains (Chapter 4). The fineness of secondary electrum ranges from 810 to 940 with an average of 850 fine. Electrum in or associated with goethite has two textures, one of which indicates no Au + Ag remobilization during oxidation and the other which suggests isochemical remobilization of Au + Ag during alteration of the primary mineral assemblage (Chapter 4). The composition of uytenbogaardtite from the Morning Star deposit appears to be enriched in sulfur and depleted in gold relative to uytenbogaardtite found in other deposits (Chapter 4 and Barton et al. 1979). Three to five weight percent Cu occurs in uytenbogaardtite from the Morning Star deposit and may be responsible for the apparent gold depletion and sulfur enrichment (Chapter 4). Primary electrum spatially associated with secondary mineralization is commonly rimmed by secondary electrum of higher fineness (Chapter 4). The difference in electrum fineness between the primary and

secondary episodes of mineralization is indicative of gold-enrichment during remobilization of Au + Ag from some primary electrum (Chapter 4).

Native bismuth laths were found around the electrum±acanthite±uytenbogaardtite +covellite mineral assemblage. The origin of the native Bi is unknown. A positive correlation exists between Cu, Mo, Pb, Bi, Ag, and Au in the high grade ore horizon. Based on the observations made above, the correlation between Cu, Bi, Ag, and Au may be due to pockets of secondary precious-metal-bearing mineralization with covellite and native bismuth laths. Ore microscopy and electron microprobe analyses have not distinguished any Mo-bearing mineral phases either in primary or secondary mineral assemblages, so the origin of these correlations remains unknown.

Fluid Inclusions

Preliminary fluid inclusion microthermometric data (Sheets et al. 1988; 1989) were obtained from euhedral quartz crystals that line vugs containing primary mineralization. No electrum or argentite was found in the particular vugs from which fluid inclusion data was obtained, but ore petrology correlates these vugs with the principal episode (stage 2) of precious-metal deposition (Figure 3.7). Base-metal mineralization post-dates quartz precipitation in the vugs studied, but other vugs contain sulfide mineral inclusions in the euhedral quartz (e.g. Figure 3.9A). Thus, the data presented here only constrain temperature and fluid composition for stage 2 mineralization.

Primary fluid inclusions occur along growth zones in the outer margins of euhedral quartz crystals that line vugs containing interstitial base-metal sulfides. Abundant small, less than 5 μm, fluid inclusions occupy quartz cores and occur as secondary and pseudosecondary planes of inclusions which cause the white coloration of the vein

quartz. No microthermometry has been conducted on these pseudosecondary and secondary inclusion types, but room temperature phase relations suggest the pseudosecondary and secondary inclusions contain fluids similar to those defined for the primary inclusions.

The primary inclusions studied range in size from 5 to 10 μm in the long dimension. Most primary inclusions have negative crystal to equant shapes and contain either two-phase or three-phases at room temperature. Three-phase inclusions contain an aqueous brine, liquid CO_2 and vapor CO_2 at 25°C, while two-phase fluid inclusions contain an aqueous brine and liquid CO_2 at 25°C. The two phase inclusions developed a CO_2 vapor phase upon cooling, but the CO_2 vapor homogenizes to the liquid between 30 to 31°C. Because the CO_2 homogenization temperatures are close to the critical temperature for pure CO_2 (31.06°C) , the two-phase inclusions may have separate liquid and vapor phases that are not easily distinguishable under the microscope until the inclusion is cooled. Room temperature phase relationships are the same for all inclusions studied with the exception of the absence of CO_2 vapor in the two-phase inclusions. Based on room temperature phase relations, primary fluid inclusions contain approximately 10 to 20 mole % CO_2.

Microthermometry was conducted on a modified USGS-type gas-flow heating-freezing stage calibrated with synthetic fluid inclusions containing pure H_2O and an H_2O-CO_2 mixture. Temperatures are accurate to within ±0.1°C of solid CO_2 melting to CO_2 homogenization temperatures and ±2.5°C for the critical point of water (373°C). Solid CO_2 and clathrate melting temperatures and CO_2 homogenization temperatures are reproducible to within ±0.1°C. Temperatures were cycled numerous times in order to enhance the visibility of clathrates and when approaching the melting temperature of clathrates and the homogenization temperature of CO_2. Total homogenization

Table 3.3. Fluid Inclusions Microthermometry

Tm CO_2 (°C)	Tm clathrate (°C)	Th CO_2 (°C)	Th total (°C)	Salinity wt.% NaCl eq.
-56.6	6.7	30.8		6.29
-56.9	6.6	30.8	305.4	5.46
-56.6	6.7	30.8		6.29
-56.8	6.8	30.8		6.12
-56.7	7.1	30.1	295.6	5.59
-56.8	6.8	30.8		6.12
-56.7	6.8	30.3		6.12
-56.6	7.0	30.6	291.5	5.77
-56.7	6.8	30.3		6.12
-56.7	7.1	30.1	297.4	5.59
-56.7	7.0	30.6	293.8	5.77
-56.8		30.5	298.2	
-56.6	6.7	30.3	284.5	6.29
-56.8		30.5	299.5	
-56.9	6.6	30.8	286.7	6.46
-56.6	6.7	30.3	280.6	6.29
-56.7	6.7	30.5	283.2	6.29
-56.7		30.4		
-56.6	6.9	30.1	301.2	5.94
-56.7	6.7	30.5	281.3	6.29
-56.7		30.4		
-56.6	6.9	30.1	303.9	5,94
-56.6	6.8	30.8	301.5	6.12
-56.7	6.8	30.6		6.12
-56.6		30.4		
-56.6	6.8	30.8	304.1	6.12
-56.6		30.3		
-56.7	6.8	30.6		6.12

Figure 3.10. Histograms of fluid inclusions melting and homogenization temperatures.

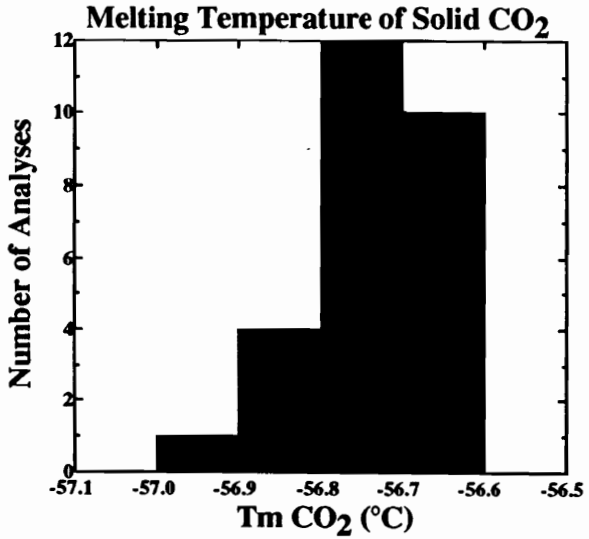
Melting Temperature of Solid CO_2
Number of Analyses
0
2
4
6
8
10
12
-57.1
-57.0
-56.9
-56.8
-56.7
-56.6
-56.5
Tm CO_2 (°C)

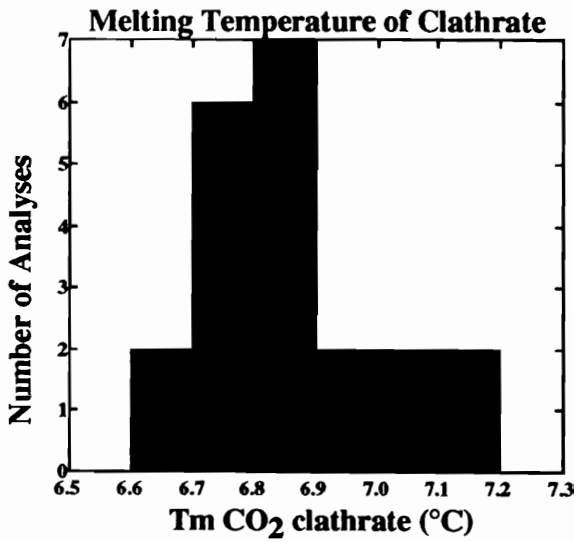
Melting Temperature of Clathrate
Number of Analyses
0
1
2
3
4
5
6
7
6.5
6.6
6.7
6.8
6.9
7.0
7.1
7.2
7.3
Tm CO_2 clathrate (°C)

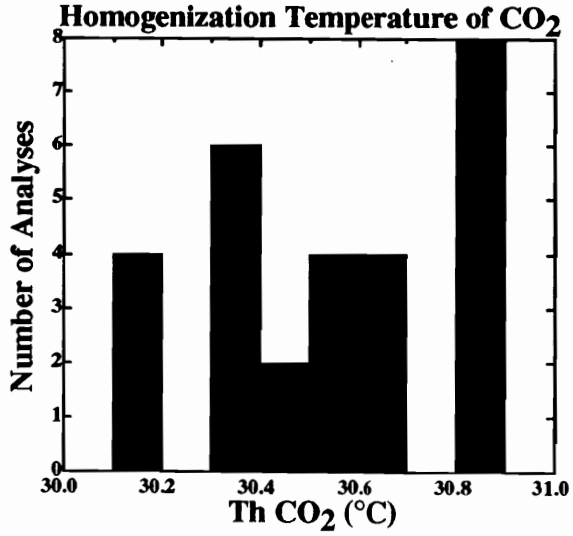
Homogenization Temperature of CO_2
Number of Analyses
0
1
2
3
4
5
6
7
8
30.0
30.2
30.4
30.6
30.8
31.0
Th CO_2 (°C)

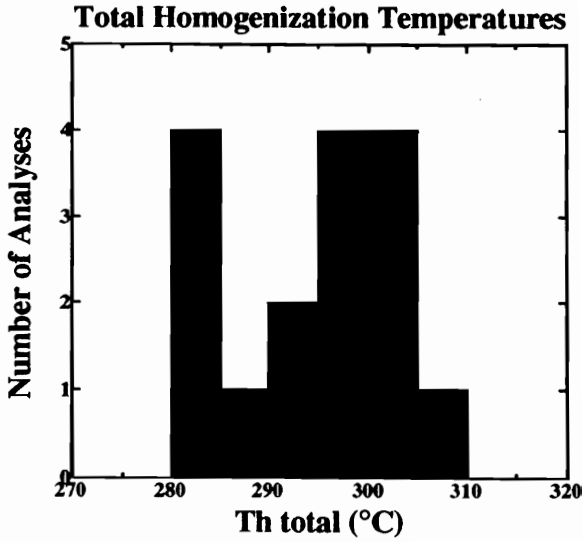
Total Homogenization Temperatures
Number of Analyses
0
1
2
3
4
5
270
280
290
300
310
320
Th total (°C)

temperatures are reproducible to within ±3.0°C. The results of microthermometric measurements are presented in Figure 3.10 with data given in Table 3.3.

CO_2 solid melting temperatures range from -56.9 to -56.6°C which is essentially the same as the triple point of pure CO_2 (-56.6°C). CO_2 clathrate melting temperatures in the presence of CO_2 vapor and H_2O and CO_2 liquid range from 6.6 to 7.1°C which corresponds to a salinity of 6.5 to 5.6 wt. % NaCl eq. using the equation of Bozzo et al. (1975). CO_2 homogenizes to the liquid phase between 30.1 and 30.8°C. Total homogenization was difficult to measure because many of the larger inclusions, 10 μm or greater, decrepitated prior to total homogenization. Decrepitation prior to homogenization occurs when the internal pressure of the fluid inclusion exceeds the yield strength of quartz at 1 atmosphere pressure. For smaller inclusions, total homogenization is to the aqueous brine in the temperature range 280 and 305°C. Decrepitation generally occurred in the temperature range 260 and 285°C. After heating samples to total homogenization, the sample were slowly cooled to room temperature and then the CO_2 homogenization temperature was redetermined. All redeterminations of CO_2 homogenization temperatures for intact fluid inclusions yielded temperatures within ±0.1°C of the initial CO_2 homogenization temperatures. These checks on the CO_2 homogenization temperatures suggest that inclusions did not leak or stretch during initial total homogenization determinations.

A number of important results can be obtained form the limited number of fluid inclusion microthermometry data. Primary fluid inclusions have consistent phase ratios at room temperature and a restricted range of melting and homogenization temperatures. The similar phase relations and restricted temperature ranges imply a single population of fluid inclusions was trapped above the H_2O-CO_2-6 wt.% NaCl solvus, but additional fluid inclusion research is required to determine how fluids changed during the evolution

of the Morning Star deposit. Thus, early mineralizing fluids can adequately be defined as H_2O-CO_2-6 wt.% NaCl with a minimum trapping temperature of 280°C for formation of the vuggy quartz and possibly the enclosed base- and precious-metal mineralization.

Lead Isotopes

The lead isotopic framework has been determined for the Early Proterozoic continental crust and Mesozoic intrusions throughout the Mojave Desert (Wooden et al. 1988; Wooden and Miller 1990). Much of the data for intrusions in the northeastern Mojave Desert is from plutonic phases of the Teutonia Batholith (Wooden et al. 1988). Because of the extensive lead isotope framework for the area, lead isotopes provide information concerning the origin of lead, and possibly gold and silver, at the Morning Star deposit. Three samples of sulfides from the high grade ore horizon within two meters of the Morning Star fault and an additional sulfide sample from the mine dump at the Sunnyside decline were analyzed for lead isotopes by Ririe (1988). The results of Ririe's Pb isotopes analyses for the Morning Star and Sunnyside samples are shown on Figure 3.11 along with the Pb isotope analyses of feldspars from Jurassic and Cretaceous intrusive phases of the Teutonia batholith (Wooden et al. 1988). These lead isotope analyses are compared to the trends established for the Mojave and Arizona Desert Precambrian crystalline basement of Wooden and Miller (1990). Also plotted on Figure 3.11 is a single Pb isotope analyses of galena from the Death Valley Ag deposit in the New York Mountains (Zartman 1974) which is hosted by Precambrian crystalline rocks (Ntiamoah-Agyakwa 1987).

The Morning Star and Sunnyside lead isotope ratios are consistent with enrichment of thorium-derived lead and depletion in uranium-derived lead (Ririe 1988). Lead isotope

Figure 3.11. Summary plots of lead isotope ratios for the northeastern Mojave Desert. The upper diagram illustrates the U-derived lead isotope ratios and the lower diagram illustrates the Th-derived lead. The diagrams plot the lead isotope values of sulfide minerals from the Morning Star area from Ririe (1988) and the Death Valley deposit from Zartman (1974). Also plotted on each diagram is the lead isotope ratio trends for Early Phanerozoic crystalline basement in the Mojave and Arizona Deserts (Wooden and Miller 1990) and lead isotope analyses of feldspars from Jurassic and Cretaceous plutons of the Teutonia batholith (Wooden et al. 1988).

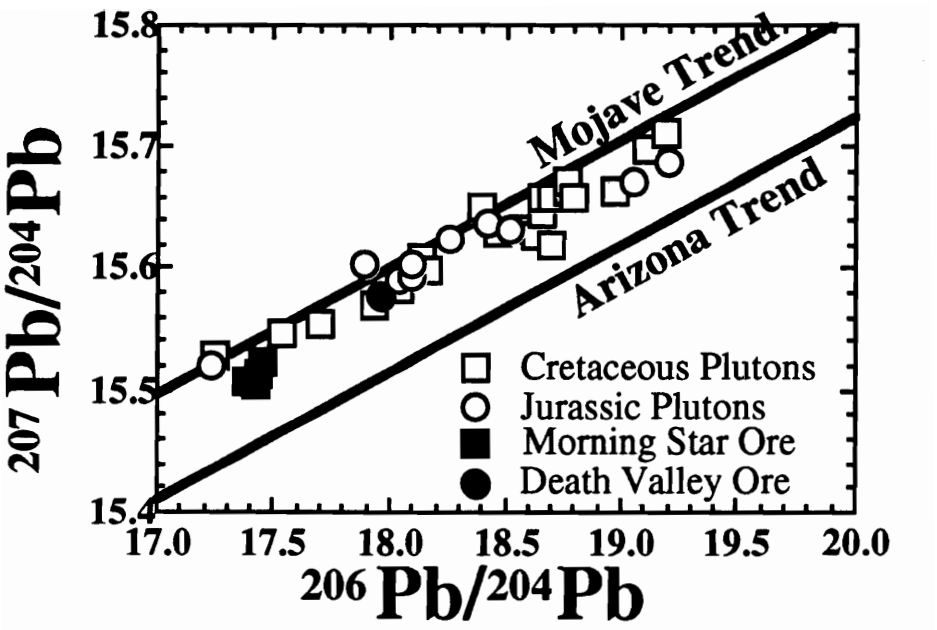
15.8
15.7
15.6
15.5
15.4
17.0
17.5
18.0
18.5
19.0
19.5
20.0
207Pb/204Pb
206Pb/204Pb
Mojave Trend
Arizona Trend
Cretaceous Plutons
Jurassic Plutons
Morning Star Ore
Death Valley Ore

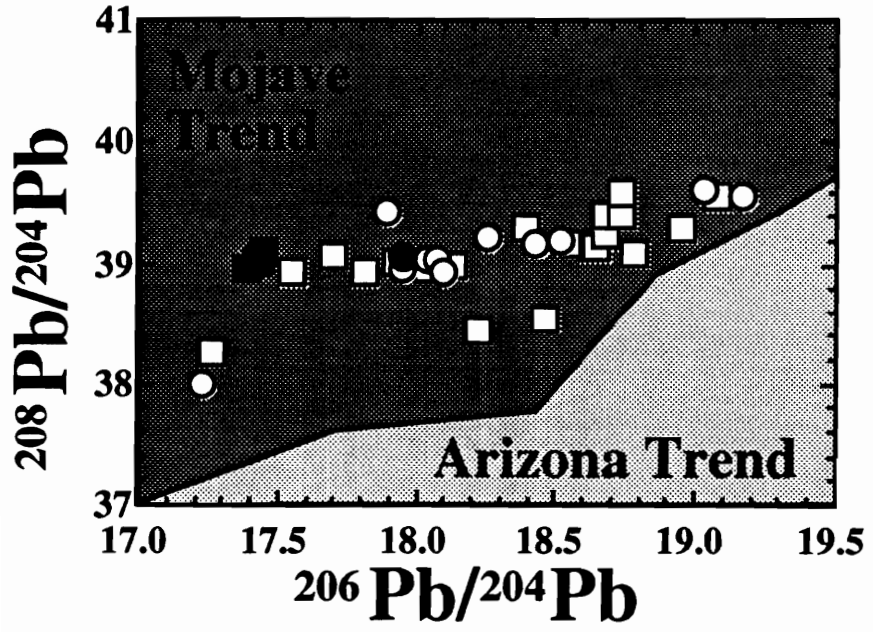
41
40
39
38
37
17.0
17.5
18.0
18.5
19.0
19.5
208Pb/204Pb
206Pb/204Pb
Mojave Trend
Arizona Trend

ratios for Jurassic-Cretaceous intrusions of the Teutonia batholith are derived from thorium-enriched and uranium-depleted Precambrian crystalline basement (Wooden et al. 1988; Wooden and Miller 1990). Lead isotope ratios of the Morning Star and Sunnyside samples are remarkable uniform and generally less radiogenic than the host Mesozoic intrusions (Figure 3.11), which implies Pb, and possibly other metals, were derived from plutonic phases of the Teutonia batholith. Alternatively, because the Teutonia batholith is ultimately derived from melting of the Precambrian basement, the Pb in the Morning Star and Sunnyside sulfide minerals may be derived form the crystalline basement. The latter interpretation is supported by mineralization hosted by Precambrian crystalline rocks at the Death Valley deposit in the New York Mountains (Ntiamoah-Agyakwa 1987) and Sulfur Queen deposit in the Clark Mountains (Olsen 1954).

Physicochemical Conditions of Mineralization

The petrology and geochemistry of the Morning Star deposit can be used to place limits on some environmental parameters for mineralization. Fluid inclusion and mineral geothermometers can be used to establish formation temperatures for the Morning Star deposit. The results of limited fluid inclusion microthermometry on vuggy quartz around stage 2 mineralization indicate a minimum formation temperature of 280°C (see above; Sheets et al. 1988; 1989).

The temperature of precious-metal mineralization can also be obtained from the silver content of electrum in equilibrium with argentite at a known sulfur activity (Barton and Toulmin, 1964). Additionally, the FeS content of sphalerite in equilibrium with pyrite can yield formation temperatures at a known sulfur activity (Barton and Toulmin, 1966; Scott and Barnes, 1971). For the assemblage electrum-argentite-sphalerite-pyrite,

Shikazono (1985) has combined these two techniques to eliminate the unknown variable, sulfur activity, and determine the formation temperature. The assemblage electrum-argentite-sphalerite-pyrite occurs with galena in vuggy quartz pockets deposited during stage 2 mineralization at the Morning Star deposit. These vugs are similar to quartz vugs from which fluid inclusion data were collected. Analytical procedures for electrum and sphalerite microprobe analyses are similar to those given in Chapter 4. Electrum composition for this assemblage ranges in XAg from 0.42 to 0.49, and the FeS content of sphalerite varies from 0.2 to 6.1 mole percent (Table 3.4). The temperature of mineralization, calculated using equations 6 and 7 of Shikazono (1985), range from 284 to 329°C and 266 to 314°C, respectively (Table 3.4). Two coexisting sphalerite-electrum pairs have anomalously low FeS and high CdS contents for sphalerite. The temperatures calculated for these anomalous sphalerites are considerably lower than the other calculated temperatures, so these anomalous data were not considered in the temperature ranges cited above. These temperature calculations also assume the mole fraction of FeS in sphalerite is independent of the CdS mole fraction and that the CdS content of sphalerite has no temperature effect (see Craig and Scott, 1974).

Mineralization temperatures for the precious-metal-bearing vug fillings agree well with fluid inclusion homogenization temperatures for quartz surrounding these vugs. The temperatures for mineralization are generally the same to slightly higher than fluid inclusion homogenization temperatures which is consistent with trapping of a single, homogeneous population of fluid inclusions above the H_2O-CO_2-6 wt.% NaCl solvus. This temperature difference is to be expected as fluid inclusions only record a minimum temperature of formation unless corrected for formation pressure.

Using the estimated formation temperatures together with ore mineral assemblages, alteration assemblages and mineral chemistry, it is possible to place some additional

Table 3.4. Sphalerite-Pyrite-Argentite-Electrum Temperature Calculations.

X_{FeS} in Sph	X_{Ag} in Electrum	eq 6[1] T (K)	eq 6[1] T (°C)	eq 7[1] T (K)	eq 7[1] T (°C)
0.024	0.448	585.24	312.10	569.44	296.29
0.024	0.448	585.35	312.20	569.55	296.40
0.024	0.452	583.82	310.67	567.90	294.75
0.002	0.441	497.80	224.65	478.37	205.22
0.023	0.430	591.49	318.34	576.21	303.06
0.023	0.468	574.15	300.10	557.55	284.40
0.009	0.461	543.11	269.96	525.09	251.94
0.016	0.477	556.90	283.75	539.33	266.18
0.019	0.472	566.24	293.09	549.19	276.04
0.017	0.438	576.40	303.25	560.21	287.06
0.026	0.419	601.75	328.60	587.17	314.02
0.021	0.475	567.78	294.63	550.77	277.62
0.028	0.481	576.38	303.23	559.77	286.62
0.061	0.492	603.50	330.35	588.38	315.23
0.036	0.466	593.47	320.32	577.96	304.81
0.037	0.460	597.31	324.16	582.10	308.95

[1] equations from Shikazono (1985)

Figure 3.12. A) An activity of sulfur verses temperature mineral stability diagram showing the relationship between primary and secondary mineralization.

B) An activity of oxygen verses activity of sulfur mineral stability diagram showing the fields of early (stage 1) pyrite-bearing veins and the bulk of the mineralization (stage 2).

C) Activity-activity relations for the system Na_2O-K_2O-Al_2O_3-SiO_2-H_2O.

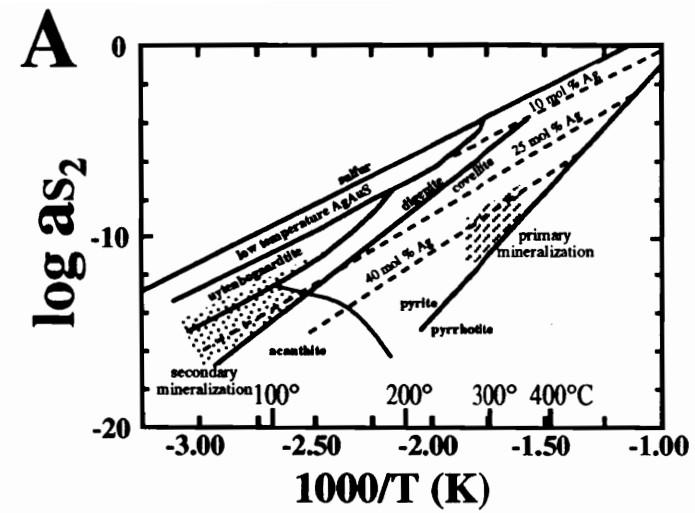
A
log as2
0
-10
-20
-3.00
-2.50
-2.00
-1.50
-1.00
1000/T (K)
100°
200°
300°
400°C
sulfur
low temperature AgAuS
10 mol % Ag
25 mol % Ag
40 mol % Ag
primary mineralization
pyrite
pyrrhotite
acanthite
secondary mineralization

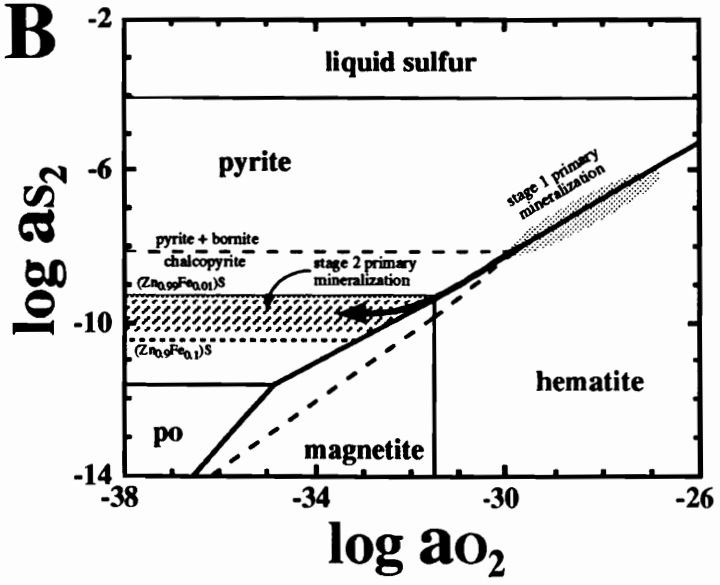
B
log as2
-2
-6
-10
-14
-38
-34
-30
-26
log ao2
liquid sulfur
pyrite
pyrite + bornite
chalcopyrite
(Zn0.99Fe0.01)S
(Zn0.9Fe0.1)S
stage 1 primary mineralization
stage 2 primary mineralization
hematite
po
magnetite

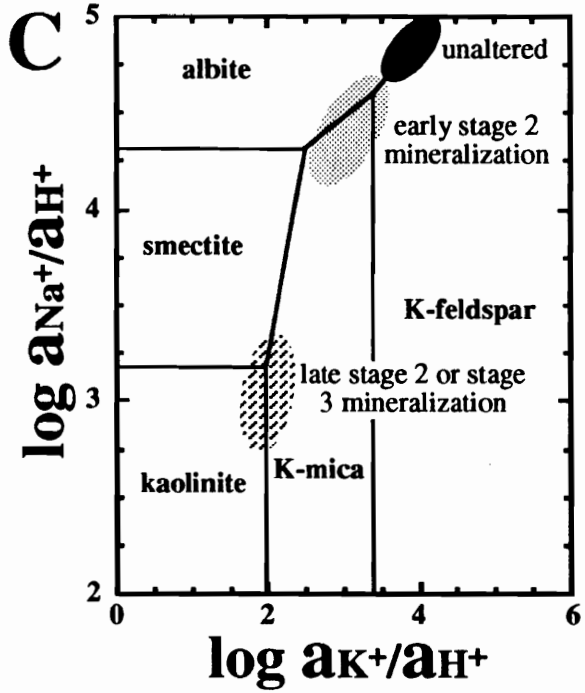
C
log aNa+/aH+
5
4
3
2
0
2
4
6
log aK+/aH+
albite
unaltered
early stage 2 mineralization
smectite
K-feldspar
late stage 2 or stage 3 mineralization
kaolinite
K-mica

constraints on the environment of deposition for the primary and secondary episodes of mineralization (Figure 3.12). The ubiquitous presence of pyrite with electrum containing 38 to 55 mole percent Ag and sphalerite with 0.2 to 6.1 mole percent FeS (Figure 3.12A) constrains the activity of sulfur for primary mineralization to between 10^{-8} to 10^{-11}. The activity of sulfur for secondary mineralization is constrained by covellite, uytenbogaardtite, acanthite and electrum containing 18 to 27 mole percent Ag to be less than 10^{-14}.

The occurrence of stage 1 pyrite-bearing veins with hematite constrains the activity of oxygen during early vein formation to be between 10^{-27} to 10^{-30} (Figure 3.12B) Stage 2 mineralization is constrained to be less then 10^{-32} based on the assemblage pyrite-chalcopyrite-sphalerite containing 0.2 to 6.1 mole percent FeS. The change in mineralogy from stage 1 to stage 2 indicates a decrease in both the activity of oxygen and sulfur

The alteration assemblage may also be used to place constraints on the evolution of hydrothermal fluids (Figure 3.12C). Changes from unaltered rock and propylitic alteration to sericitic alteration and finally to argillic alteration requires a decrease in both Na^+/H^+ and K^+/H^+ (Figure 3.12C). Na_2O is depleted in the fault zone and upper-plate rocks containing the high-grade ore zone, but K_2O shows little change across the zone of alteration (Chapter 2). Thus the decrease in Na^+/H^+ and K^+/H^+ probably also reflects a decrease in pH. The feldspar hydrolysis reaction

$$3\ \text{K-feldspar} + 2\ H^+(aq) = \text{muscovite} + 6\ \text{quartz} + 2\ K^+(aq)$$

has a pH of 6.2 for a 1 molal solution with a K^+ concentration of 0.01 at 280°C. Neutral pH occur at 5.5 for the temperature of 280°C (Henley and Brown 1985), therefore pH of the sericitic alteration at the Morning Star deposit is near neutral. Under the same conditions, the equation

$$3 \text{ muscovite} + H^+(aq) + {}^3/_2\, H_2O = {}^3/_2 \text{ kaolinite} + K^+(aq)$$

occurs at a pH of 4.6. Near neutral to acidic pH conditions are indicated for primary mineralization based on the wall rock alteration assemblages. The trend from sericitic to argillic alteration implies that fluids become more acidic during progressive mineralization and alteration. Secondary mineralization appears to be associated with supergene processes which took place under near neutral to alkaline conditions (Chapter 4). Alternatively, the occurrence of kaolinite and montmorillonite in the alteration assemblage at the upper levels of the deposit suggests the involvement of acidic late stage hydrothermal fluids.

Discussion

Two episodes of mineralization occurred at the Morning Star deposit and these two episodes formed under distinctly different conditions. Primary hypogene mineralization consists of base- and precious-metal minerals deposited at temperatures between 280 to 330°C. Early pyritic quartz veins (stage 1) exhibit ductile deformation and main-stage base- and precious-metal mineralization (stage 2) exhibits evidence of early brittle deformation. Both of these textures indicate that the initial mineralization was syn-tectonic. The bulk of the base- and precious-metal mineralization (stage 2 and 3) fills open spaces, and therefore, mineralization continued after deformation on the Morning Star fault system ceased.

The origin of hydrothermal fluids and timing of fluid migration within the Morning Star deposit is not well constrained. Faulting took place between 105 and 90 Ma based on crosscutting plutons (Chapter 1). Syn-tectonic ore textures suggest the initial stages of mineralization occurred at this time, but the bulk of the mineralization is post-tectonic and

may have formed at a later time. The CO_2 content of fluid inclusions associated with the primary mineralization indicate a deep fluid source, possibly from a metamorphic origin. Metamorphic rocks, outside the Precambrian crystalline basement, only occur in the northeast portion of the New York Mountains (Burchfiel and Davis 1977). Therefore, the Ivanpah Mountains are underlain by crust which was subjected to regional metamorphism, it is unlikely the CO_2 content of fluid inclusions an be attributed to a metamorphic source. Alternatively the CO_2 content of fluid inclusions may be produced by interaction of hydrothermal fluids with the sequence of Paleozoic carbonate rocks which surrounds the Ivanpah Mountains. The Ivanpah granite intruded a thick section of Paleozoic miogeoclinal and platform sedimentary rocks which are predominately carbonate rocks (Burchfiel and Davis 1971). However, the only carbonate rocks which crop out in the vicinity of the Morning Star deposit is an altered roof pendant in the Kewanee Hills area (Figure 4.1). The thick section of carbonate rocks in the New Trail Canyon area dip 35° to the west below the contact with the Ivanpah granite (Chapter 1; Burchfiel and Davis 1971). Deeply circulation hydrothermal fluids which migrated up the Morning Star fault system may have interacted with this sequence of carbonate rocks.

Syn-tectonic fluids probably migrated up the thrust fault via a seismic pumping mechanism (e.g. Sibson, 1987; Sibson et al., 1988) because of the repeated episodes of brittle deformation. The structurally controlled mineralization and wall rock alteration assemblages suggest the fault plane and upper-plate structures acted as major channel ways for fluid migration. Initial thrusting caused mylonite formation and multiple episodes of later brittle deformation developed cataclastic zones and breccias. Fault gouge along the Morning Star fault formed by episodic alteration of fault rocks to argillic and sericitic assemblages (Chapter 2). Development of a thick fault gouge during brittle thrusting and hydrothermal alteration formed an aquatard which restricted fluid flow to

the upper-plate and prevented mineralization in lower-plate rocks (Logen and Decker 1994). Post-tectonic fluids would only migrate though the dilatant zones formed by brittle deformation in the upper-plate rocks. Weak mineralization along the Sunnyside structure and in the Kewanee Hills area was caused by additional fluids migrating along these structures.

Alternatively, the Morning Star deposit may have formed at depth and been thrust into place by movement along the Morning star fault system. Pre-tectonic mineralization faulted into the present configuration would explain why mineralization is confined to the upper-plate rocks. Although an attractive hypothesis, pre-tectonic formation of the Morning Star deposit does not account for the observed ore textures and spatial distribution of alteration assemblages. No mineralization was detected in mylonitic rock and fault gouge, except where the fault rocks are cut by later veins. Pre-tectonic ore formation that was faulted into the present configuration would require at least minor amounts of cataclastically deformed and sheared mineralization in fault generated rocks. Secondly, most of the main base- and precious-metal mineralization (stage 2 and 3) was deposited as open space fillings and shows no textures indicative of later deformation. Ore formed prior to faulting should be deformed throughout the deposit because of the abundant shear zones and brittle fractures. Also propylitic alteration surrounds the deposit in both the upper- and lower-plate rocks which implies early fluid migration along the fault zone. Therefore, the bulk of the mineralization at the Morning Star deposit could not have formed prior to tectonic activity and subsequently been faulted into place. The restriction of ore to the upper-plate rocks is most likely related to an increased amount of fracturing which was caused by decreasing confining pressures in the upper-plate rocks relative to the lower-plate rocks during thrusting.

Stage 1 of the primary episode of mineralization occurred at a relatively higher activity for O_2 and S_2, and the main stage (stage 2) of base- and precious-metal mineralization precipitated at a relatively lower activity of O_2 and S_2. The pH conditions also appear to decrease from early propylitic alteration associated with early pyrite-bearing quartz veins to sericitic and argillic alteration associated with the main stage of mineralization. Alteration assemblages suggest a further reduction in pH as the sericite-dominated alteration converts to kaolinite-dominated alteration. The mechanism for base- and precious-metal transport and deposition at the Morning Star deposit are not adequately understood, but some inferences can be made from the activities of O_2, S_2 and H^+. Base metals are typically transported in solution as chloride complexes and precious metals are transported as bisulfide complexes at 300°C (Barnes 1979). Because base-and precious-metal mineralization are intimately intergrown in the Morning star deposit, any mechanism for deposition must destabilize both bisulfide and chloride complexes simultaneously. Base-metal deposition from near neutral alkali-chloride fluids occurs by various mechanisms which include, but are not restricted to, an increase in pH, reduction of the fluid and decrease in temperature or pressure (Barnes 1979). The general solubility reaction for gold can be written:

$$Au + (x/2)O_2(g) + xH^+ + mL^{-n} = AuL_m^{+(x-mn)} + (x/2)H_2O$$

where x depends on the gold oxidation state [Au(I) or Au(III)] and L^{-n} is the complexing agent. At a constant temperature, pressure and pH, as the oxygen activity drops any gold complex will become less stable relative to free gold so deposition will occur. If gold is transported as a bisulfide complex, a decrease in the pH will also cause deposition of gold metal (Barnes 1979). A decrease in oxygen activity due to wall rock reaction would also precipitate base-metal sulfides such as galena, chalcopyrite and sphalerite. Therefore the

reduction of near neutral to slightly acidic fluids would account for the precipitation of both base- and precious-metal mineralization at the Morning Star deposit.

The mineralogy and geochemistry of the Morning Star deposit is consistent with the base-metal rich portions of a typical epithermal deposit (Berger and Eimon 1983; Hayba et al. 1985; Silberman and Berger 1985). Epithermal deposits commonly contains bonanza Au and Ag ore in a low sulfide, silicified, stockwork system surrounded by argillic alteration which overlies a feeder vein system containing abundant quartz and base-metal sulfides in sericitic and propylitic altered host rocks (e.g. Berger and Eimon 1983). The main stage (stage 2) of Morning Star mineralization contains Au and Ag with abundant base-metal sulfides in quartz veins. Stage 2 mineralization is surrounded by sericite alteration and deeper levels of the deposit contain abundant feldspar and muscovite in the gouge zone (Chapter 2), all of which is enclosed in a peripheral zone of propylitic alteration. Late mineralization (stage 3) contains precious-metal mineralization associated with argillic alteration.

Preliminary trace element geochemistry, particularly Cu and Mo, suggests an affinity between the Morning Star mineralization and porphyry copper-molybdenum type mineralization. Ntiamoah-Agyakwa (1987) described sub-economic porphyry Cu-Mo mineralization with variable amounts of Pb, Zn and Ag centered around a dike swarm adjacent to the New York Mountain thrust fault in the New York Mountains. Also the Kessler Springs adamellite intruded into the Ivanpah Mountains at 90 Ma and cuts the northern extension of the Morning Star thrust fault. Either of these intrusions, which are spatially related to the Morning Star fault and deposit, may have contributed the Cu and Mo to the hydrothermal system which formed the Morning Star deposit. Pb isotope data from Morning Star mineralization (Ririe, 1988), Teutonia Batholith plutonic phases (Wooden et al. 1988) and Precambrian crystalline basement complex (Wooden and Miller

1990) suggest Pb, and possibly other metals, were derived from the Mesozoic intrusions which were ultimately derived from the crystalline basement. The Kessler Springs intrusion, and possibly younger intrusions of the Teutonia batholith, may have only acted as the heat source that produced the hydrothermal circulation system. Metals were leached from the Ivanpah granite host rocks by the circulating hydrothermal fluids. Skarn type Cu and Sn-W mineralization occurs around the Ivanpah Mountains associated with intrusion of the Ivanpah granite (Hewett 1956; Evans 1971; 1974; Weisenberg 1973) which confirms the possibility of the Ivanpah granite as the source of some metals. These skarns contain Au and Ag bi-product mineralization (Hewett 1956), which implies the granitic host rocks could be the source of at least some of the precious-metals. Regional circulation of hydrothermal fluids may also have scavenge metals from the surrounding Precambrian crystalline rocks which also contain small deposits with historical production of gold and silver (Olsen 1954; Ntiamoah-Aqyakwa 1987)

Secondary mineralization consists of precious-metal minerals with the oxidation products of primary minerals. Because secondary mineralization and oxidation coincides with the position of a perched water table, secondary mineralization is believed to be of a supergene origin. See Chapter 4 for further discussion on the possible origins for the secondary episode of mineralization. Gold and silver remobilization during the secondary episode of mineralization has enhance ore grades in upper levels of the deposit.

Summary and Conclusions

Base- and precious-metal mineralization at the Morning Star deposit forms a ovoid lens-shaped orebody that occurs in the upper-plate of the eastward dipping Morning Star thrust fault. Two distinct episodes of mineralization, both containing electrum, have been

defined. The primary episode of mineralization was deposited at temperatures between of 280 and 330°C from a H_2O-CO_2-6 wt. % NaCl fluid. Early primary mineralization was syn-tectonic, but the bulk of the primary mineralization followed deformation along the Morning Star fault and was deposited in open fractures and vugs. Metals were likely scavenged from the host intrusion, and other intrusive phases of the Teutonia batholith, and Precambrian crystalline rocks. The metals were transported up the Morning Star fault and precipitated in the fractured upper-plate rocks by reduction of the fluid due to wall rock interaction. The ore grades of the deposit were subsequently enhanced by the remobilization of gold and silver during the secondary episode of mineralization. Secondary mineralization coincides with a perched water table and thus probably resulted form supergene processes.

Chapter 4

Composition and Occurrence of Electrum at the Morning Star Deposit, San Bernardino County, California: Evidence for Remobilization of Gold and Silver

Abstract

Electrum (Au,Ag), acanthite (Ag_2S) and uytenbogaardtite (Ag_3AuS_2) have been examined from six depths within the tabular quartz±calcite stockwork and breccia-filled veins in the fault-zone-hosted Morning Star deposit of the northeastern Mojave Desert, California. Six distinct types of electrum have been identified on the basis of mineral association, grain morphology and composition. Two types, (1) pyrite-hosted and (2) quartz-hosted electrum, occur with acanthite after argentite and base metal sulfide minerals in unoxidized portions of the orebody; and the remaining four types, (3) goethite-hosted electrum, (4) electrum cores, (5) electrum rims and (6) wire electrum, are associated with supergene minerals in its oxidized portions. Pyrite-hosted, quartz-hosted and goethite-hosted electrum ranges in composition from 61 to 75 wt.% Au and have uniform textures and no zoning. In lower portions of the oxidized ore zone, electrum seems to replace goethite and occurs as small grains on surfaces of goethite. Textural evidence favors supergene remobilization of Au and Ag, which were deposited as secondary electrum on or replacing goethite. This type of electrum is identical in appearance and composition to primary electrum. In the upper portions of the oxidized

zone, secondary electrum occurs as a gold-rich rim on a core of electrum and as wire-like grains, both with acanthite and uytenbogaardtite. Such secondary electrum contains between 78 and 93 wt.% Au. Textural relations and associated minerals suggest that primary electrum was hydrothermally deposited and partially remobilized by supergene processes.

Introduction

Chemical models to describe the distribution of gold and silver minerals between oxidized and unoxidized portions of gold deposits remains equivocal for many deposits. Gold and silver remobilization by low-temperature oxidizing groundwater is suggested as an important supergene process leading to secondary enrichment of some precious-metal deposits (Emmons 1912, Boyle 1968, 1978, Larkin et al. 1974). Also, waning-stage hydrothermal activity may remobilize gold and silver (Barton et al. 1978). Increased fineness of electrum during mineralization is commonly cited as evidence for remobilization of gold and silver (Emmons 1912, MacKay 1944, Koshman & Yugay 1972), but recent studies (Mann 1984, Stoffregen 1986) convincingly argue for remobilization of gold and silver without an increased fineness of the deposited electrum in certain chemical environments. Other investigators have suggested that supergene remobilization of gold and silver may actually lead to a decrease in fineness of the electrum in specific circumstances (Webster & Mann 1984).

Other minerals of gold and silver may be produced during late-stage hydrothermal or supergene oxidation of precious-metal deposits. For example, uytenbogaardtite (Ag_3AuS_2), a rare silver-gold sulfide, has been reported in a small number of deposits, where it occurs as a late-stage hydrothermal or supergene phase (Barton et al. 1978,

Dunn et al. 1985, Castor & Sjoberg 1993). Uytenbogaardtite has recently been identified in the upper levels of the Morning Star deposit (Sheets et al. 1988, 1989). Stability relationships for uytenbogaardtite, acanthite and electrum in the supergene environment are not currently available, but 100°C hydrothermal equilibria predict the formation of uytenbogaardtite and acanthite by sulfidation of electrum (Barton 1980).

This paper describes the distribution and chemistry of precious-metal mineralization in the vicinity of the Morning Star deposit and places constraints on conditions attending gold and silver remobilization. As previously stated, the remobilization of gold and silver may occur either with an increase in fineness of electrum (Mann 1984) or with a constant or slightly decreasing fineness (Webster & Mann 1984, Stoffregen 1986). The Morning Star deposit is unusual in that textural and chemical evidence support both trends in the composition of electrum, at different levels within the oxidized horizon.

Location and History

The Morning Star deposit is located on the southeastern flank of the Ivanpah Mountains, northeastern Mojave Desert, California, approximately 100 km southwest of Las Vegas, Nevada (Figure 4.1A). Proven reserves at the Morning Star mine, in 1987, were approximately 7.3 million metric tons of ore averaging 2.057 g/tonne (Ausburn 1988). The mine was operated intermittently in this century, with the last episode of mining occurring from 1987 to mid-1991; heap leach extraction of gold and silver continues today. Additional subeconomic precious-metal mineralization occurs throughout a series of prospect pits in the Kewanee Hills area south of the mine and along the Sunnyside fault to the west of the mine (Figure 4.1B).

Figure. 4.1. Generalized geology and mineralization of the Morning Star mine area A. Location map. B. Geological map of the southeastern Ivanpah Mountains and Kewanee Hills areas showing the location of the seven gold-bearing samples analyzed in this study. C. Schematic cross-section of the northern portion of the Morning Star orebody. This east-west cross section contains drill holes MSE-23 and MSE-87-04. All other sample locations are plotted as points projected along the Morning Star fault at the appropriate elevations. Sample K-Hills is from a surface sample from the Kewanee Hills incline, south of the Morning Star mine, and is plotted on the cross-section according to its elevation and distance from the Morning Star fault. See text for further discussion of the geology and sample descriptions.

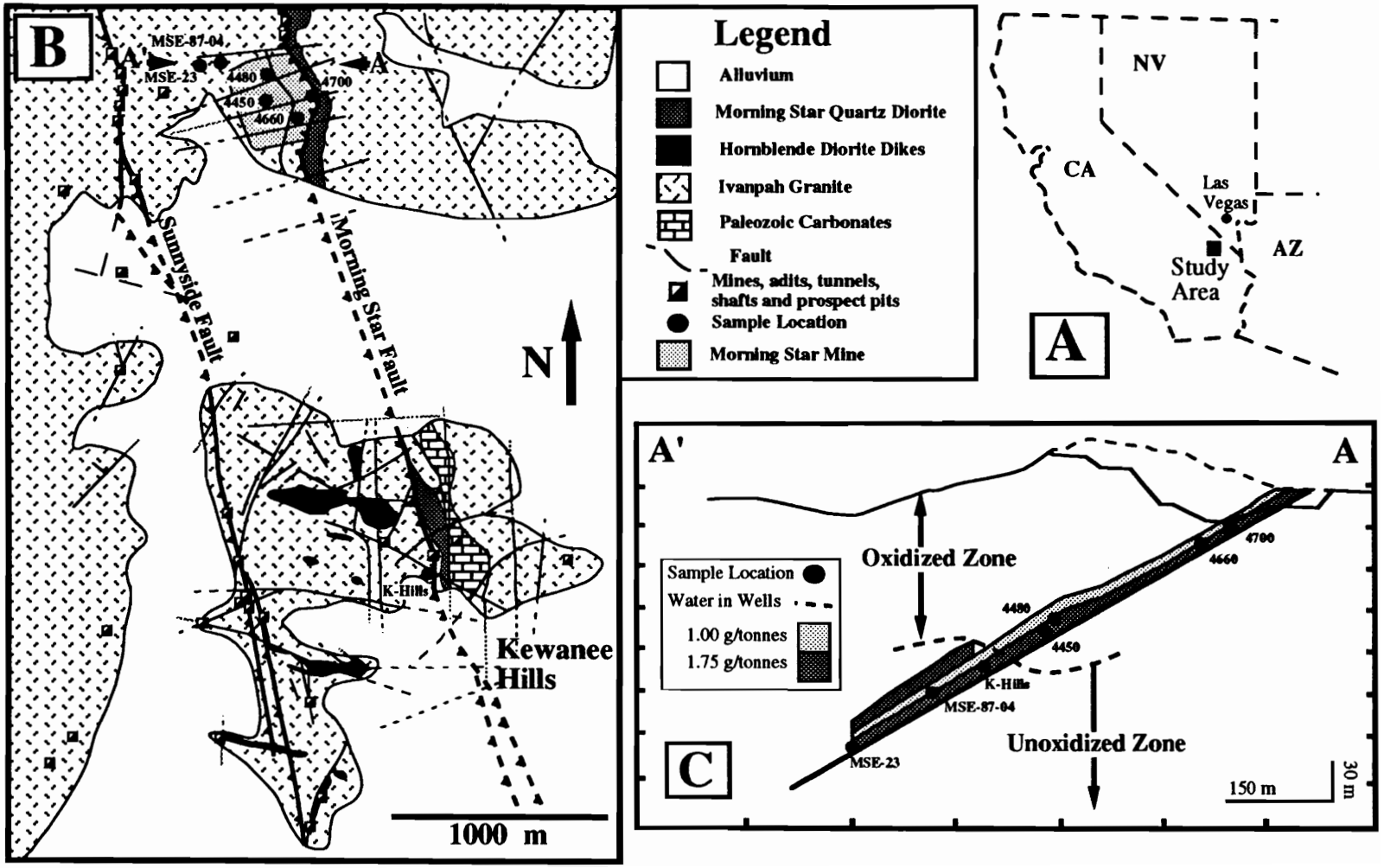
B
MSE-87-04
A'
MSE-23
4480
4700
4450
4660
A
Sunnyside Fault
Morning Star Fault
N
K-Hills
Kewanee Hills
1000 m
Legend
Alluvium
Morning Star Quartz Diorite
Hornblende Diorite Dikes
Ivanpah Granite
Paleozoic Carbonates
Fault
Mines, adits, tunnels, shafts and prospect pits
Sample Location
Morning Star Mine
NV
CA
Las Vegas
AZ
Study Area
A
A'
A
Oxidized Zone
Sample Location
Water in Wells
1.00 g/tonnes
1.75 g/tonnes
4700
4660
4480
4450
K-Hills
MSE-87-04
MSE-23
Unoxidized Zone
C
150 m
30 m

The Ivanpah Mountains are underlain by Jurassic to Cretaceous weakly peraluminous, magnetite-series granitic plutons of the Teutonia batholith, which constitutes part of the Mesozoic magmatic arc that intruded the southern portion of the Mesozoic foreland fold and thrust belt (Burchfiel & Davis 1972, 1975, 1988, Beckerman et al. 1982, Barton et al. 1988). Subeconomic porphyry copper-molybdenum and related skarn mineralization is associated with portions of the batholith in the adjacent mountains (Ntiamoah-Agyakwa 1987) and tin, tungsten and copper skarn mineralization surrounds the Ivanpah Mountains (Hewett 1956, Thompson 1978). Detailed description of the regional geological setting and associated mineralization is given in Chapter 1.

Geology of the Morning Star Deposit

The area around the Morning Star deposit is underlain by coarse-grained, equigranular Ivanpah granite of Jurassic age (Figure 4.1B). Mineralization occurs in foliated to mylonitic Ivanpah granite situated between the Morning Star and Sunnyside thrust faults, both oriented roughly N20°W/35°SW. Each fault is marked by a zone of ductile deformation (mylonite and protomylonite) overprinted by brittle deformation.

Precious-metal mineralization at the Morning Star deposit is hosted by the Ivanpah granite in the upper-plate of the Morning Star thrust fault (Figure 4.1B, C). The fault crops out at the mine site as a zone of fault gouge consisting of bleached and rounded granite fragments of variable size surrounded by anastomosing foliated, clay-rich selvages. Very rare galena and chalcopyrite have been found in fault gouge samples, but gold and silver mineralization is truncated at the gouge layer. The upper edge of the Morning Star diorite dike, which underlies the thrust fault, is truncated by the Morning Star fault, and fragments of altered diorite are found in samples of fault gouge. A series

of gouge filled E–W- to ENE–WSW-trending vertical to steeply north-dipping unmineralized structures cut the orebody, Morning Star fault and Morning Star diorite. Displacement on the E-W structures appears to be left-lateral normal oblique-slip with maximum throw of 5 meters on each E-W structure.

Disseminated base- and precious-metal mineralization at the Morning Star deposit is structurally controlled within a tabular zone of quartz±calcite stockwork vein system and silica-flooded breccia units subparallel to the Morning Star thrust fault (Figure 4.1C). The tabular orebody is truncated to the north and south by unmineralized clay-gouge-filled E-W high-angle structures, and to the east by the Morning Star fault. Horizontal thickness of the ore horizon increases below the zone of intense oxidation which occurs down to the 1340 and 1370 m elevation and corresponds to the present-day water table. Standing water in abandoned mines and perched water tables are near neutral to slightly alkaline (pH ranges from 6.5 to 8.0). The coincidence of oxidation with the present-day groundwater table has been noted in other gold deposits of the northeastern Mojave Desert (per. comm., J. Cline 1992).

Two stages of mineralization have been identified on the basis of petrographic and electron-microprobe analyses (Chapter 3). An early stage of hypogene quartz, calcite, barite, fluorite, pyrite, chalcopyrite, galena, sphalerite, tetrahedrite, acanthite after argentite and electrum occurs below the zone of oxidation, and a later stage of calcite, covellite, digenite (±chalcocite), goethite, acanthite, uytenbogaardtite, native bismuth, electrum, Pb, Zn and Cu carbonates and Cu oxides occur within the zone of oxidation. Partially oxidized remnants of primary minerals are present in most of the oxidized ore. Mineralization is confined to quartz±carbonate veins, stockwork zones and brecciated units. Early-formed quartz and pyrite veins are commonly deformed. A second episode of quartz and pyrite was precipitated as open-space fillings and base- and precious-metal

mineralization typically fills small openings in this second episode of quartz. Cavities and vugs are typically lined by euhedral quartz crystals and filled with coprecipitated pyrite, galena, sphalerite, chalcopyrite, tetrahedrite, acanthite and electrum. Quartz-absent calcite veins occur later than main-stage precious-metal mineralization and only contain galena and chalcopyrite. Carbonate veins are more abundant in upper levels of the deposit, where mafic dikes or mafic-mineral-bearing fault gouge were encountered. Factors controlling the intensity of precious-metal mineralization include fracture density, presence of pyrite with galena, sphalerite and chalcopyrite (or the oxidized equivalents), and silicification.

Pervasive propylitic alteration occurs in both the upper- and lower-plates of the Morning Star fault and envelops the area of mineralization. The intensity of the propylitic alteration decreases markedly away from the deposit and is truncated to the north by an E-W high-angle structure. Argillic±sericitic alteration occurs only adjacent to mineralization in the upper-plate. Alteration of the Morning Star fault gouge and unmineralized E-W structures is also believed to be related to the episode of argillic±sericitic alteration (Chapter 2 and 3). Quartz veins and veinlets are prevalent throughout the tabular ore horizon and at structurally higher levels of the upper-plate at the intersection of principal sets of fractures.

Although the ore horizon forms a continuous regularly shaped tabular body (Figure 4.1C), concentrations of gold within the ore horizon have a complex distribution owing to the structurally controlled nature of the deposit. Silver concentrations, where data are available, generally mirror gold concentrations. The relationship between gold and silver assay values is consistent for both oxidized portions and unoxidized portions of the deposit, but gold and silver concentrations are depleted in the zone of oxidation compared to the unoxidized zone. Also, a slight difference in Au/Ag exists between the

oxidized ore and the unoxidized ore. Au/Ag values for the oxidized portions of the orebody range from 0.005 to 1.150 and have an average ($\pm 1\sigma$) of 0.143±0.169 (N=116), whereas Au/Ag values for unoxidized portions of the orebody range from 0.010 to 5.000 and average 0.340±0.540 (N=164). Rock-chip geochemistry around the Kewanee Hills historic workings exhibits similar relationships between gold and silver for oxidized surface samples within the mine. Concentrations of gold in the Morning Star mine have a strong geochemical correlation with concentrations of Ag, As, Cu, Mo, Pb and Bi, and a moderate correlation with levels of Zn and Cd (Chapter 3). Similar correlations were seen in rock-chip and soil samples around the Kewanee Hills area (Forgerson 1974, Byington 1988). With the exception of the As and Sb anomalies, all trace element correlations have been accounted for by minerals associated with gold and silver (discussed below). For a more detailed description of the geology, mineralization and geochemistry of the Morning Star deposit, see Chapter 3.

Occurrence and Composition of Precious-metal Mineral

Electrum and silver-gold sulfide minerals have been examined petrographically and analytically for seven locations in the vicinity of the Morning Star deposit (Figure 4.1B, C). Four samples were taken from the high grade ore horizon within the open-pit mine (4700, 4660, 4480 and 4450 bench samples), and two samples represent high-grade ore from drill core (MSE-23 and MSE-87-04) outside of the current extent of the mine workings. Another sample with microscopic gold (K-Hills) was taken from an incline in the southern Kewanee Hills area. Although this latter sample has been plotted on Figure 4.1C by its elevation and distance from the Morning Star fault, it is a surface sample and has been completely oxidized. Sample descriptions are given in Appendix 4.1.

The chemical composition of electrum, silver sulfides and uytenbogaardtite was determined using Cameca SX50 and ARL-SEMQ electron microprobes. Details of analytical procedures and standards are given in Appendix 4.2. Grains smaller than three micrometers in the long dimension were analyzed as a grain composite. Larger grains of electrum were analyzed in multiple spots using various beam-sizes. Every attempt was made to analyze larger grains in at least two places in the central portion of the grain and at least two spots near the margin. The chemical compositions for electrum is summarized in Table 4.1 and shown on Figure 4.2. Representative analyses of acanthite and uytenbogaardtite are summarized in Table 4.2. The complete data-set is given in Appendix 4.3.

Electrum has been divided into six distinct types based on grain morphology, association with primary and secondary minerals and composition. These types of electrum are listed in Table 4.1.

Electrum in unoxidized ore

Primary hypogene electrum occurs with quartz and pyrite in unoxidized portions of the orebody below the 1340 to 1370 meter elevation. Rare grains of electrum were found in pyrite remnants in partially oxidized upper portions of the deposit. Precious-metal mineralization is restricted to quartz (±carbonate) veins with abundant pyrite and galena, lesser chalcopyrite and sphalerite, and minor acanthite and tetrahedrite. Early pyrite-bearing quartz veins consist of fine-grained bands of pyrite deposited at the vein-host rock contact. The early-deposited pyrite and quartz exhibit abundant evidence of deformation, manifest as brittle fracturing of pyrite and undulatory extinction, subgrain structures and grain-size reduction of the enveloping quartz. Some early pyrite-bearing

Table 4.1. Composition of types of electrum at the Morning Star deposit.

ELECTRUM TYPE	ORE TYPE	GOLD CONTENT (wt.%)	
		RANGE	MEAN±1σ
pyrite-hosted	unoxidized	63 - 75	68.3±3.4
quartz-hosted	unoxidized	65 - 72	68.7±2.2
goethite-hosted	oxidized	62 - 76	68.7±2.8
core	oxidized	61 - 72	66.1±2.5
rim	oxidized	78 - 93	83.4±5.3
wire	oxidized	81 - 90	85.4±2.7

Table 4.2. Representative electron-microprobe analyses of acanthite and uytenbogaardtite at the Morning Star deposit.

	Normalized wt. %				Mole %				Formula
	Au	Ag	Cu	S	Au	Ag	Cu	S	
Acanthite									
K-Hills-5	0.00	83.37	3.45	13.19	0.00	62.41	4.38	33.21	$Ag_{1.88}Cu_{0.13}S$
K-Hills-22	0.00	85.65	1.09	13.26	0.00	64.83	1.40	33.77	$Ag_{1.92}Cu_{0.04}S$
4700-1	6.75	78.96	1.44	12.86	2.88	61.52	1.90	33.70	$Au_{0.09}Ag_{1.83}Cu_{0.06}S$
4700-12	4.97	78.20	3.88	12.96	2.08	59.66	5.03	33.23	$Au_{0.06}Ag_{1.80}Cu_{0.15}S$
Uytenbogaardtite									
4700-3	29.26	57.23	1.99	11.52	13.89	49.6	2.93	33.58	$Au_{0.83}Ag_{2.95}Cu_{0.17}S_2$
4700-11	26.87	56.57	4.57	11.99	12.32	47.38	6.50	33.79	$Au_{0.74}Ag_{2.82}Cu_{0.39}S_2$

Figure 4.2. Composition of the six types of electrum. Each datum represents the average composition for a given grain, core, rim or wire structures. N is the number of grains, rims or wires analyzed.

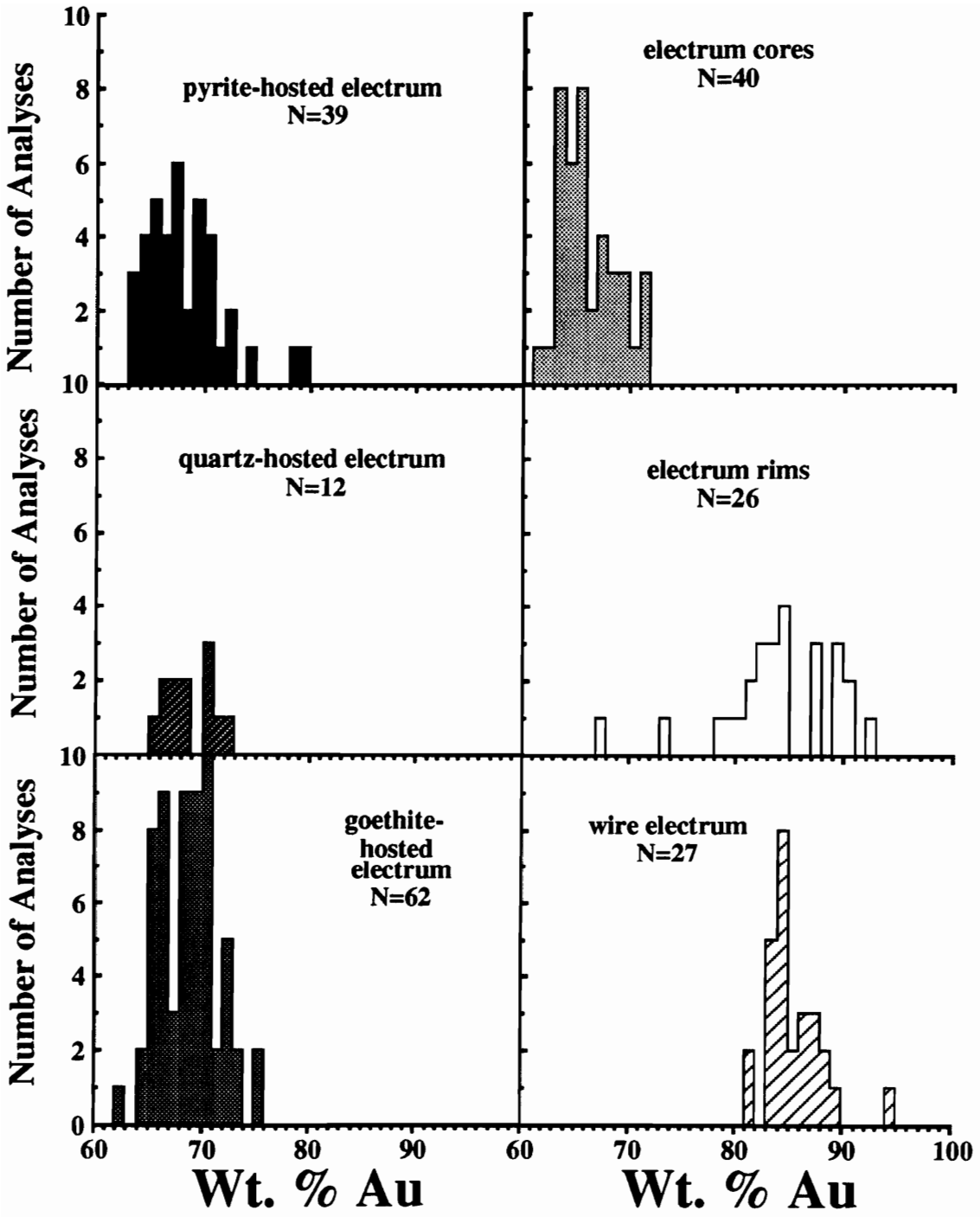
pyrite-hosted electrum
N=39
electrum cores
N=40
quartz-hosted electrum
N=12
electrum rims
N=26
goethite-
hosted
electrum
N=62
wire electrum
N=27
Number of Analyses
Number of Analyses
Number of Analyses
Wt. % Au
Wt. % Au
0
2
4
6
8
10
60
70
80
90
100

veins contain pyrite fragments cataclastically sheared into bands subparallel to the mylonitic foliation. The main stage of pyrite deposition formed euhedral isolated crystals or interpenetrating aggregates of cataclastically deformed subhedral pyrite. It is the main-stage pyrite that is spatially and temporally associated with precipitation of base-metal sulfides. In samples from drill hole MSE-23, main-stage pyrite is cut by 0.1- to 1.0-cm-wide fine-grained quartz veinlets which are free of base- and precious-metal minerals. Individual grains of pyrite can be correlated across these late quartz veinlets with little or no lateral displacement. In other samples, vein edges consist of fine-grained quartz that grades inward into open vugs encrusted by later euhedral quartz. The vugs commonly contain base-metal sulfides with pyrite, electrum and acanthite.

Pyrite-hosted electrum

Electrum in the unoxidized ore commonly occurs with galena in inclusions and fracture fillings in main-stage pyrite (Figure 4.3A, B). Pyrite-hosted electrum grains range from less than 1 to approximately 70 μm in the long dimension, with the vast majority of grains being about 10 μm long. Grain shape is largely controlled by host pyrite and its fracture geometry. Pyrite-hosted electrum in polished sections has a uniform silvery white color across individual grains. Minor acanthite was found with pyrite-hosted electrum only in the case of pyrite surrounded by abundant base-metal sulfides. No silver was detected in any galena associated with electrum and acanthite. Silver-sulfide in the primary mineral assemblage was originally deposited as argentite and has converted to the low-temperature polymorph, acanthite, upon cooling, as inferred on the basis of abundant twinning in acanthite pseudomorphs. Although twinning in acanthite has been interpreted as being indicative of inversion from the high-temperature

Figure 4.3. Line drawings from photomicrographs illustrating the typical occurrences of pyrite-hosted electrum with galena in main-stage pyrite. A. Electrum and galena inclusions in pyrite. B. Electrum and galena along fractures in cataclastically deformed pyrite.

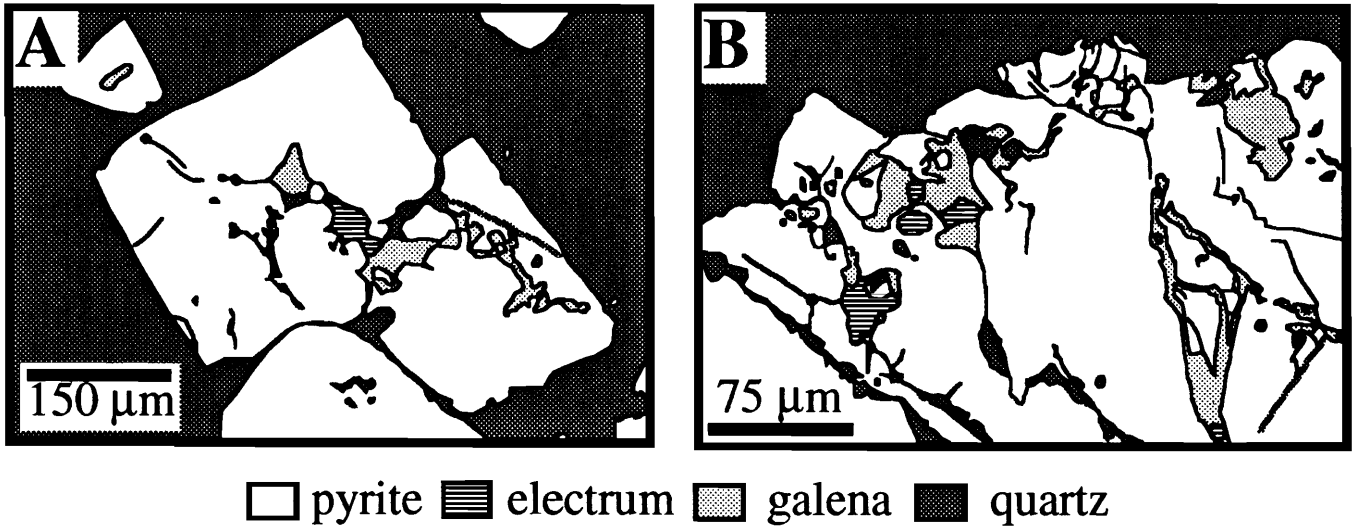
A
150 µm
B
75 µm
pyrite
electrum
galena
quartz

polymorph argentite, Taylor (1969) showed that acanthite grown at low temperatures can also be twinned; hence, twinning alone is not definitive of temperature of formation. Gold-to-silver ratios throughout unoxidized portions of the tabular orebody suggest the presence of additional silver-bearing minerals, but no other argentiferous minerals were found. The only other silver-bearing mineral found was a single grain of Ag-bearing tetrahedrite.

Quartz-hosted electrum

Electrum also occurs in unoxidized portions of the orebody in quartz surrounding pyrite from main-stage pyrite-bearing veins. Quartz-hosted electrum is slightly later in the paragenesis and occurs interstitially between euhedral crystals of quartz and along healed microfractures in quartz. Quartz-hosted electrum and electrum at the pyrite–quartz interface are generally finer grained (less than 5 μm across) than electrum in pyrite, but exhibits the same uniform texture and appearance observed in pyrite-hosted electrum. Also, electrum in quartz and on the surfaces of pyrite is not as common as pyrite-hosted electrum.

Electrum in oxidized ore

The oxidized portions of the orebody consist mainly of goethite, digenite (±chalcocite), covellite, cerussite, smithsonite, malachite and azurite in quartz±carbonate veins. Goethite occurs as a pseudomorph after pyrite and with digenite surrounding chalcopyrite. Typically, oxidation is not complete, so that remnants of pyrite and chalcopyrite persist within these pseudomorphs. Heavy metal carbonates either form

pseudomorphs after their perspective sulfide minerals or occur as fracture coatings and fillings. Goethite and malachite are the most common coatings along open fractures and joints. Covellite also forms surface coatings along open fractures in quartz. These fractures typically cross-cut the tabular ore horizon. All covellite is blaubleibender (blue-remaining) covellite, on the basis of optical identification.

Goethite-hosted electrum

Electrum occurs in the oxidized zone as fracture fillings and inclusions in goethite pseudomorphs after pyrite, interstitially between goethite pseudomorphs (Figure 4.4A) and embaying goethite or finely disseminated on goethite surfaces (Figure 4.4B). Electrum that embays goethite may result from either replacement of goethite by electrum or electrum sorption onto goethite surfaces during goethite precipitation. Schoonen et al. (1992) have shown that disseminated gold on goethite surfaces is probably not a result of sorption processes because of the low sorption efficiency of sorption of goethite, owing to either the lack of oxidizable surface-groups on goethite or low stability of Au-O surface complexes. Schoonen et al. (1992) argue that gold sorption is more likely on pre-existing electrum rather than goethite. Regardless of the mechanism of electrum formation, the textural evidence suggests remobilization of at least some gold and silver during oxidation. Both textures of goethite-hosted electrum have the same silvery white appearance and uniform texture seen in pyrite-hosted and quartz-hosted electrum. Grains of goethite-hosted electrum also have a range in size similar to that of pyrite-hosted electrum (<1 to 80 μm), but the size distribution is skewed toward larger grain-sizes.

Figure 4.4. Photomicrographs of goethite-hosted and wire electrum. A. Goethite-hosted electrum interstitial to goethite after pyrite pseudomorphs. In A, the electrum is bright white, goethite is light to dark gray, and the host quartz is black. B. Goethite-hosted electrum replacing goethite that partially replaces pyrite. In B, the electrum is bright white, goethite is light gray with low relief, pyrite is light gray with high relief, and the host quartz is darker gray. C. Wire electrum with associated covellite, acanthite and uytenbogaardtite. In C, the electrum is bright white, covellite is dark gray and bladed, acanthite and uytenbogaardtite are mottled shades of light gray, and the host quartz is black. The grain to the right of the wire electrum consists of a central zone of mixed acanthite and uytenbogaardtite with an outer zone of acanthite and bladed covellite. Scale bars are 150 μm long for both A and B, and 50 μm long for C.

B

A

C

Figure 4.5. Typical example of the occurrence and composition of a thick rim of electrum on a core grain. A. Photomicrograph of the thick rim of electrum and the core zone. The electrum rim has an irregular bright white appearance and contains inclusions of covellite, dark gray and bladed. The core zone has a uniform bright white appearance. The entire grain is encapsulated in quartz (black). B. Electron-microprobe traverse for Au, Ag and Cu across the electrum core and thick rim shown in A. Individual analyses were performed with a 1-μm beam size, and the traverse was conducted with a 0.4-μm step size.

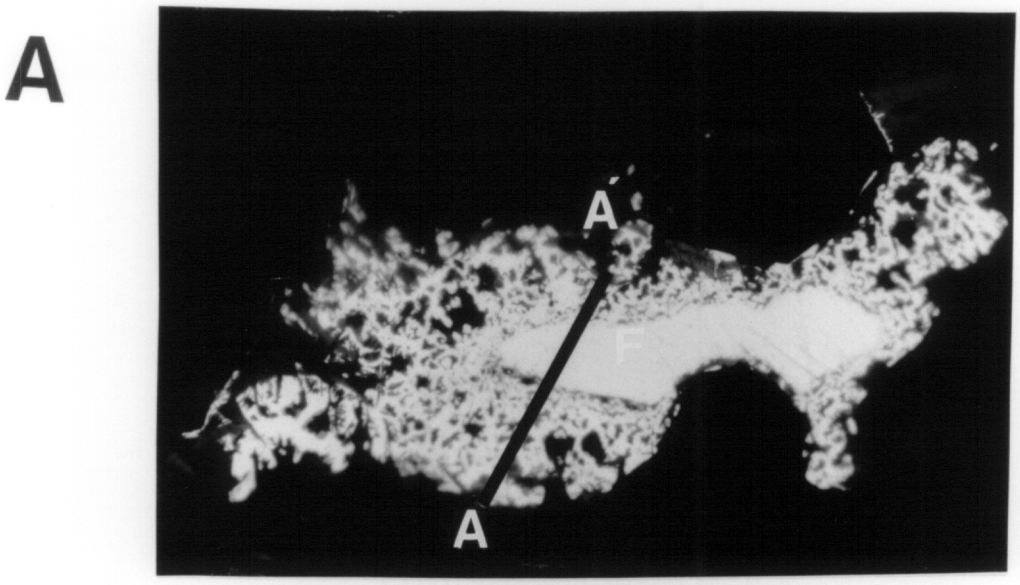
A
A'
A

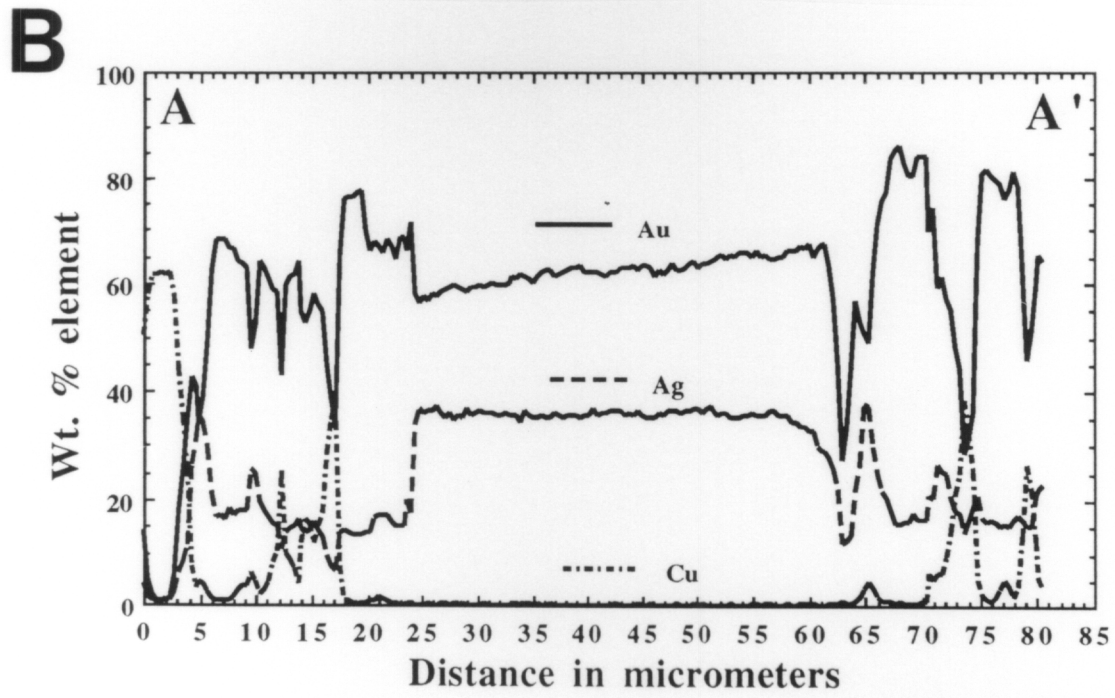
B
A
A'
Au
Ag
Cu
Wt. % element
Distance in micrometers
0
20
40
60
80
100
0 5 10 15 20 25 30 35 40 45 50 55 60 65 70 75 80 85

One grain of electrum from the high-grade ore zone in sample 4450 was found with cerussite and enclosed in a goethite pseudomorph of pyrite.

Core and rim electrum

Electrum also occurs in late cross-cutting fractures and open vugs within quartz from oxidized portions of the orebody. These fractures and vugs contain laths of covellite, Cu-oxide (cuprite±tenorite?) and native bismuth as surface coatings and grains or clusters of electrum with silver±gold sulfides. Acanthite associated with electrum in the oxidized portions of the orebody seems untwinned, which suggests low-temperature deposition as acanthite. This is different than acanthite from the unoxidized ore, which contains abundant twins that suggest higher-temperature deposition as argentite and conversion to acanthite upon cooling. This late electrum commonly has a core-rim morphology (Figure 4.5A) or a wire-like morphology (Figure 4.4C). Core and rim electrum were found in the highest level of the Morning Star orebody (sample 4700), but have not been found in surface exposures in the Kewanee Hills. One electrum grain with a rim less than 2 μm thick also was found in drill hole MSE-87-04 in the relatively unoxidized portion of the orebody. Electrum cores, which range from 6 to 140 μm long, are composed of homogeneous silvery white silver-rich electrum similar to pyrite-hosted, quartz-hosted and goethite-hosted electrum. Grain-size distribution of electrum cores also is skewed toward coarser sizes, with an average grain size larger than either pyrite- or goethite-hosted electrum. Electrum rims, which range in average thickness from <1 to 41 μm, are brilliant yellow-gold color in polished section compared to other types of electrum. Rim thickness has a bimodal distribution between thin rims, <1 to 5 μm, and thick rims, >10 μm, with thin rims being encountered twice as often as thick rims.

Electrum rims and cores also are texturally different, with rims having an irregular angular morphology and cores being massive. Electrum rims are also not uniformly developed around individual cores. Thin rims may occur on one side of a core or between adjacent cores and not occur on other parts of the same core. The extent of rim development appears to have been controlled by the location of the electrum cores within a fracture or vug (e.g., Figure 4.5A). Also, thin rims generally do not contain mineral inclusions and are surrounded by fine-grained bladed covellite, whereas thick rims typically form angular morphologies encapsulating bladed covellite and irregular grains of acanthite and uytenbogaardtite.

Wire electrum

Wire electrum (Figure 4.4C) exhibits characteristics identical to thick rims, but contains no vestiges of an electrum core. The wire electrum morphology has been designated separately, but may actually represent sections cut through thick rims that did not intersect the associated core-zone. Individual wire structures have rounded edges and smooth surface features compared to the thick rims, which have sharp angular edges (cf. Figure 4.5A). Wire electrum was found exclusively in covellite-bearing pockets which also contain Cu-oxides, silver±gold sulfides and native bismuth. Size distribution of wire electrum is similar to that of goethite-hosted electrum, but the wire texture is sponge-like, and therefore contains considerably less metal within individual wire grains as compared to other types of electrum.

Composition of Electrum

The chemical composition of pyrite-hosted, quartz-hosted and goethite-hosted electrum and electrum cores is essentially the same (Table 4.1 and Figure 4.2). The gold content of pyrite-hosted electrum forms a nearly bell-shaped distribution, which is slightly skewed toward gold-rich compositions (Figure 4.2). No difference in chemical composition was detected for electrum that occurs on the surface of pyrite or which formed inclusions and fracture fillings in pyrite. Also, pyrite-hosted electrum shows a uniform appearance and chemistry across individual grains. Quartz-hosted and goethite-hosted electrum have the same range and mean composition as pyrite-hosted electrum (Table 4.1 and Figure 4.2). No chemical distinction exists between electrum found as inclusions or fracture fillings in goethite, interstitial to goethite pseudomorphs or embaying goethite. Goethite-hosted electrum also has a uniform chemical composition for individual grains. In core zones the range and median composition of electrum are similar to those found in pyrite-hosted, quartz-hosted and goethite-hosted electrum, but core zones are skewed towards slightly lower gold content. Electrum rims are more gold-rich than electrum cores with rim composition generally greater than 78 wt.% Au. Electrum rims are skewed toward silver-enriched compositions (Figure 4.2). Two rims have a composition less than 74 wt.% Au (Figure 4.2). Both of these rims are less than 2 mm thick and formed around large core-type grains. Thin rims generally have gold contents at or below the median composition of rim electrum, which may reflect difficulty in analyzing the thin rims without obtaining X-ray scattering for the electrum core. Alternatively, the difference may be real and reflect diffusion of Ag between cores and rims or precipitation of subsequently more gold-rich electrum as the rims precipitated. These latter hypotheses are not likely correct, because no correlation exists between electrum composition in core grains and corresponding rims. Also, elemental X-ray maps show no zoning of gold and silver between electrum cores and rims across the

sharp core–rim boundaries (Figure 6). Thus, the slight enrichment in silver of thin rims relative to thick rims is likely a result of analytical difficulties. An example of the analytical difficulties can be seen in the thick rim traverse of Figure 4.5B, where analyses of electrum rims and enclosed covellite laths reveal intermediate compositions of electrum. The one grain of electrum in the unoxidized ore zone which developed a rim (sample MSE-87-04) has the same distribution of silver-rich core (71 wt.% Au) and gold-rich rim (84 wt.% Au) described above for oxidized samples from the higher levels within the Morning Star deposit. Electrum cores for any given core–rim pair are compositionally homogeneous (e.g. Figure 4.5B). Thin rims also appear to be compositionally homogeneous, but fewer analyses of each thin rim were performed. Thick rims, on the other hand, are compositionally heterogeneous, with individual segments varying by up to 12 wt.% Au (Figure 4.5B). However, no consistent change in composition was noticed along traverses away from the core zone.

Wire electrum has a distribution of compositions similar to that of electrum rims, in the range between 81 and 90 wt.% Au, with one wire grain being 94 wt.% Au. The composition of wire electrum is skewed towards gold-depleted values below the mean composition. The mean value of wire electrum is essentially identical to the mean value for rim electrum. Electrum composition is generally uniform throughout individual wire structures compared to the irregular distribution observed in thick rims.

Silver and silver-gold sulfides

Coexisting acanthite and uytenbogaardtite have been found only within thick rims of electrum or associated with wire electrum. Acanthite was found in sample K-hills which contains goethite-hosted electrum and no uytenbogaardtite. A typical occurrence

Figure 4.6 Elemental X-ray maps of Au, Ag, Cu and S and backscattered electron map (BSE) of wire electrum (A) and thick electrum rim (B). The BSE and X-ray maps in Figure 4.6A is for a portion of the grain shown in Figure 4.4C and the BSE and X-ray maps in Figure 4.6B is for a portion of the thick rim shown in Figure 4.5.

BSE
Au
Cu
Ag
S

BSE
Au
Cu
Ag
S

for silver±gold sulfide minerals includes anhedral masses of intergrown acanthite and uytenbogaardtite, which commonly contain laths and rosettes of covellite. These clusters of silver±gold sulfide and individual grains of acanthite or uytenbogaardtite are surrounded by wire electrum (Figure 4.4C) or thick rims of electrum. Secondary acanthite contains no twins, so probably formed at low temperature.

The composition of the electrum is slightly depleted in gold for wire and rims intergrown with both acanthite and uytenbogaardtite, as opposed to wire or rims without visible silver±gold sulfides. The composition of electrum ranges from 80.0 to 85.3 wt.% Au in the presence of silver±gold sulfides and ranges from 81.0 to 91.8 wt.% Au where no silver-gold sulfides are present. Acanthite composition ranges from 78.5 to 79.5 wt.% Ag in the presence of electrum and uytenbogaardtite (Table 4.2). For acanthite coexisting with electrum but not uytenbogaardtite, the composition of acanthite ranges from 82.5 to 86.5 wt.% Ag (Table 4.2). Goethite-hosted electrum coexisting with acanthite is slightly gold-rich compared to the mean value for goethite-hosted electrum. The silver±gold sulfides seem to be sulfur-rich, but all silver±gold sulfides and wire or thick-rim electrum are found in open vugs and fractures containing covellite. Because Cu appears in all analyses, the sulfur enrichment is likely due to intergrowths of covellite. Composition of uytenbogaardtite are consistent with those reported by Barton et al. (1978), who noted sulfur enrichment in supergene or Cu-rich uytenbogaardtite.

Acanthite after argentite that occurs in quartz vugs with electrum and base-metal sulfides is essentially pure (containing 86 to 87 wt.% Ag) with less than 0.05 wt. % combined gold and copper. No sulfur enrichment was observed in acanthite after argentite.

Thus, the chemical compositions of goethite-hosted, quartz-hosted and pyrite-hosted electrum and electrum cores are essentially identical. Also, no chemical distinction

exists for silver-rich electrum (pyrite-hosted, quartz-hosted, goethite-hosted and core electrum types) with depth along the tabular ore horizon. With the exception of electrum rims (discussed above), there is no relationship between grain size of electrum and chemical composition. Electrum rims and wire electrum morphologies have similar chemical compositions, and are considerably more gold-rich compared to cores, pyrite-hosted, quartz-hosted and goethite-hosted electrum.

Discussion

Two distinct stages of electrum mineralization occur in the Morning Star deposit. The principal stages of electrum deposition are primary hypogene and secondary, either supergene or late-stage, low-temperature hydrothermal. Within these two stages of deposition, multiple episodes of electrum precipitation probably occurred. Temperature estimates for primary electrum mineralization range from 280° to 315°C from fluid inclusions and electrum-argentite-pyrite-sphalerite thermometry (Chapter 3). Primary hypogene electrum was deposited in two stages from fluids moving up along the Morning Star fault (Chapter 3), both stages spatially and temporally related to pyrite and galena precipitation. The earliest electrum and argentite (now acanthite) were deposited contemporaneously with main-stage pyrite and base-metal sulfides. Silver-bearing tetrahedrite may also be part of this assemblage, as one grain of tetrahedrite was found. Trace element geochemistry also suggests a strong correlation among As, Sb, Ag and Au in the unoxidized ore (Chapter 3). No other As and Sb minerals have been identified in the primary ore. The second episode of primary electrum occurs with galena in cataclastically deformed pyrite and quartz vugs. The two episodes of primary electrum

are texturally distinct but are chemically and mineralogically similar, and may form one continuous episode of electrum deposition.

Textural evidence from the oxidized portions of the orebody support the late-stage remobilization of at least some gold and silver. In the uppermost portions of the orebody, electrum is present as a higher-fineness rim around lower-fineness core. The core zone is chemically similar to all stages of primary hypogene electrum. Lower in the oxidized orebody, the electrum is also chemically similar to primary electrum, but occurs in various textural relationships with goethite. Much of the goethite-hosted electrum is probably primary electrum that was not remobilized. Evidence for oxidation without remobilization includes electrum with cerussite as inclusions in goethite after pyrite pseudomorphs and electrum in pyrite remnants within goethite. These grains of goethite-hosted electrum grains are texturally and chemically identical to electrum with galena that occurs as inclusions in pyrite (pyrite-hosted electrum). Replacement of these sulfide minerals may have occurred without dissolution of the enclosed electrum. Additional goethite-hosted electrum occurs as large grains embaying goethite or as fine grains deposited on the surface of goethite. These latter textures suggest that remobilization of gold and silver and precipitation of electrum during late-stage hydrothermal or supergene oxidation occurred with little or no change in the composition of electrum. Thus in the highest levels of the deposit, remobilization of gold and silver caused increased fineness of electrum (rim and wire morphologies) and is associated with silver±gold sulfide minerals, but in lower levels of the deposit remobilization of gold and silver was essentially isochemical.

Uytenbogaardtite can form in equilibrium with acanthite up to 113°C (Graf 1968, Barton 1980). Thus, the assemblage Au-rich electrum+acanthite+uytenbogaardtite must have formed during the waning stage of hydrothermal processes or by supergene

processes. A supergene origin is favored because of the textural overlap with mineralization formed during oxidation of the Morning Star deposit. For example, wire and rim electrum occur with intergrown acanthite, uytenbogaardtite and bladed blaubleibender covellite. This assemblage, and especially the presence of blaubeibender covellite, is consistent with a supergene origin. Furthermore, the zone of oxidation corresponds to the present-day water table at the deposit, which argues for fairly recent supergene oxidation. In addition, only one gold-rich rim and no uytenbogaardtite were found below the zone of oxidation, suggesting that remobilization of gold and silver occurred owing to descending fluids from the surface instead of fluids rising from below. Late-stage hydrothermal fluids would rise along the Morning Star fault and should have remobilized or oxidized significant quantities of the deep ore. No evidence of this deep oxidation was found. Although mineralogical and textural evidence supports the supergene formation of silver±gold sulfide minerals and the remobilization of gold and silver, a late-stage hydrothermal origin cannot be completely ruled out at this time.

Present-day waters at the Morning Star mine, Sunnyside decline and rain water at the minesite have pH ranging between 6.5 and 8.0. The mineral assemblage malachite+cerussite+smithsonite, common in extensively altered samples, is consistent with these pH values (Mann & Deutscher 1984). Thus if recent supergene solutions are responsible for oxidation and remobilization of precious-metals at the Morning Star deposit, these solutions should have been near neutral to alkaline. Locally, acidic conditions may have prevailed owing to the breakdown of pyrite and other sulfide minerals, but the abundance of carbonate minerals, especially in the upper portions of the deposit, probably reacted to neutralize the acidic solutions. At depth within the tabular ore horizon, where the abundance of sulfide minerals increases and that of the carbonate minerals decreases, acidic conditions may prevail locally.

Gold and silver are soluble and transported in oxygenated aqueous solutions by organic complexes (Boyle et al. 1975, Baker 1979, Vlassopoulos et al. 1990), halogen complexes (Krauskopf 1951, Cloke & Kelly 1964, Seward 1976, Mann 1984, Zotov et al. 1986), hydroxide complexes (Zotov et al. 1982, Vlassopoulos & Wood, 1990) and S-donor ligand complexes such as HSO_3^- and $S_2O_3^{2-}$ (Goleva et al. 1970, Plyusnin et al. 1981, Webster 1986, Gammon & Barnes 1988, Renders & Seward 1989). If precious-metal mobilization took place at the Morning Star mine under conditions similar to present-day conditions, organic complexes are probably of no consequence because vegetation is sparse and only occurs in alluvial valleys. Chloride complexes are only significant at pH values less than 5 (Cloke & Kelly 1964, Seward 1976) and hydroxide complexes are not significant if other dissolved species, particularly sulfur-bearing species, are present (Zotov et al. 1982, Vlassopoulos & Wood 1990). For these reasons, neither halogen or hydroxide complexes are considered to be important mechanisms of transport at the Morning Star deposit.

Thus, for the proposed supergene conditions at the Morning Star deposit, thiosulfate would form metastable sulfur species that could remain in solution in high concentrations (Goldhaber 1983, Williamson & Rimstidt 1992) and could account for remobilization of gold and silver. Bisulfide species could only be responsible for transporting Au and Ag in lower portions of the deposit, where reducing conditions prevail and total dissolved sulfur in solution is higher (Webster 1986, Gammon & Barnes 1988; Vlassopoulos & Wood 1990, Benedetti & Boulegue 1991).

Webster (1986) experimentally showed that the solubility of electrum is a function of composition. Electrum containing 50 atomic % Ag (64.6 wt.% Au) has a lower solubility as thiosulfate complexes than gold-rich electrum or pure gold. Webster (1986) interpreted these results in terms of the formation of a mixed-metal complex

[$(Au,Ag)(S_2O_3)_2^{3-}$]. Whether a mixed-metal complex actually forms is beyond the scope of this paper. However, when gold and silver are dissolved from electrum with a composition between 60 and 70 wt.% Au the resulting electrum should be deposited with little or no chemical separation between gold and silver. Thus, precipitation of secondary electrum should occur with a composition similar to the initial primary electrum. Primary electrum (pyrite-hosted and quartz-hosted electrum and electrum cores) at the Morning Star deposit has a median composition of 68 wt.% Au, which is identical to goethite-hosted electrum. Goethite-hosted electrum occurs in various textural relationships that resemble both primary electrum and electrum deposited from the remobilization of gold and silver. Solubility and transport of gold and silver by thiosulfate complexes are consistent with both textures. Precipitation of secondary goethite-hosted electrum may have occurred by reduction of thiosulfate complexes, local decreases in pH or sorption onto goethite and electrum surfaces (Webster 1986; Schoonen et al. 1992).

In the highest levels of the Morning Star deposit, electrum occurs as gold-rich rims on core zones and wire structures with silver±gold sulfide minerals. In light of the phase relationships determined by Barton (1980), the higher fineness of the electrum can be accounted for by sulfidation of original electrum compositions (Figure 4.7). Reaction of primary electrum with sulfur produces the assemblage acanthite+electrum, and further sulfidation would eventually produce the assemblage acanthite +uytenbogaardtite+electrum (Figure 4.7). Each addition of sulfur and change in mineral assemblage form electrum with high concentrations of gold, driving the composition of electrum to 84.0 wt.% Au in equilibrium with ideal acanthite and uytenbogaardtite compositions (Barton 1980). Goethite-hosted electrum coexisting with acanthite is richer in gold than the mean for goethite-hosted electrum which is consistent with the sulfidation theory and the phase relationship determined by Barton (1980). Equilibrium is

Figure 4.7. Chemistry of the coexisting electrum (diamonds), acanthite (circles) and uytenbogaardtite (squares) plotted on the 100°C isothermal section showing Au-Ag-S in weight %, after Barton (1980), whose plot is given in molar units, which have been converted to units of weight in this paper. Dashed lines represent the equilibrium mineral assemblages at 100°C. The black rectangle represents the composition of the primary electrum, and the arrows indicate compositional changes due to sulfidation of electrum. The black circle (a) and square (u) show the ideal compositions of acanthite and uytenbogaardtite, respectively.

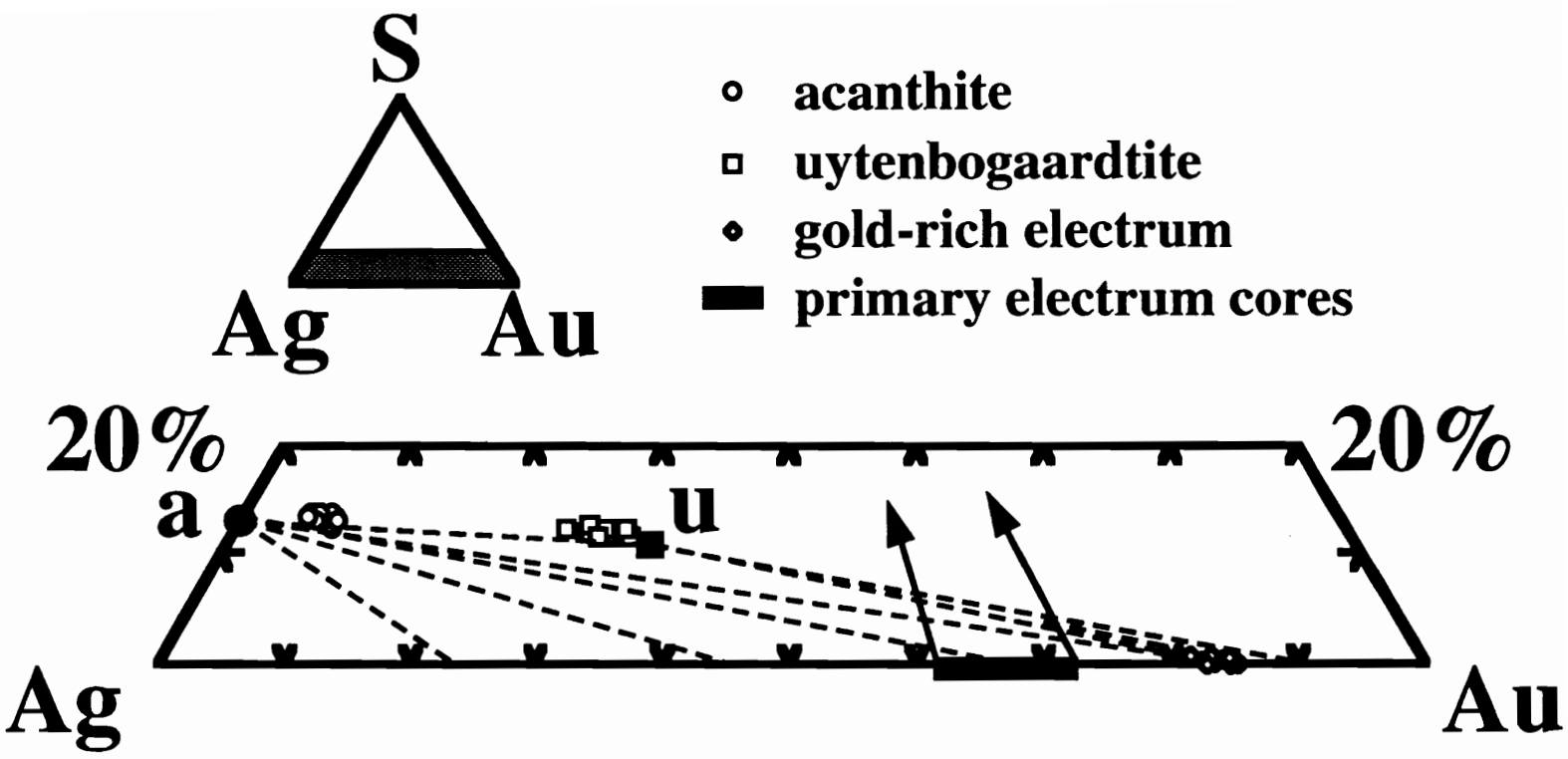
S
Ag
Au
acanthite
uytenbogaardtite
gold-rich electrum
primary electrum cores
20%
20%
a
u
Ag
Au

commonly not maintained during supergene processes, and no attempt is made to imply equilibrium conditions prevailed during supergene oxidation of the Morning Star deposit, but compositions for rim and wire electrum have a mean value of 84.4 wt.% Au, which is consistent with experimental phase equilibria. Castor & Sjoberg (1993) also found compositions of electrum in the assemblage acanthite+uytenbogaardtite+electrum, in the Bullfrog deposit of Nevada, that agree with the phase equilibria of Barton (1980). Transport by thiosulfate complexes may also produce gold-rich electrum rim and wire morphologies (Webster & Mann 1984, Webster 1986). As silver reacted to form acanthite, and silver and gold reacted to form uytenbogaardtite, the thiosulfate complexes would be destabilized and precipitate gold-rich electrum owing to the preferential loss of silver. Further data regarding the stability of acanthite and uytenbogaardtite during supergene processes, especially processes related to thiosulfate solutions, is required to verify this final hypothesis.

Conclusions

Within the structurally controlled high-grade ore horizon at the Morning Star deposit, electrum grains have been divided into six types based on associated minerals and grain morphology. These include (1) pyrite-hosted and (2) quartz-hosted electrum occurring with base-metal sulfide minerals in unoxidized portions of the orebody and (3) goethite-hosted electrum, (4) electrum cores, (5) electrum rims and (6) wire electrum associated with supergene mineral assemblages in the oxidized portions of the orebody. Pyrite-hosted and quartz-hosted electrum represent primary electrum deposited by hydrothermal processes. Electrum cores and much of the goethite-hosted electrum have chemical compositions similar to that of primary electrum that remained unaltered by

oxidation. Goethite-hosted electrum that embays goethite or was deposited on goethite surfaces has textures indicative of supergene remobilization of gold and silver, but exhibits chemical compositions similar to that of primary electrum. Remobilization of gold and silver by thiosulfate complexes can produce secondary goethite-hosted electrum with no chemical separation of gold and silver, and should form abundant metastable complexes for the inferred supergene fluids at the Morning Star deposit. Electrum cores with rims of higher-fineness electrum and wire electrum occur in the uppermost levels of the Morning Star deposit with acanthite and uytenbogaardtite. Rims of gold-rich electrum and wire structures are consistent with sulfidation of primary electrum to form silver±gold sulfide minerals. Thus, within the Morning Star deposit, remobilization of gold and silver occurs isochemically and with gold enrichment, each occurring at different levels within this one deposit.

Appendix 4.1

Sample Descriptions

Drill Core MSE-23

Pyrite- and galena-bearing quartz veins in silicified and propylitically altered, foliated granite from the 557 foot depth of drill hole MSE-23. The sample is from the basal section of the high grade ore zone 8 feet above the Morning Star fault. Gold assay values for 5 foot drill core splits around the 557 foot depth range from 0.071 to 0.212 opt. The sample consists of randomly oriented quartz veins, 0.5 to 12 mm wide, containing 1 to 10% sulfide minerals that consist exclusively of pyrite and galena. Late quartz veins, which are thinner than early veins, are typically free of sulfide minerals.

Drill Core MSE-87-04

One to two centimeter thick quartz+pyrite+galena veins from 490 foot depth of drill hole MSE-87-04. The sample is from the high grade ore zone approximately 20 feet vertically above the Morning Star fault. Gold assays range from 0.098 to 0.055 opt. The host granite is slightly foliated and silicified, and contains weak propylitic alteration. The quartz veins contain 2-4% sulfide minerals consisting of clusters of pyrite and randomly oriented stringers of pyrite and galena with trace amounts of chalcopyrite and sphalerite.

Sample K-Hills

Sample include two to four centimeter wide, oxidized, quartz veins from an incline on southern side of K-Hills. The samples location places it approximately 20 feet horizontally from surface exposure of Morning Star fault. Quartz veins containing 10 to 40% 'sulfides', which have been completely oxidized to goethite, in protomylonitic granite with propylitic alteration. No silicification occurs outside of the veins.

Sample 4450

Sample 4450 was collected from the high grade ore zone on the 4450 foot bench of the Morning Star open-pit mine. This sample contains 2 cm wide quartz veins with up to 10% sulfide minerals in relatively undeformed, propylitically altered granite. Samples were collected 30 feet horizontally from the Morning Star fault. Remnants of pyrite, galena, sphalerite and chalcopyrite occur surrounded by goethite and Pb, Zn, and Cu carbonate minerals in vuggy quartz. Up to 40% of the sulfides have been oxidized.

Sample 4480

Sample 4480 is from the high grade ore zone on the 4480 foot bench of the Morning Star open-pit mine and contains millimeter to centimeter wide quartz veins. The

sulfide content of the vein is up to 70%. Large clusters of pyrite with minor galena, sphalerite and chalcopyrite occur surrounded by goethite and other oxidation products. Veins occur in relatively undeformed, propylitically altered granite. Samples were collected 30 to 50 feet horizontally from the Morning Star fault.

Sample 4660

Centimeter thick, randomly oriented quartz+sulfide vein occur in slightly foliated, weak propylitic alteration granite at location 4660. Sulfide minerals or their oxidation products make up 1 to 10% of the veins and contain remnants of primary pyrite, galena, chalcopyrite and minor sphalerite. Samples were collected from the high grade ore zone about 25 feet horizontally from the Morning Star fault on the 4660 foot level of the Morning Star open-pit mine.

Sample 4700

Sample from the 4700 foot level of the Morning Star open-pit mine were supplied by Kent Ausburn of Vanderbilt Gold Corporation. Samples contain quartz veins which are cut, at a high angle, by veins and pockets of covellite and quartz. The quartz veins have a trend parallel to Morning Star fault. The exact distance from the fault is not given. Gold assay values of splits from the samples range from 0.060 to 0.100 opt. Covellite veins and pockets include electrum, acanthite and uytenbogaardtite with copper oxides and native bismuth. Primary stage sulfide minerals are completely oxidized except for traces of pyrite remnants.

Appendix 4.2

Analytical Techniques

The mineral chemistry for electrum, silver-sulfides and uytenbogaardtite was determined using a Cameca SX50 electron microprobe and an ARL-SEMQ electron microprobe. Both microprobes were operated at 15 KV and 20 nA for electrum analyses and 15 KV and 2.0 nA for silver±gold sulfide analyses. Lower beam currents were required for silver±gold sulfide analyses because of the photosensitive nature of the acanthite and uytenbogaardtite. Counting times of 30 seconds on peaks and 5 seconds on either side of peaks were employed for background corrections on electrum with shorter counting times (generally 10 to 15 seconds total) for silver±gold sulfides. Pure gold, silver and chalcopyrite standards were used for calibration and the following X-ray lines were utilized for quantification: AuMα, AgLα, CuKα and SKα. Data reduction was conducted using a ZAF-type data correction schemes supplied by Cameca and ARL, respectively. Additional mineral chemistry was determined using a HNU EDS System 5000 energy dispersive X-ray spectrometer coupled to a CamScan Series 2 scanning electron microscope. Operating conditions were 20 KV, 2.25 to 2.5 nA and live counting times ranged from 30 second for electrum and 15 to 20 seconds for sulfides. Well characterized, by microprobe analyses, electrum and precious-metal sulfides from Morning Star samples were used to standardize the EDS. Quantification was conducted using a standardless ZAF-type deconvolution scheme, supplied by HNU, that reproduced the microprobe results to within ±0.8 wt.% for Au, Ag and Cu and ±1.3 wt.% for S for identical spot analyses on electrum and chalcopyrite grains. X-ray mapping was done using the Cameca SX50 electron microprobe operated at 30 KV and 20 nA and utilizing

50 millisecond counting times per 0.4 mm step over a 9500 μm^2 scanning area, to determine if zoning occurred between core and rim electrum. No zoning was detected.

Grains smaller than three micrometers in the long dimension were analyzed as a grain composite. Larger electrum grains were analyzed in multiple spots using various beam sizes. Every attempt was made to analyze larger grains in at least two spots in the central portion of the grain and at least two spots on the grain margin. Spot analyses using a one micrometer spot size were compared to area analyses, up to 100 μm^2, for large core grains and yielded identical results. Copper and sulfur were included in all mineral analyses. Electrum contains only trace amounts of Cu and S (see distances from 18 to 64 μm on Figure 4.4). Analyses of electrum which contain significant Cu and S are assumed to be composite analyses of electrum and covellite. Mineral chemistry for electrum, acanthite and uytenbogaardtite are given in Appendix 4.3 and plotted on Figures 4.2, 4.4 and 4.5.

Appendix 4.3 Mineral chemistry of Morning Star deposit acanthite and uytenbogaardtite.

	Normalized Weight %				Molecular %				Formula (for 1S)		
	Au	Ag	Cu	S	Au	Ag	Cu	S	Au	Ag	Cu
ACANTHITE											
K-Hills	0.00	82.68	3.45	13.88	0.00	61.14	4.33	34.53	0.00	1.77	0.13
	0.01	82.03	4.43	13.53	0.00	60.73	5.57	33.70	0.00	1.80	0.17
	0.00	82.95	4.72	12.33	0.00	62.63	6.04	31.33	0.00	2.00	0.19
	0.00	83.38	3.78	12.84	0.00	62.70	4.83	32.48	0.00	1.93	0.15
	0.00	83.37	3.45	13.19	0.00	62.41	4.38	33.21	0.00	1.88	0.13
	0.00	78.63	7.02	14.35	0.00	56.64	8.59	34.77	0.00	1.63	0.25
	0.00	82.19	3.89	13.92	0.00	60.60	4.86	34.53	0.00	1.75	0.14
	0.00	82.05	4.88	13.07	0.00	61.09	6.17	32.74	0.00	1.87	0.19
	0.00	81.25	4.95	13.80	0.00	59.71	6.18	34.12	0.00	1.75	0.18
	0.00	83.34	4.53	12.13	0.00	63.22	5.83	30.96	0.00	2.04	0.19
	0.00	82.14	5.32	12.54	0.00	61.59	6.77	31.63	0.00	1.95	0.21
	0.00	82.82	4.68	12.50	0.00	62.36	5.98	31.66	0.00	1.97	0.19
	0.06	84.59	3.18	12.17	0.03	64.59	4.12	31.25	0.00	2.07	0.13
	0.00	82.55	4.55	12.90	0.00	61.76	5.78	32.46	0.00	1.90	0.18
	0.00	83.57	4.33	12.10	0.00	63.50	5.58	30.92	0.00	2.05	0.18
	0.03	83.79	4.74	11.45	0.01	64.27	6.17	29.54	0.00	2.18	0.21
	0.00	82.52	3.71	13.77	0.00	61.06	4.67	34.27	0.00	1.78	0.14
	0.00	84.66	2.82	12.52	0.00	64.35	3.64	32.01	0.00	2.01	0.11
	0.10	80.34	7.06	12.50	0.04	59.76	8.92	31.28	0.00	1.91	0.29
	0.28	86.21	1.60	11.91	0.12	66.75	2.10	31.02	0.00	2.15	0.07
	0.00	86.22	1.51	12.27	0.00	66.29	1.97	31.74	0.00	2.09	0.06
	0.00	85.65	1.09	13.26	0.00	64.83	1.40	33.77	0.00	1.92	0.04
ACANTHITE											
4700	6.75	78.96	1.44	12.86	2.88	61.52	1.90	33.70	0.09	1.83	0.06
	5.51	78.74	2.57	13.18	2.31	60.36	3.34	33.99	0.07	1.78	0.10
	7.22	77.68	2.14	12.97	3.07	60.27	2.81	33.85	0.09	1.78	0.08
	5.38	79.32	1.95	13.35	2.26	60.79	2.54	34.42	0.07	1.77	0.07
	5.52	78.89	2.63	12.96	2.33	60.69	3.44	33.55	0.07	1.81	0.10
	6.26	79.04	1.90	12.80	2.66	61.39	2.51	33.44	0.08	1.84	0.07
	7.45	78.40	2.01	12.14	3.22	61.87	2.69	32.22	0.10	1.92	0.08
	6.62	77.74	2.03	13.60	2.78	59.54	2.64	35.04	0.08	1.70	0.08
	5.90	77.74	3.04	13.32	2.47	59.37	3.94	34.23	0.07	1.73	0.12
	6.03	78.98	2.41	12.59	2.57	61.36	3.17	32.90	0.08	1.87	0.10
	6.94	77.53	2.32	13.21	2.93	59.77	3.03	34.26	0.09	1.74	0.09
	4.97	78.20	3.88	12.95	2.08	59.66	5.03	33.23	0.06	1.80	0.15
	Normalized Weight %				Molecular %				Formula (for 2S)		
	Au	Ag	Cu	S	Au	Ag	Cu	S	Au	Ag	Cu
UYTENBOGAARDTITE											
4700	29.18	56.30	2.91	11.62	13.74	48.41	4.24	33.60	0.82	2.88	0.25
	27.39	58.73	2.14	11.73	12.84	50.27	3.10	33.79	0.76	2.98	0.18
	28.25	57.90	1.92	11.93	13.25	49.59	2.80	34.37	0.77	2.89	0.16
	29.26	57.23	1.99	11.52	13.89	49.60	2.93	33.58	0.83	2.95	0.17
	29.94	56.67	2.02	11.38	14.29	49.38	2.99	33.35	0.86	2.96	0.18
	31.06	55.52	2.05	11.38	14.88	48.58	3.04	33.49	0.89	2.90	0.18
	30.93	55.53	2.36	11.18	14.85	48.67	3.51	32.97	0.90	2.95	0.21
	27.65	57.95	3.00	11.40	13.00	49.73	4.37	32.91	0.79	3.02	0.27
	28.75	56.91	2.39	11.95	13.47	48.68	3.48	34.38	0.78	2.83	0.20
	25.77	59.85	2.30	12.08	11.91	50.50	3.29	34.30	0.69	2.94	0.19
	26.87	56.57	4.57	11.99	12.32	47.38	6.50	33.79	0.74	2.82	0.39
	28.44	57.43	2.74	11.39	13.43	49.52	4.01	33.04	0.81	3.00	0.24
	30.52	55.40	2.25	11.84	14.44	47.86	3.29	34.41	0.84	2.78	0.19

Mineral chemistry of electrum.

		Electrum	Number	Normalized wt.%		Atomic %		
Sample	Size[1]	Type	of Analyses	Au	Ag	Au	Ag	Fineness
MSE-23	2800.00	pyrite	3	78.40	21.60	66.53	33.47	784
	66.70	pyrite	2	69.23	30.77	55.20	44.80	692
	133.20	pyrite	2	68.92	31.08	54.85	45.15	689
	44.37	pyrite	2	69.82	30.18	55.89	44.11	698
	7.93	pyrite	2	70.79	29.21	57.03	42.97	708
	19.74	quartz	2	67.51	32.49	53.22	46.78	675
	13.71	quartz	2	68.14	31.86	53.94	46.06	681
	74.94	quartz	3	66.66	33.34	52.26	47.74	667
	14.21	quartz	2	67.17	32.83	52.84	47.16	672
	3.48	quartz	1	70.06	29.94	56.16	43.84	701
	14.70	pyrite	2	71.72	28.28	58.14	41.86	717
	2.94	pyrite	1	64.49	35.51	49.87	50.13	645
	3.38	pyrite	1	66.83	33.17	52.46	47.54	668
	3.53	pyrite	1	65.31	34.69	50.76	49.24	653
	7.24	pyrite	2	67.66	32.34	53.39	46.61	677
	47.29	quartz	2	68.21	31.79	54.03	45.97	682
	27.96	quartz	2	66.32	33.68	51.89	48.11	663
	44.43	quartz	2	65.44	34.56	50.91	49.09	654
	50.63	pyrite	2	70.16	29.84	56.29	43.71	702
	176.73	pyrite	3	69.87	30.13	55.94	44.06	699
	524.87	pyrite	3	66.56	33.44	52.15	47.85	666
	363.82	pyrite	3	65.56	34.44	51.04	48.96	656

Sample	Size[1]	Electrum Type	Number of Analyses	Normalized wt.% Au	Normalized wt.% Ag	Atomic % Au	Atomic % Ag	Fineness
	629.75	pyrite	3	66.70	33.30	52.31	47.69	667
	2053.76	pyrite	3	67.00	33.00	52.64	47.36	670
	584.04	pyrite	3	66.25	33.75	51.80	48.20	662
	54.19	pyrite	2	65.25	34.75	50.70	49.30	653
	60.68	pyrite	2	63.72	36.28	49.03	50.97	637
	26.29	pyrite	2	65.63	34.37	51.12	48.88	656
	65.82	pyrite	2	64.32	35.68	49.68	50.32	643
	8.40	pyrite	1	66.99	33.01	52.64	47.36	670
	21.41	pyrite	2	79.26	20.74	67.67	32.33	793
	43.51	pyrite	2	63.93	36.07	49.26	50.74	639
	40.92	pyrite	2	65.80	34.20	51.31	48.69	658
	90.53	pyrite	3	64.06	35.94	49.39	50.61	641
	25.54	pyrite	2	64.43	35.57	49.79	50.21	644
	27.47	pyrite	2	63.22	36.78	48.49	51.51	632
	86.14	pyrite	2	67.20	32.80	52.88	47.12	672
	152.46	pyrite	3	68.14	31.86	53.95	46.05	681
	8.12	pyrite	2	67.95	32.05	53.72	46.28	679
MSE-87-04	26.43	pyrite	2	74.23	25.77	61.20	38.80	742
	15.87	pyrite	2	70.17	29.83	56.29	43.71	702
	8.69	pyrite	2	72.02	27.98	58.50	41.50	720
	66.07	pyrite	3	69.94	30.06	56.03	43.97	699
	31.72	pyrite	2	71.95	28.05	58.42	41.58	720
	1788.71	core	5	70.96	29.04	57.23	42.77	710
	2.22	rim	4	84.36	15.64	74.70	25.30	844
	456.82	quartz	4	70.48	29.52	56.66	43.34	705
	17.07	quartz	2	71.72	28.28	58.14	41.86	717
	36.45	quartz	3	72.09	27.91	58.59	41.41	721
	270.06	quartz	9	70.78	29.22	57.02	42.98	708
K-Hills	1249.28	goethite	7	68.16	31.84	53.96	46.04	682
	47.04	goethite	4	72.58	27.42	59.17	40.83	726
	8.67	goethite	2	71.07	28.93	57.37	42.63	711
	277.64	goethite	3	68.84	31.16	54.74	45.26	688
	364.62	goethite	2	69.24	30.76	55.22	44.78	692
	52.13	goethite	2	70.11	29.89	56.23	43.77	701
	138.86	goethite	3	71.25	28.75	57.57	42.43	712
	16.75	goethite	3	68.18	31.82	53.99	46.01	682
	3.18	goethite	1	70.12	29.88	56.24	43.76	701
	16.75	goethite	3	70.48	29.52	56.66	43.34	705
	1029.38	goethite	4	68.88	31.12	54.80	45.20	689
	53.31	goethite	3	72.76	27.24	59.39	40.61	728
	690.20	goethite	4	68.56	31.44	54.43	45.57	686
	2.25	goethite	1	72.50	27.50	59.08	40.92	725
	2.54	goethite	1	72.16	27.84	58.66	41.34	722
	6.75	goethite	1	70.00	30.00	56.09	43.91	700
	54.00	goethite	2	70.54	29.46	56.74	43.26	705
	221.71	goethite	2	66.31	33.69	51.88	48.12	663
	885.28	goethite	3	64.92	35.08	50.33	49.67	649
	800.00	goethite	3	65.06	34.94	50.49	49.51	651
	333.30	goethite	2	68.50	31.50	54.36	45.64	685
	1573.43	goethite	5	69.54	30.46	55.56	44.44	695
4450	108.00	goethite	2	66.05	33.95	51.58	48.42	660
	16.50	goethite	1	65.70	34.30	51.20	48.80	657
	4358.29	goethite	7	72.23	27.77	58.75	41.25	722
4480	534.45	goethite	3	75.94	24.06	63.35	36.65	759
	1622.25	goethite	4	75.83	24.17	63.21	36.79	758
	1260.00	goethite	4	73.88	26.12	60.77	39.23	739
	123.99	goethite	2	70.11	29.89	56.23	43.77	701
	93.08	goethite	2	69.06	30.94	55.01	44.99	691
	1112.75	goethite	4	69.64	30.36	55.67	44.33	696
	1483.76	goethite	3	73.88	26.12	60.77	39.23	739
	619.03	goethite	3	69.22	30.78	55.19	44.81	692
	5645.70	goethite	4	70.13	29.87	56.26	43.74	701
	108.00	goethite	2	69.27	30.73	55.24	44.76	693
	161.59	goethite	3	69.28	30.72	55.26	44.74	693
	328.67	goethite	3	70.06	29.94	56.17	43.83	701
	1197.04	goethite	4	70.73	29.27	56.96	43.04	707
	858.19	goethite	5	68.45	31.55	54.30	45.70	685
	494.49	goethite	3	65.88	34.12	51.40	48.60	659
	170.50	goethite	3	66.84	33.16	52.47	47.53	668
	5.80	goethite	1	67.18	32.82	52.85	47.15	672
	41.27	goethite	2	66.44	33.56	52.02	47.98	664
	8.19	goethite	1	66.49	33.51	52.07	47.93	665
	6.82	goethite	1	64.66	35.34	50.05	49.95	647
	5.15	goethite	1	70.11	29.89	56.22	43.78	701
	7.65	goethite	1	65.76	34.24	51.26	48.74	658
	2.89	goethite	1	67.78	32.22	53.53	46.47	678
	2.89	goethite	1	65.30	34.70	50.75	49.25	653
	171.95	goethite	3	68.19	31.81	54.00	46.00	682
	156.06	goethite	3	65.07	34.93	50.51	49.49	651
	45.94	goethite	2	62.81	37.19	48.05	51.95	628
	113.66	goethite	3	65.29	34.71	50.75	49.25	653
	5277.82	goethite	7	66.76	33.24	52.37	47.63	668
	4.93	goethite	1	65.58	34.42	51.06	48.94	656

Sample	Size[1]	Electrum Type	Number of Analyses	Normalized wt.% Au	Normalized wt.% Ag	Atomic % Au	Atomic % Ag	Fineness
	844.40	goethite	4	66.86	33.14	52.50	47.50	669
	3715.58	goethite	9	66.22	33.78	51.77	48.23	662
	74.12	goethite	3	67.32	32.68	53.01	46.99	673
	964.41	goethite	3	68.12	31.88	53.92	46.08	681
	103.79	goethite	3	69.62	30.38	55.66	44.34	696
	44.49	goethite	3	69.63	30.37	55.67	44.33	696
	998.82	goethite	4	66.72	33.28	52.34	47.66	667
4660 HG	62.50	pyrite	2	69.28	30.72	55.25	44.75	693
	833.25	pyrite	4	67.45	32.55	53.15	46.85	674
	319.29	pyrite	3	70.88	29.12	57.13	42.87	709
4700	154.48	wire	2	86.62	13.38	78.01	21.99	866
	115.27	wire	2	84.24	15.76	74.54	25.46	842
	145.63	wire	2	84.63	15.37	75.10	24.90	846
	122.63	wire	2	84.06	15.94	74.27	25.73	841
	79.42	wire	2	84.64	15.36	75.11	24.89	846
	175.15	wire	2	84.69	15.31	75.18	24.82	847
	204.09	wire	2	83.14	16.86	72.98	27.02	831
	122.70	wire	2	84.65	15.35	75.13	24.87	847
	134.01	wire	2	83.32	16.68	73.23	26.77	833
	113.42	wire	2	81.66	18.34	70.92	29.08	817
	94.06	wire	2	84.16	15.84	74.43	25.57	842
	184.94	wire	2	83.75	16.25	73.84	26.16	838
	900.00	wire	4	83.18	16.82	73.04	26.96	832
	177.29	wire	2	81.35	18.65	70.49	29.51	813
	170.64	wire	2	94.61	5.39	90.57	9.43	946
	1998.00	wire	5	87.39	12.61	79.15	20.85	874
	14.00	rim	2	81.54	18.46	70.75	29.25	815
	3920.00	core	16	64.45	35.55	49.82	50.18	645
	5.00	rim	2	82.23	17.77	71.71	28.29	822
	10.00	rim	3	82.13	17.87	71.56	28.44	821
	1534.00	core	9	64.10	35.90	49.44	50.56	641
	11.00	rim	2	80.83	19.17	69.78	30.22	808
	233.80	core	3	65.62	34.38	51.11	48.89	656
	96.12	core	3	67.50	32.50	53.22	46.78	675
	77.78	core	2	68.72	31.28	54.61	45.39	687
	88.57	core	3	65.15	34.85	50.58	49.42	651
	1.58	rim	4	79.69	20.31	68.25	31.75	797
	2.29	rim	5	84.78	15.22	75.32	24.68	848
	4.97	rim	9	80.98	19.02	69.99	30.01	810
	3.44	rim	8	83.82	16.18	73.93	26.07	838
	3.44	rim	8	83.31	16.69	73.21	26.79	833
	653.38	core	10	61.81	38.19	46.98	53.02	618
	672.16	core	10	62.32	37.68	47.53	52.47	623
	663.82	core	10	63.13	36.87	48.39	51.61	631
	658.25	core	10	63.76	36.24	49.07	50.93	638
	636.41	core	10	63.29	36.71	48.56	51.44	633
	653.38	core	10	63.79	36.21	49.10	50.90	638
	603.22	core	10	63.46	36.54	48.75	51.25	635
	539.78	core	10	64.64	35.36	50.03	49.97	646
	682.78	core	10	64.71	35.29	50.10	49.90	647
	797.50	core	9	67.82	32.18	53.58	46.42	678
	40.16	rim	9	82.61	17.39	72.23	27.77	826
	5277.82	core	100	63.89	36.11	49.21	50.79	639
	1064.55	core	3	70.83	29.17	57.08	42.92	708
	2.88	rim	5	90.08	9.92	83.26	16.74	901
	22.20	wire	3	83.71	16.29	73.79	26.21	837
	679.84	wire	4	88.17	11.83	80.32	19.68	882
	638.76	wire	3	86.67	13.33	78.07	21.93	867
	8268.75	wire	5	84.12	15.88	74.37	25.63	841
	948.60	core	3	67.79	32.21	53.54	46.46	678
	1.62	rim	3	87.62	12.38	79.50	20.50	876
	220.87	core	3	68.98	31.02	54.92	45.08	690
	8.11	rim	3	87.52	12.48	79.35	20.65	875
	136.19	core	3	69.37	30.63	55.36	44.64	694
	41.46	core	2	69.38	30.62	55.37	44.63	694
	26.29	core	3	68.56	31.44	54.42	45.58	686
	1.22	rim	3	84.90	15.10	75.49	24.51	849
	153.20	wire	3	87.26	12.74	78.95	21.05	873
	52.63	wire	2	86.58	13.42	77.95	22.05	866
	1693.02	core	6	68.03	31.97	53.82	46.18	680
	4.46	rim	4	83.17	16.83	73.02	26.98	832
	1497.60	core	31	66.10	33.90	51.64	48.36	661
	11.00	rim	7	87.42	12.58	79.19	20.81	874
	3.00	rim	2	82.16	17.84	71.61	28.39	822
	4.00	rim	2	92.10	7.90	86.46	13.54	921
	1121.00	core	11	64.87	35.13	50.28	49.72	649
	8.00	rim	3	78.11	21.89	66.15	33.85	781
	336.00	core	3	66.00	34.00	51.53	48.47	660
	4.52	rim	2	84.87	15.13	75.45	24.55	849
	2277.00	core	19	65.41	34.59	50.87	49.13	654
	1644.37	core	10	65.13	34.87	50.56	49.44	651
	1697.82	core	8	63.82	36.18	49.14	50.86	638
	2.08	rim	2	67.88	32.12	53.65	46.35	679
	3997.30	core	10	65.62	34.38	51.11	48.89	656

Sample	Size[1]	Electrum Type	Number of Analyses	Normalized wt.% Au	Normalized wt.% Ag	Atomic % Au	Atomic % Ag	Fineness
	640.21	core	6	64.59	35.41	49.98	50.02	646
	3.00	rim	4	90.09	9.91	83.28	16.72	901
	8.50	rim	4	90.11	9.89	83.30	16.70	901
	1.85	rim	2	73.16	26.84	59.88	40.12	732
	1960.95	core	6	65.53	34.47	51.01	48.99	655
	396.39	core	5	71.33	28.67	57.67	42.33	713
	254.25	core	4	71.51	28.49	57.88	42.12	715
	91.52	core	3	66.96	33.04	52.60	47.40	670
	183.04	wire	5	87.60	12.40	79.46	20.54	876
	26.14	wire	2	85.77	14.23	76.76	23.24	858
	34.90	wire	2	85.08	14.92	75.74	24.26	851
	300.67	wire	5	89.30	10.70	82.04	17.96	893
	358.23	core	5	63.84	36.16	49.16	50.84	638
	356.63	core	5	65.06	34.94	50.48	49.52	651
	255.62	core	5	65.62	34.38	51.11	48.89	656
	309.81	core	5	65.34	34.66	50.79	49.21	653

[1] rim size is given as thickness in microns and core, grain or wire size is calculated assuming oval shape and given in square microns.

Literature Cited

Adams, J.A.S., Burchfiel, B.C. & Sutter, J.F. (1967): Absolute dating of mountain building events. In International Atomic Energy Agency, V. (Eds.), *Radioactive Dating and Methods of Low-level Counting.* 453-462.

Allen, C.M., Miller, D.M. & Howard, K.A. (1983): Field, petrologic and chemical characteristics of Jurassic intrusive rocks, eastern Mojave Desert, southeastern California. *Geological Society of America Abstracts with Programs* **15**, 410-411.

Allison, L.E. (1965): Organic Carbon. In Black, C.A. (Eds.), *Methods in soil analysis, Part 1.* Madison, Wisconsin, American Society of Agronomy, 1367-1378.

Anderson, J.L., Barth, A.P., Young, E.D., Bender, E.E., Davis, M.J., Faber, D.L., Hayes, E.M. & Johnson, K.A. (1989): Plutonism across the Tujunga-North American terrane boundary: A middle to upper crustal view of two juxtaposed magmatic arcs. In Bartholomew, M.J., Hyndman, D.W., Mogk, D.V. & Mason, R. (Ed.), Characterization and Composition of Ancient (Precambrian to Mesozoic) Continental Margins: Proceedings of the 8th International Conference on Basement Tectonic., Holland: D. Reidel.

Anderson, J.L., Osborne, R.H. & Palmer, D.F. (1980): Petrogenesis of the cataclastic rocks within the San Andreas Fault Zone of southern California, U.S.A. *Tectonophy.* **67**, 221-249.

Anderson, J.L., Osborne, R.H. & Palmer, D.F. (1983): Cataclastic rocks of the San Gabriel Fault - An expression of deformation at deeper crustal levels in the San Andreas Fault Zone. *Tectonophy.* **98**, 209-251.

Armstrong, R.L. (1968): Sevier orogenic belt in Nevada and Utah. *Geology Society of America Bulletin* **79**, 429-458.

Ausburn, K.E. (1988): Geology of the Morning Star Mine. In Weide, D.L. & Faber, M.L. (Eds.), *This extended land, geological journeys in the southern Basin and Range.* Geological Society of America, 76.

Ausburn, K.E. (1991): Ore-petrogenesis of Tertiary volcanic hosted epithermal gold mineralization at the Hart mining district, Castle Mountains, NE San Bernardino County, California. In Raines, G.L., Lisle, R.E., Schafer, R.W. & Wilkinson, W.H. (Ed.), Geology and Ore Deposits of the Great Basin., (pp. 1147-1188). Reno, Nevada: Geological Society of Nevada.

Baker, W.E. (1979): The role of humic acid in the transport of gold. Geochim. Cosmochim. Acta **42**, 645-649.

Barnes, H.L. (1979): Solubilities of ore minerals. In Barnes, H.L. (ed.), *Geochemistry of Hydrothermal Ore Deposits.* John Wiley & Sons, New York, New York, 404-460.

Barton, M.D. (1980): The Ag-Au-S system. Econ. Geol. **75**, 303-306.

Barton, M.D., Battles, D.A., Debout, G.E., Capo, R.C., Christensen, J.N., Davis, S.R., Hanson, R.B., Michelson, C.J. & Trim, H.E. (1988): Mesozoic contact metamorphism in the western United States. In Ernst, W.G. (Eds.), *Metamorphism and crustal evolution of the western United States (Rubey Vol. VII).* New Jersey, Prentice Hall, 110-178.

Barton, M.D., Kieft, C., Burke, E.A.J. & Oen, I.S. (1978): Uytenbogaardtite, a new silver-gold sulfide. Can. Mineral. **16**, p. 651-657.

Barton, P.B., Jr. and Toulmin, P., III (1964): The electrum-tarnish method for the determination of the fugacity of sulfur in laboratory sulfide systems. *Geochimica et Cosmochimica Acta.*, **28**, 619-640.

Bateman, P.C. (1981): Geologic and geophysical constraints on models for the origin of the Sierra Nevada Batholith, California. In Ernst, W.G. (Eds.), *The Geotectonic Development of California (Rubey Volume 1).* New Jersey, Prentice Hall, 71-86.

Bateman, P.C., Clark, L.D., Huber, N.K., Moore, J.G. & Rinehart, C.D. (1963): The Sierra Nevada batholith: A synthesis of recent work across the central part. *U.S. Geological Survey, Prof. Paper* **414D**, 46 p.

Bateman, P.C. & Dodge, F.C.W. (1970): Variation of major chemical constituents across the central Sierra Nevada batholith. *Geol. Soc. Amer. Bull.* **81**, 409-420.

Beckerman, G.M. (1982): Petrology of the southern portion of the Teutonia Batholith: A large intrusive complex of Jurassic and Cretaceous age in the eastern Mojave Desert, California. M.S. Thesis, University of Southern California.

Beckerman, G.M., Robinson, J.P. & Anderson, J.L. (1982): The Teutonia Batholith: A large intrusive complex of Jurassic and Cretaceous age in the eastern Mojave Desert, California. In Frost, E.G.M., D.L. (Eds.), *Mesozoic-Cenozoic Tectonic Evolution of the Colorado River Region, California, Arizona and Nevada (Anderson-Hamilton Volume)* San Diego, California, Cordilleran, 205-220.

Bedford, R.H. & Johnson, F.T. (1946): Survey of tin in California. *Bureau of Mines Report of Investigations* **3876**, 14 p.

Benedetti, M. & Boul`egue, J. (1991): Mechanism of gold transfer and deposition in a supergene environment. Geochim. Cosmochim. Acta **55**, 1539-1547.

Berger, B.R. and Eimon, P.I. (1983): Conceptual models of epithermal precious-metal deposits. in Shanks, W.C., III (ed.) *Cameron Volume on Unconventional Mineral Deposits,* Society of Mining Engineers, 191-205.

Blundy, J.D. & Holland, T.J.B. (1990): Calcic amphibole equilibria and a new amphibole-plagioclase geothermometer. *Contrib. Mineral. Petrol.* **104**, 208-224.

Bouley, B.A. (1986): Descriptive model of gold on flat faults: in Cox, D. P. and Singer, D. A., eds., Mineral deposit models: *U.S. Geological Survey Bulletin* **1693**, p. 251.

Boyle, R.W. (1968): The geochemistry of silver and its deposits. Geol. Surv. Canada, Bull. 160, 455 p.

Boyle, R.W. (1978): The geochemistry of gold and its deposits. Geol. Surv. Canada, Bull. 280, 584 p.

Boyle, R.W., Alexander, W.M. & Aslin, G.E.M. (1975): Some observations on the solubility of gold. Geol. Surv. Canada Paper 75-24, 6 p.

Brown, H.J. (1986): Detailed geologic map of the eastern New York Mountains, San Bernardino County, California. *Geol. Soc. Amer. Abstr. with Prog.* **18**, 89.

Buesch, D.C. (1991): Locating the vent of the lower Miocene Peach Tree tuff, Arizona, California and Nevada: Petrofabric and other flow direction indicators. *Geol. Soc. Amer. Abstr. with Prog.* **23**, A45.

Burchfiel, B.C. & Davis, G.A. (1971): Clark Mountain Thrust Complex in the Cordillera of southeastern California: Geologic summary and field trip guide. In Elders, W.A. (Eds.), *Geological Excursions in Southern California.* Riverside, California, University of California at Riverside, 1-28.

Burchfiel, B.C. & Davis, G.A. (1972): Structural framework and evolution of the southern part of the Cordilleran Orogen, western United States. *Am. J. Sci.* **272**, 97-118.

Burchfiel, B.C. & Davis, G.A. (1975): Nature and controls of Cordilleran orogenesis, western United States: Extension of an earlier synthesis. *Am. J. Sci.* **275-A**, 363-396.

Burchfiel, B.C. & Davis, G.A. (1977): Geology of the Sagamore Canyon-Slaughterhouse Spring area, New York Mountains, California. *Geol. Soc. Amer. Bull.* **88**, 1623-1640.

Burchfiel, B.C. & Davis, G.A. (1981): Mojave Desert environs. In Ernst, W.G. (Eds.), *The Geotectonic Development of California (Rubey Volume 1).* New Jersey, Prentice Hall, 219-252.

Burchfiel, B.C. & Davis, G.A. (1988): Mesozoic thrust faults and Cenozoic low-angle normal faults, eastern Spring Mountains, Nevada, and Clark Mountains, California. In Weide, D.L. & Faber, M.L. (Eds.), *This extended land; Geological journeys in the southern Basin and Range* Geological Society of America, 87-106.

Burhnam, C.W. (1979): The importance of volatile constituents. In Yoder, H.S. (Eds.), *The Evolution of Igneous Rocks: Fifteenth Anniversary Perspective.* Princeton, N.J, Princeton University Press, 439-486.

Byerlee, J.D. & Summers, R.A. (1976): A note on the effect of fault gouge on fault stability. *Int. Jour. Mech. Min. Sci. & Geomech. Abstr.* **13**, 35-36.

Byington, C.B. (1988): Ivanpah project, Morning Star mine: Structural analysis and ore controls (unpublished mine report No. Homestake Mining Company.

Byington, C.B. (1989): The Ivanpah project of the Mojave gold province-A structural approach. In Bureau of Land Management's California Desert Mineral Symposium, 113-124

Capps, R.C. & Moore, J.A. (1991): Geologic setting of Mid-Miocene gold deposits in the Castle Mountains, San Bernardino County, California and Clark County, Nevada. In Raines, G.L., Lisle, R.E., Schafer, R.W. & Wilkinson, W.H. (Ed.), Geology and Ore Deposits of the Great Basin., (pp. 1195-1219). Reno, Nevada: Geological Society of Nevada.

Carlisle, D., Agyakwa, Y.N. & Curtis, K. (1982): Hydrothermal mineralization and intermineral intrusives associated with transverse fractures in the eastern Mojave Desert, San Bernardino County, California. In Fife, D.L. & Minch, J.A. (Eds.), *Geology and mineral wealth of the California Transverse Ranges (Mason Hill Volume).* Santa Ana, California, South Coast Geological Society, 350-353.

Castor, S.B. & Sjoberg, J.J. (1993): Uytenbogaardtite (Ag_3AuS_2) in the Bullfrog mining district, Nevada. Can. Mineral. **31**, 89-98.

Chen, J.H. & Moore, J.G. (1979): Late Jurassic independent dike swarms in eastern California. *Geology* **7**, 129-133.

Chester, F.M. & Logan, J.M. (1986): Implications for mechanical properties of brittle faults from observations of the Punchbowl Fault Zone, California. *Pure Applied Geophy.* **124**, 79-106.

Christe, G. & Hannah, J.L. (1990): High-K, continental-arc volcanism in the Kettle Rock sequence of the eastern Mesozoic belt, northern Sierra Nevada, California: Implications for lower Mesozoic Cordilleran tectonics. In Anderson, J.L. (Eds.), *The Nature and Origin of Cordilleran Magmatism.* Geological Society of America, 315-329.

Cloke, P.L. & Kelly, W.C. (1964): Solubility of gold under inorganic supergene conditions. Econ. Geol. **59**, 259-270.

Cosca, M.A., Essene, E.J. & Bowman, J.R. (1991): Complete chemical analysis of metamorphic hornblendes: implications for normalizations, calculated H_2O activities and thermobarometry. *Contrib. Mineral. Petrol.* **108**, 472-484.

Craig, J.R. and Scott, S.D. (1974): Sulfide phase equilibria. *Mineralogical Society of America Short Course Notes*, **1**, CS1-CS110.

Day, P.R. (1965): Particle fractionation and particle-size analysis. In Black, C.A. (Eds.), *Methods of soil analysis - Part I.* Madison, Wisconsin, American Society of Agronomy, Inc., 545-567.

DeWitt, E. (1980): Geology and geochronology of the Halloran Hills, southeastern California, and implications concerning Mesozoic tectonics of the southern Cordillera. Ph.D. dissertation, Pennsylvania State University.

DeWitt, E., Armstrong, R.L., Sutter, J.F. & Zartman, R.E. (1984): U-Th-Pb, Rb-Sr and Ar-Ar mineral and whole-rock isotopic systematics in a metamorphosed granitic terrane, southeastern California. *Geological Society of America Bulletin* **95**, 723-739.

Dokka, R.K. (1989): The Mojave extensional belt of southern California. *Tectonics* **8**, 363-390.

Drobeck, P.A., Frost, E.G., Hillemeyer, F.L., and Liebler, G.S. (1986): The Picacho mine: a gold mineralized detachment in southern California: in Beatty, B. and Wilkinson, P.A.K., eds., Frontiers in geology and ore deposits of Arizona and the southwest: *Arizona Geological Society Digest*, **16**, p. 187-221.

Dunn, P.J., Ferraiolo, J.A., Fleischer, M., Gobel, V., Grice, J.D., Langley, R., Shigley, J.E., Vanko, D.A. & Zilczer, J.A. (1985): New mineral names. Am. Mineral. **70**, 1329-1335.

Emmons, W.H. (1912): The agency of manganese in the superficial alteration and secondary enrichment of gold-deposits in the United States. A.I.M.E. Trans. **42**, 3-73.

Evans, J.R. (1958): Geology of the Mescal Range Quadrangle, San Bernardino County, California. M.S. Thesis, University of Southern California.

Evans, J.R. (1971): Geology and mineral deposits of the Mescal Range Quadrangle, San Bernardino County, California. Geologic Map, No. California Division of Mines and Geology. Scale.

Evans, J.R. (1974): Relationship of mineralization to major structural features in the Mountain Pass area, San Bernardino County, California. *California Geology* **27**, 147-157.

Everndon, J.F. & Kistler, R.W. (1970): Chronology of emplacement of Mesozoic batholithic complexes in California and western Nevada. *U.S. Geological Survey Professional Paper* **623**, 42 p.

Fleck, R.J. (1970): Tectonic style, magnitude and age of deformation in the Sevier Orogenic Belt in southern Nevada and eastern California. *Geol. Soc. Amer. Bull.* **81**, 1705-1720.

Forgerson, F.D. (1974): The Morning Star mine area, Ivanpah quadrangle, California. unpublished mine report for U.S. Borax & Chemical Corporation, 21 p.

Foster, D.A., Harrison, T.M. & Miller, C.F. (1989): Age, inheritance and uplift history of the Old Women-Piute Batholith, California and implications from K-feldspar age spectra. *Jour. Geol.* **97**, 232-243.

Foster, D.A., Harrison, T.M. & Miller, C.F. (in press): Mesozoic and Cenozoic thermal history of the eastern Mojave Desert, California, and adjacent western Arizona: Insights from $^{40}Ar/^{39}Ar$ geochronology. *Jour. of Geophy. Review.*

Fox, L.K. & Miller, D.M. (1990): Jurassic granitoids and related rocks of the southern Bristol Mountains, southern Providence Mountains and Colten Hills, Mojave Desert, California. In Anderson, J.L. (Eds.), *The nature and origin of Cordilleran magmatism.* Geological Society of America, 111-132.

Gammon, C.H. & Barnes, H.L. (1989): The solubility of Ag_2S in near-neutral aqueous sulfide solutions. Geochim. Cosmochim. Acta **53**, 279-290.

Gibbs, R.J. (1971): X-ray diffraction mounts. In Carver, R.E. (Eds.), *Procedures in sedimentary petrology.* New York, New York, John Wiley International, 531-539.

Gill, J. (1981): *Orogenic andesites and plate tectonics.* New York, New York, Springer-Verlag, Pages.

Glazner, A.F. (1990): Recycling of continental crust in Miocene volcanic rocks from the Mojave block, southern California. In Anderson, J.L. (Eds.), *The nature and origin of Cordilleran magmatism.* Geological Society of America, 147-168.

Goldhaber, M.B. (1983): Experimental study of metastable sulfur oxyanion formation during pyrite oxidation at pH 6-9 and 30°C. Am. J. Sci. **283**, 193-217.

Goleva, G.A., Krivenokov, V.A. & Gutz, Z.G. (1970): Geochemical trends in the occurrence and migration of gold in natural water. Geochem. Int. **7**, 518-529.

Graf, R.B. (1968): The system Ag_3AuS_2 - Ag_2S. Am. Mineral. **53**, 496-500.

Guilbert, J.M. & Parks, C.F., Jr. (1986): *The Geology of Ore Deposits.* New York, New York, W. H. Freeman and Company, 567 pp.

Hammerstrom, J.M. & Zen, E.-A. (1986): Aluminum in hornblende: an empirical igneous geobarometer. *Am. Mineral.* **64**, 953-965.

Hanmer, S. & Cees, P. (1991): Shear-sense indicators: A review. *Geological Survey of Canada Paper* **90-17,** 72 p.

Hawthorne, F.C. (1981): Crystal chemistry of the amphiboles. In Veblen, D.R. (Eds.), *Amphiboles and other hydrous pyriboles - mineralogy.* Washington, D.C., Mineralogical Society of America, 1-93.

Hayba, D.O., Bethke, P.M., Heald, P. and Foley, N.K. (1985): Geologic, mineralogic and geochemical characteristics of volcanic-hosted epithermal precious-metal deposits. *Reviews in Economic Geology*, **2**, 129-167.

Hazlett, R.W. (1990): Extension-related volcanism in the Mopah Range volcanic field, southeastern California. In Anderson, J.L. (Eds.), *The nature and origin of Cordilleran magmatism.* Geological Society of America, 133-145.

Henley, R.W. and Brown, K.L. (1985): A practical guide to the thermodynamics of geothermal fluids and hydrothermal ore deposits. *Reviews in Economic Geology*, **2**, 25-44.

Hewett, D.F. (1956): Geology and mineral resources of the Ivanpah Quadrangle California and Nevada. *U.S. Geological Survey, Professional Paper* **275**, 172 p.

Hewett, D.F., Strong, J. & Stieff, L.R. (1969): The ages of three uranium minerals, Mojave Desert, California. *U. S. Geological Survey, Professional Paper* **650-B**, B84-B88.

Higgins, M.W. (1971): Cataclastic rocks. *U. S. Geological Survey, Professional Paper* **687**, 97 p.

Hoisch, T.D., Heizler, M.T., Harrison, T.M., Miller, C.F. & Stoddard, E.F. (1988): Late Cretaceous regional metamorphism in southeastern California. In Ernst, W.G. (Eds.), *Metamorphism and Crustal Evolution of the Western United States (Rubey Volume 7)* New Jersey, Prentice Hall, 538-571.

Hollister, L.S., Grissom, G.C., Peters, E.K., Stowell, H.H. & Sisson, V.B. (1987): Confirmation of the empirical correlation of Al in hornblende with products of solidification in calc-alkaline plutons. *Am. Mineral.* **72**, 231-239.

Howard, K.A. & John, B.E. (1987): Crustal extension along a rooted system of imbricate low-angle faults: Colorado River Extensional Corridor, California and Arizona. *Geological Society London Special Publication* **28**, 299-311.

Howard, K.A., John, B.E. & Miller, C.F. (1987): Metamorphic core complexes, Mesozoic ductile thrusts and Cenozoic detachment: Old Women Mountains-Chemehuevi Mountains transect, California and Arizona. In Davis, G.H. & VandenDolder, E.M. (Eds.), *Geologic diversity of Arizona and its margins.* Arizona Bureau of Geology and Mineral Technology, Geological Survey Branch, 365-382.

Irvine, T.N. & Baragar, R.A. (1971): A guide to chemical classification of the common volcanic rocks. *Can. Jour. Earth Sci.* **8**, 523-548.

Ishihara, S. (1977): The magnetite-series and ilmenite-series granitic rocks. *Mining Geol.* **27**, 293-305.

Jackson, M.L., Whittig, L.D. & Pennington, R.P. (1949): Segregation procedure for the mineralogical analysis of soils. *Soil Sci. Soc. Amer. Proc.* **14**, 77-81.

Jaffe, H.W., Gottfried, D., Waring, C.L. & Worthing, H.W. (1959): Lead-alpha age determinations of accessory minerals in igneous rocks (1953-1957). *U. S. Geological Survey Bulletin* **1097-B**, 148 pp.

Jessey, D.R. & Fallis, C.N. (1989): The Mohawk mine: A base metal-silver deposit related to possible Late Cretaceous normal-slip movement within the Clark Mountain

thrust complex, San Bernardino County, California. In Bureau of Land Management's California Desert Mineral Symposium, Compendium Volume (pp. 163-176).

John, B.E. & Wooden, J.L. (1990): Petrology and geochemistry of the metaluminous to peraluminous Chemehuevi Mountain plutonic suite, southeastern California. In Anderson, J.L. (Eds.), *The nature and origin of Cordilleran magmatism.* Geological Society of America, 111-132.

Johnson, M.C. & Rutherford, M.J. (1989): Experimental calibration of the aluminum-in-hornblende geobarometer with applications to Long Valley Caldera (California) volcanic rocks. *Geology* **17**, 837-841.

Katz, M. & Boettcher, A. (1980): The Cima volcanic field. In Fife, D.L. & Brown, A.R. (Eds.), *Geology and Mineral Wealth of the California Desert (Dibblee Volume).1* Santa Ana, California, South Coast Geological Society, 236-24.

Kerrich, R. (1986): Fluid infiltration into fault zones: Chemical, isotopic, and mechanical effects: *Pure Applied Geophysics*, **124**, p. 225-268.

Kerrich, R. and Allison, I. (1986): Vein geometry and hydrostatics during Yellowknife mineralization. *Canadian Jour. Earth Science*, **15**, 1653-1660.

Kistler, R.W. (1974): Phanerozoic batholiths in western North America. *Annual Rev. Earth Planet. Sci.* **2**, 403-418.

Kistler, R.W., Everndon, J.F. & Shaw, H.R. (1971): Sierra Nevada plutonic cycles: Part 1, Origin of composite granitic batholiths. *Geologic Society of America Bulletin* **82**, 853-868.Koshman, P.N. & Yugay, T.A. (1972): The causes of variation in fineness levels of gold placers. Geochem. Int. **9**, 481-484.

Krauskopf, K.B. (1951): The solubility of gold. Econ. Geol. **46**, 858-870.

Kretz, R. & Jen, L.S. (1978): Effect of temperature on the distribution of Mg and Fe(+2) between calcic pyroxene and hornblende. *Can. Mineral.* **16**, 533-537.

Kunze, G.W. (1965): Pretreatment for mineralogical analysis. In Black, C.A. (Eds.), *Methods of soil analysis - Part I.* Madison, Wisconsin, American Society of Agronomy, Inc., 568-577.

Labotka, T.C., Albee, A.L., Lanphere, M.A. & McDowell, S.D. (1980): Stratigraphic, structural and metamorphism in the central Panamint Mountains (Telescope Peak Quadrangle), Death Valley area, California. *Geol. Soc. Amer. Bull.* **91**(Part II), 843-933.

Labotka, T.C., Warasila, R.L. & Spangler, R.R. (1985): Polymetamorphism in the Panamint Mountains, California, $^{39}Ar/^{40}Ar$ study. *Journal of Geophysics Research* **90**, 10359-10372.

Lanphere, M.A. (1964): Geochronologic studies in the eastern Mojave desert, California. *Jour. Geol.* **72**, 381-399.

Larkin, H.W., Curtin, G.C. & Hubert, A.E. (1974): Geochemistry of gold in the weathering cycle. U.S. Geol. Surv. Bull. 1330, 80 pp.

Law, R.D. (1990): Crystallographic fabrics: a selective review of their applications to research in structural geology. In Knipe, R.J. & Rutter, E.H. (Eds.), *Deformation Mechanisms, Rheology and Tectonic.* Geological Society, 335-352.

Lister, G.S. (1977): Discussion: Crossed girdle c-axis fabrics in quartzites plastically deformed by plane strain and progressive simple shear. *Tectonophy.* **39**, 51-54.

Lister, G.S. & Hobbs, B.E. (1980): The simulation of fabric development during plastic deformation of quartzite and its application to quartzite: The effect of deformation history. *Journal of Structural Geology* **2**, 355-370.

Lister, G.S. & Snoke, A.W. (1984): S-C mylonites. *Journal of Structural Petrology* **6**, 617-638.

Logan, J.M. & Decker, C.L. (1994): Cyclic fluid flow along faults. Proc. Conf. LXIII, *The Mechanical Involvement of Fluids in Faulting, U. S. G. S. Open-file Report* **94-228**, 190-203.

Logan, J.M., Friedman, M., Higgs, N., Dengo, C., & Shimamoto, T., (1979): Experimental studies of simulated gouge and their application to studies of natural fault zones. Proc. Conf. VIII, *Analysis of Actual Crustal Rocks, U. S. G. S. Open-file Report* **79-1239**, 305-43.

MacEwan, D.M.C. & Ruiz-Amil, A. (1975): Interstratified clay minerals. In Giesenking, J.E. (Eds.), *Soil components, Volume 2: Inorganic components.* New York, New York, Springer-Verlag, 265-334.

Mackay, R.A. (1944): The purity of native gold as a criterion in secondary enrichment. Econ. Geol. **39**, 56-68.

Mancktelow, N. (1991): A least-squares method for determining the best-fit point maxima, great circle and small circle to nondirectional orientation data. *Mathematical Geology* **13**, 507-521.

Mann, A.W. (1984): Mobility of gold and silver in lateritic weathering profiles: Some observations from western Australia. Econ. Geol. **79**, 38-49.

Mann, A.W. & Deutscher, R.L. (1984): Solution geochemistry of lead and zinc in water containing carbonate, sulfate and chloride ions. Chem. Geol. **29**, 293-311.

Marryott, R.A. (1986): Some petrologic and geochemical characteristics of the San Andreas fault at the Stone Canyon Well, San Benito County, California. M.S. Thesis, University of California at Riverside.

Martin, D.L., Krummenacher, D. & Frost, E.G. (1982): K-Ar Geochronologic record of Mesozoic and Tertiary tectonics of the Big Maria-Little Maria-Riverside Mountain

Terrane. In Frost, E.G. & Martin, D.L. (Eds.), *Mesozoic-Cenozoic Tectonic Evolution of the Colorado River Region, California, Arizona and Nevada (Anderson-Hamilton Volume).* San Diego, Cordilleran Publishing, 518-549.

McCurry, M. (1980): A preliminary report of a large silicic volcanic center in the eastern Mojave Desert, San Bernardino County, California. In Fife, D.L. & Brown, A.R. (Eds.), *Geology and Mineral Wealth of the California Desert (Dibblee Volume).* Santa Ana, California, South Coast Geological Society Publishing, 495-504.

Mehra, O.P. & Jackson, M.L. (1960): Iron oxide removal from soils and clays by a diathionite-citrate system buffered with sodium bicarbonate. *Clays and Clay Mineralogy* **7**, 317-327.

Miller, C.F. (1978): Monzonite plutons, California, and a model for generation of alkali-rich, near silica-saturated magmas. *Contrib. Mineral. Petrol.* **67**, 349-355.

Miyashiro, A. (1974): Volcanic rock series in island arcs and active volcanic margins. *Am. J. Sci.* **274**, 321-355.

Nelson, E.P. (1976): Analysis of foreland basement deformation associated with the Clark Mountain Thrust Complex. M. S. Thesis, Rice University.

Nelson, E.P. & Burchfiel, B.C. (1979): Deformation of autochthonous foreland basement, Clark Mountain thrust complex, southeastern California. In Newman, G.W. & Goode, H.D. (Ed.), Basin and Range Symposium and Great Basin Field Conference., (pp. 107-114). Rocky Mountain Association of Geologist-Utah Geological Association.

Ntiamoah-Agyakwa, Y. (1987): Geology, hydrothermal mineralization and geochemical exploration, New York Mountains and northern Mid Hills areas, San Bernardino County, California. Ph.D. Dissertation, University of California at Los Angeles.

Olsen, J.C. (1954): Rare earth mineral deposits of the Mountain Pass District, San Bernardino County, California. *U.S.G.S. Prof. Paper* **261**.

Plyusnin, A.M., Pogrelnyak, Y.F., Mironov, A.G. & Zhmodik, S.M. (1981): The behavior of gold in the oxidation of gold-bearing sulfides. Geochem. Int. **18(3)**, 116-123.

Price, G.P. (1985): Preferred orientations in quartzites. In Wenk, H.-R. (Eds.), *Preferred Orientation in Deformed Metals and Rocks: An Introduction to Modern Texture Analysis.* Orlando, Florida, Academic Press, Inc., 385-406.

Renders, P.J. & Seward, T.M. (1989): The solubility of hydrosulfido- and sulfido-complexes of Au(I) and Ag(I) at 25°C. Geochim. Cosmochim. Acta. **53**, 245-253.

Rich, C.I. & Barnhisel (1977): Preparation of clay samples for X-ray diffraction analysis. In Dixon, J.B.W., S. B. (Eds.), *Minerals in soil environments.* Madison, Wisconsin, Soil Science Society of America, 797-808.

Ririe, G.T. (1988): Report to Vanderbilt Gold Corporation on a lead isotope study of the Morning Star gold mine. unpublished report, 6 pp.

Robinson, J.P. (1979): Petrology and petrochemistry of granitic intrusives of the Cima Dome-southern Ivanpah Mountains area, southeastern California. M.S. Thesis, University of Southern California.

Rutter, M.J., Van der Laan, S.R. & Wyllie, P.J. (1989): Experimental data for a proposed empirical igneous geobarometer: aluminum in hornblende at 10 Kbars pressure. *Geology* **17**, 897-890.

Sammis, C.G., Osborne, R.H., Anderson, J.L., Mavonwe, B. & White, P. (1986): Self-similar cataclasis in the formation of fault gouge. *Pure Applied Geophy.* **124**, 53-78.

Schmid, S.M. & Casey, M. (1986): Complete fabric analysis of some commonly observed quartz c-axis patterns. In Hobbs, B.E. & Heard, H.C. (Eds.), *Mineral and Rock Deformation: Laboratory Studies - The Paterson Volume.* American Geophysical Union, 263-286.

Scholz, C.H., Molnar, P. & Johnson, T. (1972): Detailed studies of frictional sliding of granite and implications for earthquake mechanism. *Jour. Geophy. Res.* **77**, 6392-6402.

Schoonen, M.A.A., Fisher, N.S. & Wente, M. (1992): Gold sorption onto pyrite and goethite: A radiotracer study. Geochim. Cosmochim. Acta **56**, 1801-1814.

Scott, S.D. and Barnes, H.L. (1971): Sphalerite geothermometry and geobarometry. *Economic Geology*, **66**, 653-669.

Seward, T.M. (1976): The solubility of chloride complexes of silver in hydrothermal solutions up to 350°C. Geochim. Cosmochim. Acta **40**, 1329-1341.

Sharp, J.E. (1984): A gold mineralized breccia pipe complex in the Clark Mountains, San Bernardino County, California. In Wilkins, J., Jr. (Eds.), *Gold and Silver Deposits of the Basin and Range Province Western U. S. A.* Tucson, Arizona, Arizona Geological Society, 119-139.

Shea, W.T. & Kronenberg, A.K. (1992): Rheology and deformation mechanisms of an isotopic mica schist. *Jour. Geophys. Res.* 97, 15201-15237.

Sheets, R.W., Bodnar, R.J., Craig, J.R. & Ausburn, K.E. (1988): Precious-metal mineralization at the Morning Star deposit, San Bernardino County, California. Geol. Soc. Am. Abstr. Program **20**, p. A142.

Sheets, R.W., Ausburn, K., Bodnar, R.J., Craig, J.R. & Law, R.D. (1989): Geology and precious-metal mineralization at the Morning Star deposit, San Bernardino County, California. In Bureau of Land Management's California Desert Mineral Symposium, Compendium Volume (pp. 219-232). Los Angles, California: Bureau of Land Management.

Sibson, R.H. (1977): Fault rocks and fault mechanisms. *Jour. Geol. Soc. London* **133**, 191-213.

Sibson, R. H. (1987): Earthquake rupturing as a mineralizing agent in hydrothermal systems: *Geology*, **15**, p. 701-704.

Sibson, R. H., Roberts, F., and Poulsen, K. H. (1988): High-angle reverse faults, fluid pressure cycling, and mesothermal gold-quartz deposits: *Geology*, **16**, p. 551-555.

Silberman, M.L. and Berger, B.R. (1985): Relationship of trace-element patterns to alteration and morphology in epithermal precious-metal deposits. *Reviews in Economic Geology*, **2**, 203-232.

Simpson, C. (1985): Deformation of granitic rocks across the brittle-ductile transition. *Journal of Structural Geology* **7**, 503-511.

Smith, E.I., Feuerbach, D.L., Naumann, T.R. & Mills, J.G. (1991): Mid-Miocene volcanic and plutonic rocks in the Lake Mead area of Nevada and Arizona: Production of intermediate igneous rocks in an extensional environment. In Anderson, J.L. (Eds.), *The nature and origin of Cordilleran magmatism.* Geological Society of America, 169-194.

Speer, J.A. (1984): Micas in igneous rocks. In Bailey, S.W. (Eds.), *Micas.* Washington, D.C., Mineralogical Soc. America, 299-356.

Starkey, J. (1989): The contouring of oriented data represented in spherical projection. *Can. Jour. Earth Sci.* **20**, 268-277.

Stoffregen, R. (1986): Observations on the behavior of gold during supergene oxidation at Summitville, Colorado, U.S.A., and implications for electrum stability in the weathering environment. Applied Geochem. **1**, 549-558.

Streckheisen, A. (1976): To each plutonic rock its proper name. *Earth Sci. Review* **12**, 1-33.

Suppe, J. (1985): *Principles of Structural Geology.* Newark, New Jersey, Prentice-Hall, Pages.

Sutter, J.F. (1968): Geochronology of major thrusts, southern Great Basin, California. M.S. Thesis, Rice University.

Tanner, C.B. & Jackson, M.L. (1947): Nonographs of sedimentation times for soil particles under gravity or centrifugal acceleration. *Soil Sci. Soc. Amer. Proc.* **12**, 60-65.

Taylor, L. A. (1969): The significance of twinning in Ag_2S. Amer. Mineral., **54**, 961-963

Thomas, W.M. & Ernst, W.G. (1990): The aluminum content of hornblende in calc-alkaline granitic rocks: A mineralogic barometer calibrated experimentally to 12 Kbars. In Spencer, R.J. & Chou, I.-M. (Eds.), *Fluid-mineral interactions: A tribute to H. P. Eugster.* Geochemical Society, 59-63.

Thompson, D.F. (1978): The geology of the Evening Star Tin Mine and surrounding region, San Bernardino, California. M. S. Thesis, University of Missouri-Rolla.

Thorez, J. (1975): Phyllosilicates and clay minerals. 6th Ed., Lelotte, Dison, Belgique, 579 pp.

Tosdal, R.M., Haxel, G.B. & Wright, J.E. (1989): Jurassic geology of the Sonoran Desert region, southern Arizona, southeastern California and northern Sonora: Construction of a continental-margin magmatic arc. In Jenney, J.P. & Reynolds, S.J. (Eds.), *Geologic evolution of Arizona.* Tuscon, Arizona, Arizona Geological Society,

Tucker, W.B. & Sampson, R.J. (1943a): Los Angeles Field District: Current mining activity in southern California. *California Journal of Mines and Geology State Mineralogists Report* **39**, 118-138.

Tucker, W.B. & Sampson, R.J. (1943b): Los Angeles Field District: Mineral resources of San Bernardino County. *California Journal of Mines and Geology State Mineralogists Report* **39**, 427-549.

Tullis, J., Christe, J.M. & Griggs, D.T. (1973): Microstructures and preferred orientation of experimentally deformed quartzites. *Bulletin of the Geological Society of America* **84**, 297-314.

Vlassopoulos, D. & Wood, S.A. (1990): Gold speciation in natural waters: I. Solubility and hydrolysis reactions of gold in aqueous solutions. Geochim. Cosmochim. Acta. **54**, 3-12.

Vlassopoulos, D., Wood, S.A. & Mucci, A. (1990): Gold speciation in natural waters: II. The importance of organic complexing - Experiments with some simple organic complexing. Geochim. Cosmochim. Acta. **54**, 1575-1586.

Wahlstom, E.E., Robinson, C.S. & Nichols, T.C. (1968): Swelling of rocks in faults in the Roberts Tunnel, Colorado. In Kiersch, G.A. (Eds.), *Engineering geology case histories.* Geological Society of America, 83-89.

Walker, J.P. (1987): Permian and Triassic rocks of the Mojave Desert. In Dickenson, W.R. & Klute, M.A. (Eds.), *Mesozoic rocks of southern Arizona and adjacent areas.* Tuscon, Arizona, Arizona Geological Society, 1-14.

Webster, J.G. (1986): The solubility of gold and silver in the system Au-Ag-S-O_2-H_2O at 25°C and 1 atm. Geochim. Cosmochim. Acta. **50**, 1837-1845.

Webster, J.G. & Mann, A.W. (1984): The influence of climate, geomorphology and primary geology on the supergene migration of gold and silver. J. Geochem. Expl. **22**, 21-42.

Weisenberg, C.W. (1973): Petrology and structure of the Ivanpah Mountains area, California. M.S. Thesis, Rice University.

White, S.H. (1976): The effects of strain on the microstructures, fabric and deformation mechanism in quartzite. *Philos. Trans. R. Soc. Lond. Ser. A* **283**, 69-86.

Wilkins, J., Jr. (1984): The distribution of gold- and silver-bearing deposits in the Basin and Range Province, western United States. In Wilkins, J., Jr. (Eds.), *Gold and Silver Deposits of the Basin and Range Province Western U. S. A.* Tucson, Arizona, Arizona Geological Society, 1-27.

Wilkins, J. Jr., Beane, R. E., and Heidrick, T. L., 1986, Mineralization related to detachment faults: a model: in Beatty, B. and Wilkinson, P. A. K., eds., Frontiers in geology and ore deposits of Arizona and the southwest: *Arizona Geological Society Digest*, **16**, p. 108-117.

Williamson, M.A. & Rimstidt, J.D. (1992): Correlation between structure and thermodynamic properties of aqueous sulfur species. Geochim. Cosmochim. Acta **56**, 3867-3880.

Wones, D.R. (1981): Mafic silicates as indicators of intensive variables in granitic magmas. *Mining Geol.* **31**, 191-212.

Wooden, J.L. & Miller, D.M. (1990): Chronologic and isotopic framework for Early Proterozoic crustal evolution in the eastern Mojave Desert region, SE California. *Jour. Geophy. Res.* **95B**, 20133-20146.

Wooden, J.L., Stacey, J.S., Howard, K.A., Doe, B.R. & Miller, S.M. (1988): Pb isotopic evidence for the formation of Proterozoic crust in the southwestern United States. In Ernst, W.G. (Eds.), *Metamorphism and Crustal Evolution of the Western U.S.* Englewood Cliffs, N.J., Prentice Hall, 68-86.

Wright, L.A., Stewart, R.M., Gay, T.E., Jr. & Hazenbush, G.C. (1953): Mines and mineral deposits of San Bernardino County, California. *California Journal of Mines and Geology* **49**, 49-259.

Wu, F.T. (1978): Mineralogy and physical nature of clay gouge. *Pure Applied Geophy.* **116**, 655-689.

Wyllie, P.J. (1977): Crustal anatexis: an experimental review. *Tectonophy.* **43**, 41-72.

Young, E.D. & Wooden, J.L. (1988): Mid-Crustal emplacement of Mesozoic granitoids, eastern Mojave Desert: Evidence from crystallization barometry. *Geological Society of America Abstracts with Programs* **20**, 244.

Yund, R.A. & Tullis, J. (1991): Compositional changes of minerals associated with dynamic recrystallization. *Contrib. Mineral. Petrol.* **108**, 346-355.

Zartman, R.E. (1974): Lead isotopic provinces in the Cordilleran of the western United States and their geologic signatures. *Economic Geology*, **69**, 792-805.

Zotov, A.V., Levin, K.A., Katova, Z.Y. & Volchenkova, V.A. (1982): An experimental study of the stability of silver hydroxy-chloride complexes in hydrothermal solutions. Geochem. Int. **19**, 151-164.

Zotov, A.V., Levin, K.A., Khodakovskiy, I.L. & Kozlov, V.K. (1986): Thermodynamic parameters of Ag(I) chloride complexes in aqueous solutions at 273-623 K. Geochem. Int. **23**, 156-158.

Appendix A

Petrology of the Teutonia Batholith

Sixteen polished slabs and 86 polished thin sections were studied for petrologic relationships and modal analysis of the plutonic phases (Appendix A.1). Modal analysis was conducted by counting 500 to 1000 pionts per thin section. Mineral chemistry was determined using a Cameca SX50 electron microprobe operated at 25 KV, 20 nA and employing a ZAF-type data correction scheme supplied by Cameca. Twenty five whole rock samples were analyzed by Chemex Labs Ltd. (Spark, Nevada) for whole rock chemistry using ICP-AES (Appendix A.2). Detection limits for ICP-AES analyses are 0.01 weight percent per oxide, and duplicate samples and well characterized standards were analyzed to assess precision and accuracy.

Regional Geology

The Teutonia batholith intrudes Precambrian metasediments and meta-igneous basement complex, Grand Canyon series autochthonous and parautochthonous platform sedimentary rocks and Mojave Desert series allochthonous miogeoclinal sedimentary rocks (Chapter 1). These sedimentary sequences exhibit a weak regional metamorphism and localized contact metamorphism adjacent to igneous intrusions. The regional metamorphism is manifest by a regional resetting of K-Ar and Ar-Ar age dates that extends beyond the exposure of metamorphic rocks. Sedimentary rocks have been divided into an eastern section of Paleozoic-Mesozoic autochthonous and parautochthonous platform sedimentary facies, seen in the New Trail Canyon area, and a

western section of Precambrian-Permian allochthonous miogeoclinal sedimentary facies, seen in the Striped Hills area (Hewett, 1956; Burchfiel & Davis, 1971; Evans, 1971; Evans, 1974; Burchfiel & Davis, 1981; Burchfiel & Davis, 1988; Chapter 1).

The Teutonia batholith is overlain by Cenozoic volcanic and volcaniclastic units. A thick section of the Miocene Cima Dome volcanics rests unconformably on Teutonia batholith intrusions on the western flanks of Cima Dome and southern Mid Hills areas (Katz & Boettcher, 1980; McCurry, 1980; Buesch, 1991). Other volcanic and volcaniclastic units, especially south of Mid Hills area, include a sequence of extension related Miocene (26 to 6 Ma) extrusive volcanics also found elsewhere in the the Mojave Desert of California (Glazner, 1990; Hazlett, 1990; Buesch, 1991; Smith et al., 1991).

Teutonia Batholith

The Teutonia batholith is a composite batholith containing numerous intrusive phases. In this study, plutons have been divided into those that outcrop in the Ivanpah Mountains and those which are not found in the Ivanpah Mountains. Pluton names used in this study have been adopted from Weisenberg (1973) and Beckerman et al. (1982). This study concentrated on the plutons within the Ivanpah Mountains, but the other plutons are briefly described for completeness and comparison. Modal analyses, by point-counting, for plutons in the Ivanpah Mountains are summarized in Table A.1 and plotted on Figure A.1. Complete modal analyses for samples used in this study are given in Appendix A.1. Whole rock chemistry is given in Appendix A.2 and shown on Figures A.2 and A.3.

Table 2.1. Average modal analyses of Teutonia Batholith plutons.

PLUTON	Porphyritic Mid Hills	Equigranular Mid Hills	Live Oak Canyon	Black Canyon	Silica-rich Rock Springs	Silica-poor Rock Springs	Kessler Springs	Kessler Springs	Ivanpah	Ivanpah	Mafic Inclusion in Ivanpah	Striped Hills	Teutonia	Oro Wash	Morning Star Dike	Hornblende Diorite Dike
Number of Samples	17	4	5	3	7	4	5	4	8	15	2	5	5	2	8	2
Quartz	28.8±3.1	29.6±2.8	25.4±1.9	-	15.9±6.3	3.5±1.1	20.6±1.5	23.2±1.7	28.1±4.7	27.5±4.7	22.6±2.1	21.8±2.2	27.4±1.4	20.1±0.8	9.7±2.2	12.1±3.5
Alkali Feldspar	30.2±5.6	32.9±4.1	19.1±3.2	-	12.1±4.4	11.0±4.1	23.1±1.5	25.8±1.9	43.4±8.2	40.7±7.3	28.7±0.1	13.1±3.8	42.7±4.3	11.0±0.8	7.9±2.5	4.1±0.7
Plagioclase	36.8±4.5	30.3±6.1	43.6±3.2	44.2±16.2	53.1±4.1	57.7±2.8	41.1±3.2	39.7±3.5	19.2±5.7	19.1±4.0	30.9±2.4	35.3±3.5	23.9±5.8	38.8±0.1	39.5±8.2	46.1±4.2
Biotite	2.7±1.7	5.0±0.7	9.5±4.0	1.2±2.0	10.8±4.8	14.6±4.8	7.7±1.5	5.8±2.1	4.5±2.3	5.9±4.5	9.9±1.0	14.2±6.0	2.9±3.1	6.9±1.3	6.4±5.6	9.5±5.8
Hornblende	0.4±1.0	-	0.1±0.1	44.7±17.3	5.8±3.4	7.9±4.8	2.2±1.7	1.1±2.3	0.4±0.8	0.5±1.0	1.8±0.8	7.7±5.1	-	19.1±2.7	5.2±4.5	14.±01.8
Clinopyroxene	-	-	-	3.0±3.9	-	1.5±2.2	-	-	-	-	-	-	-	-	-	-
Opaque	0.5±0.3	1.9±0.8	1.2±0.5	6.5±3.2	1.0±0.4	1.8±1.2	1.5±1.0	2.2±1.5	1.0±0.2	3.2±1.9	3.9±2.2	2.4±1.2	0.8±0.4	2.3±0.8	8.3±3.1	8.0±7.4
Apatite	0.2±0.1	0.2±0.1	0.3±0.2	0.2±0.1	0.5±0.2	0.9±0.5	0.5±0.3	0.2±0.2	0.5±0.4	0.7±0.7	1.3±0.4	0.6±0.5	0.2±0.1	-	0.4±0.3	0.6±0.8
Sphene	0.1±0.2	0.2±0.3	0.3±0.2	0.2±0.3	0.7±0.3	0.9±0.3	1.7±0.5	0.8±0.8	0.8±1.3	0.2±0.2	0.2±0.1	0.3±0.3	0.0±0.1	0.7±0.9	0.2±0.3	-
Allanite	0.0±0.1	0.1±0.1	0.1±0.1	-	0.0±0.1	-	1.5±1.1	0.7±0.7	1.2±1.5	0.0±0.1	-	-	1.0±0.9	-	-	-
Zircon	0.0±0.1	0.1±0.2	0.1±0.2	0.1±0.1	-	0.1±0.1	0.1±0.1	0.2±0.1	0.1±0.0	0.7±0.8	0.2±0.1	0.6±0.7	0.1±0.0	0.1±0.1	0.4±0.6	-
Chlorite	-	-	-	-	-	-	-	0.1±0.1	-	1.0±1.5	0.1±0.1	1.8±1.6	-	0.6±0.7	12.0±4.0	3.8±1.5
Epidote	-	-	-	-	-	-	0.1±0.1	0.1±0.1	0.2±0.2	0.4±0.8	0.8±1.1	2.3±1.7	0.0±0.1	0.7±0.5	7.8±4.0	2.0±1.5
Calcite	-	-	-	-	-	-	-	0.1±0.2	-	-	-	-	-	-	1.0±1.9	-
Muscovite	-	-	-	-	-	-	-	0.2±0.5	0.5±0.9	0.2±0.5	-	-	1.1±1.8	0.1±0.1	1.2±1.6	-
Garnet	-	-	-	-	-	-	-	-	-	0.1±0.2	-	-	-	-	-	-
Total	99.7	100.2	100.2	100.1	99.9	99.9	100.1	100.2	99.9	100.2	100.4	100.1	100.1	100.4	100.0	100.2
Reference	Beckerman, 1982	Beckerman, 1982	Beckerman, 1982	Beckerman, 1982	Beckerman, 1982	Beckerman, 1982	Robinson, 1979	This Study	Robinson, 1979	This Study	This Study	This Study	Robinson, 1979	This Study	This Study	This Study

Figure A.1. Modal composition of Teutonia Batholith plutonic rocks. Nomenclature after Streckeisen (1976). Large fields are plotted from the data of Weisenberg (1973), Robinson (1979), Beckerman (1982) and Beckerman et al. (1982) and small data symbols are from this study.

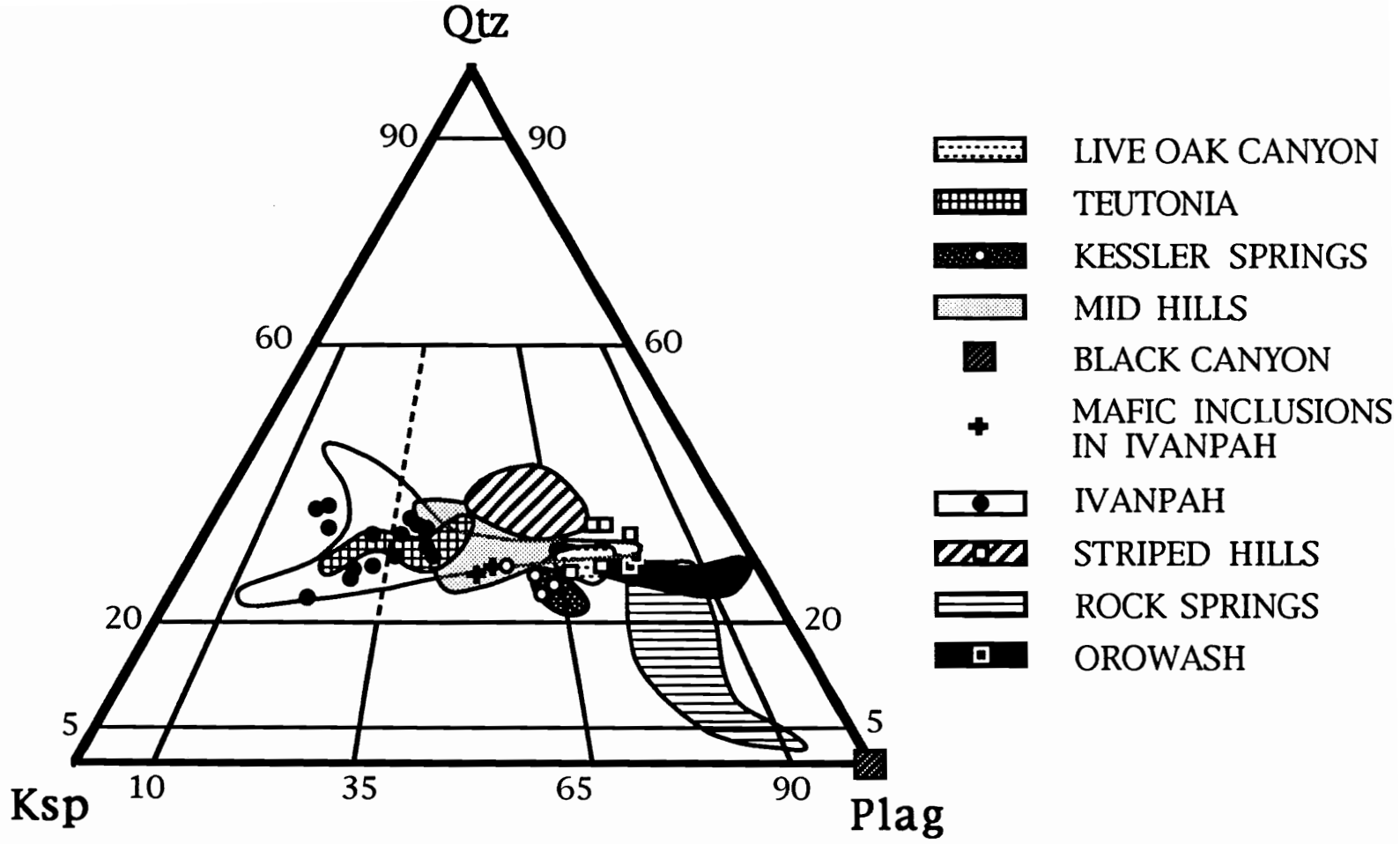
Qtz
90
90
60
60
20
20
5
5
Ksp
10
35
65
90
Plag
LIVE OAK CANYON
TEUTONIA
KESSLER SPRINGS
MID HILLS
BLACK CANYON
MAFIC INCLUSIONS IN IVANPAH
IVANPAH
STRIPED HILLS
ROCK SPRINGS
OROWASH

Plutonic Phases within the Ivanpah Mountains

Oro Wash Granodiorite

The Oro Wash granodiorite intrudes autochthonous Cambrian to Devonian platform sedimentary rocks and crops out as a series of small (3 to 4 km^2) plugs at the southeast end of Oro Wash (Figure 1.3). Weisenberg (1973) correlated the Oro Wash granodiorite with the 190 to 200 Ma Breccia pluton and the Pachulka Springs pluton in the Clark Mountains, because of similar petrographic characteristics, whereas Burchfiel and Davis (1971; 1988) assumed all similar granodiorites in the Clark and Ivanpah Mountains were temporally and genetically related. The Oro Wash pluton, a uniform fine-grained hornblende granodiorite, is highly fractured and has near vertical contacts with the platform sedimentary rocks. Skarn mineralization, some of which may be related to subsequent intrusion of the Ivanpah granite, forms at the Oro Wash pluton contacts. Euhedral zoned plagioclase (An_{33-48}) and prismatic hornblende comprise the major modal constituents of the granodiorite. Fine-grained hornblende commonly occurs in multigrain clusters, with biotite, apatite and magnetite forming rims around hornblende clusters. Fine-grained slightly altered augite also occurs in some of these clusters. Large poikilitic hornblendes are slightly zoned with more actinolitic cores, and contain plagioclase laths and opaque minerals inclusions throughout the whole mineral. Biotite and amphibole are commonly altered to chlorite, epidote and sphene. Quartz and perthitic alkali feldspars form interstitial masses and accessory zircon is also present. Accessory minerals crystallized early followed in order by plagioclase, clinopyroxene, hornblende, biotite, quartz and alkali feldspar.

Striped Hills Granodiorite

The Striped Hills granodiorite only crops out on the western margins of the Ivanpah Mountains where batholithic rocks intrude folded Paleozoic miogeoclinal sediments (Figure 1.3). Overturned folds in the carbonate sequence formed prior to intrusion of the pluton (Burchfiel & Davis, 1971). Sutter (1968) obtained K-Ar hornblende ages of 164.2±2.5 Ma for granodiorite at the eastern margin of the Striped Hills and younger reset ages ranging from 90 to 125 Ma .

The western contact is marked by up to 50 meter thick zones of skarn mineralization, silicification and recrystallization of the dolomitic limestone adjacent to the sharp, but irregular igneous contact. Granodiorite within a few meters of the contact is very fine-grained and extensively altered (endoskarn), but grain size increases and alteration decreases easterly away from the contact. The contact dips moderately westward along the western margin, but at the eastern extent of the Evening Star spur the dip shallows considerably.

The eastern contact between the Striped Hills granodiorite and Ivanpah granite is gradational although the exact contact is obscured by random aplite intrusions, discontinuous shear zones and brecciation. Modal abundance of hornblende and total mafic minerals decreases across the contact and grain size and modal biotite increase from the granodiorite into the granite. The gradational igneous contact roughly parallels the sharp igneous-sedimentary contact to the west.

The medium-grained biotite-hornblende granodiorite is slightly altered throughout and is cut by numerous aplite and pegmatite dikes. Mafic inclusions, similar to less altered inclusions found in the Ivanpah granite, occur but are very rare. Plagioclase, the most abundant mineral, occurs as large euhedral poikilitic laths. These laths are zoned

from calcic oligoclase and andesine cores (An_{25-33}) to albite and oligoclase rims (An_{5-18}), but cores are often preferentially saussuritized. Quartz occurs as large partially resorbed grains with a pronounced cataclastic texture or as interstitial masses around feldspars. Hornblende forms either large oikocrysts with inclusions of plagioclase, magnetite, apatite and zircon or as small interpenetrating aggregates with biotite and magnetite. The clusters of hornblende and biotite always exhibit alteration to epidote and sphene (subsolidus) and chlorite (hydrothermal?). Large isolated biotites are rare, but when present always contain abundant rutile needles. No other titaniferous opaque minerals were found in the granodiorite (see Mineral Chemistry section). Accessory zoned allanite is also present in the granodiorite. Crystallization sequence started with accessory minerals, then plagioclase and hornblende crystallized. Hornblende and biotite crystallization probably overlap in time with biotite crystallizing slightly later and for a longer period of time. These early minerals are followed by crystallization of Na-rich plagioclase, quartz and finally alkali feldspar.

Ivanpah Granite

The compositionally zoned Ivanpah granite underlies most of the Ivanpah Mountains (Figure 1.2 and 1.3). A minimum K/Ar age of 138 Ma has been determined for the Ivanpah granite (Sutter, 1968), and subsequent workers have suggested the granite may belong to a 158 to 132 Ma magmatic epoch (Robinson, 1979). Burchfiel and Davis (1971) and Weisenberg (1973) distinguished the Striped Hills granodiorite and Ivanpah granite during mapping, but believed that the Striped Hills granodiorite constituted a mafic differentiate of the Ivanpah granite that was produced when the Ivanpah granite reacted with the carbonate sequence. If this hypothesis is correct, an

approximate age of 165 Ma established for the Striped Hills granodiorite (Sutter, 1968), would also apply for the Ivanpah granite.

In the northeast Ivanpah Mountains, the Ivanpah granite is in contact with platform sedimentary rock of the New Trail Canyon and forms a thin, discontinuous (less than 1 meter thick) zone of sheared calc-silicate mineralization that grades into recrystallized dolomite. The majority of the New Trail Canyon skarn mineralization is located east of this contact or along parautochthonous thrusts (Figure 1.3). The carbonate-igneous rock contact has been mapped as a thrust fault dipping 35 to 45° westward under the main portion of the granite pluton. No mafic differentiate (Striped Hills granodiorite) occurs around the eastern contact. Further south, in the Kewanee Hills, a roof pendant of recrystallized Bonanza King Formation dolomite is enclosed in Ivanpah granite. No skarn mineralization is present, but the dolomite is completely recrystallized. Exploration drill holes that intersect the contact at variable depths cut interfingered granite and carbonate. The overall dip of the contact is approximately 45° to the southwest. The irregular nature of the contact and recrystallized dolomite favor an igneous contact instead of the previously mapped fault contact (Hewett, 1956) for the Kewanee Hills area.

The western margin forms a gradational igneous contact with the Striped Hills granodiorite and that contact mirrors the granodiorite-sediment contact farther west (described above). The southwestern margin forms a sharp igneous contact where intruded by Kessler Springs adamellite. A northwest trending wedge of Ivanpah granite also crops out between Kessler Springs and Teutonia adamellites on the northeastern edge of Cima Dome (Figure 1.3). Beckerman et al. (1982) also mapped small outliers of equigranular Ivanpah granite in the Ivanpah Valley and New York Mountains.

The Ivanpah granite ranges from coarse-grain to porphyritic and contains 5 to 25 percent mafic minerals, that are chiefly biotite. The general appearance is equigranular

with a slight magmatic foliation defined by aligned feldspar phenocrysts and mafic minerals, especially west of the Morning Star fault system. Locally, especially in the Cima Dome wedge and adjacent to the Striped Hills pluton, the foliation intensifies as mafic mineral abundance increases. The foliation was originally mapped as magmatic because it resembles flow structures around mafic inclusions and is truncated, without folding, by intrusion of the Kessler Springs adamellite (Robinson, 1979). The foliation is rare to absent northeast of the Morning Star fault system.

Another notable feature, although rare, is the occurrence of altered mafic to intermediate inclusions, mostly granodiorite, in the Ivanpah granite. The inclusions are fine grained and commonly contain chilled margins adjacent to the host granite. Subhedral plagioclase and prismatic hornblende occur in ophitic clusters with biotite and opaque minerals in the inclusions. Plagioclase is more abundant than alkali feldspar and quartz, in contrast to the granite where alkali feldspar dominates. Biotite is the most common mafic mineral followed by opaques. Accessory minerals include apatite, sphene and zircon. Minor chlorite and epidote alteration is sporadic in the inclusion cores but ubiquitous along the chill margins. These inclusions are mineralogically and texturally similar to biotite-rich portions of the Striped Hills granodiorite. Weisenberg (1973) also reported inclusions of porphyritic dacite and metasomatized Precambrian gneiss in the Ivanpah granite. None of these latter inclusions were found in Ivanpah granite on the eastern side of the Ivanpah Mountains. Aplite, pegmatite and hornblende diorite dikes are also common throughout the pluton. White bull quartz veins are common, even outside areas of known mineralization.

Poikilitic alkali feldspars are modally more abundant than oscillatory zoned plagioclase (An_{18-30}) and quartz in the Ivanpah granite. Perthitic intergrowths are common in all alkali feldspars in the pluton. Quartz forms large rounded grains which

exhibit undulatory extinction with cataclastic overprints, as well as small interstitial masses between euhedral to subhedral plagioclase laths and around large alkali feldspars. Biotite is the primary mafic mineral with a few samples containing hornblende. Primary muscovite was observed in a few samples and one muscovite-bearing sample also contained garnet. Although not observed in thin section, considerable fluorite was found in the heavy mineral separate of one sample (RWS-078) prepared for U-Pb geochronology. This sample is unaltered and far from all known areas of mineralization, so the fluorite may be magmatic in origin. Accessory minerals include allanite, sphene, opaques, apatite and zircon. Most samples exhibit subsolidus development of epidote, chlorite and sphene and hydrothermal alteration is prevalent around most mineral deposits.

Kessler Springs Adamellite

The porphyritic Kessler Springs adamellite (Weisenberg, 1973; Robinson, 1979; Beckerman et al., 1982) crops out in the valley between Cima Dome and Ivanpah Mountains and forms intrusive contacts with the Ivanpah granite and Teutonia adamellite (Figure 1.2 and 1.3). Kessler Springs adamellite is recognized by large (up to 8 cm) alkali feldspar oikocrysts, with subordinate amounts of plagioclase (An_{23-31}) phenocrysts in a medium grained, granular groundmass in which zoned plagioclase (An_{29-21}) is modally dominant over alkali feldspar and quartz. Near the intrusive contacts phenocrysts decrease in size and abundance and become elongated (Robinson, 1979). Biotite, minor hornblende, magnetite, sphene, allanite, apatite and zircon also occur in the Kessler Springs adamellite. Apatite and zircon are generally larger and more abundant in the Kessler Springs adamellite than in other plutons of the Teutonia batholith. Subsolidus

sphene, epidote and opaque minerals alter portions of biotite and hornblende clusters and chlorite rims biotite. Whole rock and hornblende K-Ar ages of 92.9±1.3 and 92.1±0.5 Ma, respectively, have been reported for the Kessler Springs adamellite (Sutter, 1968). Aplite dikes are abundant, but pegmatite dikes are rarer than in other plutons.

A small porphyritic pluton containing oikocrysts of alkali feldspar in a medium grained adamellite intruded the northern Ivanpah Mountains along the northern extension of the Morning Star fault system (Figure 1.3). This small intrusion is mineralogically and texturally the same as the Kessler Springs adamellite. The area where this pluton crops out has a low hummocky weathering pattern which is similar to the outcrop pattern of Kessler Springs adamellite in the northeastern Cima Dome area. For these reasons the pluton is considered to be part of the Kessler Springs adamellite.

Morning Star Dike

The Morning Star dike crops out below the Morning Star thrust fault in the eastern Ivanpah Mountains and Kewanee Hills (Figure 1.3 and also see Figure 3.1). Because of the dikes association with the thrust and Morning Star mineral deposit, the dike always exhibits some deformation textures and is hydrothermally altered. The freshest Morning Star dike samples crop out north of the Morning Star mine along the northern extension of the Morning Star thrust fault. Dike samples from the Kewanee Hills area exhibit more deformation but less alteration than samples in the vicinity of the Morning Star deposit. The Morning Star dike thins from the north (Morning Star mine area) to the south (Kewanee Hills area) and is truncated by the Morning Star fault, which requires pre-thrusting emplacement of the Morning Star dike. This field-based interpretation is

corroborated by exploration drill holes in the Kewanee Hills area which intersect granite carbonate contacts without the presence of the Morning Star dike.

Compositionally, the dike ranges from diorite to quartz monzodiorite (Table A.1). The freshest samples contain interpenetrating clusters of prismatic hornblende with anhedral biotite and euhedral magnetite. These mafic mineral clusters typically have rims of epidote with minor chlorite and sphene. Large isolated hornblende and biotite oikocrysts occur in some samples. Large biotites commonly contain rutile needle inclusions, but the needles are less abundant than in other granitic phases of the batholith. Some large biotites have kink bands and folded basal cleavage planes. Euhedral to subhedral plagioclase (An_{23-35}) is modally more abundant than anhedral alkali feldspar and quartz; the latter minerals form interstitial masses. Little or no zoning was observed in the plagioclase. Accessory minerals include magnetite, sphene and zircon. The order of crystallization was accessory minerals first followed by plagioclase and hornblende. Biotite crystallization overlapped with hornblende, but continued well beyond that of hornblende. Alkali feldspar and quartz crystallized last.

Mafic minerals are commonly altered to chlorite and epidote and in the most altered samples feldspars are completely replaced by sericite. Monomineralic shear bands of chlorite and veins of carbonate increase in abundance towards the Morning Star thrust fault in the Morning Star mine area. Quartz always exhibits some evidence of cataclastic deformation and bands of cataclastic diorite occur at structurally higher levels in the dike. A more detailed description of the deformation and alteration of the Morning Star diorite is presented in Chapter 2.

Delfonte Formation Volcanics

The Delfonte Formation, composed of four basaltic to rhyolitic pyroclastic and volcaniclastic sedimentary units, crops out in the southern Clark Mountains where it is cut by the basal thrust of the Keaney/Mollusk Mine thrust plate (Sutter, 1968; Burchfiel & Davis, 1971). Although the volcanic units rest unconformably on the lower Jurassic Aztec sandstone and are assumed to be Jurassic in age (Hewett, 1956; Burchfiel & Davis, 1971), Sutter (1968) obtained a whole rock K-Ar age of 86.2±1.0 Ma for a rhyolite tuff unit within the formation. Weisenberg (1973) hypothesized that the flow banded rhyolitic Piute Valley Plug, found in the northern New Trail Canyon area at the Ivanpah granite-Bonanza King Formation contact, represent the feeder zones for the Delfonte Formation volcanics. Numerous small volcanic dikes occur throughout the Ivanpah Mountains, although no other Mesozoic pyroclastic or volcaniclastic units have been found.

Dikes

Weisenberg (1973) described a series of fine-grained dacite dikes, the Cima Road dikes, which crop out on the west and south sides of the Ivanpah Mountains and throughout Cima Dome area. Smaller versions (less than 1 meter wide) of this suite of dikes occur in the eastern Ivanpah Mountains and within the Morning Star mine. The dacite dikes of the eastern Ivanpah Mountains contain plagioclase (An_{23-29}), biotite and chloritized hornblende microcrysts in a fine grained feldspar plus quartz groundmass. Accessory sphene, allanite and opaques are common. No age determinations are available for these dikes, but they clearly post date intrusion of the Ivanpah granite (>138 Ma) and pre-date ductile deformation on the Morning Star fault zone (105 to 90 Ma).

Plutonic Phases outside the Ivanpah Mountains

Plutonic phases outside the Ivanpah Mountains will be briefly described because they place constraints on the geologic evolution of the Ivanpah Mountains. This summary is taken from Robinson (1979), Beckerman (1982) and Beckerman et al. (1982) and for a more detailed description of the plutonic phases outside the Ivanpah granite refer to these references. The Kessler Springs adamellite and Ivanpah granite which are largely confined to the Ivanpah Mountains were described in the section above although they have been mapped in other areas underlain by the Teutonia batholith (Beckerman et al., 1982).

Rock Springs Monzodiorite

The compositionally zoned Rock Springs monzodiorite, which underlies most of the southeastern Mid Hills (Figure 1.2), intruded Precambrian metamorphic rocks and is cut by the Mid Hills adamellite (Beckerman, 1982; Beckerman et al., 1982). A K-Ar hornblende age of 168.4±11.8 Ma indicates a Jurassic age for the intrusion (Beckerman, 1982), thus making the Rock Springs monzodiorite, Striped Hills granodiorite and possibly Ivanpah granite the only Jurassic plutons of the batholith. Composition varies from biotite-clinopyroxene diorite to hornblende-biotite quartz monzodiorite to granodiorite (Beckerman, 1982; Beckerman et al., 1982). Mineralogy includes oscillatory zoned plagioclase (An_{22-38}), quartz, titaniferous biotite, alkali feldspar, magnetite, clinopyroxene and/or hornblende and accessory sphene, allanite, apatite, garnet and zircon (Beckerman, 1982). Elongated and oriented mafic inclusions which are aligned to form a weak magmatic foliation are common features in the Rock Springs pluton (Beckerman, 1982; Beckerman et al., 1982), where the magmatic foliation is

similar to the foliation defined by Robinson (1979) and Weisenberg (1973) for the Ivanpah granite west of the Morning Star fault. Beckerman et al. (1982) interpreted these inclusions to be cognate xenoliths derived from an early chill margin, which is also similar to inclusions found in the Ivanpah granite (discussed above).

Mid Hills Adamellite

The equigranular to porphyritic Mid Hills biotite-bearing adamellite, the volumetrically largest intrusive phase of the Teutonia batholith (Figure 2.1), intrudes Precambrian gneisses and Paleozoic to Mesozoic platform sedimentary rocks in the New York Mountains and Mid Hills areas (Beckerman, 1982; Beckerman et al., 1982). The adamellite is leucocratic and contains plagioclase (An_{20-34}), alkali feldspar, quartz, biotite, minor hornblende, and accessory apatite, zircon, magnetite, sphene and allanite (Beckerman, 1982; Beckerman et al., 1982). Beckerman (1982) and Beckerman et al. (1982) define the crystallization sequence, which is nearly identical for all other Cretaceous plutons in the batholith including those found in the Ivanpah Mountains, to consists of early accessory minerals and magnetite followed in order by plagioclase, hornblende if present, biotite, quartz, and finally large alkali feldspar oikocrysts. K-Ar dates for hornblende and biotite vary considerably with the oldest being 104.5±3.7 Ma (Beckerman et al., 1982).

Black Canyon Hornblende Gabbro

The Black Canyon gabbro intruded as a plug into the Mid Hills adamellite (Figure 1.2). Beckerman et al. (1982) interpret the Black Canyon gabbro and Mid Hills

adamellite to be synchronous because of K-Ar hornblende ages of 107.2±8.0 Ma and 104.5±3.8 Ma for the Black Canyon gabbro and Mid Hills adamellite, respectively. Texturally the Black Canyon pluton ranges from a plagioclase cumulative to an equigranular to porphyritic gabbro, but always contains hornblende and plagioclase (An_{51-70}) with minor amounts of clinopyroxene and biotite, and accessory apatite, magnetite, sphene and zircon (Beckerman, 1982; Beckerman et al., 1982).

Teutonia Adamellite

The medium to coarse grained, equigranular Teutonia adamellite occurs exclusively in the Cima Dome area (Figure 1.2 and 1.3). This pluton differs from other phases of the batholith in that it contains only a few aplite and pegmatite dikes, but contains considerably more quartz veins (Beckerman et al., 1982). The modal abundance of alkali feldspar is dominant over plagioclase and quartz (Robinson, 1979), but alkali feldspar is not as modally abundant as in the Ivanpah granite (see Table A.1). Biotite, primary muscovite, Fe-Ti-oxides, allanite, apatite and zircon also occur in the adamellite (Robinson, 1979; Beckerman et al., 1982) Sphene, epidote, chlorite, carbonate and kaolinite occur as subsolidus or hydrothermal alteration phases (Robinson, 1979). The Teutonia adamellite is the only pluton in the batholith to contain ilmenite and magnetite (all others contain only magnetite) and no primary sphene (Beckerman et al., 1982).

Live Oak Canyon Granodiorite

The Live Oak Canyon granodiorite, which grades from porphyritic at the margins to massive and equigranular in the core (Beckerman et al., 1982), intrudes Paleozoic

platform sedimentary rocks in the northeastern New York Mountains (Figure 1.2). The eastern margin is truncated by the Slaughterhouse fault (Burchfiel & Davis, 1977; Beckerman et al., 1982). K-Ar age dates of the pluton range from 71.7±0.8 Ma, for an impure mineral separate from a porphyritic dike (Burchfiel & Davis, 1977), to 79.9±2.4 Ma for a biotite separate from the main pluton (Beckerman et al., 1982). The Live Oak Canyon granodiorite is chemically and modally similar to the Kessler Springs adamellite and contains oscillatory zoned plagioclase (An_{25-32}), quartz, alkali feldspar, biotite, sphene, magnetite, rare hornblende and accessory allanite, apatite and zircon (Beckerman et al., 1982).

Dikes

Dikes are abundant throughout the Ivanpah Mountains, Cima Dome and New York Mountains, and cut all plutonic phases of the batholith. These dikes have been divided into a syn-batholith fine-grained granitic suite and a post-batholith aphanitic andesite-rhyolite suite (Weisenberg, 1973; Robinson, 1979; Beckerman, 1982). Dikes of the granitic series range in composition from granite to granodiorite and in texture from leucocratic aplites to porphyries (Weisenberg, 1973; Beckerman et al., 1982). These dikes are most abundant near intrusion contacts and especially in the younger plutons (Cretaceous) of the batholith (Weisenberg, 1973; Beckerman et al., 1982). Phenocrysts of alkali feldspar, quartz and minor biotite occur in a groundmass of alkali feldspar, plagioclase, biotite with accessory allanite, opaques, apatite and zircon (Weisenberg, 1973; Beckerman et al., 1982). Hornblende is rare and primary muscovite was only

Figure A.2. Compositional trends of Teutonia Batholith plutons in terms of (A.) molecular ratio of $Al_2O_3/(CaO+Na_2O+K_2O)$ verse silica content, (B.) total alkalies verses silica content and (C.) FeO*/(FeO*+MgO) verses silica where FeO* represents total iron oxide. For samples containing both solid and open symbols, solid symbols represent data from Robinson (1979), Beckerman (1982) and Beckerman et al. (1982) and open symbols represent data from this study. Morning Star dike samples are from this study. The alkalic-subalkalic boundary is after Irvine and Barager (1971) and the tholeiitic-calc-alkaline boundary is after Miyashiro (1974).

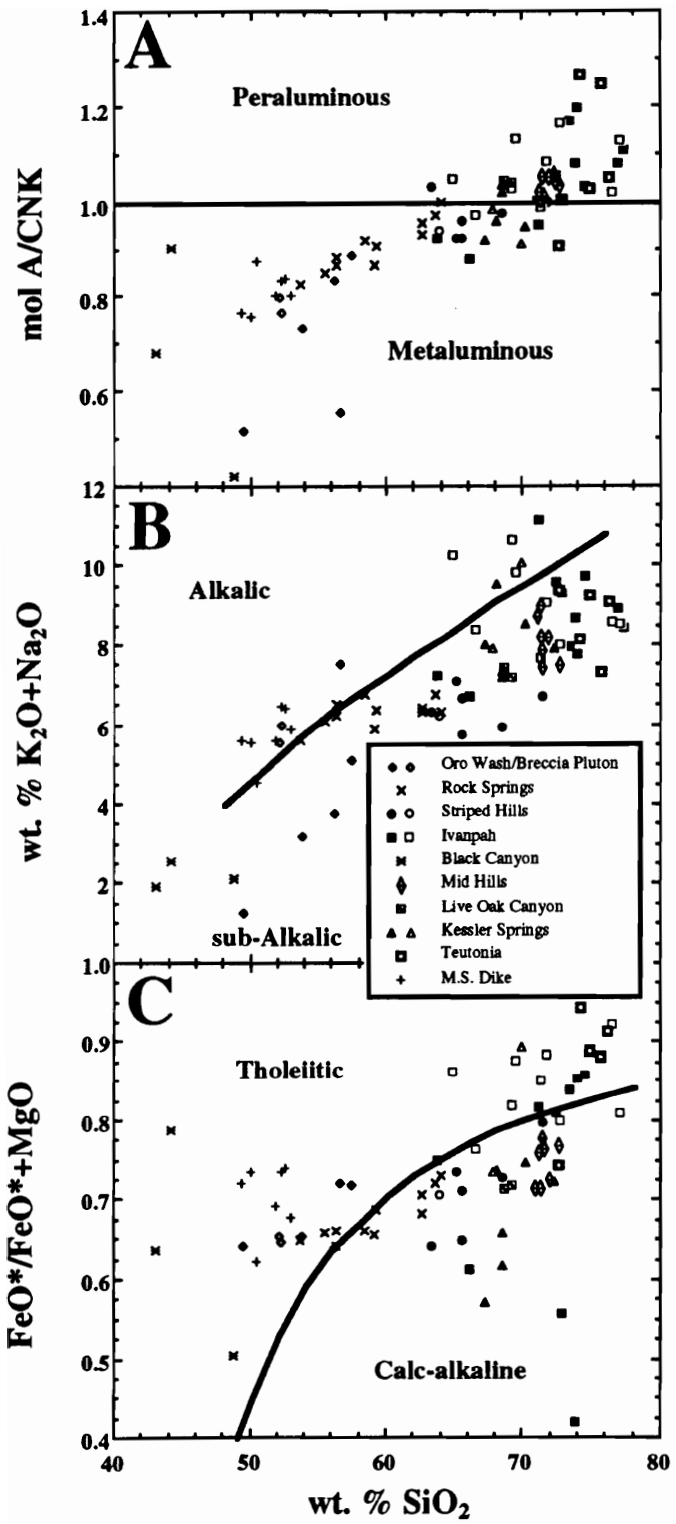
A
Peraluminous
Metaluminous
mol A/CNK
B
Alkalic
sub-Alkalic
wt. % K2O+Na2O
Oro Wash/Breccia Pluton
Rock Springs
Striped Hills
Ivanpah
Black Canyon
Mid Hills
Live Oak Canyon
Kessler Springs
Teutonia
M.S. Dike
C
Tholeiitic
Calc-alkaline
FeO*/FeO*+MgO
wt. % SiO2

Figure A.3. Major element variation diagrams for Teutonia batholith plutons. Symbols are the same as those used in Figure A.2. K_2O-SiO_2 boundary divisions are after Gill (1981).

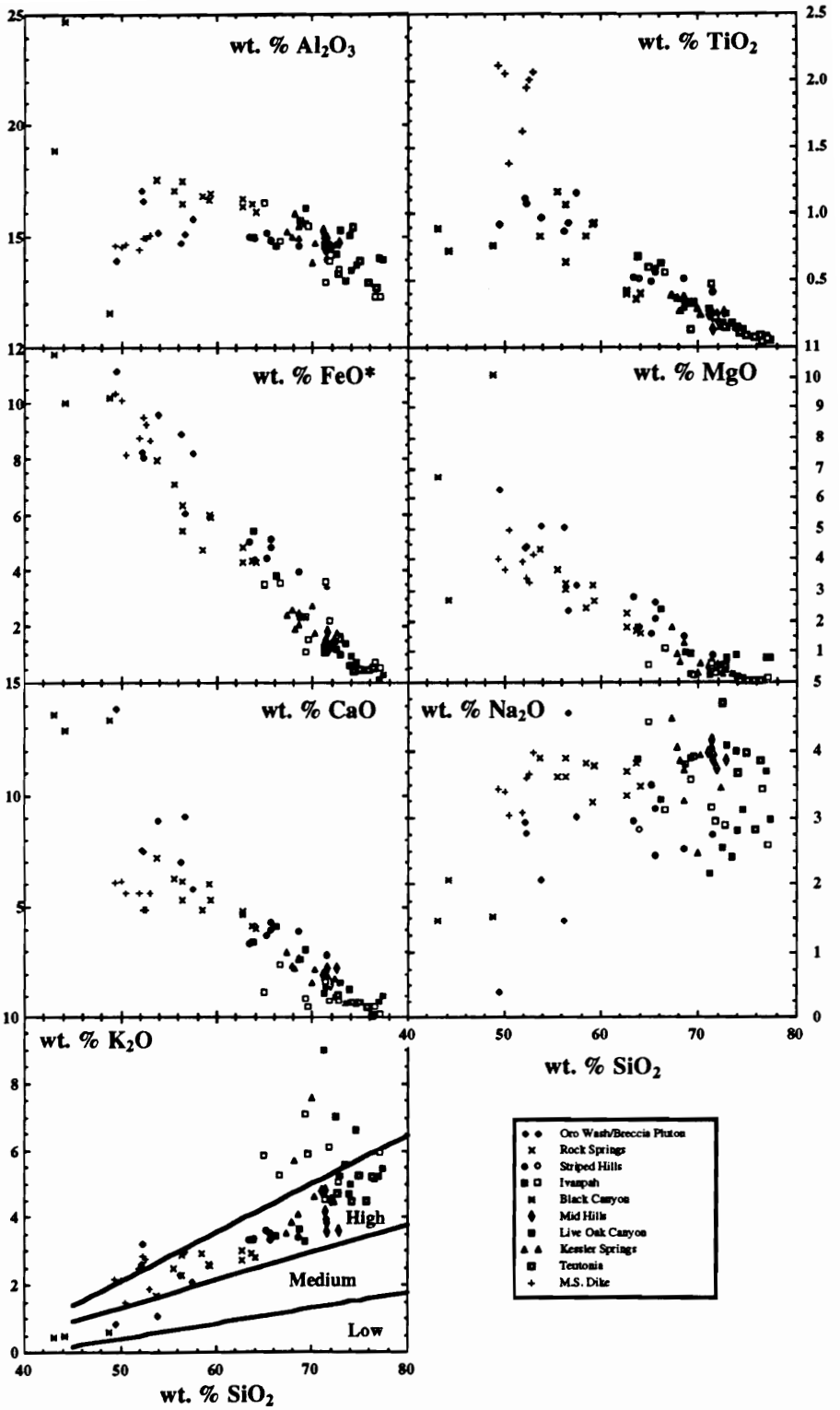
wt. % Al_2O_3
wt. % TiO_2
wt. % FeO*
wt. % MgO
wt. % CaO
wt. % Na_2O
wt. % K_2O
High
Medium
Low
wt. % SiO_2
wt. % SiO_2
Oro Wash/Breccia Pluton
Rock Springs
Striped Hills
Ivanpah
Black Canyon
Mid Hills
Live Oak Canyon
Kessler Springs
Teutonia
M.S. Dike

reported in one sample (Robinson, 1979). This suite of dikes can be traced to differentiated phases of the younger silicic portions of the Teutonia batholith (Beckerman et al., 1982). Other workers have correlated the granitic dikes to a regional set of east-west striking dike swarms found throughout the northeastern Mojave desert (Carlisle et al., 1982).

Post-batholithic porphyritic andesitic to dacitic dikes are prominent in the Cima Dome area (Weisenberg, 1973; Robinson, 1979), but less abundant in other areas of the Ivanpah Mountains. Phenocrysts and microcrysts of hornblende, biotite, plagioclase and sanidine occur in a matrix of predominantly plagioclase and quartz with minor hornblende, biotite, alkali feldspar and accessory sphene, opaques, allanite, apatite and zircon for dikes in the south and west portions of the Ivanpah Mountains (Weisenberg, 1973; Robinson, 1979). Dikes in the eastern portions of the Ivanpah Mountains are described above. The origin and age of post-batholith dikes are uncertain (Beckerman et al., 1982).

Composition and Mineral Chemistry of the Batholith

Whole Rock Chemistry

Whole rock chemistry for Teutonia batholithic rocks of the Ivanpah Mountains is given in Appendix A.2 and plotted on Figures A.2 and A.3. Robinson (1979), Beckerman (1982) and Beckerman et al. (1982) provide additional whole rock and trace element chemical data for batholithic rocks in the southernmost Ivanpah Mountains and New York Mountains-Mid Hills area. Data of Robinson (1979), Beckerman (1982) and

Beckerman et al. (1982) are plotted on Figures A.2 and A.3 for comparison to the data reported in this study.

All plutonic phases of the batholith are predominantly subalkalic except the late Morning Star dike (Figure A.2B). The Ivanpah granite is marginally alkalic as it straddles the alkalic-subalkalic divide defined by Irvine and Baragar (1971). A majority of the granitic intrusions have calc-alkaline affinities, while all mafic plutons have tholeiitic affinities according to the trends defined by Miyashiro (1974) (Figure A.2C). The Teutonia adamellite and Ivanpah granite have both calc-alkaline and tholeiitic affinities (Figure A.2C). The Rock Springs monzodiorite exhibits a trend which evolves from tholeiitic to calc-alkaline with increasing silica content (Figure A.2C).

All mafic plutons are metaluminous, except for the granitic plutons which straddle the metaluminous-peraluminous boundary defined by the molecular proportions of Al_2O_3 relative to the alkali and alkali-earth oxides (Figure A.2A). Only the Rock Springs monzodiorite and Striped Hills granodiorite are predominantly metaluminous and only the Mid Hills adamellite is competely peraluminous (Figure A.2A). Granitic rocks also exhibit evolutionary trends from metaluminous to peraluminous compositions with increasing silica contents. The most pronounced trend is exhibited by the Rock Springs monzodiorite which never achieves peraluminous $Al_2O_3/CaO+K_2O+Na_2O$ contents, and the Ivanpah granite. The marginally metaluminous and calc-alkaline affinities of the Teutonia batholith are similar to plutons of the Sierra Nevada batholith (Bateman et al., 1963; Bateman & Dodge, 1970; Miller, 1978; Christe & Hannah, 1990), but differs from most Mesozoic granitic plutons of the Mojave desert (Anderson et al., 1989, and references within). This affinity suggests the Teutonia Batholith may have formed by processes more typical of those found in central and northern California instead of the processes typical of the Mojave Desert plutonism.

Table 2.2. Average chemical analysis of mafic minerals for Teutonia batholithic phases in the Ivanpah Mountains area.

Mineral	clinopyroxene	hornblende	hornblende	hornblende	hornblende	biotite	biotite	biotite	biotite	biotite
Rock Type	Oro Wash	Oro Wash	Ivanpah	Kessler Springs	M.S. Dike	Oro Wash	Striped Hills	Ivanpah	Kessler Springs	M.S. Dike
Number	10	54	93	65	12	7	9	12	45	16
SiO_2	50.89±0.82	47.61±2.17	43.82±1.21	48.87±1.03	48.08±0.91	32.01±1.24	37.28±0.61	36.53±0.91	37.59±1.02	38.40±1.73
Al_2O_3	1.91±0.60	6.37±0.72	10.61±0.72	5.50±0.69	7.02±0.86	15.27±0.75	16.09±0.45	15.06±0.37	13.82±0.24	16.15±0.74
TiO_2	0.44±0.16	0.88±0.34	1.28±0.14	0.63±0.11	0.91±0.37	3.22±1.01	1.83±0.20	2.45±0.84	2.84±0.39	2.40±1.16
FeO*	10.46±0.62	17.45±0.61	16.40±0.86	14.14±0.59	15.69±0.90	25.51±1.61	19.62±0.94	21.62±0.50	17.30±0.65	17.81±0.88
MnO	0.39±0.10	0.39±0.06	0.51±0.06	0.89±0.06	0.35±0.05	0.21±0.05	0.34±0.39	0.34±0.04	0.67±0.05	0.19±0.03
MgO	13.95±0.55	12.88±0.66	11.78±0.55	14.87±0.58	13.19±0.71	12.34±1.07	11.12±0.72	10.07±0.54	14.33±0.49	12.00±0.83
CaO	21.25±1.12	11.51±0.28	11.74±0.47	11.77±0.14	11.60±0.53	1.50±0.94	0.03±0.03	0.04±0.02	0.12±0.12	0.19±0.40
Na_2O	0.32±0.10	0.91±0.16	1.24±0.18	1.17±0.14	0.80±0.11	0.05±0.03	0.10±0.05	0.06±0.04	0.08±0.03	0.05±0.04
K_2O	0.04±0.04	0.52±0.11	1.25±0.18	0.53±0.08	0.59±0.12	3.09±1.41	9.30±0.29	9.52±0.17	8.86±0.65	8.63±0.59
F	—	0.08±0.06	0.24±0.12	0.37±0.06	0.20±0.04	0.14±0.07	0.67±0.10	0.57±0.09	0.72±0.11	0.16±0.09
Cl	—	0.04±0.02	0.06±0.02	0.02±0.02	0.08±0.03	0.09±0.04	0.11±0.06	0.07±0.02	0.03±0.02	0.06±0.02
Total	99.65±0.95	98.59±1.23	98.64±1.33	98.34±0.85	98.28±0.52	93.43±1.62	96.49±0.61	96.32±1.47	96.35±1.83	96.01±0.78
Si	1.92±0.02	6.99±0.44	6.52±0.11	7.15±0.10	7.06±0.10	2.53±0.07	2.83±0.04	2.81±0.03	2.83±0.03	2.86±0.10
$Al^{(IV)}$	0.09±0.03	0.95±0.12	1.48±0.11	0.85±0.10	0.94±0.10	1.42±0.07	1.17±0.04	1.19±0.03	1.17±0.03	1.14±0.10
$Al^{(VI)}$	—	0.16±0.04	0.38±0.07	0.10±0.04	0.27±0.08	—	0.26±0.03	0.18±0.03	0.06±0.02	0.28±0.08
Ti	0.01±0.01	0.10±0.04	0.14±0.02	0.07±0.01	0.11±0.03	0.19±0.06	0.10±0.01	0.14±0.05	0.16±0.02	0.13±0.07
Fe	0.33±0.02	2.16±0.09	2.04±0.11	1.73±0.08	1.93±0.12	1.68±0.12	1.24±0.07	1.39±0.03	1.09±0.04	1.11±0.06
Mn	0.01±0.00	0.05±0.01	0.06±0.01	0.11±0.01	0.04±0.01	0.14±0.00	0.02±0.00	0.02±0.00	0.04±0.00	0.01±0.00
Mg	0.79±0.03	2.84±0.13	2.613±0.114	3.24±0.11	2.89±0.14	1.45±0.12	1.26±0.08	1.16±0.07	1.61±0.06	1.33±0.10
Ca	0.86±0.04	1.82±0.05	1.87±0.08	1.84±0.02	1.82±0.08	0.13±0.08	0.00±0.00	0.00±0.00	0.01±0.01	0.02±0.03
Na	0.02±0.01	0.26±0.05	0.36±0.05	0.33±0.04	0.23±0.03	0.01±0.00	0.01±0.01	0.01±0.01	0.01±0.01	0.01±0.01
K	0.00±0.00	0.10±0.02	0.26±0.02	0.10±0.02	0.11±0.02	0.91±0.14	0.90±0.03	0.94±0.02	0.85±0.06	0.82±0.06

FeO* = total iron oxide.

±value is the standard deviation (1σ).

With the exception of the mafic plutonic phases of the batholith, all other plutons exhibit major element oxide trends similar to Mesozoic margin-related batholiths (Beckerman et al., 1982). These trends include decreasing Al_2O_3, TiO_2, total Fe, MgO and CaO with increasing silica content (Figure A.3). K_2O increases with increasing silica content and Na_2O increases slightly, but in the latter case the data exhibit too much scatter to assign any definite trend (Figure A.3). All granitic plutons and the Morning Star dike have high K_2O contents according to the classification of Gill (1981). The Ivanpah granite has anomalously high K_2O contents which is consistent with the high modal abundance of alkali feldspar (Table A.1). The alkali feldspar enrichment of the Ivanpah granite may also account for the slightly lower Al_2O_3, CaO and Na_2O contents. The high K_2O content of the Morning Star dike may result from hydrothermal alteration.

Mineral Chemistry

Pyroxenes

In the Ivanpah Mountains augite was only found in the Oro Wash granodiorite. Beckerman et al. (1982) also report clinopyroxenes in the Black Canyon hornblende gabbro and silica-poor portions of the Rock Springs monzodiorite within of the Teutonia batholith. Pyroxenes of the Oro Wash pluton range in composition from $Ca_{45}Fe_{17}Mg_{38}$ to $Ca_{40}Fe_{19}Mg_{41}$ and are all augites (Table A.2). Augites from the Oro Wash granodiorite contain a larger ferrosilite component than pyroxenes in Black Canyon and Rocks Springs samples.

Fe-Ti oxides

Magnetite is the only Fe-Ti oxide that was observed in batholithic rocks of the Ivanpah Mountains. This is consistent with the findings of Beckerman et al. (1982) who report magnetite in all plutonic phases except the Teutonia adamellite which contains coexisting ilmenite and magnetite. The magnetite in Ivanpah Mountains plutons is essentially pure Fe_3O_4 with only minor amounts of other major element oxides (≤0.20 wt. % MnO; ≤0.10 wt. % Al_2O_3 and Na_2O; ≤0.05 wt. % CaO and K_2O). Magnetite from the Oro Wash granodiorite contains up to 5.75 wt. % TiO_2, but magnetite from all other plutons in the Ivanpah Mountains contain less than 0.50 wt. % TiO_2. Beckerman et al. (1982) report minor SiO_2, MnO and TiO_2 in magnetite for batholithic phases outside the Ivanpah Mountains and interpret these trace components as evidence for subsolidus re-equilibration. The presence of predominantly magnetite places plutons of the Teutonia batholith in the Magnetite-series granitoids of Ishihara (1977).

Amphiboles

All plutonic phases of the Ivanpah Mountains contain at least minor amounts of hornblende (Table A.1) and most Teutonia batholith plutons outside the Ivanpah Mountains also contain hornblende (Beckerman et al., 1982). Hornblende is never the sole mafic mineral in any plutonic phase; in granitic plutons hornblende is always subordinate to biotite. Hornblendes generally occur in metaluminous samples of individual plutons, especially those plutons that evolve from metaluminous to peraluminous compositions. Hornblende from the Striped Hills granodiorite is always altered to chlorite, epidote, sphene and opaques so no microprobe analyses of pristine hornblende are reported. Amphibole analyses for the remainder of the Ivanpah

Figure A.4. Classification of amphiboles from plutonic rocks in the Ivanpah Mountains area. Classification and nomenclature after Hawthorne (1981).

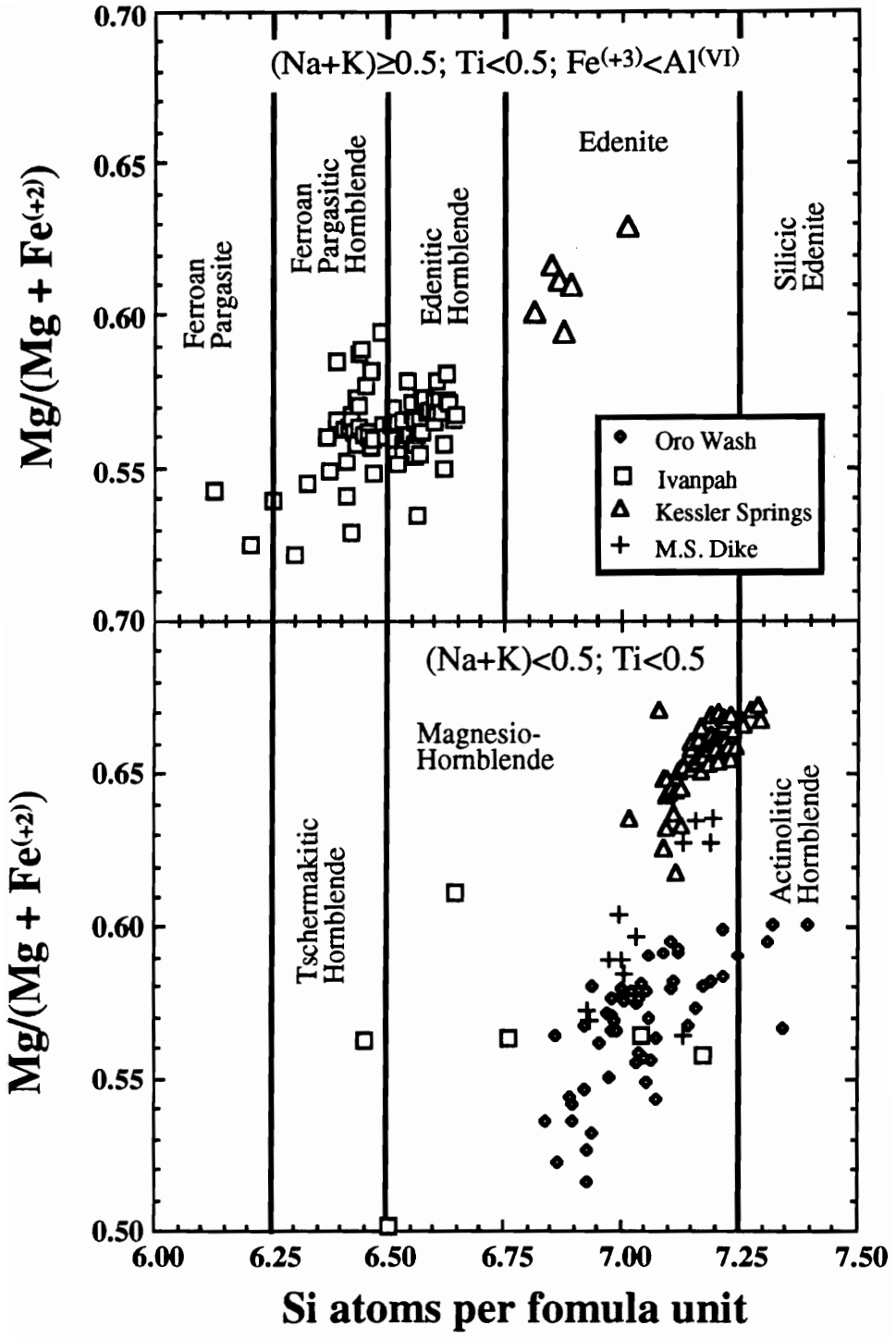
(Na+K)≥0.5; Ti<0.5; Fe(+3)<Al(VI)
Ferroan Pargasite
Ferroan Pargasitic Hornblende
Edenitic Hornblende
Edenite
Silicic Edenite
Oro Wash
Ivanpah
Kessler Springs
M.S. Dike
(Na+K)<0.5; Ti<0.5
Tschermakitic Hornblende
Magnesio-Hornblende
Actinolitic Hornblende
Mg/(Mg + Fe(+2))
Si atoms per fomula unit
0.70
0.65
0.60
0.55
0.50
6.00
6.25
6.50
6.75
7.00
7.25
7.50

Figure A.5. Classification of biotites from pluton rocks in the Ivanpah Mountains area based on mineral compositions in terms of FeO*/(FeO*+MgO) and total atomic Al per unit formula. FeO* represents total iron and symbols are the same as Figure A.4.

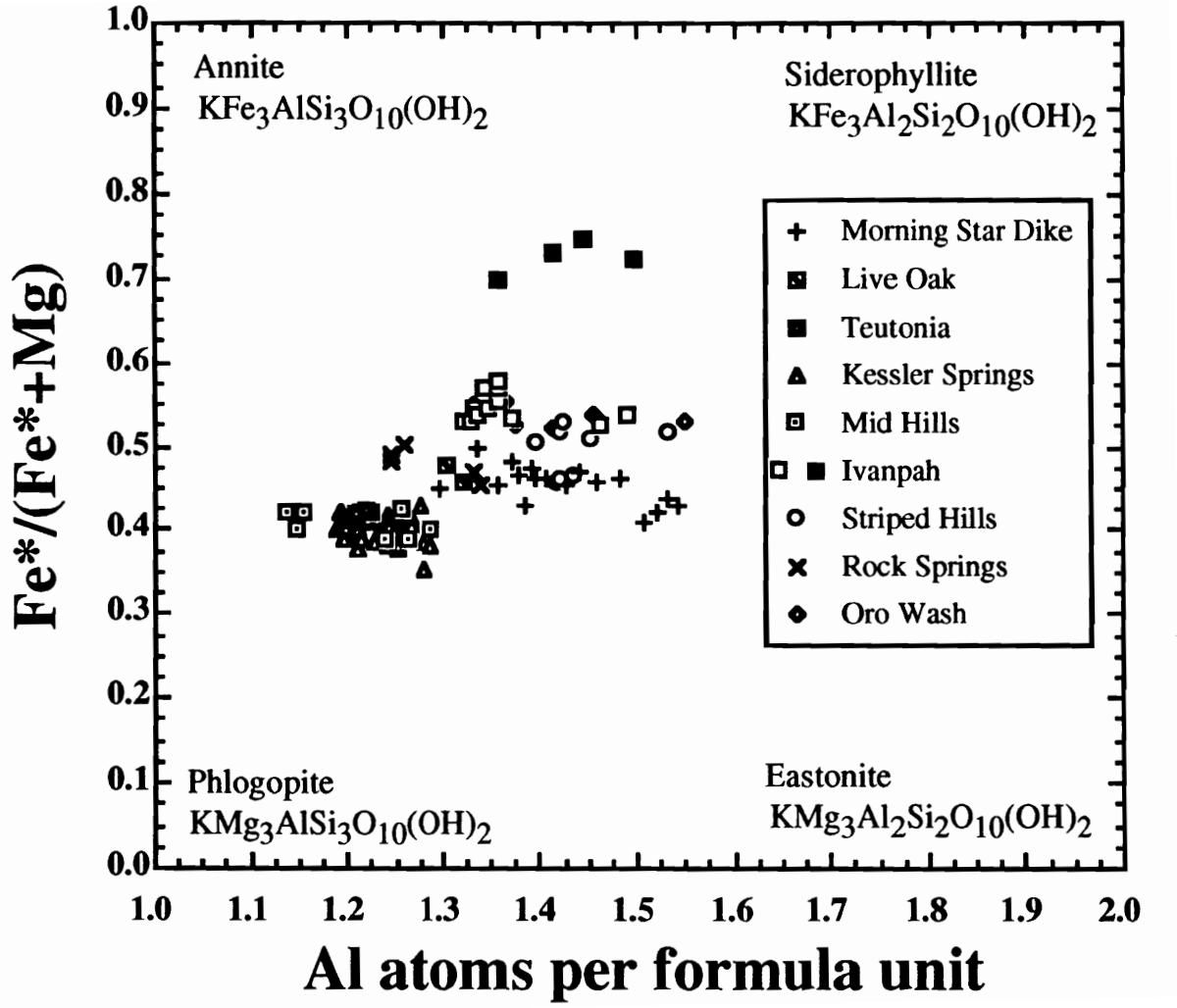
Annite
$KFe_3AlSi_3O_{10}(OH)_2$
Siderophyllite
$KFe_3Al_2Si_2O_{10}(OH)_2$
Phlogopite
$KMg_3AlSi_3O_{10}(OH)_2$
Eastonite
$KMg_3Al_2Si_2O_{10}(OH)_2$
Morning Star Dike
Live Oak
Teutonia
Kessler Springs
Mid Hills
Ivanpah
Striped Hills
Rock Springs
Oro Wash
Fe*/(Fe*+Mg)
Al atoms per formula unit
1.0
0.9
0.8
0.7
0.6
0.5
0.4
0.3
0.2
0.1
0.0
1.0
1.1
1.2
1.3
1.4
1.5
1.6
1.7
1.8
1.9
2.0

Mountains plutons are reported in Table A.2 and nomenclature is given in Figure A.4 where mineral formulas are calculated after the method described by Hawthorne (1981). All amphiboles belong to the calcic amphibole group. Amphiboles from the Oro Wash pluton, Morning Star dike and Kessler Springs adamellite are magnesio-hornblende to actinolitic hornblende, and amphiboles from the Ivanpah granite are ferroan pargasitic hornblende to edenitic hornblende (Figure A.4). Combined Cl and F contents of hornblende are less than 0.46 wt % for all plutons in the Ivanpah Mountains. Amphibole rim compositions are generally less actinolitic and more pargasitic, respectively, for the two groups, but compositional variations are generally small. Beckerman et al. (1982) found edenitic hornblende in the Rock Springs monzodiorite and magnesio-hornblende in all other plutons of the batholith. Low aluminum contents of amphiboles (4.85 to 7.82 wt .% Al_2O_3) are common in granitic plutons of the batholith which is characteristic of calc-alkaline metaluminous granitic rocks of orogenic belts (Anderson et al., 1980). The Ivanpah granite is the only granitic pluton with high Al in hornblende; the Ivanpah granite hornblendes have Al_2O_3 contents (10.61±0.72 wt. %) more typical of anorogenic granites (9-11 wt. % Al_2O_3; Anderson et al., 1980). Mg/Fe ratios for all amphiboles are similar to those in coexisting biotite (see below). TiO_2 contents are generally low except for the more mafic plutons and the Ivanpah granite.

Biotite

Biotite is the principal mafic mineral in all Teutonia batholith plutons except for the Oro Wash granodiorite and Black Canyon hornblende gabbro. Biotite compositions are relatively uniform for each pluton in the Ivanpah Mountains (Table A.2 and Figure A.5) and in other parts of the batholith (Beckerman et al., 1982). The only exception to this

uniformity is the Fe-rich biotites reported by Beckerman et al. (1982) from Ivanpah granite samples taken at the Ivanpah granite-Kessler Springs adamellite contact in the southern Ivanpah Mountains. Biotites from the contact zone contain 25.78±0.47 wt. % total FeO (FeO*) and have a FeO*/(FeO*+MgO) ratio of 0.73±0.03 (Beckerman et al., 1982) compared to 21.62±0.50 and 0.55±0.02, respectively, for biotites from other parts of the Ivanpah granite (Table A.2). Biotites from the main portions of the pluton also contain less fluorine than biotites from the contact zone (0.57±0.09 verses 2.23±0.41). Throughout the Ivanpah granite biotites from more differentiated portions of the intrusion have a higher iron content and modal magnetite decreases with increased differentiation. Ivanpah granite samples at the contact have a lower modal abundance of both biotite and magnetite (Robinson, 1979), the principal Fe-bearing phases, than samples from the main portions of the pluton (Table A.1) and thus iron may be preferentially partitioned into biotite. An alternative theory is that of re-equilibration of biotite, and possibly other mineral phases, during intrusion of the later Kessler Springs adamellite may have affected the mineral compositions. This latter theory may also account for the increased fluorine content of biotites in Ivanpah granite contact rocks because the Kessler Springs adamellite has a higher fluorine content (Robinson, 1979). The uniform FeO*/(FeO*+MgO) ratio throughout individual plutonic phases of the batholith may be interpreted either as crystallization under constant oxygen fugacity and temperature, or constant oxygen fugacity during cooling and/or re-equilibration (Speer, 1984).

Feldspar

Plagioclase and perthitic alkali feldspar coexist in all plutons in the Ivanpah Mountains. This is also the case for other Teutonia batholith plutons, except for the

Black Canyon hornblende gabbro (Beckerman et al., 1982). No attempt was made to analyze exsolutions in the perthitic feldspars for this study, but Beckerman et al. (1982) report microprobe and atomic absorption analyses of perthitic alkali feldspar for the Ivanpah granite and Mid Hills adamellite; Beckerman et al. (1982) obtained compositions of $Or_{78.5\text{-}79.0}Ab_{20.8\text{-}19.6}An_{0.7\text{-}0.8}$ and $Or_{73.3\text{-}79.3}Ab_{24.5\text{-}19.4}An_{0.7\text{-}2.6}$ for the Ivanpah granite and Mid Hills adamellite, respectively. Plagioclase in the granitic plutons is predominantly intermediate oligoclase (An_{18}) to sodic andesine (An_{35}) with very low orthoclase contents ($Or_{1\text{-}6}$). Black Canyon hornblende gabbro contains labradorite plagioclase ($An_{51\text{-}70}$) (Beckerman et al., 1982).

Conditions of Emplacement for the Teutonia Batholith

Geologic mapping combined with petrographic and chemical data presented above were used to estimate the conditions of emplacement for batholithic phases of the Ivanpah Mountains.

Depth of Partial Melting and Source of Plutons

Assuming anatectic compositions and using water-saturated minimum melting experiments for the assemblage quartz-orthoclase-albite-anorthite, after the method outlined by Anderson and Cullers (1978), Beckerman et al (1982) estimated the depth of partial fusion for the plutonic phases of the Teutonia batholith. Mid- to lower-crustal depths of 27 to 38 km (7 to 10 kbars) were identified for all the major plutonic phases in the batholith (Beckerman et al., 1982). No estimates of partial fusion depth are available from this current work. At 190 Ma, the onset of magmatic activity within the Teutonia

batholith, eastward directed thrusting of the Winter Pass and Mesquite Pass thrust plates along the Mesozoic foreland fold and thrust belt would cause crustal thickening which could account for anatexis of the lower crustal materials and in particular the Precambrian basement complex. Lead isotopic systematics indicate that Mesozoic plutons of the Teutonia batholith were derived from partial melting of Mojave Desert crystalline basement (Wooden et al., 1988; Wooden & Miller, 1990). All Teutonia batholith plutons, except the Teutonia adamellite, are magnetite-series plutons which also implies the granitoids crystallized from magmas generated by melting of crustal materials (Wones, 1981).

Also from the normative quartz-albite-orthoclase diagram, major and trace element chemistry, and modal analyses, Beckerman et al. (1982) suggested that the Rock Springs monzodiorite was derived from eclogite or LILE-enriched mantle source materials. Based on the same data, Beckerman et al. (1982) also suggested the Ivanpah granite was derived by either fusion under drier conditions or from a smaller percentage of partial melting of a more calcic-rich quartzofeldspathic source rock. Both of these models are consistent with Pb isotopic data of Wooden et al. (1988) and Wooden and Miller (1990) and the evolution of the Mesozoic foreland fold and thrust belt (Burchfiel & Davis, 1972; Burchfiel & Davis, 1975; Burchfiel & Davis, 1981).

Crystallization Model

The Teutonia batholith resulted from cogenetic emplacement of seven non-comagmatic plutonic suites which include the Rock Springs monzodiorite, Ivanpah granite, Mid Hills adamellite, Black Canyon gabbro, Teutonia adamellite, Kessler Springs Adamellite and Live Oak Canyon adamellite (Beckerman et al., 1982).

Weisenberg (1973) distinguished a eighth plutonic suite, the Oro Wash granodiorite/Breccia Pluton suite, which is also cogenetic and non-comagmatic with other plutons in the batholith. The Striped Hills granodiorite and Ivanpah granite appear to be a comagmatic suite of plutons related by fractional crystallization and crustal assimilation, or interaction between the early Ivanpah granite and the Paleozoic country rocks.

Compositional trends within the Rock Springs monzodiorite can be accounted for by 51% fractional crystallization consisting of plagioclase (55 wt. %), biotite (24 wt. %), hornblende (12 wt. %), clinopyroxene (7 wt. %) and Fe-Ti oxide minerals (2 wt. %) (Beckerman et al., 1982). This fractional crystallization model includes cognate inclusions which are chemically, mineralogically and texturally similar to the main plutonic phases (Beckerman et al., 1982). Beckerman et al. (1982) also modeled fractional crystallization of the Ivanpah granite by 39 % fractionation dominated by alkali feldspars (54.5 wt. %), plagioclase (25.5 wt %) and hornblende (20.0 wt. %). Additional fractional crystallization modeling (this study) of the 'Ivanpah granite' which includes samples from the Striped Hills granodiorite as an approximation of the parent magma compositions account for the compositional trends observed in the Striped Hills granodiorite and Ivanpah granite suite (Figure A.2 and A.3) by 36.7 to 41.6 % fractionation of alkali feldspars (58.8 wt. %), plagioclase (24.1 wt. %) and hornblende (17.1 wt. %). Although this does not prove that the Striped Hills granodiorite is a differentiate of the Ivanpah granite, it does lend credence to this model which was propsed by Weisenberg (1973). This new fractional crystallization models also imply that a more mafic endmember of the 'Ivanpah granite', i.e. the Striped Hills granodiorite, may exist outside the Ivanpah Mountains and was not identified by Robinson (1979), Beckerman (1982) or Beckerman et al. (1982). A complete set of trace element chemistry is required to verify these fractional crystallization models and better define the

relationship between the Striped Hills granodiorite and Ivanpah granite. Given the current chemical and textural data, the Striped Hills granodiorite represents a more mafic enriched pluton that is cogenetic and comagmatic with the Ivanpah granite. Cretaceous plutons of the Teutonia batholith are non-comagmatic with compositional variations accounted for by plagioclase dominated fractional crystallization (Beckerman et al., 1982).

Estimates of T, P, fH_2O and fO_2

The occurrence of hornblende or biotite with plagioclase on or near the granite liquidus at pressures up to 20 kbars requires water contents greater than 3 wt. % (Wyllie, 1977). Hornblende and biotite appear early in the crystallization sequence, with plagioclase, in all plutonic phases of the batholith, which implies moderate to high magma water contents. Beckerman et al. (1982) also argue for high water contents and late stage water saturation because of the numerous pegmatite and aplite dikes associated with the batholith. Late Cretaceous plutons have fewer associated pegmatite and aplite dikes than older plutons of the batholith. Moderate to high magma water contents can also be inferred from the numerous skarn and metasomatic deposits associated with pluton emplacement, but these deposits are only common in Early Cretaceous and older plutons. Therefore, plutonism in the Teutonia batholith appears to have evolved from near water-saturated Jurassic to Early Cretaceous intrusions to dryer conditions for Late Cretaceous intrusions. This evolution to dryer magmatic conditions also implies shallower levels of emplacement for younger plutons (Burhnam, 1979).

The principal Fe-Ti oxide in the batholith is magnetite, which appears early in the crystallization sequence of all plutons. Ishihara (1977) and Anderson et al. (1989) argued

for relatively high oxygen fugacities (fO_2>Ni-NiO buffer) for magnetite-series granitic plutons. Beckerman et al. (1982) calculated fO_2 for granitic plutons at slightly higher than the Ni-NiO buffer using the annite content of biotite coexisting with alkali feldspar and magnetite at 2 to 4 kbars emplacement pressure, wet granite solidus temperatures and assuming PH_2O=PTotal. Although the pressure determinations have changed (see below), the oxygen fugacity for granitic phases of the batholith still remain on or slightly above the Ni-NiO buffer recalculated using the same method of Beckerman et al. (1982). Initial estimates of oxygen fugacity for the Ivanpah granite were slightly lower than those for other granitic plutons, but new biotite chemistry data (Figure A.5) recalculates the fO_2 to the same conditions as the other granitic phases. The higher FeO* contents of biotite and hornblende in Ivanpah granite, reported by Beckerman et al. (1982), may reflect higher fO_2 during emplacement. Alternatively, since Fe diffuses more readily than Al, the higher FeO* contents of Ivanpah granite biotite and amphiboles may reflect subsolidus re-equilibration of the Ivanpah granite at shallower depth after emplacement. This subsolidus re-equilibration may have occurred during the extensive Cretaceous plutonic events.

Temperature of emplacement were initially constrained by the water saturated solidus and two-feldspar thermometry for granitic phases of the batholith, which yield minimum temperatures of 642±13° and 631±12°C for the Mid Hills adamellite and Ivanpah granite, respectively (Beckerman et al., 1982). Both methods yield similar temperatures and are consistent with magma water content estimates. The more mafic members of the batholith, e.g. Rock Springs monzodiorite, Black Canyon hornblende gabbro and Oro Wash granodiorite, crystallized at higher temperatures with hornblende, clinopyroxene, and plagioclase on the liquidus. Crystallization temperatures, calculated by Mg and Fe partitioning between hornblende and clinopyroxene (Kretz & Jen, 1978),

yield emplacement temperatures of 975±17°C for Rock Springs monzodiorite (Beckerman et al., 1982), 942±9°C for Black Canyon hornblende gabbro (Beckerman et al., 1982), and 931±20°C for Oro Wash granodiorite (this study). Calculated oxygen fugacities for the more mafic plutons are below the quartz-fayalite-magnetite buffer at these temperatures and are distinctly different from fO_2 conditions calculated for granitic phases of the batholith.

Estimates of T, fH_2O and fO_2 suggest crystallization of the suite of plutons occurs at relatively restricted ranges of T and fO_2, and moderate to high fH_2O. Mafic phases crystallized at higher T and lower fO_2 than granitic plutons, but have a similar restricted range of conditions. The consistent FeO*/(FeO*+MgO) ratio of biotite and amphiboles for individual plutons also argues for little change in fO_2 during plutons crystallization and cooling.

Beckerman et al. (1982) initially estimated a 2 kbars pressure (7-8 kilometers depth) of emplacement for the entire Teutonia batholith. Anderson et al. (1989) used the data of Beckerman et al. (1982) for the Rock Springs monzodiorite, Mid Hills adamellite and Kessler Springs Adamellite to calculate depth of pluton emplacement using the total Al-in-hornblende geobarometer (Hammerstrom & Zen, 1986; Hollister et al., 1987; Johnson & Rutherford, 1989; Rutter et al., 1989; Thomas & Ernst, 1990). The quantitative use of Al-in-hornblende as an independent barometer has recently been criticized because it depends on other intensive variables, mineral assemblage and mineral solid solutions (Blundy & Holland, 1990; Cosca et al., 1991). Estimates of the intensive variables combined with mineral chemistry (see above) indicate individual plutons crystallized under a relatively restricted range of temperature and oxygen fugacity at moderate to high water contents. Additional Al-in-hornblende barometry was determined for batholithic plutons of the Ivanpah Mountains. Pressures were calculated using the

equation of Hollister et al. (1987) are shown in Figure A.6 and compared to the data of Beckerman et al. (1982) and Anderson et al. (1989). Other Al-in-hornblende barometry equations (Hammerstrom & Zen, 1986; Johnson & Rutherford, 1989; Rutter et al., 1989; Thomas & Ernst, 1990; Cosca et al., 1991), yield similar pressures of emplacement. Cretaceous plutons (Mid Hills and Kessler Springs) were emplaced at less than 2 kbars (7-8 Km depth) in good agreement with the initial estimate of Beckerman et al. (1982). Jurassic plutons, however, have a wide range of emplacement pressures. The 190 Ma Oro Wash granodiorite and 168 Ma rock Springs monzodiorite yield pressures of 2.0±0.2 kbars (7-8 Km) and 3.2±0.2 kbars (11-13 Km), respectively. Only the Ivanpah granite which yielded 6.0±0.5 kbars (21-24 Km), is vastly different from other plutons in the Teutonia batholith. Attempts to obtain microprobe analyses of hornblende from the Striped Hills granodiorite were unsuccessful due to extensive subsolidus and hydrothermal alteration. Thus, no comparison between Striped Hills granodiorite and Ivanpah granite, or other plutons in the Ivanpah Mountains, is available. The large difference in total Al-in-hornblende of the Ivanpah granite may reflect deeper levels of emplacement or different physical and chemical conditions during pluton emplacement. Temperatures and oxygen fugacity calculated for the Ivanpah granite are similar to those for the Mid Hills adamellite, which suggests that neither of these parameters can account for the different Al contents of hornblende between these two plutons. Mineralogy and crystallization sequence are also similar between the two plutons, so can not account for the relative differences in Al content. Ivanpah granite does have tholeiitic affinities, buthornblende only occurs in metaluminous portions of the pluton that plot in the calc-alkaline field (Figure A.2). The Al-in-hornblende barometer is only calibrated for calc-alkaline plutons so part of the unusually high total Al content of Ivanpah granite may be due to it marginal alkalic chemical affinity. Hornblendes from other batholithic plutons

Figure A.6. Al-in-hornblende barometry of Teutonia batholith plutons. Open symbols represent data from this study and darkened symbols represent data from Anderson et al. (1989). Pressures were calculated using the equation of Hollister et al. (1987).

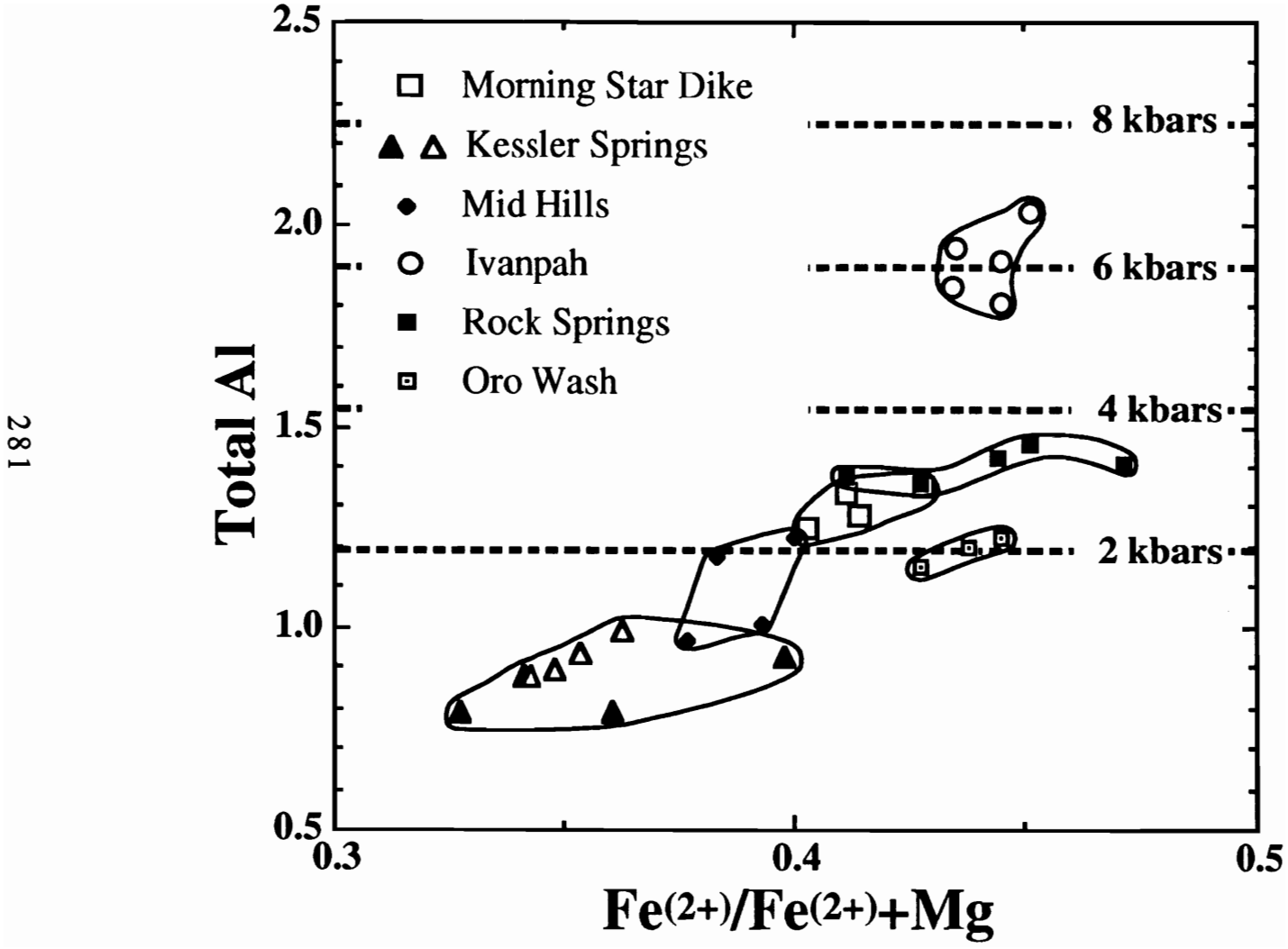
Morning Star Dike
Kessler Springs
Mid Hills
Ivanpah
Rock Springs
Oro Wash
8 kbars
6 kbars
4 kbars
2 kbars
Total Al
2.5
2.0
1.5
1.0
0.5
0.3
0.4
0.5
Fe(2+)/Fe(2+)+Mg

occur in less differentiated metaluminous samples which have calc-alkaline affinities according to Miyashiro's (1974) classification, so the source rocks chemical affinity is not likely to account for the total difference between Al contents in the Ivanpah granite and other plutons of the batholith.

Howard et al. (1987), Young and Wooden (1988), John and Wooden (1990) and Anderson et al. (1989) have identified other Jurassic plutons in the eastern Mojave Desert which were emplaced at depths between 15 to 30 kilometers. Thus, depth estimates calculated from Al-in-hornblende for the Ivanpah granite are not unreasonable for Jurassic plutonism in the Mojave Desert. Because granitic plutons of the Teutonia batholith were emplaced under similar chemical conditions, the high Al contents of hornblende in Ivanpah granite is accepted as evidence of deeper levels of emplacement or increased pressure during granite emplacement.

Summary and Conclusions

The Ivanpah granite, which underlies most of the Ivanpah Mountains and host mineralization at the Morning Star mine, appears to be chemically and mineralogically distinct from other plutonic phases in the Teutonia batholith. Mid-crustal levels of emplacement for the Ivanpah granite are derived from total Al-in-hornblende barometer compared to shallower levels of emplacement for both older and younger plutonic phases of the Teutonia batholith. A model involving crustal upwarping during Early to Late Cretaceous may account for the juxtaposition of mid- and upper-crustal level plutonism, Late Mesozoic thrust faulting and the absence of the latest thrusting event in the Ivanpah Mountains (Chapter 1). The tectonomagmatic model constrains intrusion of the Morning Star dike to be between 138 to 105 Ma and ductile deformation on the Morning Star fault

system to be between 105 and 90 Ma. The transition from ductile to brittle deformation on the Morning Star fault system may be related to waning stages of magmatic activity associated with Cretaceous pluton emplacement, doming, and thermal dissipation.

Appendix A.1

Modal composition of Teutonia batholith plutonic phases in the Ivanpah Mountains.

SAMPLE	90-012	90-012	070	90-011A	89-052
PLUTON	Kessler Springs	Kessler Springs	Kessler Springs	Kessler Springs	Dacite Dike
Quartz	23.20	25.50	22.40	21.60	2.90
Alkali Feldspar	24.90	28.30	23.90	26.20	72.50
Plagioclase	43.30	36.30	37.10	41.90	18.80
Biotite	7.60	5.60	7.20	2.90	0.50
Hornblende	0.00	0.00	4.50	0.00	0.00
Clinopyroxene	0.00	0.00	0.00	0.00	0.00
Opaque	0.60	4.10	1.50	2.40	3.70
Apatite	0.10	0.00	0.50	0.20	0.00
Sphene	0.10	0.00	1.50	1.50	0.00
Allanite	0.10	0.10	1.20	1.50	0.00
Zircon	0.10	0.20	0.20	0.20	0.00
Chlorite	0.00	0.00	0.20	0.00	0.00
Epidote	0.00	0.00	0.00	0.20	0.00
Calcite	0.00	0.00	0.00	0.40	0.00
Muscovite	0.00	0.00	0.00	0.90	1.70
Orthopyroxene	0.00	0.00	0.00	0.00	0.00
Garnet	0.00	0.00	0.00	0.00	0.00
TOTAL	100.00	100.10	100.20	99.90	100.10

SAMPLE	068C-1	068C-2	89-012	122	89-063
PLUTON	Hornblende Diorite	Hornblende Diorite	Ivanpah	Ivanpah	Ivanpah
Quartz	9.60	14.50	29.30	24.80	21.70
Alkali Feldspar	4.60	3.60	44.60	42.70	28.50
Plagioclase	43.10	49.10	13.20	20.70	20.20
Biotite	5.40	13.60	5.30	4.10	17.40
Hornblende	15.20	12.70	0.00	0.40	0.30
Clinopyroxene	0.00	0.00	0.00	0.00	0.00
Opaque	13.20	2.70	3.50	4.10	6.00
Apatite	1.20	0.00	1.20	1.20	2.30
Sphene	0.00	0.00	0.30	0.40	0.40
Allanite	0.00	0.00	0.00	0.00	0.00
Zircon	0.00	0.00	0.60	0.00	0.60
Chlorite	4.80	2.70	0.60	0.00	0.00
Epidote	3.00	0.90	1.20	1.60	2.60
Calcite	0.00	0.00	0.00	0.00	0.00
Muscovite	0.00	0.00	0.30	0.00	0.00
Orthopyroxene	0.00	0.00	0.00	0.00	0.00
Garnet	0.00	0.00	0.00	0.00	0.00
TOTAL	100.10	99.80	100.10	100.00	100.00

SAMPLE	89-010	89-030C	068A-1	90-09A1	90-10B
PLUTON	Ivanpah	Ivanpah	Ivanpah	Ivanpah	Ivanpah
Quartz	36.10	24.60	30.00	26.00	34.30
Alkali Feldspar	48.70	37.10	38.80	48.10	48.90
Plagioclase	13.30	21.10	22.40	19.80	11.40
Biotite	0.00	8.00	6.60	4.40	3.50
Hornblende	0.00	0.00	1.10	0.00	0.10
Clinopyroxene	0.00	0.00	0.00	0.00	0.00
Opaque	1.90	5.70	0.70	1.00	1.60
Apatite	0.00	0.10	0.40	0.70	0.30
Sphene	0.00	0.10	0.10	0.10	0.10
Allanite	0.00	0.00	0.00	0.00	0.00
Zircon	0.00	0.10	0.10	0.10	0.10
Chlorite	0.00	3.40	0.00	0.00	0.00
Epidote	0.00	0.00	0.00	0.00	0.00
Calcite	0.00	0.00	0.00	0.00	0.00
Muscovite	0.00	0.00	0.00	0.00	0.00
Orthopyroxene	0.00	0.00	0.00	0.00	0.00
Garnet	0.00	0.00	0.00	0.00	0.00
TOTAL	100.00	100.20	100.20	100.20	100.30

SAMPLE	90-09A2	054-2	068AA	095	075
PLUTON	Ivanpah	Ivanpah	Ivanpah	Ivanpah	Ivanpah
Quartz	21.10	22.90	27.60	21.40	30.70
Alkali Feldspar	41.70	31.30	31.90	52.90	43.00
Plagioclase	17.10	23.60	22.50	15.50	19.70
Biotite	12.90	4.90	5.70	2.90	2.50
Hornblende	0.20	3.80	1.00	0.00	0.00
Clinopyroxene	0.00	0.00	0.00	0.00	0.00
Opaque	2.80	3.90	6.70	3.60	3.20
Apatite	1.20	0.90	1.40	0.20	0.00
Sphene	0.10	0.60	0.20	0.00	0.00
Allanite	0.00	0.00	0.00	0.00	0.20
Zircon	1.20	1.60	3.00	0.90	0.60
Chlorite	1.60	5.00	0.00	2.00	0.00
Epidote	0.20	0.00	0.00	0.00	0.00
Calcite	0.00	0.00	0.00	0.00	0.00
Muscovite	0.00	0.20	0.00	0.50	0.00
Orthopyroxene	0.00	0.00	0.00	0.00	0.00
Garnet	0.00	0.00	0.00	0.20	0.20
TOTAL	100.10	98.70	100.00	100.10	100.10

SAMPLE	90-09A1	078	90-09A2	90-09B	058B
PLUTON	Ivanpah	Ivanpah	Mafic Inclusion in Ivanpah	Mafic Inclusion in Ivanpah	Oro Wash
Quartz	30.40	31.40	24.00	21.10	19.50
Alkali Feldspar	35.00	37.00	28.60	28.70	11.50
Plagioclase	21.20	24.10	32.60	29.20	38.70
Biotite	8.60	1.70	9.20	10.60	5.90
Hornblende	0.00	0.00	2.30	1.20	21.00
Clinopyroxene	0.00	0.00	0.00	0.00	0.00
Opaque	2.20	0.40	2.30	5.40	1.70
Apatite	0.00	0.20	1.00	1.50	0.00
Sphene	0.50	0.00	0.10	0.20	1.30
Allanite	0.00	0.00	0.00	0.00	0.00
Zircon	0.80	1.50	0.10	0.20	0.00
Chlorite	1.40	0.60	0.00	0.20	0.10
Epidote	0.10	0.00	0.00	1.50	0.30
Calcite	0.00	0.00	0.00	0.00	0.00
Muscovite	0.00	2.10	0.00	0.00	0.00
Orthopyroxene	0.00	0.00	0.00	0.00	0.00
Garnet	0.00	0.60	0.00	0.00	0.00
TOTAL	100.20	99.60	100.20	99.80	100.00

SAMPLE	063	039-1	035-1	035-2	035
PLUTON	Oro Wash	Striped Hills	Striped Hills	Striped Hills	Striped Hills
Quartz	20.70	18.20	23.20	21.90	22.10
Alkali Feldspar	10.40	12.90	12.30	10.60	19.50
Plagioclase	38.90	33.70	32.80	32.00	39.40
Biotite	7.80	12.40	22.20	18.60	10.20
Hornblende	17.20	14.20	1.70	7.00	4.10
Clinopyroxene	0.00	0.00	0.00	0.00	0.00
Opaque	2.80	1.90	3.30	3.90	1.00
Apatite	0.00	0.50	1.30	0.90	0.10
Sphene	0.00	0.50	0.70	0.30	0.10
Allanite	0.00	0.00	0.00	0.00	0.00
Zircon	0.10	0.00	1.30	1.30	0.10
Chlorite	1.10	4.30	1.00	1.70	0.00
Epidote	1.00	1.40	0.30	1.90	3.40
Calcite	0.10	0.00	0.00	0.00	0.00
Muscovite	0.00	0.00	0.00	0.00	0.00
Orthopyroxene	0.00	0.00	0.00	0.00	0.00
Garnet	0.00	0.00	0.00	0.00	0.00
TOTAL	100.10	100.00	100.10	100.10	100.00

SAMPLE	039-2	006-3	104	103	89-019
PLUTON	Striped Hills	M.S. Diorite	M.S. Diorite	M.S. Diorite	M.S. Diorite
Quartz	23.70	10.60	9.50	7.60	11.70
Alkali Feldspar	10.00	10.60	4.30	8.50	6.20
Plagioclase	38.70	52.60	50.30	37.00	34.50
Biotite	7.70	6.80	2.00	2.20	12.40
Hornblende	11.30	6.00	2.60	3.10	9.00
Clinopyroxene	0.00	0.00	0.00	0.00	0.00
Opaque	2.00	4.50	9.80	12.50	11.00
Apatite	0.10	0.80	0.00	0.40	0.00
Sphene	0.10	0.00	0.00	0.00	0.00
Allanite	0.00	0.00	0.00	0.00	0.00
Zircon	0.10	0.50	0.00	0.00	0.00
Chlorite	2.00	4.50	13.10	12.00	12.40
Epidote	4.70	2.30	6.60	14.00	2.80
Calcite	0.00	0.00	0.70	0.00	0.00
Muscovite	0.00	0.80	0.70	1.80	0.00
Orthopyroxene	0.00	0.00	0.00	0.00	0.00
Garnet	0.00	0.00	0.00	0.00	0.00
TOTAL	100.40	100.00	99.60	99.10	100.00

SAMPLE	90-045A	90-043	89-002	006-3
PLUTON	M.S. Diorite	M.S. Diorite	M.S. Diorite	M.S. Diorite
Quartz	9.80	9.30	13.20	6.10
Alkali Feldspar	5.20	9.30	11.20	7.60
Plagioclase	30.90	31.40	41.40	37.60
Biotite	14.40	1.60	0.60	11.20
Hornblende	12.10	0.00	0.00	9.10
Clinopyroxene	0.00	0.00	0.00	0.00
Opaque	5.70	10.10	8.30	4.60
Apatite	0.60	0.80	0.00	0.50
Sphene	0.60	0.70	0.10	0.00
Allanite	0.00	0.00	0.00	0.00
Zircon	1.70	0.70	0.10	0.50
Chlorite	7.90	15.40	15.20	15.70
Epidote	9.50	11.60	8.70	7.10
Calcite	1.70	5.40	0.00	0.00
Muscovite	0.00	4.70	1.20	0.00
Orthopyroxene	0.00	0.00	0.00	0.00
Garnet	0.00	0.00	0.00	0.00
TOTAL	100.10	101.00	100.00	100.00

Appendix A.2

Geochemical data for Teutonia batholith plutonic phases in the Ivanpah Mountains.

SAMPLE	RWS-078	RWS-095	RWS-90-009A	RWS-90-012	RWS-89-012
Rock Unit	Ivanpah	Ivanpah	Ivanpah	Ivanpah	Ivanpah
SiO_2	76.57	69.53	71.34	74.43	71.70
TiO_2	0.04	0.34	0.47	0.11	0.22
Al_2O_3	12.31	15.46	12.93	12.16	13.93
FeO*	0.73	1.56	3.61	6.53	2.23
MgO	0.06	0.22	0.63	0.15	0.29
MnO	0.01	0.01	0.06	0.05	0.02
CaO	0.46	0.46	1.68	0.95	0.78
BaO	0.01	0.07	0.02	0.01	0.04
K_2O	5.16	5.89	4.52	3.94	6.11
Na_2O	3.44	3.92	3.15	3.70	2.95
P_2O_5	0.02	0.05	0.11	0.04	0.06
L.O.I.	0.68	1.27	0.51	0.01	0.61
Total	99.51	98.79	99.02	99.08	98.93
K_2O+Na_2O	8.60	9.81	7.67	7.64	9.06
FeO*/FeO*+MgO	0.92	0.88	0.85	0.98	0.88
moles A/CNK	1.36	1.51	1.38	1.42	1.42
K_2O/Na_2O	1.50	1.50	1.43	1.06	2.07
CIPW Norm					
Quartz	35.79	23.01	31.49	35.68	29.22
Orthoclase	30.49	34.81	26.71	23.28	36.11
Albite	29.11	33.17	26.65	31.31	24.96
Anorthite	2.15	1.96	7.62	4.45	3.45
Corundum	0.28	1.92	0.06	0.18	1.19
Nephaline	0.00	0.00	0.00	0.00	0.00
Diopside	0.00	0.00	0.00	0.00	0.00
Hyperstene	0.15	0.55	1.57	0.37	0.72
Olivine	0.00	0.00	0.00	0.00	0.00
Ilmenite	0.02	0.02	0.13	0.11	0.04
Magnetite	0.00	0.00	0.00	0.00	0.00
Hematite	0.73	1.56	3.61	3.53	2.23
Rutile	0.03	0.33	0.40	0.05	0.20
Sphene	0.00	0.00	0.00	0.00	0.00
Apatite	0.05	0.12	0.25	0.09	0.14
Calcite	0.00	0.00	0.00	0.00	0.00
AN/(AN+AB)	6.88	5.58	22.24	12.44	12.14

SAMPLE	RWS-075	RWS-011	RWS-097	RWS-89-030C	RWS-89-063
Rock Unit	Ivanpah	Ivanpah	Ivanpah	Ivanpah	Ivanpah
SiO_2	72.70	77.17	66.56	69.26	64.91
TiO_2	0.25	0.84	0.56	0.13	0.60
Al_2O_3	13.55	7.98	14.83	15.58	16.49
FeO*	1.65	6.87	3.55	1.13	3.54
MgO	0.41	0.42	1.09	0.25	0.56
MnO	0.03	0.01	0.05	0.01	0.06
CaO	0.77	0.35	2.45	0.90	1.20
BaO	0.01	0.01	0.09	0.08	0.13
K_2O	5.08	2.92	5.26	7.09	5.85
Na_2O	2.90	0.13	3.11	3.57	4.41
P_2O_5	0.02	0.10	0.17	0.09	0.20
L.O.I.	1.63	2.26	0.97	1.45	1.10
Total	99.09	99.06	98.67	99.52	99.04
K_2O+Na_2O	7.98	3.05	8.37	10.66	10.26
FeO*/FeO*+MgO	0.80	0.94	0.77	0.82	0.86
moles A/CNK	1.55	2.35	1.37	1.35	1.44
K_2O/Na_2O	1.75	22.46	1.69	1.99	1.33
CIPW Norm					
Quartz	34.18	64.14	21.96	19.31	14.03
Orthoclase	30.02	17.26	31.09	41.90	34.57
Albite	24.54	1.10	26.32	30.21	37.32
Anorthite	3.69	1.08	10.97	3.88	4.65
Corundum	1.93	4.21	0.00	0.61	1.20
Nephaline	0.00	0.00	0.00	0.00	0.00
Diopside	0.00	0.00	0.00	0.00	0.00
Hyperstene	1.02	1.05	2.71	0.62	1.39
Olivine	0.00	0.00	0.00	0.00	0.00
Ilmenite	0.06	0.02	0.11	0.02	0.13
Magnetite	0.00	0.00	0.00	0.00	0.00
Hematite	1.65	6.87	3.55	1.13	3.54
Rutile	0.22	0.83	0.48	0.12	0.53
Sphene	0.00	0.00	0.05	0.00	0.00
Apatite	0.05	0.23	0.39	0.21	0.46
Calcite	0.00	0.00	0.00	0.00	0.00
AN/(AN+AB)	13.07	49.54	29.42	11.38	11.08

SAMPLE	RWS-89-010	RWS-90-009B	RWS-90-010B	RWS-070	RWS-035
Rock Unit	Ivanpah	Mafic Inclusion in Ivanpah	Kessler Springs	Kessler Springs	Striped Hills
SiO_2	77.11	70.41	69.93	67.81	63.89
TiO_2	0.06	0.42	0.29	0.37	0.51
Al_2O_3	12.28	13.69	13.88	14.97	14.94
FeO*	0.51	2.87	2.75	2.61	4.39
MgO	0.12	0.47	0.33	0.94	1.83
MnO	0.01	0.05	0.03	0.05	0.09
CaO	0.11	1.36	1.63	2.42	4.17
BaO	0.02	0.02	0.08	0.08	0.08
K_2O	5.96	5.63	7.60	3.84	3.39
Na_2O	2.59	3.38	2.46	4.06	2.84
P_2O_5	0.05	0.10	0.11	0.11	0.09
L.O.I.	0.75	0.79	0.18	0.90	1.85
Total	99.57	99.17	99.26	98.16	98.07
K_2O+Na_2O	8.55	9.01	10.06	7.90	6.23
FeO*/FeO*+MgO	0.81	0.86	0.89	0.74	0.71
moles A/CNK	1.42	1.32	1.19	1.45	1.44
K_2O/Na_2O	2.30	1.67	3.09	0.95	1.19
CIPW Norm					
Quartz	38.96	25.98	23.50	23.22	23.44
Orthoclase	35.22	33.27	44.91	22.69	20.03
Albite	21.92	28.60	20.82	34.35	24.03
Anorthite	0.22	5.56	4.39	11.28	18.01
Corundum	1.49	0.00	0.00	0.00	0.00
Nephaline	0.00	0.00	0.00	0.00	0.00
Diopside	0.00	0.00	1.63	0.00	0.52
Hyperstene	0.30	1.17	0.07	2.34	4.32
Olivine	0.00	0.00	0.00	0.00	0.00
Ilmenite	0.20	0.11	0.06	0.11	0.19
Magnetite	0.00	0.00	0.00	0.00	0.00
Hematite	0.51	2.87	2.75	2.61	4.39
Rutile	0.05	0.21	0.00	0.31	0.00
Sphene	0.00	0.38	0.63	0.00	1.00
Apatite	0.15	0.23	0.25	0.25	0.21
Calcite	0.00	0.00	0.00	0.00	0.00
AN/(AN+AB)	0.99	16.28	17.41	24.72	42.84

SAMPLE	RWS-063-1	RWS-063-2	RWS-066A	RWS-006	RWS-103-1
Rock Unit	Oro Wash	Oro Wash	Oro Wash	M.S. Dike	M.S. Dike
SiO_2	52.17	52.24	47.31	53.06	52.37
TiO_2	1.11	1.07	0.05	2.07	1.95
Al_2O_3	17.05	16.59	4.21	15.07	14.94
FeO*	8.23	8.03	16.06	8.69	9.48
MgO	4.39	4.41	12.83	4.17	3.42
MnO	0.15	0.15	1.53	0.15	0.13
CaO	7.55	7.47	11.60	5.61	4.89
BaO	0.07	0.09	0.01	0.03	0.08
K_2O	2.62	3.22	1.02	1.89	2.84
Na_2O	2.94	2.77	0.05	3.97	3.60
P_2O_5	0.22	0.19	0.10	0.33	0.31
L.O.I.	2.31	2.24	1.85	4.07	4.93
Total	98.80	98.46	97.54	99.09	98.94
K_2O+Na_2O	5.56	5.99	1.07	5.86	6.44
FeO*/FeO*+MgO	0.65	0.65	0.56	0.68	0.73
moles A/CNK	1.30	1.23	0.33	1.31	1.32
K_2O/Na_2O	0.89	1.16	20.40	0.48	0.79
CIPW Norm					
Quartz	5.19	4.46	10.22	7.63	7.16
Orthoclase	15.48	19.03	6.03	11.17	16.78
Albite	24.88	23.44	4.32	33.59	30.46
Anorthite	25.59	23.33	6.19	17.72	16.22
Corundum	0.00	0.00	0.00	0.00	0.00
Nephaline	0.00	0.00	0.00	0.00	0.00
Diopside	5.57	7.28	30.37	0.00	0.00
Hyperstene	8.35	7.61	17.87	10.38	8.52
Olivine	0.00	0.00	0.00	0.00	0.00
Ilmenite	0.32	0.32	0.97	0.32	0.28
Magnetite	0.00	0.00	3.52	0.00	0.00
Hematite	8.23	8.03	13.64	8.69	9.48
Rutile	0.00	0.00	0.00	0.26	0.08
Sphene	2.31	2.21	0.00	4.03	4.24
Apatite	0.51	0.44	0.23	0.76	0.72
Calcite	0.00	0.00	4.21	0.00	0.00
AN/(AN+AB)	50.70	49.88	58.90	34.54	34.75

SAMPLE	RWS-103-2	RWS-104-1	RWS-104-2	RWS-89-019	RWS-90-021
Rock Unit	M.S. Dike	M.S. Dike	M.S. Dike	M.S. Dike	M.S. Dike
SiO_2	52.56	50.01	49.36	51.93	50.50
TiO_2	2.01	2.06	2.12	1.62	1.38
Al_2O_3	14.94	14.49	14.60	14.42	14.63
FeO*	9.27	10.11	10.38	8.75	8.15
MgO	3.28	3.67	4.02	3.91	4.96
MnO	0.13	0.15	0.15	0.13	0.11
CaO	4.87	6.15	6.08	5.63	5.58
BaO	0.07	0.04	0.04	0.06	0.02
K_2O	2.77	2.13	2.18	2.50	1.50
Na_2O	3.65	3.40	3.43	3.08	3.04
P_2O_5	0.32	0.29	0.29	0.32	0.32
L.O.I.	5.30	5.61	5.28	5.48	7.54
Total	99.15	98.12	97.93	97.83	97.74
K_2O+Na_2O	6.42	5.53	5.61	5.58	4.54
FeO*/FeO*+MgO	0.74	0.73	0.72	0.69	0.62
moles A/CNK	1.32	1.24	1.25	1.29	1.45
K_2O/Na_2O	0.76	0.63	0.64	0.81	0.49
CIPW Norm					
Quartz	7.57	6.55	5.08	9.12	9.44
Orthoclase	16.37	12.59	12.88	14.77	8.86
Albite	30.89	28.77	29.02	26.06	25.72
Anorthite	16.20	17.99	18.00	18.14	21.85
Corundum	0.00	0.00	0.00	0.00	0.00
Nephaline	0.00	0.00	0.00	0.00	0.00
Diopside	0.00	3.15	2.70	2.00	0.00
Hyperstene	8.17	7.68	8.76	8.81	12.35
Olivine	0.00	0.00	0.00	0.00	0.00
Ilmenite	0.28	0.32	0.32	0.28	0.24
Magnetite	0.00	0.00	0.00	0.00	0.00
Hematite	9.27	10.11	10.38	8.75	8.15
Rutile	0.18	0.00	0.00	0.00	0.18
Sphene	4.14	4.64	4.79	3.62	2.64
Apatite	0.74	0.67	0.67	0.74	0.74
Calcite	0.00	0.00	0.00	0.00	0.00
AN/(AN+AB)	34.40	38.47	38.28	41.04	45.64

VITA

If I am to repent of anything
it is likely to be of my good behavior.

Henry David Thoreau

Stretched to the point of no turning back ... I kept my sense of humor.

...Your beloved Schopenhauer once said that people in their misery are unable to achieve tragedy but are condemned to remain stuck in tragi-comedy. How true it is, and how often I have felt this impression. Yesterday idolized, today hated and spit upon, tomorrow forgotten, and the day after tomorrow promoted to Sainthood. The only salvation is a sense of humor, and we will keep that as long as we still draw breath.

Albert Einstien

P.S. Entropy requires no maintenance.

Micheal Anton Wilson

Ronald Wynn Sheets

is the Navajo symbol for Morning Star which represents guidence, especially guidence into the new day in which all things are possible.